



LIBRARY  
Michigan State  
University

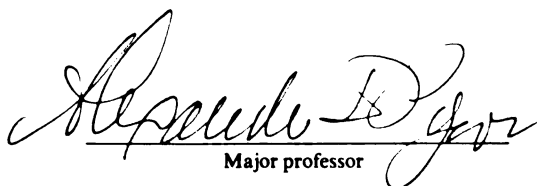
This is to certify that the  
dissertation entitled  
PHYSICOCHEMICAL STUDIES OF LITHIUM ION SOLVATION AND  
MACROCYCLIC COMPLEXATION IN  $\text{AlCl}_3$ -BPCl MOLTEN SALTS

presented by

Rick R. Rhinebarger

has been accepted towards fulfillment  
of the requirements for

Ph.D. degree in Chemistry

  
Major professor

Date November 7, 1985



RETURNING MATERIALS:  
Place in book drop to  
remove this checkout from  
your record. FINES will  
be charged if book is  
returned after the date  
stamped below.

--	--	--





PHYSICOCHEMICAL STUDIES OF LITHIUM ION SOLVATION AND  
MACROCYCLIC COMPLEXATION IN  $\text{AlCl}_3$ -BPCl MOLTEN SALTS

By

Rick R. Rhinebarger

A DISSERTATION

Submitted to

Michigan State University

in partial fulfillment of the requirements

for the degree of

DOCTOR OF PHILOSOPHY

Department of Chemistry

1985

## ABSTRACT

### PHYSICOCHEMICAL STUDIES OF LITHIUM ION SOLVATION AND MACROCYCLIC COMPLEXATION IN $\text{AlCl}_3$ -BPCl MOLTEN SALTS

By

Rick R. Rhinebarger

Multinuclear NMR measurements have been used to study the solvation of various metal ions in the  $\text{AlCl}_3$ -N-butylpyridinium chloride molten salt system. Potentiometry, far-IR spectrophotometry, and x-ray crystallography have provided important supplemental information regarding the nature of the various species and their interactions which occur in this ionic liquid. In addition, the complexation of the lithium ion by crown ethers and cryptand complexants in basic  $\text{AlCl}_3$ -BPCl melts has been investigated.

Lithium-7 NMR studies indicate that in basic melt at  $40^\circ\text{C}$ , the lithium ion exists as both the monomer ( $\text{LiCl}_2^-$ ) and the dimer ( $\text{Li}_2\text{Cl}_4^{2-}$ ) chlorocomplexes, with the latter species predominating by a factor of 9:1 at an analytical lithium ion concentration of 1.0 mol%. Potentiometric data confirm that two chloride ions are associated with each lithium ion in basic melt solutions. Lithium-7 chemical shift and spin-lattice relaxation measurements, and the potentiometry results indicate that anions (other than the chloride ion) which are added to basic melt as the lithium salts do not interact with the lithium ion.

Concentration formation constants for the 12C4, 15C5, B15C5, and 18C6 crown complexes of the lithium ion in basic melt have been determined from the variations of the  $^7\text{Li}$  chemical shifts with the crown/ $\text{Li}^+$  mole ratios. The strong ion pairing occurring in these solutions tends to reduce the selectivity of complexation. The crown complex stabilities decrease in the order  $15\text{C5} \sim \text{B15C5} > 12\text{C4} > 18\text{C6}$ .

Slow chemical exchange has been observed in  $^7\text{Li}$  NMR studies of the complexation of the lithium ion with cryptands C211, C221, C222, and C2 $\beta$ 22 at 40°C and a field strength of 42.28 kG. Concentration formation constants for the C221, C222, and C2 $\beta$ 22 complexes have been determined, with the complex stabilities decreasing in the order  $\text{C221} > \text{C222} > \text{C2}\beta\text{22}$ . The C2 $\beta$ 22·LiAlCl<sub>4</sub> complex has been isolated from basic melt, and its crystal structure determined.

Potentiometric titrations of LiCl in basic melt with 15C5 and C2 $\beta$ 22 indicate that complexation proceeds with retention of the chloride ions in the crown complex, while the chloride ions are released into the solution in the process of cryptate formation.

Far-IR and multinuclear NMR methods have been used to confirm the existence of chlorocomplexes of various heavy metal ions in dilute basic melt solutions of the parent heavy metal chlorides. These complexes appear to be discrete, rather than polymeric species in these solutions.

### **DEDICATION**

It has been said that tolerance, sensitivity, kindness, love, patience, and a willingness to work hard are all important in the pursuit of an advanced degree. Seemingly endless quantities of these things have been supplied by my wife Carolyn throughout this experience. So to her, and to my daughter Rachel, I dedicate this dissertation.



I have always had warm regard for the teachers; those who have helped me to learn. However, I have never had much use for professors of knowledge.



## **ACKNOWLEDGEMENTS**

I would like to thank all of the professional staff for their fine work on my behalf over the past four years. I refuse to refer to these people as just "technical staff" since this devalues their true worth; without them, the job just does not get done.

I would like to thank Professor Popov for his guidance and friendship throughout this study. I would also like to thank Dr. Klaus Hallenga for his patience as I struggled to learn the NMR technique, and for our many helpful discussions.

My very special thanks goes to Sharon Corner who put up with all of my mistakes and the many corrections during the typing of this dissertation. Her fine skills have helped to make this work something of which I can truly be proud.



## TABLE OF CONTENTS

CHAPTER	PAGE
LIST OF TABLES .....	x
LIST OF FIGURES.....	xiv
CHAPTER I - INTRODUCTION AND HISTORICAL PART.....	1
A. Introduction .....	1
B. Historical Part .....	2
1. Molten Salts .....	2
a. Semi-empirical models .....	2
b. Computer simulations .....	4
c. Experimental studies.....	7
(1) general.....	7
(2) ambient temperature systems.....	11
(3) chlorocomplex formation.....	19
2. Multinuclear NMR .....	34
a. Introduction .....	34
b. Lithium-7 .....	35
c. Other metal nuclei.....	41
3. Crown and Cryptand Complexation of Lithium Ion .....	42
a. Introduction .....	42
b. Solution studies .....	43
c. Complex structures .....	47

<b>CHAPTER</b>	<b>PAGE</b>
<b>CHAPTER II - EXPERIMENTAL PART AND DATA TREATMENT.....</b>	<b>51</b>
<b>A. Experimental Part.....</b>	<b>51</b>
1. Molten Salts .....	51
a. Melt Preparation.....	51
(1) $\text{AlCl}_3$ distillation.....	51
(2) $\text{BPCl}$ synthesis .....	53
(3) melt batch mixtures .....	54
b. Purification of Solutes.....	55
(1) lithium salts .....	55
(2) heavy metal compounds .....	55
(3) crown and cryptand ligands.....	56
c. Melt Solution Preparation .....	56
(1) mole ratio samples .....	56
(2) isolation of solid compounds .....	58
2. Lithium-7 NMR.....	59
a. NMR of Solutions .....	59
(1) chemical shift measurements.....	59
(2) spin-lattice relaxation measurements.....	61
b. NMR of Solids .....	63
3. NMR of Other Nuclei .....	65
4. Potentiometry .....	67
a. Cell Design .....	67
b. Titration Methods .....	74
(1) titration of pure basic melt and basic melt solutions of lithium salts .....	74



CHAPTER	PAGE
<ul style="list-style-type: none"> <li> <ul style="list-style-type: none"> <li> <ul style="list-style-type: none"> <li>(2) titration of LiCl-basic melt solutions with crown and cryptand ligands.....</li> </ul> </li> </ul> </li> <li>5. Infrared Spectrophotometry.....</li> <li> <ul style="list-style-type: none"> <li>a. Instrumentation .....</li> <li>b. Cell Configuration .....</li> </ul> </li> <li>B. Data Treatment .....</li> <li> <ul style="list-style-type: none"> <li>1. Lithium-7 NMR .....</li> <li> <ul style="list-style-type: none"> <li>a. KINFIT Nonlinear Least Squares Curve Fitting Program.....</li> <li>b. Nicolet 1180 NTCCAP Subroutine.....</li> <li>c. Relaxation Data Reduction.....</li> </ul> </li> <li>2. Potentiometry .....</li> </ul> </li> </ul>	<ul style="list-style-type: none"> <li>75</li> <li>75</li> <li>75</li> <li>76</li> <li>76</li> <li>76</li> <li>77</li> <li>78</li> <li>80</li> </ul>
CHAPTER III - SOLVATION AND CROWN ETHER COMPLEXATION OF THE LITHIUM ION IN THE $\text{AlCl}_3$ -BPCl SYSTEM.....	84
<ul style="list-style-type: none"> <li>A. Introduction .....</li> <li>B. Solvation of Lithium Salts in Basic and Acidic <math>\text{AlCl}_3</math>-BPCl Melts .....</li> <li> <ul style="list-style-type: none"> <li>1. Lithium-7 NMR .....</li> <li> <ul style="list-style-type: none"> <li>a. Chemical Shift Studies.....</li> <li> <ul style="list-style-type: none"> <li>(1) Lithium Salts in Basic Melt .....</li> <li>(2) Lithium Salts in Acidic Melt.....</li> </ul> </li> <li>b. Spin-Lattice Relaxation Measurements.....</li> </ul> </li> <li>2. Aluminum-27 NMR.....</li> <li>3. Potentiometry.....</li> <li>4. Far-IR Measurements .....</li> </ul> </li> <li>C. Complexation of the Lithium Ion in Basic Melt by Crown Ethers.....</li> <li> <ul style="list-style-type: none"> <li>1. Lithium-7 NMR.....</li> <li>2. Potentiometry.....</li> </ul> </li> </ul>	<ul style="list-style-type: none"> <li>84</li> <li>84</li> <li>84</li> <li>84</li> <li>84</li> <li>95</li> <li>98</li> <li>109</li> <li>113</li> <li>121</li> <li>126</li> <li>126</li> <li>136</li> </ul>

CHAPTER	PAGE
D. Conclusions.....	140
CHAPTER IV - LITHIUM CRYPTATE FORMATION IN THE $\text{AlCl}_3$ -BPCl SYSTEM .....	142
A. Introduction .....	142
B. Basic Melt Solution Studies .....	142
1. Lithium-7 NMR .....	142
2. Potentiometry .....	165
C. Characterization of the Solid Lithium Cryptate Complexes .....	168
1. Elemental Analyses .....	168
2. Lithium-7 Magic Angle Spinning NMR .....	170
3. The X-ray Crystal Structure of $\text{C}_{22}\text{B}_{10}\cdot\text{LiAlCl}_4$ .....	177
D. Conclusions .....	184
CHAPTER V - HEAVY METAL CHLOROCOMPLEX FORMATION IN THE $\text{AlCl}_3$ -BPCl SYSTEM .....	188
A. Introduction .....	188
B. Solvation of Heavy Metal Salts in Basic and Acidic $\text{AlCl}_3$ -BPCl Melts.....	188
1. Basic Melt Solutions .....	188
2. Acidic Melt Solutions .....	192
C. Solution NMR Studies .....	194
1. Cadmium-113 NMR .....	194
2. Tin-119 and Tin-117 NMR.....	196
3. Zinc-67 NMR .....	201
4. Mercury-199 NMR .....	201
5. Copper-63 and Lead-207 NMR .....	205
D. Far-IR Measurements of Heavy Metal Salt-Basic $\text{AlCl}_3$ -BPCl Melt Mixtures .....	205
E. Conclusions .....	213



CHAPTER	PAGE
CHAPTER VI - SUGGESTIONS FOR FUTURE STUDIES .....	217
A. Lithium Chlorocomplexes in Basic Melt .....	217
B. Macrocyclic Complexation of the Lithium Ion and Other Alkali Metal Ions.....	217
C. Heavy Metal Ion Chlorocomplex Formation .....	218
APPENDICES .....	220
Appendix 1.....	220
A. The Two-Site Fast Exchange Model for the Determination of Equilibrium Constants.....	220
1. SUBROUTINE EQNS. ....	223
B. The Three-Site Fast Exchange Model for the Determination of Equilibrium Constants .....	227
1. SUBROUTINE EQN. ....	229
Appendix 2 .....	231
A. Crystallographic Data for the $C_{2v}22 \cdot LiAlCl_4$ Complex .....	231
1. Bond Distances and Bond Angles.....	231
2. Least Squares Planes .....	231
REFERENCES .....	241





## LIST OF TABLES

Table	Page
1     Melting Points of Some Low-Melting ( $T_m < 300^\circ\text{C}$ ) Organic Salts. ....	9
2     Low and Ambient Temperature Halocuprate Molten Salt Mixtures. ....	12
3     Physical and Transport Properties of the $\text{AlCl}_3\text{-BPCl}$ and $\text{AlCl}_3\text{-ImCl}$ Molten Salt Systems. ....	17
4     Species Characterization in the $\text{AlCl}_3\text{-BPCl}$ and $\text{AlCl}_3\text{-ImCl}$ Molten Salt Systems. ....	23
5     Absorption Spectroscopic Parameters for Chlorocomplexes in $\text{AlCl}_3\text{-BPCl}$ and $\text{AlCl}_3\text{-ImCl}$ Melts. ....	32
6     Lithium-7 $T_1$ Relaxation Times in Various Media. ....	38
7     Crystalline Crown Complexes of the Lithium Ion. ....	49
8     NMR Characteristics of Selected Nuclei Studied in $\text{AlCl}_3\text{-BPCl}$ Melts.....	66
9     Chemical Shift Reference Solutions Used in NMR Measurements of Other Nuclei in $\text{AlCl}_3\text{-BPCl}$ Melts. ....	69
10    Lithium-7 Chemical Shift Data for $\text{LiCl}$ -Basic Melt Solutions at $40^\circ\text{C}$ . ....	88
11    Lithium-7 Chemical Shift Data for $\text{LiCl}$ -Acidic Melt Solutions at $40^\circ\text{C}$ . ....	99



<b>Table</b>		<b>Page</b>
12	Lithium-7 $T_1$ Relaxation times for Aqueous LiCl and LiClO <sub>4</sub> Solutions at 25°C and 40°C. ....	101
13	Lithium-7 $T_1$ Relaxation Times for Some Lithium Salts in the AlCl <sub>3</sub> -BPCl System at 25°C and 40°C.....	103
14	Lithium-7 Nuclear Quadrupole Coupling Constants in Various Substances. ....	106
15	Lithium-7 $T_1$ Relaxation Times for 1.0 Mol% LiCl in Basic Melt as a Function of Temperature (40°C to 85°C). ....	107
16	Linewidths ( $\Delta\nu_{1/2}$ ) and Apparent Spin-Spin Relaxation Times ( $T^*_2$ ) for the <sup>7</sup> Li NMR Signal of 1.0 Mol% LiCl in Basic Melt as a Function of Temperature (27°C to 150°C).....	110
17	Potentiometric Titration Data: Corrected Values of X <sub>Cl<sup>-</sup></sub> Calculated by Using Equation 53; pCl = -Log X <sub>Cl<sup>-</sup></sub> . ....	117
18	Values for $n^D \gg e$ , $n^*Cl^-$ , $n^o_{LiX}$ , and $n^*_{total}$ Used in the Calculation of x for the Assumed LiCl <sub>x</sub> <sup>(1-x)</sup> Chlorocomplexes Formed in LiCl and LiClO <sub>4</sub> -Basic Melt Solutions.....	122
19	Lithium-7 Chemical Shifts as a Function of Crown/Lithium Ion Mole Ratio in Basic Melt at 40°C. ....	128
20	Lithium Ion-Crown Complex Formation Constants and Limiting Chemical Shifts for the Crown Complexes in Basic Melt at 40°C. ....	134
21	Log $K_F$ and $\delta_C$ Values for Lithium Ion-Crown Complexes in Basic AlCl <sub>3</sub> -BPCl Melts and in Various Nonaqueous Solvents. ....	135

<b>Table</b>	<b>Page</b>
22 Potentiometric Titration Data: Observed Cell Potentials as a Function of 15C5 Titrant(mg) and the 15C5/Lithium Ion Mole Ratio at 35°C.....	137
23 Lithium-7 Chemical Shifts Observed for the Cryptand C211, C221, C222, and C2B22 - Lithium Ion Mole Ratio Studies in Basic Melt at 40°C.....	152
24. Calculated Linewidths of the $^7\text{Li}$ NMR Signals of the $\text{Li}^+$ -C222 Complex in Basic Melts at 40°C. ....	158
25 The Fractions of "Free" and Complexed Lithium Ion Obtained by Deconvolution of $^7\text{Li}$ NMR Spectra in the Cryptand/Lithium Ion Mole Ratio Studies in Basic Melt. Cryptate Complex Formation Constants Calculated by Using Equation 13. ....	162
26 Lithium Cryptate Stability Constants in Basic Melt, Water, and Various Nonaqueous Solvents. ....	164
27 Potentiometric Titration Data: Observed Cell Potentials as a Function of C2B22 Titrant(mg) and the C2B22/Lithium Ion Mole Ratio. ....	167
28 Summary of the Elemental Analyses of the $\text{C2B22}\cdot\text{LiAlCl}_2$ and $\text{C211}\cdot\text{LiAlCl}_4$ Cryptate Complexes.....	169
29 Lithium-7 Solid State NMR Results for Various Lithium Compounds.....	175
30 Crystallographic Parameters and Data Collection Conditions for the Determination of the Structure of the $\text{C2B22}\cdot\text{LiAlCl}_4$ Cryptate Complex. ....	179

<b>Table</b>	<b>Page</b>
31    Some Important Bond Distances ( $\overset{\text{O}}{\text{\AA}}$ ) and Bond Angles (Degrees) for the $\text{C}_{2\text{B}}22\cdot\text{LiAlCl}_4$ Cryptate Complex. ....	180
32    Least Squares Calculations: The Deviations ( $\overset{\text{O}}{\text{\AA}}$ ) of the Lithium Ion from Coincidence with Planes Defined by Sets of Oxygen and Nitrogen Atoms in the $\text{C}_{2\text{B}}22\cdot\text{LiAlCl}_4$ Cryptate Complex. ....	186
33    Heavy Metal Chlorides in Basic $\text{AlCl}_3$ -BPCl Melt: Minimum Solubilities at 25°C. ....	189
34    Elemental Analyses of the Solid Adduct of $\text{SnCl}_4$ Isolated from Basic $\text{AlCl}_3$ -BPCl Melt Solution. ....	193
35    Mercury-199 NMR Chemical Shift Data for $\text{HgCl}_2$ -Basic $\text{AlCl}_3$ -BPCl Melt Solutions. ....	203
36    Far-IR Bands and Assignments for the Normal Mode Vibrations of the $\text{AlCl}_4^-$ Ion in Basic $\text{AlCl}_3$ -BPCl Melt. ....	208
37    Far-IR Studies of Heavy Metal Chloride-Basic $\text{AlCl}_3$ -BPCl Melt Solutions: Band Frequencies and Assignments. ....	210
38    Raman and Far-IR Studies of the $\text{SnCl}_6^{2-}$ Chlorocomplex in the Solid State. ....	215

## LIST OF FIGURES

Figure	Page
1      Log N versus Mol% AlCl <sub>3</sub> : Populations of AlCl <sub>4</sub> <sup>-</sup> , Al <sub>2</sub> Cl <sub>7</sub> <sup>-</sup> , and Cl <sup>-</sup> ions as a function of mole fraction AlCl <sub>3</sub> in the AlCl <sub>3</sub> -BPCl molten salt system. ....	15
2      E(V) <u>vs.</u> Al reference electrode versus mole fraction AlCl <sub>3</sub> : Potentiometric titration curve for the Co/Co <sup>2+</sup> couple as a function of mole fraction AlCl <sub>3</sub> in the AlCl <sub>3</sub> -BPCl molten salt system. Taken from reference 74. ....	29
3      Schematic curve depicting the potentiometric titration of dilute metal chloride - basic AlCl <sub>3</sub> -BPCl melt solutions. ....	30
4      Pyrex ampule used for AlCl <sub>3</sub> distillations.....	52
5      Intensities of the <sup>7</sup> Li NMR signal of 4 M LiClO <sub>4</sub> in D <sub>2</sub> O versus pulse width for the 10 mm high frequency probe.....	64
6      Concentration electrochemical cell used in potentiometric titrations of basic AlCl <sub>3</sub> -BPCl melt solutions. ....	73
7      Lithium-7 NMR spectrum: 1.0 Mol% LiCl in basic AlCl <sub>3</sub> -BPCl melt at 40°C. ....	85
8      Concentration dependence of the <sup>7</sup> Li chemical shift of LiCl in basic melt at 40°C. ....	87
9      Computer analysis of the observed dependence of <sup>7</sup> Li chemical shifts on LiCl concentration in basic melt. ....	90



<b>Figure</b>		<b>Page</b>
10	Structures of the LiSCN dimers and tetramers in nonaqueous solvents: A. Dimer; B. Tetramer. Taken from references 164 and 165. ....	91
11	Proposed structure of the lithium enolate triple ion - $\text{Li}^+\text{C}_{211}$ complex. ....	93
12	Proposed structure of the lithium dimer chlorocomplex in LiCl-basic melt solutions. ....	94
13	Lithium-7 chemical shifts versus temperature for 1.0 mol% LiCl in basic melt. ....	96
14	Lithium-7 NMR spectrum: 1.0 mol% LiCl in acidic $\text{AlCl}_3\text{-BPCl}$ melt at 40°C. ....	97
15	Lithium-7 NMR spectra: Signal intensities versus delay time for 4 <u>M</u> $\text{LiClO}_4$ in $\text{D}_2\text{O}$ at 40°C. ....	100
16	$\text{Ln}(1/T_1)$ versus $1/T(\text{K})$ for $^7\text{Li}$ in 1.0 mol% LiCl-basic melt solution. ....	108
17	$\text{Ln}(1/T^*_2)$ versus $1/T(\text{K})$ for $^7\text{Li}$ in 1.0 mol% LiCl-basic melt solution. ....	111
18	Aluminum-27 NMR spectrum: 45 mol% $\text{AlCl}_3\text{-BPCl}$ melt at 40°C. ....	112
19	Aluminum-27 NMR: linewidth as a function of composition in $\text{AlCl}_3\text{-BPCl}$ melts at 36°C. Taken from reference 182. ....	114



Figure		Page
20	Potentiometry: $E_{\text{cell}}$ versus acidic melt titrant (g) for the titration of 45 mol% $\text{AlCl}_3$ - $\text{BPCl}$ melt. The results for duplicate titrations are shown: Titration #1 (O), Titration #2 (●). The uncertainties in the cell potentials and in the mass of the titrant are smaller than the size of the data points. ....	115
21	Potentiometry: $E_{\text{cell}}$ versus $\text{pCl}$ (corrected) for the titration (#1) of basic melt with acidic melt titrant. ....	119
22	Potentiometry: $E_{\text{cell}}$ versus acidic melt titrant (g) for the titrations of 0.977 mol% $\text{LiCl}$ -basic melt (O) and 0.960 mol% $\text{LiClO}_4$ -basic melt (□) solutions. The uncertainties in the cell potential and in the mass of the titrant are smaller than the size of the data points. ....	120
23	Far-IR spectra (150 to 600 $\text{cm}^{-1}$ ): A. Basic melt; B. 1 mol% $\text{LiCl}$ -basic melt solution; C. 1 mol% $\text{LiCl}$ -1.5 mol% $\text{C}_{211}$ -basic melt solution. ....	123
24	Far-IR spectrum (150 to 650 $\text{cm}^{-1}$ ): 1.0 mol% $^6\text{LiCl}$ in basic melt. ....	125
25	The structures of 12C4, 15C5, B15C5, and 18C6. ....	127
26	Lithium-7 chemical shifts as a function of ligand/lithium ion mole ratio for the determination of the concentration formation constants of $\text{Li}^+$ -crown complexes in basic melt at 40°C. Solid lines are the computer-generated curves. ....	132
27	Potentiometry: $E_{\text{cell}}$ versus 15C5 titrant (mg) and 15C5/lithium ion mole ratio. ....	139

<b>Figure</b>		<b>Page</b>
28	The structures of C211, C221, C222 and C2 <sub>B</sub> 222. ....	143
29	Lithium-7 NMR spectrum: 0.985 mol% LiCl-0.888 mol% C211 in basic melt at 40°C. The upfield signal is assigned to the complexed lithium ion site.....	144
30	Lithium-7 NMR spectrum: 0.992 mol% LiCl-0.988 mol% C221 in basic melt at 40°C. The upfield signal is assigned to the complexed lithium ion site. ....	145
31	Lithium-7 NMR spectrum: 0.980 mol% LiCl-0.987 mol% C222 in basic melt at 40°C. The position of the maximum of the unresolved bandshape is taken to correspond to the chemical shift of the complexed lithium ion site. ....	146
32	Lithium-7 NMR spectrum: 1.00 mol% LiCl-0.949 mol% C2 <sub>B</sub> 222 in basic melt at 40°C. The upfield signal is assigned to the complexed lithium ion site. ....	147
33	Lithium-7 chemical shifts for "free" and complexed lithium ion at 40°C as functions of the C211/lithium ion mole ratio in basic melt. Uncertainties in the chemical shifts are indicated by the size of the data points. ....	149
34	Lithium-7 chemical shifts for "free" and complexed lithium ion at 40°C as functions of the C221/lithium ion mole ratio in basic melt. ....	150
35	Lithium-7 chemical shifts for "free" and complexed lithium ion at 40°C as functions of the C2 <sub>B</sub> 222/lithium ion mole ratio in basic melt.....	151
36	Lithium-7 NMR spectra: Observed bandshapes at 40°C for C222/lithium ion mole ratios of 0.757 to 2.80:1. ....	155

<b>Figure</b>		<b>Page</b>
37	Lithium-7 chemical shifts for the $\text{Li}^+$ -C222 complex in basic melt at 40°C as a function of the C222/lithium ion mole ratio. ....	157
38	Potentiometry: $E_{\text{cell}}$ versus C2B22 titrant (mg) and the C2B22/lithium ion mole ratio. ....	166
39	Lithium-7 solid state NMR spectra: Static (top) and magic angle spinning (@2.7 kHz) (bottom) spectra for polycrystalline LiCl at 22°C (100 scans). ....	171
40	Lithium-7 Solid State NMR spectra: Static (top) and magic angle spinning (@1.8 kHz) (bottom) spectra for polycrystalline $\text{LiAlCl}_4$ at 22°C (100 scans). ....	172
41	Lithium-7 solid state NMR spectra: Static (top) and magic angle spinning (@2.1 kHz) (bottom) spectra for polycrystalline $\text{C}_2\text{B}_{22}\cdot\text{LiAlCl}_4$ at 22°C (20,000 scans). ....	173
42	Lithium-7 solid state NMR spectra: Static (top) and magic angle spinning (@0.8 kHz) (bottom) spectra for polycrystalline $\text{C}_{211}\cdot\text{LiAlCl}_4$ at 22°C (20,000 scans). ....	174
43	Atomic numbering scheme for heavy atoms in the C2B22 molecule. ....	178
44	The crystal structure of $\text{C}_2\text{B}_{22}\cdot\text{LiAlCl}_4$ : The $\text{C}_2\text{B}_{22}\cdot\text{LiAlCl}_4$ molecule viewed along the <u>b</u> axis. ....	181
45	The crystal structure of $\text{C}_2\text{B}_{22}\cdot\text{LiAlCl}_4$ : A view of the unit cell along the <u>b</u> axis. ....	182
46	The crystal structure of $\text{C}_2\text{B}_{22}\cdot\text{LiAlCl}_4$ : A view of the unit cell along the <u>a</u> axis. ....	183

Figure		Page
47	The crystal structure of $C_{2B}22 \cdot LiAlCl_4$ : A closeup view of the cryptated lithium ion. The oxygen and nitrogen atoms are labeled according to the scheme in Figure 43. ....	185
48	Cadmium-113 NMR spectrum: 2.88 mol% $CdCl_2$ in basic $AlCl_3$ -BPCl melt at 40°C. Chemical shifts are scaled to 0.5 M $CdCl_2/D_2O$ taken as 0.0 ppm. ....	195
49	Cadmium-113 NMR spectrum: 3.95 mol% $CdCl_2$ in acidic $AlCl_3$ -BPCl melt at 40°C. Chemical shifts are scaled as in Figure 48. ....	197
50	Tin-119 NMR spectra: 3.29 mol% $SnCl_2$ (A) and 0.955 mol% $SnCl_2$ (B) in basic $AlCl_3$ -BPCl melt. ....	198
51	Tin-117 NMR spectrum: 3.29 mol% $SnCl_2$ in basic $AlCl_3$ -BPCl melt. ....	200
52	Zinc-67 NMR Spectrum: 1.56 mol% $ZnCl_2$ in Basic $AlCl_3$ -BPCl melt. ....	202
53.	Mercury-199 NMR: Chemical shifts versus mol% $HgCl_2$ in basic $AlCl_3$ -BPCl melts. ....	204
54	Far-IR spectrum (150 to 600 $cm^{-1}$ ): Basic $AlCl_3$ -BPCl melt; A. 0.05 mm spacer; B. 0.1 mm spacer. ....	207
55	Far-IR spectra (150 to 600 $cm^{-1}$ ): Basic $AlCl_3$ -BPCl melt solutions of heavy metal chlorides. A. 2.98 mol% $CdCl_2$ ; B. 1.56 mol% $ZnCl_2$ ; C. 6.66 mol% $CuCl$ ; D. 2.37 mol% $HgCl_2$ ; E. 3.29 mol% $SnCl_2$ .....	209
56	Far-IR spectrum (200 to 515 $cm^{-1}$ ): The $SnCl_4$ adduct isolated from Basic $AlCl_3$ -BPCl melt solution. ....	214

## **CHAPTER I**

### **INTRODUCTION AND HISTORICAL PART**

## **A. Introduction**

A comprehensive theory of liquids must account for the physical chemical behavior exhibited by all classes of liquids. The historical development and refinement of this theory has largely proceeded from the viewpoint of molecular liquids and dilute electrolyte solutions. The wealth of experimental data and theoretical contributions of such notables as Raoult, Henry, Gibbs, Fuoss, and many others testify to the tremendous interest in these systems.

For molten salts, no less effort has been expended in the development of theoretical models for melt structure, mass transport in molten salts, and melt thermodynamic properties. However, generation of a similarly large experimental data base which could be used to refine these models, has proceeded more slowly than for aqueous and nonaqueous solutions. This information gap has been most pronounced in the area of spectroscopy. Information from this source could provide valuable insight into melt structure, and aid in the identification of discrete complex ions, whose existence can be inferred from thermodynamic and transport property measurements. Spectroscopic studies have been hampered, at least in part, by the extensive instrumental modifications and special containment methods required for measurements on corrosive, high temperature molten salts. These limitations have had significant impact in the area of nuclear magnetic resonance, where few investigations of molten salts exist. With the recent expansion of the NMR technique to include dozens of nuclei in the periodic table besides proton and carbon-13, the potential for applications of this method to studies of molten salts is clear.

The feasibility for such investigations by NMR techniques has been dramatically improved through the recent development of a new class of molten salts. These compounds and mixtures have been found to exist as stable,

anhydrous ionic liquids near, or even below room temperature. These materials, which usually contain large organic cations and polyatomic inorganic anions, contain several NMR-active nuclei which can be used to probe the chemical and magnetic environment of the melt. Their structural diversity gives rise to numerous vibrational modes that can be studied by using infrared and Raman spectroscopy.

Studies of the thermodynamics and kinetics of metal ion solvation and complexation in nonaqueous solvents by using NMR and vibrational spectroscopy have been conducted in this laboratory for many years. Therefore, it seemed logical to include a molten salt as a unique alternative medium, with which similar investigations could be performed. The system chosen for these studies consists of mixtures of aluminum chloride and N-butylpyridinium chloride ( $\text{AlCl}_3\text{-BPCl}$ ), which are found to be stable liquids near room temperature.

Recent work has shown that several alkali metal ions, heavy metal ions, and neutral synthetic ionophores (crowns and cryptands) are soluble in these media. NMR, vibrational spectroscopy, and potentiometry have been used to study ionic association (aggregate formation, metal ion chlorocomplexation) and macrocyclic complex formation in the melt. In this dissertation, the chemical and structural factors that influence these interactions are discussed.

## **B. Historical Part**

### **B.1. Molten Salts**

#### **B.1.a. Semi-empirical models**

Theoretical treatments of the structural features of ionic liquids are usually derived from one of two viewpoints. Lattice-oriented models are formulated by considering the liquid state to originate from the fusion of a solid ionic lattice. For gas-oriented models, the liquid is obtained by condensing a vapor

of ions. The principal observation that a given model must account for is that the volume of an ionic substance usually increases on fusion, while the mean interionic distance usually decreases (electrostriction). Empty space is therefore introduced in the melting process. The description of this empty space, how it is distributed within the melt, and how it arises (from ionic lattice or ionic vapor), are the main features which differentiate these various models.

An early (1964) review by Bloom and Bockris (1) traces the chronological development of these theories from their first formulations in the late 1800's. Based on its ability to better predict thermodynamic and transport properties, Bockris (2) has argued that the hole model (lattice-oriented) originally proposed by Furth (3) must be considered superior to both gas-oriented models, and rigid lattice models. The success of this model may be attributed to its greater structural flexibility, which rigid lattice models do not possess. Holes are imagined to be of variable size, randomly distributed throughout the liquid. More stringent limitations are placed on the size and distribution of the vacancies proposed in the quasi-lattice model of Frenkel (4). The main difficulties encountered with the gas-oriented models are their inability to account for the observed entropies of fusion, and the aforementioned positive volume change and electrostriction on melting (5).

It should be noted that the models just described are semi-empirical in nature. Macroscopic properties are calculated as adjustable parameters in the phenomenological expressions for these properties. None of these models provide a complete description of the microphysical situation concerning the type and magnitude of interactions of species in the molten salt.



### **B.1.b. Computer simulations**

Methods which provide a theoretically more satisfying modeling of molten salt physical properties than empirical models are Monte Carlo (MC) or molecular dynamics (MD) calculations. In these techniques, a mathematical expression assuming pair-wise potential of interaction of the ions is used to compute thermodynamic, transport and structural properties of the ionic liquid. The potential function can include terms for charge-charge, charge-dipole, dipole-dipole, and higher order charge-multipole and multipole-multipole interactions. The starting point for the simulation is usually taken as the rigid ionic lattice at a given temperature (MC), or total energy (MD). Experimental values for lattice distances, ionization energies, and electron affinities are provided for the system to be simulated. With the ever-increasing speed and capacity of modern digital computers, simulations of 1000 or more interacting ions are becoming feasible. The simulation proceeds by first allowing the ionic lattice to "melt", so that a thermally-equilibrated liquid state can be achieved after a number of incremental steps. Pre-equilibrated or "aged" liquid configurations may also be chosen as the starting point of the simulation.

In the Monte Carlo method, the multidimensional integrals derived from statistical mechanics are evaluated numerically, allowing calculation of the average energy of the system. A series of configurations (and associated energies) are generated by a random walk procedure, in which the position of a random particle is varied in small, random steps. A comparison of the energy of the new configuration with the previous one is made. If the new configuration is of higher energy, it is discarded. If lower in energy, the new configuration is retained. The resulting configuration chain is used to calculate ensemble average properties. This process can provide exact values in the limit of infinite chain length. To alleviate problems with edge or boundary

limits, the small system can be made to behave as an infinite (macroscopic) one by surrounding it with periodically repeated images of itself. Due to the practical (computer time) limits on ensemble size and chain length, the accuracy of calculations of, for example, specific heats or hydrostatic pressures can be poor (6).

The molecular dynamics method performs a numerical solution of Newton's equations of motion for a group of particles (ions) constituting a system. The increment used here is a time step, and the computer calculates the forces acting on each particle once during each time step of the simulation. This method enables calculation of time-dependent (transport) phenomena as well as the system thermodynamic properties. The longest calculations of this type cover a time span of about  $10^{-9}$  seconds, with time steps ranging from  $10^{-15}$  to  $10^{-11}$  seconds.

The first extensive Monte Carlo computation for an ionic liquid was by Woodcock and Singer (6). These workers calculated the radial distribution function (RDF), normal melting point, and a number of thermodynamic properties (molar heat capacity, compressibility, entropy, etc.) for potassium chloride by using a Born-Mayer-Huggins pair potential of the form

$$\phi_{ij}(r) = \zeta_i \zeta_j r^{-1} + b e^{(B(\sigma_{ij}-r))} + C_{ij} r^{-6} + d_{ij} r^{-8} \quad (1)$$

where  $\sigma_{ij}$ ,  $c_{ij}$ , and  $d_{ij}$  are obtained from X-ray and spectroscopic data for this salt. By using the MC method, Larsen and co-workers (7) calculated the molar volume, internal energy, entropy, and free energy at zero pressure for liquid sodium chloride and potassium chloride at 1083 K, as well as  $\Delta V$ ,  $\Delta E$ ,

$\Delta S$ , and  $\Delta G$  of mixing for the 1:1 (Na,K)Cl system under the same conditions. The agreement between the calculated and experimental RDF's for the mixture was excellent.

Recently, analyses of structure and deviations from ideal behavior for binary molten salt mixtures have been carried out in MD studies of the LiCl-KCl system. In the work by Caccamo and Dixon (8), partial RDF's were calculated for all possible (+,+), (+,-), and (-,-) interactions as functions of melt composition and temperature. Their results indicated that the coordination number ( $n$ ) of lithium ion was four, and that the partial RDF for  $\text{Li}^+-\text{Cl}^-$  ( $g_{\text{Cl-Li}}(r)$ ) had a well-defined peak at  $2.2 \text{ \AA}$ . Both of these results were unaffected by composition or temperature. For comparison, the sum of the Pauling ionic radii for lithium and chlorine is  $2.4 \text{ \AA}$  (9). These authors also noted an increase in the calculated Coulombic energy as the concentration of lithium ions was increased.

In a latter MD study of the LiCl-KCl eutectic (58.3 mol% LiCl) by Okada et al. (10), a coordination number of four was also obtained for lithium ion. In addition, the angular distribution function ( $P_{-+-}(\theta)$ ) was determined at 668 and 913 K. The  $P_{-+-}(\theta)$  curves for  $\text{Cl}^--\text{Li}^+-\text{Cl}^-$  interaction showed maxima at  $\theta = 100^\circ$  and  $105^\circ$ , respectively. This indicated that lithium ion has a nearly regular tetrahedral environment of chloride ions in this melt. Moreover, the tendency was toward the perfect tetrahedral angle ( $109.47^\circ$ ) with increasing temperature, or decreasing lithium ion concentration. Both of these factors would be assumed to produce less interference from the second-neighbor lithium ions.

An additional MD study of MX,  $\text{AX}_3$ , and  $\text{MAX}_4$  mixtures by Sabounji et al. (11) relates most closely to the  $\text{AlCl}_3\text{-BPCl}$  system studied in this dissertation. Their results showed that characteristics of binary  $\text{MAX}_4$  melts

(eg.  $\text{NaAlCl}_4$ ) ascribed to covalency and other nonionic pair interactions could be simulated by using the MD technique. Coordination numbers and angular distribution functions indicated the presence of  $\text{A}_2\text{X}_7^-$  ( $\text{Al}_2\text{Cl}_7^-$ ) and  $\text{A}_3\text{X}_{10}^-$  ( $\text{Al}_3\text{Cl}_{10}^-$ ) complexes. For the  $\text{NaAlCl}_4$  system, the equilibrium constants involving these species were far too large in comparison with experimental data for this system. These authors stated that this lack of quantitative agreement with experiment was due to the fact that no dispersion force terms (which could have produced polarization or covalency effects) were not included in the pair interaction potential. Woodcock has recently reviewed progress in the application of MD calculations to ionic liquids (12).

To date, no similar studies of ambient temperature binary molten salt mixtures such as the  $\text{AlCl}_3$ - $\text{BPCl}$  system have been published. In addition, the potentially powerful local ordering effect of lithium ion (thus providing a ternary salt system) has not been studied in an ambient temperature mixture. In view of the extensive organometallic chemistry exhibited by lithium, it is possible that the polarizing influence and/or covalent bonding tendency of lithium could result in the formation of lithium complexes with polarizable anions (such as chloride) in a room-temperature melt.

### **B.1.c. Experimental Studies**

#### **B.1.c.(1) general**

Experimental investigations of molten salts date back to Michael Faraday, who studied about fifty of these materials. A comparative electromotive force series of the elements, and the fundamental law of electrolysis which bears his name were obtained in these studies (13).

Molten salts may be conveniently catagorized in terms of the temperature at which these exist as stable liquids. Alkali and alkaline earth halides, metal

chalcogenides, and most transition metal halides and oxides have melting points above 300°C, and are thus referred to as high temperature molten salts. In the liquid state these materials are usually highly corrosive, requiring special containment such as noble metal, quartz, or refractory oxide vessels.

A wide range of inorganic and organic salts and their mixtures have melting points between room temperature and 300°C, and may be termed as low-melting molten salts. Silver nitrate (m.p. = 212°C), potassium thiocyanate (m.p. = 173°C), and thallium(III) carbonate (m.p. = 273°C) are typical of the few anhydrous inorganic salts that melt within this temperature range (14). The organic salts in this group possess tremendous structural diversity, combining large organic cations with inorganic (halide, nitrate, perchlorate, etc.) or organic (picrate, benzoate, etc.) anions. A representative list of some of these compounds and their melting points is provided in Table 1.

These organic salts are generally non-corrosive to borosilicate glass, and may be handled with high vacuum and controlled atmosphere techniques. A liquid range of 30°C to 100°C is normally accessible for the measurement of temperature-dependent properties, which is small compared to the ranges for high temperature melts. For example, the liquid range for NaCl is in excess of 600°C (14). However, some organic salts, such as 4-methyl-N-methylpyridinium chloride, decompose at their melting points (18).

The third class of salts are liquid at, or below, room temperature, and sometimes are referred to as room, or ambient temperature melts. Examples of pure compounds of this type are ethylammonium nitrate (m.p. = 8°C) and tetra-N-hexylammonium benzoate (m.p. = -50°C) (15). In addition, 4-ethyl-N-methylpyridinium bromide is a viscous red oil at 25°C (26). However, the majority of ambient temperature melts developed since the early 1950's

**Table 1. Melting Points of Some Low-Melting ( $T_m < 300^\circ\text{C}$ ) Organic Salts**

<b>Compound</b>	<b>Melting Point (<math>^\circ\text{C}</math>)</b>	<b>Ref.</b>
alkylammonium and quaternary ammonium salts:		
tri-isopentylammonium iodide	100	15
tetramethylammonium bromide	230	14
tetra-N-butylammonium perchlorate	208	15
tetra-N-pentylammonium thiocyanate	51	15
ethoxymethyldiethyl-methylammonium iodide	84	15
tetra-N-propylammonium picrate	118	15
quaternary arsonium and phosphonium salts:		
tetraphenylarsonium chloride	247	15
tributylbenzylphosphonium chloride	162	14
anilinium, pyridinium, and imidazolium salts:		
N,N-dimethylanilinium bisulphate	88	15
N-ethylanilinium chloride	179	17
pyridinium chloride	146	18
pyridinium bromide	220	16
4-methylpyridinium bromide	162	19
4-tertbutylpyridinium chloride	154	20
2-methylpyridinium iodide	132	21
3-methylpyridinium bromide	96	22
1-methyl-3-ethylimidazolium chloride	124	23
1-isobutylimidazolium picrate	95	24
1-ethyl-3-methylimidazolium tetraphenylborate	140	25

are mixtures of aluminum halides with organic halides.

The first system of this type was reported in 1951 by Hurley and Wier (27), who studied the electrodeposition of several metals from a 2:1 mixture of aluminum chloride and N-ethylpyridinium bromide ( $\text{AlCl}_3\text{-EPBr}$ ; m.p. =  $-40^\circ\text{C}$ ). The same solvent was used by Chum *et al.* (28) in electrochemical studies of organometallic iron complexes and hexamethylbenzene at  $25^\circ\text{C}$ . Osteryoung and co-workers also investigated the electrochemical properties of transition metal carbonyls (28), and electroinitiated Friedel-Crafts transalkylations (29) in  $\text{AlCl}_3\text{-EPBr}$  mixtures with benzene. The principal disadvantage of this molten salt system is that only a very narrow composition range, close to the 2:1 mole ratio, is liquid at room temperature.

In 1979, Robinson and Osteryoung (20) reported the synthesis of a closely related system composed of aluminum chloride and N-butylpyridinium chloride ( $\text{AlCl}_3\text{-BPCl}$ ). It was found that these mixtures are stable liquids at  $40^\circ\text{C}$  over the composition range 0.75:1 to 2:1  $\text{AlCl}_3\text{-BPCl}$ . Since this initial investigation, more than 100 papers have been published describing various studies of this, and other room temperature melts. Chum and Osteryoung (30) have reviewed some of this work (through 1981).

In 1981, Wilkes and Levisky (31) described the synthesis of a series of dialkylimidazolium halide salts which, when combined with  $\text{AlCl}_3$  ( $\text{AlCl}_3\text{-ImX}$  mixtures), give ionic liquids at or below room temperature across an even wider composition range (0.30:1 to 2:1  $\text{AlCl}_3\text{-ImX}$ ) than that of the  $\text{AlCl}_3\text{-BPCl}$  system. Two of these salts, 1-methyl-3-butylimidazolium iodide and 1-methyl-3-benzyl-imidazolium chloride, were found to be liquid at room temperature. Because of accessibility as liquids at room temperature across a wider composition range, the imidazolium salts have been used more frequently than BPCl in recent room temperature molten salt studies.

A novel group of low-melting and ambient temperature molten salt mixtures has been reported by Yoke (32-34) and Bowmaker (25). These materials are combinations of tertiary or quaternary arsonium, phosphonium, piperidinium, or ammonium halides, with cuprous halides. A list of these is given in Table 2. These systems are of interest mainly due to the presence of copper chlorocomplexes such as  $\text{CuCl}_2^-$  in these melts.

In this historical review, no attempt is made to thoroughly discuss the considerable body of data which has been generated concerning the chemical, spectroscopic, and transport properties of the high temperature and low-melting molten salts. However, specific information on these systems which relates to this work, particularly in regard to NMR and chlorocomplex formation in molten salts, is referred to as necessary.

Readers interested in these data for the high and low-melting systems are referred to the extensive compilations of Janz and various co-workers (35-42). Reviews by Boston (43) and Lind (44) cover progress in the investigations of molten haloaluminate salts, and the physical properties of molten organic salts, respectively. Additional periodic reviews of all aspects of molten salt chemistry by Blomgren and Van Artsdalen (13), Kleppa (45), Yosim and Reiss (46), and Angell (47) are recommended.

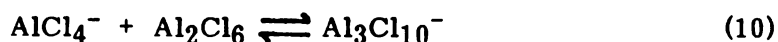
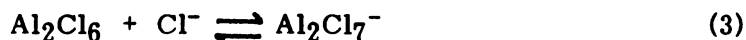
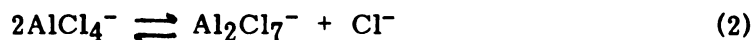
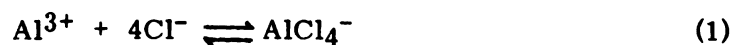
#### **B.1.c. (2) ambient temperature systems**

Mixtures of  $\text{AlCl}_3$  and  $\text{BPCl}$  constitute an acid-base system where  $\text{AlCl}_3$  serves as a Lewis acid (chloride ion acceptor), and  $\text{BPCl}$  as a Lewis base (chloride ion donor). By analogy with the low-melting  $\text{AlCl}_3\text{-MCl}$  ( $\text{M}$  = alkali metal cation) systems, a number of equilibria involving various melt species have been proposed as follows (48).



**Table 2. Low and Ambient Temperature Halocuprate Molten Salt Mixtures**

Mixture	Melting Point (°C)	Ref.
low -melting (25-300°C):		
tri-N-butylammonium chloride/CuCl (nBu) <sub>3</sub> NH <sup>+</sup> <sub>2</sub> CuCl <sub>3</sub> <sup>2-</sup> @ 2:2	?	33
tetraethylammonium chloride/CuCl	105-108	33
ethylammonium chloride/CuCl	109	35
tetra-N-butylammonium chloride/CuCl	68	34
tetraphenylarsonium chloride/CuCl	176-178	34
tetraethylammonium bromide/CuBr	149-151	34
tetra-N-butylammonium bromide/CuBr	84	34
ambient:		
triethylphosphonium chloride/CuCl CuCl <sub>2</sub> <sup>-</sup> @ 1:1 and CuCl <sub>3</sub> <sup>2-</sup> @ 2:1	--	33
N-ethylpiperidinium chloride/CuCl CuCl <sub>2</sub> <sup>-</sup> @ 1:1 and Cu <sub>2</sub> Cl <sub>3</sub> <sup>-</sup> @ 1:1	--	33
tri-N-butylammonium chloride/CuCl CuCl <sub>2</sub> <sup>-</sup> @ 1:1 and Cu <sub>2</sub> Cl <sub>3</sub> <sup>-</sup> @ 1:2	--	33



On the basis of Raman vibrational spectra, Gale et al. (49) reported that unlike the  $\text{AlCl}_3\text{-MCl}$  systems, no evidence for free  $\text{AlCl}_3$  or  $\text{Al}_2\text{Cl}_6$  could be found for the  $\text{AlCl}_3\text{-BPCl}$  system, even at high (2:1)  $\text{AlCl}_3\text{-BPCl}$  mole ratios. Assuming that the activities of  $\text{Al}^{3+}$  and  $\text{Al}_3\text{Cl}_{10}^-$  ions were negligible, Gale and Osteryoung (48) found that potentiometric data could be adequately fitted to the equilibrium shown in equation (2). Thus, a mole fraction scale equilibrium constant of  $3.8 \times 10^{-13}$  at  $30^\circ\text{C}$  was obtained. As the temperature was increased to  $175^\circ\text{C}$ , this constant increased to values approaching those found in the  $\text{AlCl}_3\text{-MCl}$  systems at  $400^\circ\text{C}$  or  $450^\circ\text{C}$ . Schoebrechts and Gilbert (50) obtained a value of  $1.2 (\pm 0.2) \times 10^{-13}$  at  $40^\circ\text{C}$ . Robinson and Osteryoung (51) later found that addition of 50% (v/v) of benzene in a similar titration had little effect on the equilibrium constant ( $K_{\text{eq}} = 2.2 \times 10^{-13}$  at  $30^\circ\text{C}$ ).

In solution,  $\text{Al}_2\text{Cl}_7^-$  and  $\text{Cl}^-$  ions are the predominant acidic and basic species, respectively. The melt acidity can be changed by variation of the starting component mole ratio within which a homogeneous liquid state is attainable at a given temperature. A convenient means by which the melt acidity can be monitored is by measurement of the chloride ion concentration,

or  $pCl$ , which is defined by

$$pCl \equiv -\log X_{Cl^-} \quad (6)$$

where  $X_{Cl^-}$  is the mole fraction of free chloride ion in the melt. From the standpoint of  $Al_2Cl_7^-$  ion, an expression analogous to equation (6) can be defined for  $p(Al_2Cl_7^-)$ , but the  $pCl$  definition is traditionally used in the literature.

This definition presumes the Temkin ideal solution model (52), where the activity of an ion is equal to its mole fraction in solution. Thus, the  $pCl$  range for the  $AlCl_3$ - $BPCl$  system spans about  $10^{15}$  in  $X_{Cl^-}$  at room temperature, which is comparable to the pH acidity scale for aqueous solutions. Mixtures containing excess  $AlCl_3$  ( $X_{AlCl_3} > 0.5$ ) are referred to as acidic melts, while melts with  $X_{AlCl_3} < 0.5$  are termed as basic. The neutral melt naturally corresponds to the 50:50  $AlCl_3$ - $BPCl$  composition.

In acidic melts,  $Al_2Cl_7^-$  and  $AlCl_4^-$  ions are the predominant anionic species, and  $Cl^-$  and  $AlCl_4^-$  ions predominate in basic melts. A graphical representation of the populations of these anions as a function of  $AlCl_3$  mole fraction is shown in Figure 1.

In the Raman experiments cited above (49), bands consistent with chloroaluminate ions were observed at  $40^\circ C$ . The four observed bands were assigned to the  $AlCl_4^-$  ion (1:1 melt), verifying the supposed  $T_d$  symmetry for this species. The relatively poor quality of spectra for the 2:1 melt did not allow an unequivocal interpretation to confirm the expected  $D_{3d}$  symmetry for the  $Al_2Cl_7^-$  ion. This symmetry group would have been appropriate for an assumed linear  $Al-Cl-Al$  bridge.

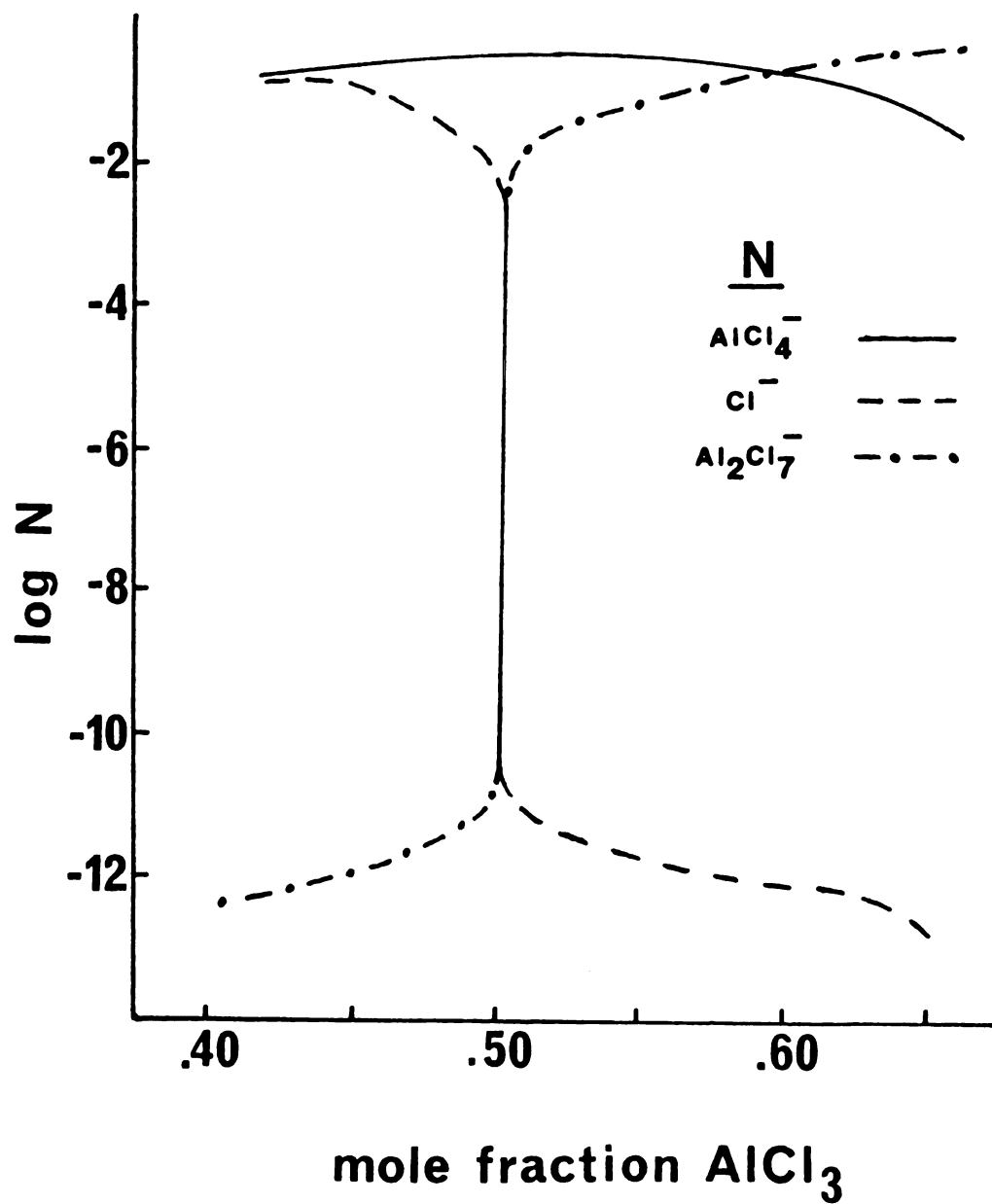


Figure 1.  $\log N$  versus mol%  $\text{AlCl}_3$ : Populations of  $\text{AlCl}_4^-$ ,  $\text{Al}_2\text{Cl}_7^-$ , and  $\text{Cl}^-$  ions as a function of mole fraction  $\text{AlCl}_3$  in the  $\text{AlCl}_3$ - $\text{BPCl}$  molten salt system.

Infrared measurements by Gale and Osteryoung (53), and Tait and Osteryoung (54) showed that the  $\nu_3(F_2)$  band for  $AlCl_4^-$  ion ( $490\text{ cm}^{-1}$ , strong) was split into three bands. Thus, the normally infrared-inactive  $\nu_1(A_1)$  and  $\nu_2(E)$  modes appeared as shoulder bands at  $476\text{ cm}^{-1}$  and  $525\text{ cm}^{-1}$ , respectively. This strong perturbation was cited as evidence for substantial association between  $BP^+$  and  $AlCl_4^-$  ions in these melts. The latter work (54), which included study of the  $AlCl_3$ -ImCl (ImCl = 1-methyl-3-ethylimidazolium chloride) system, provided a detailed interpretation of the vibrational modes observed for the  $BP^+$  and  $Im^+$  cations. The broadening and low frequency shifts (by 2 to  $6\text{ cm}^{-1}$ ) of the cation bands, as compared with those reported for solid N-methylpyridinium iodide, were cited as support for the idea of strong cation-anion associations in the melts. These effects were minimized in highly acidic melts.

Only a few investigations of the transport properties of the  $AlCl_3$ -BPCl melts have been reported. Carpio et al. (55) determined the density, specific conductance, and dynamic viscosity of several N-alkyl-pyridinium halides and their mixtures with  $AlCl_3$  (including 2:1  $AlCl_3$ -BPCl) as functions of temperature. Nanjundiah and co-workers (56) measured the density and dynamic viscosity of the  $AlCl_3$ -BPCl system at  $40^\circ\text{C}$  as functions of melt composition. Fannin et al. (57) conducted similar studies on several  $AlCl_3$ -1,3-dialkylimidazolium chloride mixtures at various temperatures and compositions. Some representative data from these and other studies are shown in Table 3.

Ultraviolet and visible spectrophotometric studies of the  $AlCl_3$ -BPCl melts have been directed mainly to the investigation of chlorocomplexes of various metal cation solutes. A discussion of these studies is given in the following section on chlorocomplexation.

Table 3. Physical and Transport Properties of the  $\text{AlCl}_3\text{-BPCl}$  and  $\text{AlCl}_3\text{-ImCl}$ (1) Molten Salt Systems

Melt System	Temp. ( $^{\circ}\text{C}$ )	Density ( $\text{g/cm}^3$ )	Specific Conductance ( $\Omega^{-1}\text{ cm}^{-1}$ )	Viscosity (poise)	Ref.
2:1 $\text{AlCl}_3\text{-BPCl}$	25	1.33	$5.8 \times 10^{-3}$	0.272	59
	25	1.346	$6.8 \times 10^{-3}$	0.210	56
	40	1.334	$1.0 \times 10^{-2}$	0.141	55
	40	1.328	--	0.143	57
1:1 $\text{AlCl}_3\text{-BPCl}$	40	1.244	--	0.243	57
	40	1.224	$3.9 \times 10^{-3}$	0.211	59
0.8:1 $\text{AlCl}_3\text{-BPCl}$	40	1.220	--	0.370	57
2:1 $\text{AlCl}_3\text{-ImCl}$	40	1.370	$2.1 \times 10^{-2}$	0.097	58
1:1 $\text{AlCl}_3\text{-ImCl}$	40	1.279	$3.2 \times 10^{-2}$	0.122	58
0.8:1 $\text{AlCl}_3\text{-ImCl}$	40	1.245	$1.7 \times 10^{-2}$	0.271	58

(1) ImCl = 1-methyl-3-ethylimidazolium chloride

The majority of NMR studies of the  $\text{AlCl}_3$ -BPCl melts have been devoted to characterization of ionic associations in these media. Robinson *et al.* (58) obtained the  $^1\text{H}$  and  $^{13}\text{C}$  NMR spectra for the 1:1 and 2:1  $\text{AlCl}_3$ -BPCl melts, as well as solutions of these melts with benzene. Upon addition of benzene, the aromatic carbon signals of the  $\text{BP}^+$  cation were observed to shift upfield compared to their positions in the pure melts. This was interpreted as indicating that addition of benzene was responsible for the disruption of cation-anion ion pairing in the 1:1 or 2:1 melt solutions.

Taullele and Popov (59) obtained similar results in a high resolution  $^1\text{H}$  and  $^{13}\text{C}$  NMR study of 1:1  $\text{AlCl}_3$ -BPCl melt, and mixtures of this melt with nitromethane- $\text{D}_3$ . For the pure melt, sharp breaks in the  $^1\text{H}$  chemical shift versus  $\text{AlCl}_3$ -BPCl mole ratio curves occurred at the 1:1 composition at  $40^\circ\text{C}$ . These authors concluded that  $\text{BP}^+ - \text{AlCl}_4^-$  association was essentially quantitative at this temperature. It was also reported in this study that  $\text{LiCl}$  is soluble in several basic ( $0.45 \leq X_{\text{AlCl}_3} \leq 0.47$ ) and acidic ( $0.50 \leq X_{\text{AlCl}_3} \leq 0.67$ )  $\text{AlCl}_3$ -BPCl mixtures, as evidenced by the observation of  $^7\text{Li}$  NMR signals in these samples at  $40^\circ\text{C}$ . Lithium chloride appeared to be insoluble (no  $^7\text{Li}$  NMR signal observed) in melts with the composition of  $0.48 \leq X_{\text{AlCl}_3} \leq 0.50$ .

Matsumoto and Ichikawa (60) have recently measured the  $^{27}\text{Al}$  NMR spin-lattice ( $T_1$ ) relaxation times for the  $\text{AlCl}_3$ -BPCl system at various compositions and temperatures. Single-exponential magnetization recovery curves (inversion-recovery method) were observed for melts with  $0.45 \leq X_{\text{AlCl}_3} \leq 0.50$  and  $X_{\text{AlCl}_3} = 0.67$  compositions. The resulting relaxation rates ( $R_i$ ) were  $R_{\text{AlCl}_4^-} = 55 \pm 5 \text{ sec}^{-1}$  ( $T_1 = 18.2 \pm 1.7 \text{ ms}$ ) and  $R_{\text{Al}_2\text{Cl}_7^-} = \text{ca. } 1000 \text{ sec}^{-1}$  ( $T_1 \sim 1 \text{ ms}$ ). Between 50 mol%  $\text{AlCl}_3$  and 67 mol%  $\text{AlCl}_3$ , and above 67 mol%  $\text{AlCl}_3$  compositions, nonlinear logarithmic recovery curves were

obtained, indicating the presence of chemical exchange between  $\text{AlCl}_4^-$  and  $\text{Al}_2\text{Cl}_7^-$ , and  $\text{Al}_2\text{Cl}_7^-$  and  $\text{Al}_3\text{Cl}_{10}^-$  ions, respectively.

Wilkes et al. (61) and Fannin et al. (62) have used  $^1\text{H}$  NMR to study the  $\text{AlCl}_3$ - $\text{ImCl}$  molten salt system and its mixtures with  $\text{LiCl}$  or nonaqueous solvents. In the former study, correlations between  $^1\text{H}$  NMR chemical shifts of the  $\text{Im}^+$  cation with melt composition were cited as a suitable basis for an analytical method for determining melt composition. In the latter study, the dependence of proton chemical shifts of the 1-methyl-3-ethylimidazolium cation on the mole fraction of  $\text{AlCl}_3$  was observed to be qualitatively similar to that observed for the  $\text{AlCl}_3$ - $\text{BPCl}$  system (58,59), with a clear break in the chemical shift - mole fraction  $\text{AlCl}_3$  curve at  $X_{\text{AlCl}_3} = 0.5$ . It was observed that the proton at ring position 2 (H-2) of the  $\text{Im}^+$  cation exhibited even greater chemical shift sensitivity to melt composition than that of the ring protons adjacent to nitrogen in the  $\text{BP}^+$  cation ( $\Delta\delta = -1.6$  ppm versus  $-0.45$  ppm, respectively). The H-2 proton also showed a small effect ( $\Delta\delta = -0.40$  ppm) on addition of  $\text{LiCl}$  as a third component. This was interpreted as indicating that the  $\text{Li}^+$  cation was competing with the  $\text{Im}^+$  cation for the  $\text{Cl}^-$  anion in the melt. The authors devised a quantitative model to fit these chemical shift data by assuming association of the  $\text{Im}^+$  ion with two or more of the  $\text{Cl}^-$ ,  $\text{AlCl}_4^-$ , or  $\text{Al}_2\text{Cl}_7^-$  ions in the melt (triple ions or higher aggregates; 5-site fast chemical exchange). Efforts to obtain a good fit of chemical shift data for the ternary system containing  $\text{LiCl}$  were not successful.

### **B.1.c.(3) chlorocomplex formation**

One of the most controversial concepts in studies of the structure of molten salts is the existence of discrete complex ions. These species have been invoked to explain the non-ideal behavior sometimes exhibited by these systems. For



example, for molten mixtures of KCl and  $\text{CdCl}_2$  at  $780^\circ\text{C}$ , a minimum of equivalent conductance is observed near  $2\text{KCl}-\text{CdCl}_2$  stoichiometry, implying the existence of the  $\text{CdCl}_4^{2-}$  chlorocomplex (63).

The microscopic structural situation in a molten salt is clearly different from that found in an aqueous or nonaqueous electrolyte solution. In the latter, ions are solvated by neutral solvent molecules, whereas in the former, ions are "solvated" by other ions. Therefore, one is faced with the difficult task of trying to distinguish a particular set ( $m$ ) of  $\text{X}^-$  anions clustered about an  $\text{M}^{n+}$  cation (forming a  $\text{MX}_m^{(n-m)}$  chlorocomplex) from all other  $\text{X}^-$  anions in the molten salt.

Most workers in this area have taken the observation of a vibrational spectrum, consistent with the number of fundamental modes predicted for the assumed symmetry group for the complex, as "proof" of the existence of that species. However, Wilmschurst (64) has argued that for most binary molten salt systems, one can not distinguish between a discrete complex species (a kinetic entity exhibiting normal mode vibrations), and a polymeric complex (exhibiting quasi-lattice vibrations).

Although UV-visible absorption spectrophotometry has been used in numerous molten salt studies, the time scale for this technique ( $\sim 10^{-15}$  sec) is too short compared to the diffusion time ( $10^{-5}$  to  $10^{-8}$  sec) for the term "complex ion" to be meaningful. Terms such as "configuration" or "center" are used to describe the local structure about the metal ion. Typical examples of these studies are the investigations of nickel(II) coordination ( $\text{NiCl}_4^{2-}$  chlorocomplex) in molten  $\text{ZnCl}_2$ -KCl mixtures at  $250$ - $900^\circ\text{C}$  by Angell and Gruen (65), and cobalt(II) coordination ( $\text{CoCl}_4^{2-}$  chlorocomplex) in molten  $\text{AlCl}_3$ -KCl mixtures at  $300^\circ\text{C}$  by Oye and Gruen (66).

With a time scale of  $10^{-5}$  to  $10^{-8}$  seconds, the NMR technique has the

potential for providing more convincing evidence for the existence of a complex species in a molten salt than any other experimental method (67). The earliest reported use of NMR to investigate halocomplex formation in these media was by Rowland and Bromberg (68) who observed  $^{205}\text{Tl}$  NMR resonance lines for both  $\text{Tl}^+$  and  $\text{TlX}_4^-$  ( $\text{X} = \text{Cl}^-$  or  $\text{Br}^-$  ions) in molten  $\text{TlX-TlX}_3$  mixtures. They estimated the average lifetimes of these species to be  $10^{-5}$  seconds at  $500^\circ\text{C}$ . Hafner and Nachtrieb (69) concluded that overlap of the cation-anion wavefunctions (incipient covalency), rather than induced polarization of the thallium ion by halide ions, was the cause of the observed high sensitivity of  $^{205}\text{Tl}$  chemical shifts ( $\Delta\delta \sim 2500$  ppm) to changes in counterion.

Chlorocomplex formation is, of course, a central feature in the  $\text{AlCl}_3\text{-BPCl}$  molten salts. Evidence for the  $\text{AlCl}_4^-$  and  $\text{Al}_2\text{Cl}_7^-$  chloroaluminate ions in this system has already been discussed.

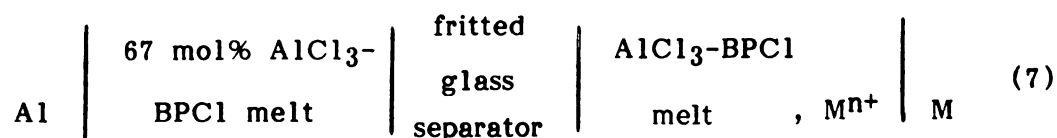
One of the principal practical reasons for studies of ambient temperature molten salts is their potential use as anhydrous electrolytes in new high specific energy battery systems (70). In the development of such a system, the performance characteristics of anodic and cathodic materials, as well as identification of the majority charge carriers and their transport properties, are of fundamental interest. Therefore, much attention has been devoted to characterizing the properties of metal-metal ion couples, and chlorocomplexes of these metal ions in these melts. Electrochemical methods, UV-visible spectrophotometry, and transport property measurements have been used to acquire this information.

Chlorocomplexes of representative, transition, lanthanide, and actinide elements have been studied in the  $\text{AlCl}_3\text{-BPCl}$  system. In addition, chlorocomplexes of halogens, coordination complexes of several transition metal ions, and the behavior of electrically-conducting polymer films have

been studied in these melts (56,71-92). A list of these systems and the techniques used in these investigations is given in Table 4. Chlorocomplex formation constants, where available, are also shown.

For dilute solutions of solute metal ions in basic melts, free chloride ion is available for coordination of these metal ions, thus forming the metal chlorocomplexes. Chlorocomplexes can also form in acidic melt mixtures that contain these metal ions, but the resulting chlorocomplexes have chloride ion/metal ion stoichiometries that are different from those observed in basic melts (see, eg., ref. 89 and 91). With the exception of  $W_2Cl_9^{3-}$  and  $W_2Cl_9^{2-}$  (83), only mononuclear chlorocomplexes have been observed in the  $AlCl_3$ -BPCl or  $AlCl_3$ -ImCl melts.

Potentiometry has been used to determine the coordination numbers and chlorocomplex formation constants for these species at various temperatures. Using standard cell notation, the cell used in these studies is



(see, eg., ref. 76).

In this cell, the aluminum electrode dipping into an acidic melt serves as the reference electrode. The working metal electrode (M) is made reversible to  $Mn^{+}$  activity by the addition of the metal chloride salt to the working compartment, or electrolytic oxidation of the M electrode just prior to the titration. Considering, for a moment, the symmetric concentration cell configuration where  $M = Al$ , the reaction at the cathode is

**Table 4. Species Characterization in the  $\text{AlCl}_3\text{-BPCl}$  and  $\text{AlCl}_3\text{-ImCl}$  Melts**

Species	Methods Used	Molten Salt System	Log $\beta_F$	Temp. ( $^{\circ}\text{C}$ )	Ref.
$\text{NiCl}_4^{2-}$	AS, PT	$\text{AlCl}_3\text{-BPCl}$	46	40	71
$\text{Fe(III)/Fe(II)}$	RD, CV, PT	$\text{AlCl}_3\text{-BPCl}$	--	40	72
$\text{TiCl}_6^{2-}$ , $\text{TiOCl}_4^{2-}$	NP, CV, CP, RP, CA	$\text{AlCl}_3\text{-BPCl}$	--	40	73
$\text{CoCl}_4^{2-}$	AS, PT, CV, CA	$\text{AlCl}_3\text{-BPCl}$	46	40	74
$\text{FeCl}_4^-$ , $\text{FeCl}_4^{2-}$	CP, CV, RD, PT	$\text{AlCl}_3\text{-BPCl}$	-, 37	40	56
$\text{AgCl}_2^-$ , $\text{AgCl}_3^{2-}$ , $\text{AgCl}_4^{3-}$	PT	$\text{AlCl}_3\text{-BPCl}$	20, 21, 23	40	76
$\text{AgCl}_3^{2-}$ , $\text{AgCl}_4^{3-}$	PT	$\text{AlCl}_3\text{-ImCl}$	20, 22	40	76
$\text{CuCl}_4^{3-}$ , $\text{CuCl}_6^{4-}$	PT, RD, CV	$\text{AlCl}_3\text{-BPCl}$	23, 52	40	77
$\text{CuCl}_2^-$ , $\text{CuCl}_3^{2-}$ , $\text{CuCl}_4^{3-}$	AS, PT	$\text{AlCl}_3\text{-ImCl}$	23, --, 26 22, 24, 25 19, 21, 22	40 60 100	81 81 81
$\text{MoCl}_6^{2-}$ , $\text{MoCl}_6^{3-}$	AS, CV, CP RD	$\text{AlCl}_3\text{-BPCl}$ & $\text{-ImCl}$	--	40	78

Table 4 continued

Species	Methods Used	Molten Salt System	Log $\beta_F$	Temp. (°C)	Ref.
$WCl_6^-$ , $WCl_6^{2-}$ , $WCl_6^{3-}$	AS, CV, RD, CP	$AlCl_3$ -ImCl	--	40	82
$W_2Cl_9^{3-}$ , $W_2Cl_9^{2-}$					
$SmCl_2^+$ , $SmCl_6^{3-}$	NP, CV, AS, CA	$AlCl_3$ -BPCl	$SmCl_2^+ = 11$	40	79
$YbCl_2^+$ , $YbCl_6^{3-}$ , $YbCl^{2+}$					
$EuCl_6^{3-}$					
$TmCl_2^+$ , $TmCl^{2+}$	AS, NP, CV, CA	$AlCl_3$ -BPCl	--	40	80
$UCl_3^+$ , $UCl_2^{2+}$ , $UCl^{3+}$	RD, AS, CP	$AlCl_3$ -BPCl	--	40	90
$UCl_6^-$					
$NpCl_3^+$ , $NpCl_2^{2+}$ , $NpCl^{2+}$	AS, RD, CV	$AlCl_3$ -BPCl	--	40	92
$SbCl_2^+$ , $SbCl_4^-$ , $SbCl_6^-$	CV, RD, CP, PT	$AlCl_3$ -BPCl	22, 65, --	40	88
$Cl_3^-$	RD, CV, AS, CP	$AlCl_3$ -BPCl & - ImCl	--	40	83
$AlCl_3I^-$ , $ICl$ $Al_2Cl_6I^-$	CV, RD, CA, AS, NP, RP	$AlCl_3$ -BPCl	--	40	86

Table 4 continued

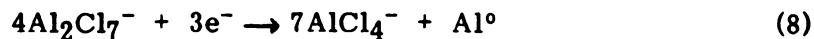
Species	Methods Used	Molten Salt System	Log $\beta_F$	Temp. (°C)	Ref.
$\text{Fe}(\text{bpy})_3^{2+/3+}$	CV, RD, AS	$\text{AlCl}_3\text{-BPCl}$	--	40	84
$\text{Ru}(\text{bpy})_3^{2+/3+}$					
$\text{Fe}(\text{phen})_3^{3+/2+}$					
$\text{Ru}(\text{bpy})_2(\text{vp})_3^{3+/2+}$	CV, CA, LSV	$\text{AlCl}_3\text{-BPCl}$ & - $\text{ImCl}$	--	40	91
polypyrrole/ ferrocene	CV	$\text{AlCl}_3\text{-BPCl}$	--	40	85
ferrocene/ ferrocenium	CV, RD, CP, RP	$\text{AlCl}_3\text{-BPCl}$	--	40	87
$\text{Ru}(\text{bpy})_2(\text{vp})_2^{3+/2+}$	CV	$\text{AlCl}_3\text{-BPCl}$	--	40	89
polyvinylferrocene thionine					

**Abbreviations:**

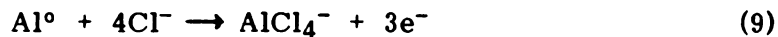
CV - cyclic voltammetry  
 PT - potentiometry  
 AS - UV-visible absorption spectroscopy  
 CA - chronoamperometry  
 RD - rotating disk electrode voltammetry  
 NP - normal pulse voltammetry  
 CP - controlled potential coulometry  
 RP - reverse pulse voltammetry  
 LSV - linear sweep voltammetry

**Table 4 continued**

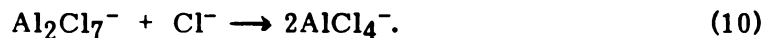
bpy - 2,2'-bipyridine  
phen - 1,10-phenanthroline  
vp - vinyl pyridine



and at the anode,

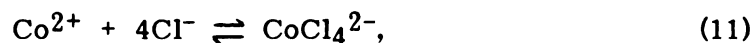


with the overall cell reaction (93) written as



For the cases where other  $\text{M}/\text{M}^{n+}$  couples are used in the working compartment, a specific example illustrating the determination of chlorocomplex coordination number ( $n$ ) and the mole fraction scale formation constant ( $K_X$ ) is useful.

Hussey and Laher (74) studied potentiometrically the  $\text{Co}/\text{Co}^{2+}$  couple in the  $\text{AlCl}_3$ - $\text{BPCl}$  system at  $36^\circ\text{C}$ . For the reaction



the cobalt electrode potential is given by

$$E_W = E_X^{\circ'} + \frac{RT}{2F} \ln X_{\text{Co}^{2+}} \quad (12)$$

where  $E_X^{\circ'}$  is the mole fraction-based apparent standard potential of the  $\text{Co}/\text{Co}^{2+}$  couple in a 67 mol%  $\text{AlCl}_3$ - $\text{BPCl}$  melt at  $36^\circ\text{C}$ . The titration is carried out by measuring the cell potential as weighed amounts of  $\text{AlCl}_3$  are added to the working compartment to increase the melt acidity. The titration curve



which is obtained in this experiment is shown in Figure 2.

Substituting the equilibrium expression for reaction (11) into the Nernst equation (12) yields

$$E_W = E^{\circ'}_X + \frac{RT}{2F} \ln X_{\text{CoCl}_4^{2-}} - \frac{RT}{2F} \ln K_X - \frac{RT}{2F} \ln X_{\text{Cl}^-}^4 \quad (13)$$

where the liquid junction potential is assumed to be negligible (82). A plot of  $E_{\text{cell}}$  versus  $\ln X_{\text{Cl}^-}$  gives a straight line with a least squares slope of  $121 \pm 2$  mV, in good agreement with the theoretical value of 122 mV predicted for fourth-power dependence of the cell potential on  $X_{\text{Cl}^-}$  for the  $\text{CoCl}_4^{2-}$  chlorocomplex. In a separate experiment, a value for  $E^{\circ'}_X$  for the  $\text{Co}/\text{Co}^{2+}$  couple is determined by adding weighed amounts of  $\text{CoCl}_2$  to 67 mol%  $\text{AlCl}_3$ - $\text{BPCl}$  melt in the working compartment, and measuring the cell potential. Using equation (12), the intercept of a plot of  $E_{\text{cell}}$  versus  $\ln X_{\text{Co}^{2+}}$  is  $+0.894 \pm 0.002$  Volts at  $36^\circ\text{C}$ . An average  $K_X$  value is then calculated from several  $X_{\text{Cl}^-}$  values. Thus, a  $K_X$  value of  $1.6 \times 10^{46}$  for  $\text{CoCl}_4^{2-}$  is obtained at this temperature.

The curves obtained in titrations of this type can be broken down into three regions. This is shown in Figure 3. In the first region, free chloride ion from the melt reacts with the solid  $\text{AlCl}_3$  titrant to form  $\text{AlCl}_4^-$  ion in solution



Once the free chloride ion is consumed, chloride ion from the metal chlorocomplex (with general formula  $\text{MCl}_x^{(n-x)}$ ) reacts with  $\text{AlCl}_3$  according to

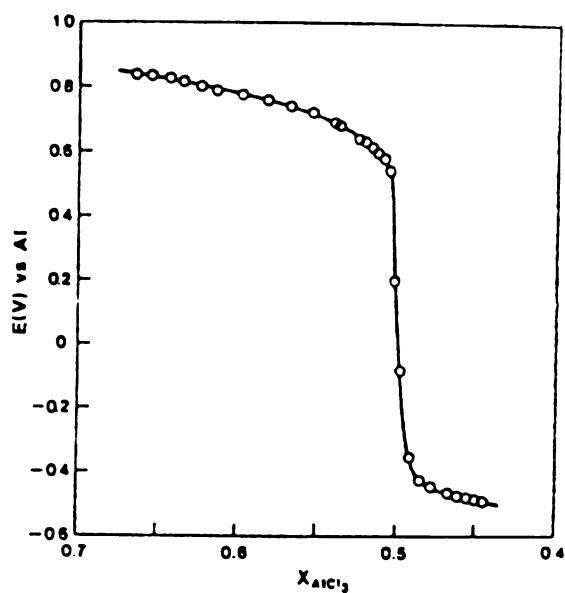


**Figure 2.**  $E$  (V) vs. Al reference electrode versus mole fraction  $\text{AlCl}_3$ : Potentiometric titration curve for the  $\text{Co}/\text{Co}^{2+}$  couple as a function of mole fraction  $\text{AlCl}_3$  in the  $\text{AlCl}_3$ -BPCl molten salt system. Taken from reference 74.

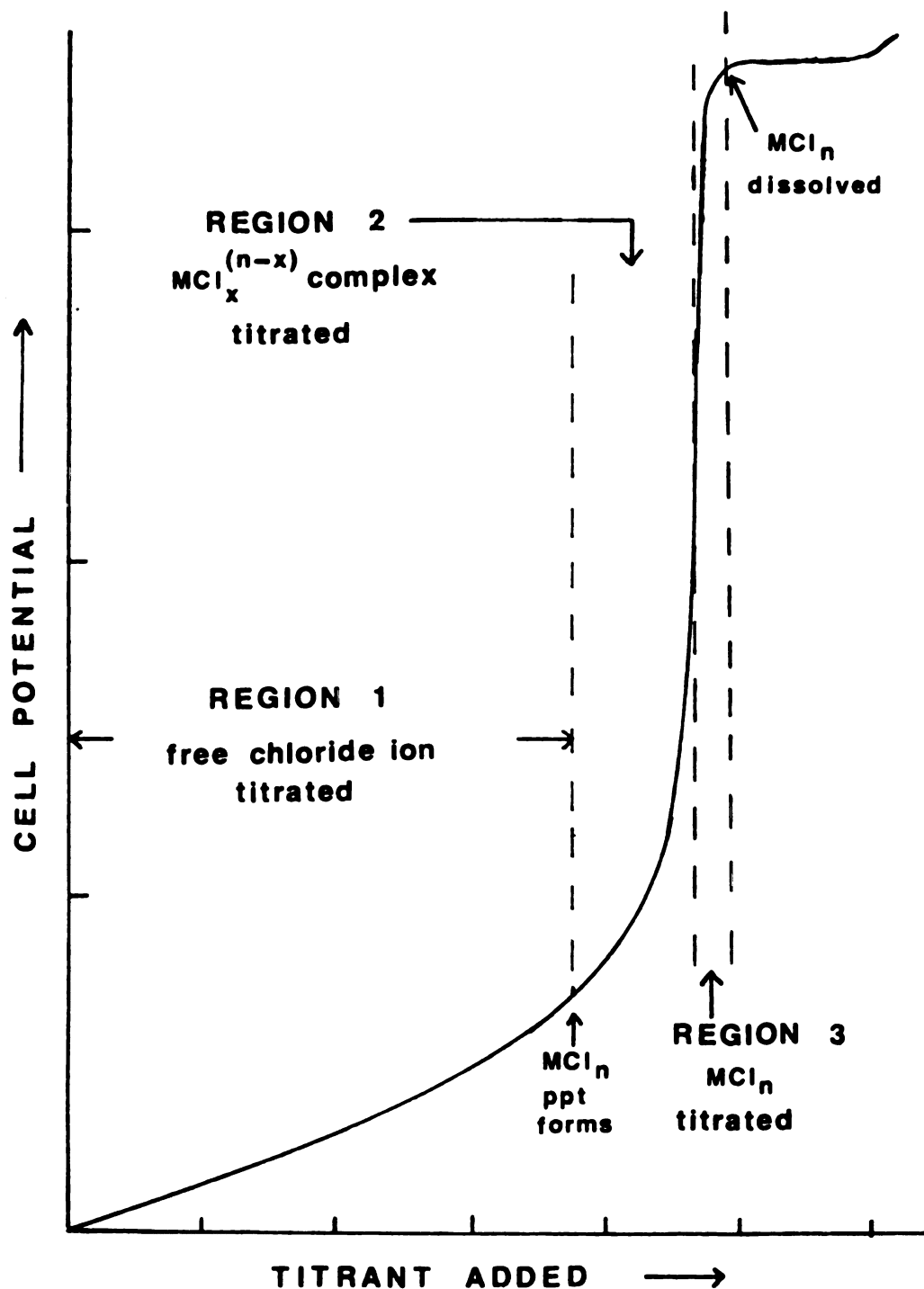


Figure 3. Schematic curve depicting the potentiometric titration of dilute metal chloride - basic  $\text{AlCl}_3$ - $\text{BPCl}$  melt solutions.

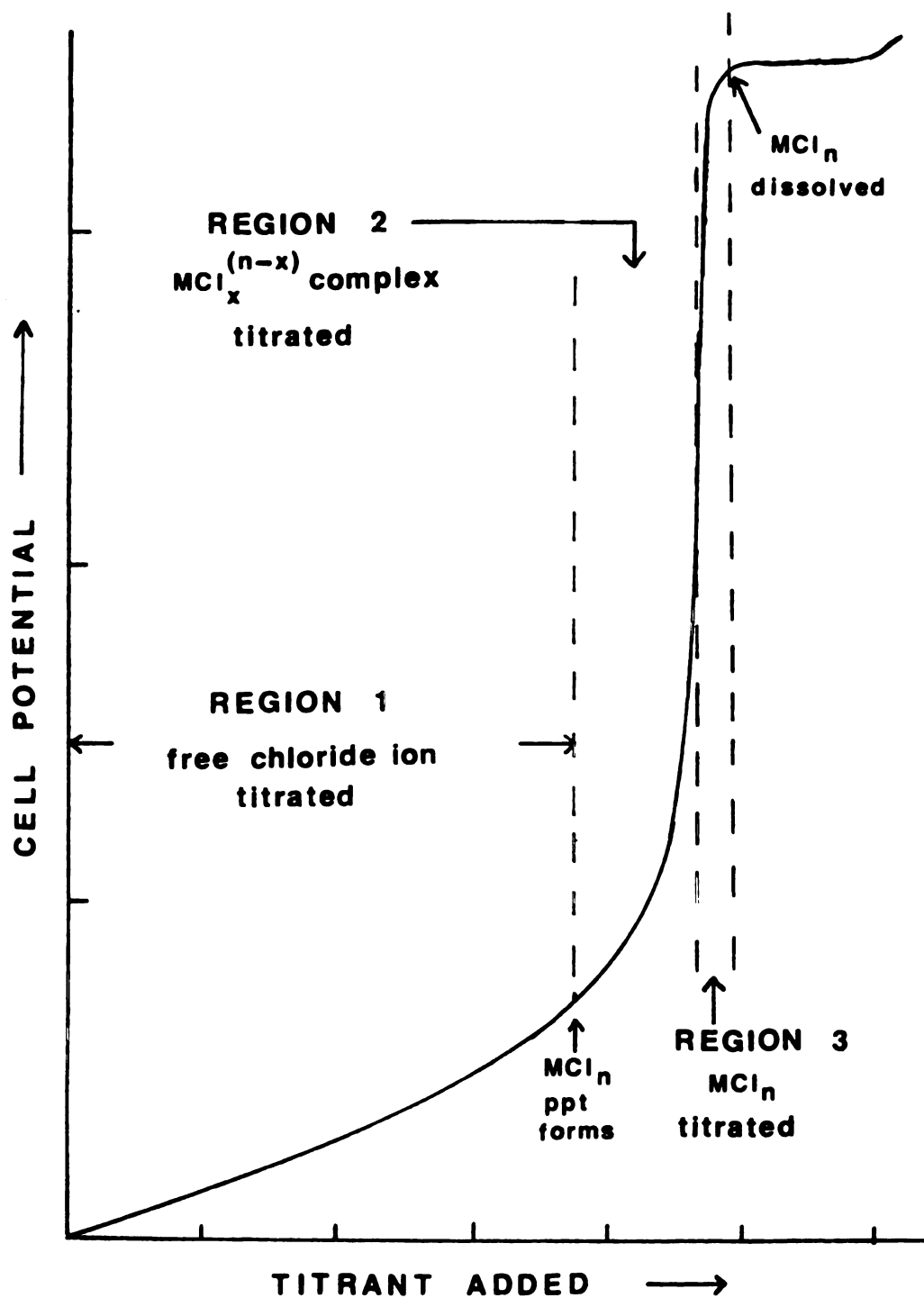
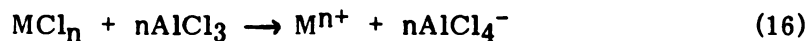


Figure 3. Schematic curve depicting the potentiometric titration of dilute metal chloride - basic  $\text{AlCl}_3$ -BPCl melt solutions.

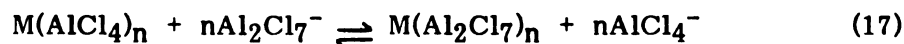


Precipitation of the metal chlorides has been reported in potentiometric studies in the  $\text{AlCl}_3$ -BPCl and  $\text{AlCl}_3$ -ImCl molten salt systems ( $\text{FeCl}_2$ , refs. 56,76;  $\text{CoCl}_2$ , ref. 74;  $\text{NiCl}_2$ , ref. 71;  $\text{AgCl}$ , ref. 76; and  $\text{CuCl}$ , refs. 77,81).

From the equivalence point of the titration, the dispersed  $\text{MCl}_n$  precipitate reacts with the titrant to produce the  $\text{M}^{n+}$  cation in solution.



Further addition of titrant at this point alters the coordination of the metal ion from  $\text{AlCl}_4^-$  to  $\text{Al}_2\text{Cl}_7^-$  ions (eq. 17).



Supporting evidence for the existence of chlorocomplex species and their inferred structures in the  $\text{AlCl}_3$ -BPCl or  $\text{AlCl}_3$ -ImCl systems has been given by UV-visible and near-IR spectroscopic studies. A summary of these results is given in Table 5. The number and positions of band maxima observed in these studies are consistent with results previously obtained in aqueous, nonaqueous, or other molten salt media. The UV cutoff of the  $\text{AlCl}_3$ -BPCl melts in ca. 275 nm, and ca. 300 nm for the  $\text{AlCl}_3$ -ImCl mixtures. This has proven to be a serious limitation in the case of  $\text{FeCl}_4^{2-}$  (75), where the nature of the coordination of the metal ion could not be determined due to background absorption of the melt.

In summary, electrochemical techniques have been the methods of choice

**Table 5**  
**Absorption Spectroscopic Parameters for Chlorocomplexes in**  
 **$\text{AlCl}_3\text{-BPCl}$  and  $\text{AlCl}_3\text{-ImCl}$  Melts**

<b>Complex</b>	<b>Melt</b>	<b>Band Maximum (nm)</b>	<b>(l/mol cm)</b>	<b>Symmetry</b>	<b>Ref.</b>
$\text{NiCl}_4^{2-}$	0.8:1 (BPCl)	658	169	$T_d$	71
$\text{CoCl}_4^{2-}$	0.8:1 (BPCl)	633 669 696	428 593 662	$T_d$	74
$\text{MoCl}_6^{3-}$	0.8:1 (ImCl)	439 542 685	32 26 1.3	$O_h$	78
$\text{CuCl}_4^{2-}$	47.3 mol% $\text{AlCl}_3\text{-ImCl}$	293 407	8652 2596	dist. $T_d$	81
$\text{WCl}_6^-$	44.4 mol% $\text{AlCl}_3\text{-ImCl}$	275 (sh) 299	-- 15000	$O_h$	81
$\text{WCl}_6^{2-}$	44.4 mol% $\text{AlCl}_3\text{-ImCl}$	287 308 (sh) 350	7900	$O_h$	82
$\text{W}_2\text{Cl}_9^{2-}$	44.4 mol% $\text{AlCl}_3\text{-ImCl}$	460 626 764	4000 70 35	confacial biectahedron	82

Table 5 continued

Complex	Melt	Band Maximum (nm)	(l/mol cm)	Symmetry	Ref.
ICl	2:1 (BPCl) 1:1 (BPCl)	490 480	-- --	linear linear	86 86
Cl <sub>3</sub> <sup>-</sup>	1:1 (ImCl)	320 (sh)	--	linear	83
YbCl <sub>2</sub> <sup>+</sup>	60 mol% AlCl <sub>3</sub> - BPCl	350	--	?	79
YbCl <sub>6</sub> <sup>3-</sup>	"basic" AlCl <sub>3</sub> - BPCl	285	--	O <sub>h</sub>	79
SmCl <sub>2</sub> <sup>+</sup>	"acidic" AlCl <sub>3</sub> - BPCl	283	--	?	79
TmCl <sub>2</sub> <sup>+</sup>	"acidic" AlCl <sub>3</sub> - BPCl	285	--	?	82
UCl <sub>6</sub> <sup>-</sup>	1.6:1 AlCl <sub>3</sub> - BPCl	3 sharp bands centered at 1449	--	O <sub>h</sub>	92
		1871 1000 950 859			

Note: Quotation marks are used wherever specific melt compositions were not given in the original references.

in investigations of chlorocomplexation in the ambient temperature melts. While a few studies have included UV-visible spectrophotometric measurements, no detailed studies that use vibrational spectroscopy or multinuclear NMR techniques to investigate chlorocomplexes in the melts have been published. Although the solute metal ions studied thus far in the melts possess NMR-active nuclei, the lack of NMR data is somewhat understandable. With a few possible exceptions ( $^{95}\text{Mo}/^{97}\text{Mo}$  and  $^{63}\text{Cu}/^{65}\text{Cu}$ ), the nuclei of these metal ions have low receptivities, large quadrupole moments, or oxidation states which are not observable by NMR. These factors, or combinations of them, can render NMR measurements difficult (94).

However, some other metal chlorides, such as  $\text{HgCl}_2$ ,  $\text{SnCl}_2$ , and  $\text{CdCl}_2$ , which have not been studied in these melts, have nuclei with favorable NMR characteristics. Moreover, these solutes have a marked tendency to form chlorocomplexes in solvents with high chloride ion activities. Such a condition, without the influence of molecular solvents, is provided in the ambient temperature molten salt environment.

In addition, the solvation of alkali metal salts in these molten salts has not been studied. Since several of these  $\text{M}^+$  ions have NMR-active nuclei which are easily observed (eg.,  $^6\text{Li}$ ,  $^7\text{Li}$ ,  $^{23}\text{Na}$ ,  $^{133}\text{Cs}$ ), it would be possible to probe their chemical environment in the melt by using NMR.

## **B.2 Multinuclear NMR**

### **B.2.a. Introduction**

The rapidly expanding interest in multinuclear NMR for the study of solution chemistry has resulted from dramatic technological advances in this field. The development of powerful microcomputers which use fast Fourier transform algorithms and sophisticated software, pulse programming units for tailor-made



pulse sequences, and high efficiency wide-bore superconducting magnets, has made NMR experiments feasible for most elements in the periodic table. High resolution NMR spectra have now been obtained for nuclei with very low natural abundances (eg.,  $^2\text{H}$ ,  $^{17}\text{O}$ ,  $^{43}\text{Ca}$ ) or low sensitivities (eg.,  $^{109}\text{Ag}$ ,  $^{183}\text{W}$ ). An extensive amount of thermodynamic, kinetic, and structural information has been obtained from these NMR studies in various solvents.

For thorough treatments of the basic theory and practice of NMR, the texts of Abragam (95), Martin, Delpeuch, and Martin (96), and Farrar and Becker (97) are recommended. Periodic reviews of progress in selected NMR topics are available (98,99). Excellent reviews of recent multinuclear NMR results are given by Harris and Mann (100), Lambert and Riddell (101), and Laszlo (102). In the following two sections, the NMR characteristics and selected literature results for  $^7\text{Li}$  and other metal nuclei NMR solution studies are discussed.

### B.2.b. Lithium-7

By virtue of its high receptivity (1540 vs.  $^{13}\text{C}$ ),  $^7\text{Li}$  is one of the easiest nuclei in the periodic table to detect in an NMR experiment. With a spin of  $3/2$ , it is a quadrupolar nucleus, and the quadrupolar relaxation mechanism is expected to contribute to the observed spin-lattice ( $T_1$ ) relaxation rate in solution. The expression for this relaxation pathway is given in equation (18).

$$R_1^Q = 1/T_1^Q = \frac{3\pi^2}{10} \frac{2I+3}{I^2(2I-1)} \left(1 + \frac{\sigma^2}{3}\right) \left(\frac{e^2qQ(1-\gamma_\infty)}{h}\right)^2 \tau_c \quad (18)$$

In this expression,  $I$  is the nuclear spin,  $\sigma$  is the asymmetry parameter,  $Q$  is the nuclear quadrupole moment (in  $\text{m}^2/\text{C}$ ),  $\gamma_\infty$  is the Sternheimer antishielding factor,  $eq$  is the electric field gradient (EFG;  $eq = \partial^2 V / \partial Z^2$ , ref, 101) about the nucleus, and  $\tau_c$  is the molecular rotational correlation time (isotopic tumbling). Several of the quantities in this expression are sometimes grouped together to define the nuclear quadrupole coupling constant ( $\chi$ ) as

$$\chi = e^2 q Q / h \quad (19)$$

The asymmetry parameter measures the deviation of the electronic environment of the nucleus from axial symmetry, and is given by

$$\sigma = (q_{xx} - q_{yy}) / q_{zz} ; 0 \leq \sigma \leq 1. \quad (20)$$

For axial or spherical symmetry,  $\sigma = 0$ , and quadrupolar relaxation becomes inoperative. The Sternheimer factor is a correction for the screening influence of the closed shell electrons intervening between the bare nucleus and the EFG produced by the ions or molecules which make up the coordination shell of the ion. For the lithium ion, this factor is 0.249, which is the smallest of all of the alkali metal cations (101).

Lithium-7 has the eight-smallest quadrupole moment ( $Q = -4.5 \times 10^{-30} \text{ m}^2$ ) of all quadrupolar nuclei. Therefore, other relaxation mechanisms can make large contributions to the observed  $R_1$  relaxation rate. From measurements of  $^7\text{Li}$   $T_1$  relaxation times in  $\text{D}_2\text{O}$  and  $\text{H}_2\text{O}$ , Hertz and co-workers (103) determined that the quadrupolar and dipole-dipole (intermolecular) mechanisms contribute about equally to the observed relaxation rate at  $25^\circ\text{C}$ . The intermolecular dipole-dipole mechanism is given by

$$R_1^{\text{inter. DD}} = 1/T_1^{\text{inter. DD}} = \frac{\mu_0^2 N_S \gamma_I^2 \gamma_S^2 \hbar^2 S(S+1) \tau_c}{20 r_{I-S}^3} \quad (21)$$

where  $\mu_0$  is the permeability of vacuum ( $\mu_0 = 4\pi \times 10^{-7} \text{ Kg ms}^{-2} \text{ amp}^{-2}$ ),  $N_S$  is the concentration of spins per unit volume,  $S$  is the spin number for the nucleus coupled to the nucleus in question, and  $r_{I-S}$  is the bond distance between spins  $I$  and  $S$ .

A brief compilation of literature values for  $^7\text{Li}$   $T_1$  relaxation times for ionic and covalently bonded lithium in various media is given in Table 6.

In aqueous and nonaqueous solutions,  $T_1$  relaxation times for the  $\text{Li}^+$  ion range from  $10^0$  to  $10^1$  seconds. The contribution of the intermolecular dipole-dipole mechanism can be quantitatively evaluated through the use of deuterated solvents. In general, the  $T_1$  relaxation times of  $^7\text{Li}$  in compounds are one to three orders of magnitude less than for ionic lithium. In molten salts, the dipolar contribution to the  $^7\text{Li}$   $T_1$  relaxation rates is assumed to be negligible (107,109). The surrounding shell of neighboring anions induces a fluctuating EFG at the  $^7\text{Li}$  nucleus due to the translational and rotational motion of these ions relative to the lithium ion. As can be seen in Table 6, in molten salt media, this collisionally-induced quadrupolar mechanism is rather inefficient. It can be seen that  $T_1$  in supercooled  $\text{LiNO}_3$  is quite similar to that of  $\text{LiCl}$  in water at  $25^\circ\text{C}$ . The collisionally-induced quadrupolar relaxation mechanism is discussed in reference 101, and references cited therein.

No clear evidence has been obtained for contributions to  $^7\text{Li}$   $T_1$  relaxation

**Table 6**  
**Lithium-7 T<sub>1</sub> Relaxation Times in Various Media**

<b>System</b>	<b>T<sub>1</sub> (sec.)</b>	<b>Temp. (°C)</b>	<b>Ref.</b>
aqueous and nonaqueous solvents:			
LiCl/H <sub>2</sub> O*	18.2	25	103
LiCl/D <sub>2</sub> O*	37.0	25	103
LiCl/HCOOH*	5.9	25	104
LiCl/DCOOD*	6.7	25	104
LiCl/ethanol*	5.6	25	105
LiCl/methanol*	28.6	25	105
LiCl/DMSO*	5.9	25	105
LiCl/DMF*	6.7	25	105
LiCl/acetone*	14.3	25	105
LiCl/acetonitrile*	20.0	25	105
0.90 M CH <sub>3</sub> Li/ diethyl ether	3.8	25	106

Table 6 continued

System	$T_1$ (sec.)	Temp. ( $^{\circ}\text{C}$ )	Ref.
1.9 M $\text{CH}_3\text{CH}_2\text{Li}/$ diethyl ether	1.1	25	106
0.64 M $\text{C}_6\text{H}_5\text{Li}/$ diethyl ether	0.33	25	106
2 M $\text{C}_6\text{H}_5\text{Li}/$ 70:30 $\text{C}_6\text{H}_6$ -diethylether	0.047	28	110
2 M $\text{N}$ -butyllithium/ N-hexane	0.083	28	110
Molten Salts:			
$\text{LiNO}_3$ (supercooled)	17.8	25	107
$\text{LiAlCl}_4$	6.4	156	108
4:1 (Li, Cs) $\text{NO}_3$	15.2	300	109
3:2 (Li, Cs) $\text{NO}_3$	13.1	300	109

\* at infinite dilution

by the spin rotation, nuclear shielding anisotropy, or scalar coupling mechanisms. However, Hartwell and Allerhand (106) have suggested that spin rotation could account for the observed increased relaxation rate of  $\text{CH}_3\text{Li}$  in diethyl ether with increasing temperature. Increasing relaxation rate with increasing temperature is the type of behavior expected when the spin rotation relaxation mechanism is dominant, as opposed to other identified relaxation mechanisms. The expression for the spin rotation mechanism is

$$R_1^{\text{SR}} = 1/T_1^{\text{SR}} = \frac{u^2 (C_{\parallel}^2 + 2C_{\perp}^2)}{9 \hbar^2 \tau_c} \quad (22)$$

$$1/T_1^{\text{SR}} = \frac{u^2 (C_{\parallel}^2 + 2C_{\perp}^2)}{9 \hbar^2 \eta V f} \quad (23)$$

where  $u$  is the amount of inertia,  $C_{\parallel}$  and  $C_{\perp}$  are the parallel and perpendicular components of the spin rotation tensor, respectively,  $\eta$  is the dynamic viscosity,  $V$  is the molecular volume, and  $f$  is the microviscosity factor defined by

$$f = \left[ 6(a_S/a) + \frac{1}{\left(1 + \frac{a_S}{a}\right)^3} \right]^{-1} \quad (24)$$

The quantities  $a$  and  $a_S$  are the radii of the molecule containing the relaxing nucleus, and the radius of the solvent molecules, respectively. For neat liquids,

this factor is ca. 0.16 (112).

Previous studies by several research groups (113-115) have amply demonstrated the sensitivity of  $^7\text{Li}$  chemical shifts to changes in the immediate environment of the lithium ion. The infinite dilution chemical shifts for the lithium ion range from +2.54 ppm in pyridine, to -2.80 ppm in acetonitrile (ref. 116). Khazaeli has reviewed work through 1982 concerning the use of alkali metal NMR relaxation and chemical shift measurements to investigate ion associations in nonaqueous solvents (117).

### **B.2.c. Other metal nuclei**

In addition to the alkali metal nuclei, other metals have nuclei which possess NMR characteristics sufficiently favorable to enable investigation of the chemical species they form, and their structures in solution, and in the solid state. In solution the chemical environment exerts a strong influence on the nuclear shielding of these nuclei, often resulting in very large chemical shift ranges ( $10^2$  to  $10^4$  ppm). Resonance frequencies characteristic of different donor atoms or donor groups have been established for many of these nuclei (101, 94).

Multinuclear NMR methods have been used in several studies of halocomplex formation in solution and the solid state. Maciel and co-workers have calculated the characteristic chemical shifts of individual halide complexes of Zn(II) and Cd(II) in aqueous solution by using  $^{67}\text{Zn}$  and  $^{113}\text{Cd}$  NMR (118, 119, respectively). Chemical shift data, as a function of halide concentration, were fitted to a multi-site fast exchange model by using the known equilibrium constants for halocomplex formation in these systems. Excellent agreement was obtained in the latter study between the calculated solution chemical shifts, and values for the solid salts of the respective cadmium chlorocomplexes. Mercury-199

NMR chemical shift assignments for  $\text{HgCl}_4^{2-}$  and  $\text{HgCl}_3^-$  halide complexes have also been established in water and in dichloromethane solutions (120,121).

The majority of previous  $^{119}\text{Sn}$  NMR studies have been devoted to the study of organotin compounds in aqueous or nonaqueous solutions (122). Tin-119 chemical shifts have been shown to be sensitive to changes in the coordination geometry and type of donor group. In a very early  $^{119}\text{Sn}$  NMR study of mixtures of  $\text{SnCl}_4$ ,  $\text{SnBr}_4$ , and  $\text{SnI}_4$ , resonance lines for all twelve possible mixed halide tin compounds were observed at 27°C, and appropriate assignments made for each of these species (123). One recent investigation of tin chlorocomplexes by  $^{119}\text{Sn}$  NMR has been reported. In this study,  $\text{SnCl}_3^-$  was used as a ligand in the preparation of the  $\text{IrH}(\text{SnCl}_3)_5^{3-}$  and  $\text{RhH}(\text{SnCl}_3)_5^{3-}$  anionic complexes (124). Separate resonances were observed for axial and equatorial  $\text{SnCl}_3^-$  groups ( $\delta_a = -185.5$  ppm and  $\delta_e = -318.8$  ppm, respectively versus external  $(\text{CH}_3)_4\text{Sn}$ ).

### **B.3. Crown and Cryptand Complexation of Lithium Ion**

#### **B.3.a. Introduction**

Since the first reports on the syntheses of the synthetic macrocyclic crown (125) and cryptand (126) polyethers in the late 1960's, a large body of literature has developed devoted to characterization of the complexation reactions of these ligands with metal cations in solutions. It is now recognized that many different factors can influence the extent of interaction between these ionophores and cations, as well as the structures of complex species formed in solutions. Lehn has discussed the effects of ligand parameters such as cavity size, flexibility and conformation, and number and type of donor atoms, as well as the effects of counterion, cation charge, and solvent donicity on the macrocyclic complexation of metal ions (127).



Several comprehensive reviews have been published which include discussions of the syntheses of the crown and cryptand ligands (128,129), and current progress in the application of these compounds to the study of complexation in solution (130). The ability of these ligands to complex alkali metal cations has generated considerable interest in determining the thermodynamic and kinetic parameters which govern these reactions. Alkali metal NMR has been shown to be useful in ascertaining these parameters. Popov has reviewed progress in the use of this technique through 1979 (131).

Considering the large amount of information which has been published on alkali metal macrocyclic complexation reactions, the remainder of this historical section concentrates on crown and cryptate complexes of the lithium ion (to the exclusion of other alkali metal cations), since this narrower topic relates more closely to the subject of this dissertation. Literature results pertinent to this topic from 1980 to the present are discussed, focussing on NMR data, and solid state lithium complex structure determinations. The Ph.D. theses of Cahen (132) and Smetana (133) provide excellent reviews of the subject of lithium ion macrocyclic complexation prior to 1980.

#### **B.3.b. Solution studies**

The effects of ring size, number and type of donor atoms, and ligand flexibility on macrocyclic complexation of the lithium ion have received much attention recently. The lithium ion is small and non-polarizable, and is expected to interact most strongly with "hard" donor atoms such as oxygen, as opposed to "soft" nitrogen or sulfur donor atoms. Rounaghi and Popov (134) have observed no measurable effect on the  $^7\text{Li}$  NMR resonance line chemical shift of  $\text{LiClO}_4$  in acetonitrile (AN), acetone (AC), tetrahydrofuran (THF), propylene carbonate (PC), nitromethane (NM), or pyridine (PYR) on addition of

trithia-12-crown-4 (TT12C4), indicating very little interaction between  $\text{Li}^+$  ion and the sulfur donor atoms of this ligand.

These results can be compared to those of Smetana and Popov (135), who observed strong interaction between  $\text{Li}^+$  and 12-crown-4 in NM, AN, AC, and PYR. These authors obtained crown complex formation constants by a nonlinear least-squares fit of the observed variation of the  $^7\text{Li}$  chemical shifts as functions of ligand-to-metal ion mole ratio. It was found that the Li-15C5 complex formation constants in these solutions were larger than those for the Li-12C4 system.

Consonance between the size of the cavity formed by a crown molecule, and the size of the ion to be complexed has long been recognized as an important, if not dominant factor in the stability of a crown complex. "Goodness of fit" maximizes the electrostatic interaction of the cationic charge with the donor atom lone pair electrons, thus producing the enthalpic driving force for complex formation. This issue has been clouded somewhat by the considerable variation in the literature in estimates of the diameters of alkali metal, and other metal cations. Ladd (136) has noted at least five different computations of the radius of the lithium cation, with values ranging from  $0.60 \text{ \AA}$  (Pauling) to  $0.93 \text{ \AA}$  (Morris). Ladd's own values were based on a combination of the geometrical method of Lande, and experimental electron density maps. The value which Ladd obtained for lithium ion is  $r_{\text{Li}^+} = 0.86 \text{ \AA}$ .

Assuming that the crown cavity diameters measured from space-filling molecular models are the most reliable estimates of these quantities, Pauling's value of  $r_{\text{Li}^+} = 0.60 \text{ \AA}$  predicts stronger interaction with 12-crown-4 (dia. = 1.2 to  $1.5 \text{ \AA}$ ) than with 15-crown-5 (dia. = 1.7 to  $2.2 \text{ \AA}$ ), or larger crowns. The results of the complexation study cited above (135) indicate that Pauling's

value is too small, and that the values due to Ladd ( $0.86 \text{ \AA}$ ) or Morris ( $0.93 \text{ \AA}$ ) are in better agreement with these experimental results.

Mandolini and Masci (137) have recently observed a similar preference of lithium ion for the 15-crown-5 ring size over that of 12-crown-4. They obtained  $\log K_F$  values of 1.96 for benzo-15-crown-5, versus 1.67 for benzo-12-crown-4 in dimethylsulfoxide (DMSO) solutions at  $25^\circ\text{C}$ . From measurements of potentiometric selectivity coefficients for polymeric membranes containing alkyl-substituted crown ether analogues, Kitazawa and co-workers (138) have proposed a selectivity scale as



for lithium ion in water.

Using the  $^7\text{Li}$  NMR method described in reference 135, Chen et al. (139) have determined the formation constants for complexation of lithium ion with a series of alkyl-substituted dibenzo-14-crown-4 derivatives in seven nonaqueous solvents. In comparing their results to those cited in reference 135, these authors stated that the larger ring size (14-membered vs. 12-membered) accounted for the larger stability constants obtained for the 14-crown-4 derivatives. In addition, the observed increasing  $K_F$  values as a function of increased alkyl substitution on the benzo rings was attributed to greater electron-release of these substituents to the coordinating oxygen atoms, thus increasing the basicity of these donor atoms.

In another  $^7\text{Li}$  NMR study of the effect of heteroatom replacement on  $\text{Li}^+$ -crown complexation, Shamsipur and Popov (140) investigated the complexation of lithium ion with 18-crown-6 and 1,10-diaza-18-crown-6 in several nonaqueous solvents. With the single exception of pyridine, the  $K_F$

values for the diaza-analogue exceeded those for 18-crown-6 in these solvents. Assuming direct interaction between  $\text{Li}^+$  and the two nitrogen donor atoms of the diaza-crown molecule, these results were difficult to reconcile with the hard-soft interaction argument outlined at the beginning of this section.

One possible explanation for these data would be that in solution, the diaza-crown molecule does not assume, on average, a conformation which makes all donor atoms coplanar. Instead, it may assume a slightly folded conformation, such that the four oxygen donor atoms are presented in a 12-crown-4 - type of arrangement. Thus, it is possible that the nitrogen atoms do not participate in the coordination of the lithium ion. However, the influence of solvent-ligand interactions must also be considered, since it has been shown recently (141) that these interactions can have significant impact on the macrocyclic complexation of metal cations.

Cryptand ligands provide three-dimensional cavities for complexation of metal ions. The hydrophobic outer "skin" of these molecules tends to screen out interactions between the cation being complexed, and the counterion and solvent molecules outside the cavity. The completeness of this screening effect is dependent on the match between cation size and ligand cavity size, as well as the other factors just discussed for crown complexation.

The importance of cation/cavity size matching was demonstrated by Cahen et al. (142) in a  $^7\text{Li}$  NMR study of lithium ion complexation with cryptands C211, C221, and C222 in NM, DMSO, THF, PC, chloroform, dimethylformamide (DMF), formamide, and water at 30°C. When corrected for differences in solvent magnetic susceptibilities, the chemical shifts of the  $^7\text{Li}$  NMR signals observed for the Li-C211 complexes were found to be independent of solvent and counterion ( $\delta_c = -0.41$  ppm vs. infinite dilution). Similar constancy of complex chemical shifts versus solvent was not observed for cryptands C221

and C222, whose cavity sizes are somewhat too large for the lithium ion. The authors interpreted these results as indicating that the C211 molecule was able to completely shield the lithium ion from the solvent molecules, whereas cryptands C221 and C222 could not, due to their larger cavity sizes. In addition, slow chemical exchange between free and complexed lithium sites (at ligand/lithium ion mole ratios  $< 1.0$ ) was observed at 30°C and a magnetic field strength of 14.09 kG only for the Li-C211 and Li-C221 systems. Fast chemical exchange was observed for the other two cryptand ligands under these conditions.

Hourdakis and Popov (143) have also used  $^7\text{Li}$  NMR to study complexation of lithium ion by C222-dilactam in water, and four nonaqueous solvents. They reported that the complexing ability of this cryptand was somewhat weaker than C222, and that fast chemical exchange was observed at 33°C and 14.09 kG at all C222-dilactam/lithium ion mole ratios studied.

Since these two previous studies, only one additional  $^7\text{Li}$  NMR study of lithium ion-cryptand complexation has been reported (ref. 117). Khazaeli observed slow chemical exchange for the Li-C211 system in methylamine and liquid ammonia at -51°C and 14.09 kG, with  $\delta_c = -0.42$  ppm. Thus, in these two additional solvents, it was shown that the C211 molecule effectively isolates the lithium cation from the surrounding environment of anions and solvent molecules.

Lithium cryptate complex formation constants (determined by several techniques) in various solvents have been recently compiled by Chantooni and Kolthoff (144).

### **B.3.c. Complex structures**

Since 1980, several crystalline lithium-crown complexes have been isolated, and their crystal structures determined. A summary of these results is provided

in Table 7. In only two of the nine structures listed  $\text{Li}(\text{18C6})\text{ClO}_4 \cdot 2\text{H}_2\text{O}$  and  $(\text{LiSCN})_2(\text{18C6}) \cdot 2\text{H}_2\text{O}$  does the lithium ion reside in the basal plane formed by the crown ether oxygen atoms. These deviations from the plane appear to be larger for the smaller rings (12C4 and 13C4) than the larger 14C4 and 18C6 rings. The large deviation observed in the case of the Li-sym-dibenzo-14C4-oxyacetate complex most likely is due to the steric requirements of the two bulky benzene rings, and participation by the side arm carboxylate group in lithium ion coordination. For the 18C6 complexes, conformational flexibility allows the ring skeleton to elongate so that only two of the six ether oxygen atoms are in close proximity to the lithium ion. The remaining coordination sites are supplied by encapsulated water molecules (perchlorate complex), or thiocyanate ions. In the benzo-15C5 complex, bidentate coordination by the picrate ion, and monodentate coordination by two water molecules effectively remove the lithium ion from any influence which could be exerted by the crown ether.

While these data (and attendant interpretations) seem to support the idea of complex stability being promoted by a good fit between the cation and crown cavity sizes, one must be careful not to make direct comparisons between the solid state (static) structures, and the dynamic structural situations in solutions. Structure determinations for lithium ion-crown complexes which contain large, non-coordinating counterions, and no waters of crystallization could enable a more straightforward assessment of the effect of cavity size on cation coordination geometries.

Since the original crystal structure determination for the  $\text{Li}(\text{C211})\text{I}$  cryptate by Moras and Weiss (153) in 1973, no further lithium cryptate structures have been reported. The structure of C221 or C222 cryptates of lithium ion would be very interesting to aid in the evaluation of the effect of the lithium

Table 7

## Crystalline Crown Complexes of the Lithium Ion

Complex	Coordination Number for $\text{Li}^+$	Distance of $\text{Li}^+$ to The Plane of the Crown Ether Oxygens ( $\text{\AA}$ )	Reference
$\text{Li}(\text{benzo-15C5})$ $\text{picrate} \cdot 2\text{H}_2\text{O}$	4	(a)	145
$\text{Li}(\text{12C4})\text{SCN}$	5	0.55	146
$\text{Li}(\text{18C6})\text{ClO}_4 \cdot 2\text{H}_2\text{O}$	4	0	147
$(\text{LiSCN})_2(\text{18C6}) \cdot 2\text{H}_2\text{O}$	4	0	147
$\text{Li}(\text{benzo-13C4})\text{SCN}$	5	0.8	148
$\text{Li}(\text{benzo-14C4})\text{NO}_3$	6	0.24	149
$\text{Li}(\text{sym-dibenzo-14C4-oxyacetate}) \cdot 7.5\text{H}_2\text{O}$	5	0.84	150
$\text{Li}(\text{12C4})\text{N}(\text{SiCH}_3)_2$	5	1	151
$(\text{Li picrate})$ $(\text{dibenzo-36C12}) \cdot 2\text{H}_2\text{O}$	5	0.12	152

(a) Lithium ion is not coordinated by the crown ether ring.

ion-cryptand cavity size relationship on the observed coordination symmetry about the lithium ion.



## **CHAPTER II**

### **EXPERIMENTAL PART AND DATA TREATMENT**

## **A. Experimental Part**

### **A.1. Molten Salts**

#### **A.1.a. Melt Preparation**

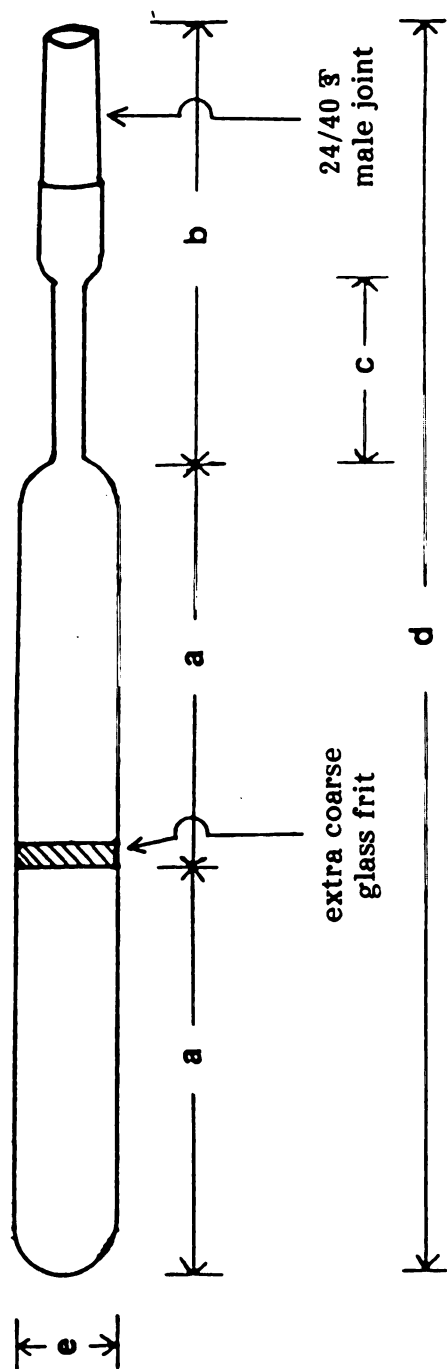
##### **A.1.a.(1). $\text{AlCl}_3$ distillation**

Aluminum chloride (Fluka AG; > 99% as  $\text{AlCl}_3$ ) contained trace amounts of boron and iron from the commercial manufacture of this compound. To remove these impurities, and to reduce any aluminum oxide contaminant, the  $\text{AlCl}_3$  was distilled in a sealed Pyrex ampule over aluminum wire (Alfa; n5N purity) through an extra coarse (150-250 micron) Pyrex glass frit. A schematic diagram of the ampule is shown in Figure 4.

The aluminum wire (1.0 mm dia. ) was cut to 3 or 4 cm lengths, and each segment allowed to soak in a 30:30:40  $\text{H}_2\text{SO}_4$ - $\text{HNO}_3$ - $\text{H}_3\text{PO}_4$  (v/v/v) concentrated acid solution for thirty seconds to remove any oxide coating. The segments were then rinsed with deionized water and technical grade acetone, and briefly air-dried. The cleaned wire was stored in a Vacuum/Atmospheres Corp. DRI-LAB HE-43-2 dry atmosphere box (combined  $\text{H}_2\text{O}$  and  $\text{O}_2$  estimated to be < 10 ppm).

In the dry box, the  $\text{AlCl}_3$  was first inspected visually for contaminants. The boron and iron impurities may be identified as yellow, reddish-orange, or grey granules dispersed throughout the white solid. Any granular pieces exhibiting this discoloration were removed from the bulk material with tweezers. The ampule was loaded with three aluminum wire segments and ca. 30 g of  $\text{AlCl}_3$ . After filling, the ampule was capped, removed from the dry box, and placed on a high vacuum line ( $\leq 10^{-5}$  torr) for evacuation. After 24 h of pumping at this pressure, the ampule was flame-sealed in preparation for the distillation step.

The ampule was inverted (empty chamber up) and suspended vertically



- a: 10 cm
- b: 12 cm
- c: 4 cm
- d: 32
- e: 2.5 cm

Figure 4. Pyrex ampule used for  $\text{AlCl}_3$  distillations.

in an aluminum-body tube furnace fitted with a small mica observation window. Temperature was adjusted with a Love Controls Corp. model 149 proportional controller equipped with a chromel-alumel thermocouple. Over a period of three hours, the ampule temperature was raised slowly ( $\approx 5^{\circ}\text{C}$  per 5 min.) to ca.  $190^{\circ}\text{C}$ . Between  $190$  and  $205^{\circ}\text{C}$ , the solid melted to give a clear colorless liquid. Because of the volatility of  $\text{AlCl}_3$  near its melting point, extreme care was taken to avoid sudden jumps in ampule temperature which would produce surges in pressure (est. 3 to 5 atmospheres). Despite all precautions, ampule explosions did occur occasionally, with sufficient force to crack laminated safety glass hood sashes.

After melting of the  $\text{AlCl}_3$ , the ampule was raised ( $\approx 1$  cm per hour) out of the furnace exposing the upper part of the empty chamber to the cooler atmosphere. Thus, the thermal gradient required to begin distillation was established. After passing through the glass frit, the  $\text{AlCl}_3$  vapor crystallized in the upper chamber forming very large transparent crystals. The ampules were opened in the dry box, and the crystals of  $\text{AlCl}_3$  ground for use in preparing the  $\text{AlCl}_3$ - $\text{BPCl}$  melts.

#### **A.1.a.(2) $\text{BPCl}$ synthesis**

Pyridine (MCB; A.C.S. reagent grade) was refluxed over barium oxide for two to three days, and fractionally distilled under nitrogen atmosphere. The 1-chlorobutane (Eastman; 98%) was washed with concentrated sulfuric acid, deionized water, dilute aqueous sodium carbonate solution, and again with deionized water. The material was then fractionally distilled over  $\text{P}_2\text{O}_5$  under nitrogen atmosphere. Acetonitrile (Mallinckrodt; analytical reagent grade) was refluxed over calcium hydride for two days, and fractionally distilled under nitrogen atmosphere. Ethyl acetate (Mallinckrodt; analytical reagent grade) was fractionally distilled under nitrogen atmosphere.

The 1-chlorobutane (975 ml) was added dropwise (2 ml/min.) to a three-liter reaction vessel containing 750 ml of pyridine under nitrogen atmosphere. The reaction mixture was maintained at 70°-80°C for three days, or until no additional white needle-like crystalline product was formed. The mother liquor was decanted off, and the product rinsed with acetonitrile to remove traces of the mother liquor. The crude product was recrystallized from 1 liter of acetonitrile at 60°C. On cooling to room temperature, 5 ml portions of ethyl acetate were added to promote precipitation of the product from solution. Addition of the ethyl acetate was halted when no further precipitate was observed to form. The acetonitrile and ethyl acetate were pumped off at  $10^{-3}$  torr until the purified crystals of BPCl were just slightly damp with solvent. The product was ground to a powder and dried at 60°C under high vacuum ( $\leq 10^{-5}$  torr) for four days. The melting point of the dried product was  $131 \pm 2^\circ\text{C}$  determined using a Thomas Hoover capillary melting point apparatus.

#### **A.1.a.(3) melt batch mixtures**

Melt batches were prepared by mixing weighed amounts of  $\text{AlCl}_3$  and BPCl in Pyrex weighing bottles, using Teflon-coated magnetic stirring bars. All operations were carried out at room temperature in the molten salt dry box described in section A.1.a.(1). Since the reaction was exothermic, initially small weights (0.1 g) of each component were added together to avoid thermal decomposition. Once a 1-2 ml volume of melt was prepared, larger amounts (0.5 g) of each component could be added until the desired mole ratio and final batch size were obtained. Batches of 2 to 45 g of melt were prepared in this manner. After stirring for one day, each batch was vacuum-filtered through a medium porosity Pyrex glass frit (5-15 micron), and stored in a capped weighing bottle in the dry box.

In the absence of thermal decomposition or contamination from oxygen or moisture, the melts were clear and colorless. While exclusion of these contaminants was largely accomplished through the use of high purity starting materials in the dry, oxygen-free atmosphere of the dry box, thermal decomposition on mixing was difficult to avoid completely. As a result, the melt solutions usually exhibited a very pale yellow color. A darkening of the color was observed whenever oxygen or moisture contamination occurred. Acidic melt mixtures ( $X_{\text{AlCl}_3} > 0.5$ ) were more sensitive to this contamination, showing more rapid and deeper coloration. Any melts with color darker than the minimum pale yellow were discarded.

#### **A.1.b. Purification of Solutes**

##### **A.1.b.(1). Lithium salts**

Lithium chloride and lithium bromide (Fisher; analytical reagent grade), lithium perchlorate and lithium hexafluoroarsenate (Alfa; reagent grade), and lithium fluoride (Allied; reagent grade) were dried for three days at 100°C. Lithium chloride enriched with  $^6\text{Li}$  was prepared by treating  $^6\text{Li}_2\text{CO}_3$  (originally  $^6\text{Li}$  metal from Oak Ridge National Laboratory; 95%  $^6\text{Li}$  isotopic enrichment) with concentrated hydrochloric acid, and evaporated to dryness. The product was then ground and further dried at 100°C for three days. Lithium tetrachloroaluminate was prepared by fusing equimolar amounts of  $\text{LiCl}$  (1.2062 g) and  $\text{AlCl}_3$  (3.7983 g) in an evacuated ( $< 10^{-5}$  torr) Pyrex ampule at 150°C. The resulting grey crystalline solid was ground and stored in the dry box. The melting point of this product was  $144 \pm 2^\circ\text{C}$ .

##### **A.1.b.(2) heavy metal compounds**

Lead chloride (99.9999%), cuprous chloride (99.99%), and stannic chloride (99.999%) were used as received from Aldrich. Mercuric chloride (Mallinckrodt; analytical reagent grade), zinc chloride (Alfa; ultrapure grade), lead nitrate

(Fisher; A.C.S. reagent grade), stannous chloride (Alfa; A.C.S. reagent grade), and cadmium chloride (J.T. Baker; A.C.S. reagent grade) were dried for three days at 100°C, and stored in the dry box. Silver acetate (Matheson, Coleman and Bell; 99.5%) was used as received.

#### **A.1.b.(3) crown and cryptand ligands**

The 12-crown-4 (Aldrich; 98%) was dried at room temperature under vacuum ( $\leq 10^{-5}$  torr) for eight hours. The 15-crown-5 (Aldrich; 98%) was distilled, then dried under vacuum ( $\sim 10^{-2}$  torr) for three days. Benzo-15-crown-5 (Parish; reagent grade) was recrystallized from n-heptane, and dried under vacuum ( $\sim 10^{-2}$  torr) for three days. The 18-crown-6 (Aldrich; 99%) was recrystallized from acetonitrile and pumped under high vacuum ( $\leq 10^{-5}$  torr) for one day to remove the weakly bound acetonitrile.

Cryptands C211, C221, C222, and C2B22 (MCB) were used as received.

#### **A.1.c. Melt Solution Preparation**

##### **A.1.c.(1) mole ratio samples**

All samples for NMR measurements were contained in 5 mm o.d. Pyrex NMR tubes (Wilmad) which had been washed with hot concentrated nitric acid, rinsed with deionized water and acetone, and oven-dried. Once filled with a sample, the tubes were degassed and flame-sealed under high vacuum ( $\leq 10^{-5}$  torr).

Initial samples were prepared by combining weighed amounts of melt and solutes (both to  $\pm 0.0001$  g) in the NMR tubes in the dry box prior to flame-sealing. Thereafter, a batch processing technique was developed to provide more precise control of the ligand-metal chloride salt mole ratio in the melt. In this method, a stock solution was prepared by adding the metal chloride (eg. LiCl) to the melt, and the mixture stirred until it was homogeneous (ca. 24 hr.). Ligand was then added to the stock solution by weight in small

(0.01 g, typically) amounts. After each addition of ligand, the solution was stirred for 0.5 to 1 hr. to ensure complete mixing. After this waiting time, a 0.5 g sample was removed from the solution, and loaded into a 5 mm NMR tube. This procedure was repeated, enabling the preparation of 12 to 17 NMR tube samples from a 10 g stock solution. Thus, mole ratios of up to 5 to 1 were attainable with very little (0.05 mol%) dilution of the salt of the metal ion.

After flame-sealing under vacuum, all NMR tube samples were conditioned for at least three weeks at 70°C to ensure sample equilibration. In the cases of some of the heavy metal salts, this period was extended to several months.

A variation of this method was used to prepare basic melt samples containing LiCl at various concentrations. In this case, a 2.0 mol% LiCl - basic melt stock solution was prepared as just described. Pure basic melt was then added so as to dilute the LiCl (by 0.1 mol% increments). Stock solution mixing and sampling procedures were the same as those used for the mole ratio studies described above. The lowest LiCl concentration obtained in basic melt using this procedure was 0.10 mol% LiCl, which was close to the detection limit for the NMR sample configuration used in these studies (see section A.2.a(1)).

In the remainder of this work all molten salt compositions and solute concentrations are expressed in mole per cent (mol%). Thus, a melt with a 2:1  $\text{AlCl}_3$ -BPCl mole ratio is referred to as 67 mol%  $\text{AlCl}_3$  melt. For solutes in the melts, a benchmark for comparison with molar concentrations is useful; a 1.0 mol% LiCl-45 mol%  $\text{AlCl}_3$  melt is equivalent to 0.077 M LiCl. For convenience, 45.0 mol%  $\text{AlCl}_3$  melt is referred to simply as the "basic melt". Likewise 67 mol%  $\text{AlCl}_3$  is the "acidic melt". For any other  $\text{AlCl}_3$ -BPCl mixtures used in this study, the full composition (in mol%  $\text{AlCl}_3$ ) is given



explicitly.

#### A.1.c.(2) isolation of solid compounds

Stock solutions of 1.0 mol% LiCl in basic melt (10.0 g total weight) were prepared as described in section A.1.c(1). Weights of cryptands C211, C221, and C222 were added to the stock solutions to obtain the 1:1 ligand-to-lithium ion mole ratio. These solutions were stirred at room temperature in the dry box for 2-3 days.

One liter of benzene (Fisher; A.C.S. spectrophotometric grade) was washed with successive 250 ml portions of concentrated sulfuric acid until no visible yellow color (thiophene impurity) was observed in the acid layer. In practice, three portions of acid were usually required to obtain this colorless condition. The material was washed with deionized water, and distilled over calcium hydride. The benzene was further dried over freshly activated (at 300°C) 3 Å molecular sieves (Davison) for three days, then stored over additional sieves. The water content of the purified benzene was less than 10 ppm as determined by gas chromatography (154).

Benzene (ca. 10 ml) was added to each LiCl-cryptand-basic melt solution, and the mixtures shaken. Only partial miscibility of the two liquids was observed. After initial emulsion formation, layer separation ensued, with benzene floating on top of the benzene-saturated basic melt solution. This behavior is in contrast to that observed by Robinson et al. (51), who reported complete miscibility of benzene with acidic AlCl<sub>3</sub>-BPCl melts. After allowing to stand overnight, transparent crystalline products assumed to be the lithium cryptate complexes were precipitated from solution (bottom of the melt layers).

The liquid layers from each solution were decanted off and the crystals washed with three successive 2 ml portions of benzene to remove the adhering melt. The crystals were then dried at 10<sup>-5</sup> torr and room temperature for

one week to remove the benzene.

In the case of cryptand C2B22, treatment of the melt solution with benzene to force crystal growth was unnecessary. Precipitation of the lithium cryptate complex occurred as soon as the 1:1 ligand-lithium ion mole ratio was reached. The product was isolated by vacuum filtration of the solution in the dry box. The material was then washed with benzene, and dried on the vacuum line as described for the other cryptate complexes. It should be noted that for this ligand, the solid which was obtained was granular in appearance, with no transparent single crystals obtained, as with the other three cryptands. Samples of these solids were submitted to Galbraith Laboratories for carbon, hydrogen, nitrogen, oxygen, lithium, aluminum, and chlorine elemental analyses.

## **A.2 Lithium-7 NMR**

### **A.2.a. NMR of Solutions**

#### **A.2.a.(1) chemical shift measurements**

All  $^7\text{Li}$  NMR measurements were performed on a Bruker WH-180 superconducting NMR spectrometer (field strength = 42.28 kG) equipped with a Nicolet 1180 minicomputer, quadrature phase detection circuitry, deuterium lock system, and a temperature control unit. Spectra were obtained at a resonance frequency of 69.951 MHz using a home-built 10 mm bore probe which is tunable from 25 to 75 MHz. The 5 mm NMR sample tubes were mounted coaxially within 10 mm o.d. Pyrex NMR tubes (Wilmad) using Teflon spacers. The outer NMR tubes contained the external chemical shift reference solutions for the  $^7\text{Li}$  nucleus.

Two different external reference solutions were used for chemical shift measurements. The primary reference solution was 0.015 M LiCl in  $\text{D}_2\text{O}$ . Within experimental error ( $\pm 0.02$  ppm), the chemical shift of the signal observed for this solution is equal to the infinite dilution value for  $^7\text{Li}$  in water (taken

as 0.00 ppm). For samples with resonance lines which overlapped the signal of the primary reference, a secondary reference solution was used. This secondary reference is 0.015 M LiCl in pyridine, whose  $^7\text{Li}$  NMR signal is +3.39 ppm downfield from the signal of the primary reference. When the secondary reference solution was used, the NMR spectra were obtained without deuterium lock. The pyridine reference was checked against the aqueous reference every third sample to ensure accuracy in sample signal chemical shifts corrected to aqueous lithium at infinite dilution.

All  $^7\text{Li}$  NMR data were collected with a sweep width of  $\pm 1000$  Hz and 4K memory size, with zero-filling to 16K prior to Fourier transformation. Free induction decay (FID) signals were stored on a magnetic hard disk (Diablo disk drive).

For a superconducting magnet, the observed chemical shift can be corrected for the differences in the magnetic susceptibilities of various solvents by the relationship (94)

$$\delta_{\text{corr}} = \delta_{\text{obs}} + \frac{4\pi}{3}[\chi^{\text{ref}} - \chi^{\text{sample}}] \times 10^6. \quad (26)$$

where  $\chi^{\text{ref}}$  and  $\chi^{\text{sample}}$  are the magnetic susceptibilities of the reference and sample solutions, respectively. The magnetic susceptibility of basic melt at 40°C was determined by J. Rovang using an S.H.E. Corp. 800 Series SQUID (Superconducting Quantum Interference Device) Susceptometer at a magnetic field strength of 5000 G. A value of  $\chi = -0.761 \times 10^{-6}$  was obtained for this sample. Thus, the correction factor (the second term in equation 26) for basic melt was determined to be +0.176 ppm versus water (reference solvent).

This correction factor was not applied to the  $^7\text{Li}$  NMR chemical shift data for the calculations of crown complex formation constants reported herein

since this factor is a constant. However, the factor was applied to  $^7\text{Li}$  chemical shift data obtained in the cryptate complexation studies. This was necessary to permit direct comparison regarding structural details of cryptate complexes of lithium ion in basic melts with previous data in nonaqueous solvents.

#### **A.2.a.(2). spin-lattice relaxation measurements**

For spin-lattice relaxation measurements, data were collected on smaller block sizes (1K or 2K) than for the chemical shift studies. This enabled accumulation of more scans in a shorter time span, thereby maintaining adequate signal-to-noise (S/N) ratios while keeping the total experiment times to a manageable length (2-3 hr). In addition, no zero-filling prior to transformation was utilized.

In these measurements, the outer 10 mm NMR tube contained no lithium ion, but was filled with  $\text{D}_2\text{O}$  for field locking. Data were obtained using the fast inversion-recovery technique (FIRFT) of Canet and co-workers (155). The pulse sequence for this method is identical to that used in the standard inversion-recovery (IRFT) method, and is given by

$$\text{PD} - [180^\circ - \tau - 90^\circ - \text{AT} - \text{PD}]_N \quad (27)$$

where PD is the sequence recycle time,  $\tau$  is the post- $180^\circ$  pulse delay time, AT is the post- $90^\circ$  acquisition time, and N is the number of times that the pulse sequence is repeated for a given  $\tau$  value. In the IRFT Method, PD is set to a value which is greater than, or equal to five times the longest  $T_1$  value to be measured, so that the magnetization of the spin ensemble may recover completely along the axis of the applied field (in the rotating frame). In the FIRFT method, time savings are realized by setting  $\text{PD} \approx 2T_1$ , and later correcting for incomplete magnetization recovery in the calculation of  $T_1$

values. This is discussed in the Data Treatment section of this chapter.

The value of N was set to 500 to 1000 scans so as to obtain S/N ratios of at least 5:1. This ratio was deemed necessary to clearly distinguish the signals from noise in the baseline. For signal intensities which were very low ( $\tau \propto T_1$ ), this was particularly important. The total experiment time for the FIRFT method is given by

$$T.T. = N \left\{ E \cdot (AT + PD) + \sum_{i=1}^E \tau_i \right\} \quad (28)$$

where E is the total number of  $\tau$  values used (156).

The LI (Link) command in the Nicolet 1180 software enables construction of automation sequences for data acquisition and manipulation. For relaxation measurements, the sequence is

$$LI = ZG \ BC \ QS \ SA \quad (29)$$

In this list, ZG zeros the computer memory block and starts the FIRFT pulse sequence. BC corrects the dc offset of the real and imaginary parts of the FID when N is not an integer multiple of four (quadrature phase detection). QS corrects any mismatch between the quadrature phase detection channels using a Gram-Schmidt procedure which orthonormalizes the signals. Finally, SA stores each FID on the hard disk for processing. In each experiment, 14 spectra (one per  $\tau$  value) were obtained to calculate  $T_1$  values. In addition, duplicate runs were performed at each temperature for most samples.

The inhomogeneity factor (W) for the Helmholtz coil of the 10 mm high frequency probe was measured by using the method of Hanssum, Maurer, and Ruterjans (157). In this method, the intensities of the single  $^7\text{Li}$  resonance

line for 4 M LiClO<sub>4</sub> in D<sub>2</sub>O were measured as a function of the pulse width for single-scan spectra. A plot of intensities versus pulse width is shown in Figure 5. The pulse width corresponding to the 90° flip angle (P2) determined from this plot was 15 μsec. This P2 value was used for all chemical shift, as well as T<sub>1</sub> relaxation measurements. The 180° flip angle corresponded to a pulse width (P1) of 27 μsec. The value for W was calculated from the expression

$$W = 0.5 \left( 1 + \frac{|A_{270^\circ}|}{A_{90^\circ}} \right) \quad (30)$$

where A<sub>270°</sub> and A<sub>90°</sub> are the intensities of the signals obtained at the 270° and 90° flip angles, respectively.

All <sup>7</sup>Li NMR spectra for solutions were obtained at 40 ± 1°C unless otherwise indicated. Temperature was measured by using a copper-constantan thermocouple, with temperature readout on a Doric Trendicator Type T digital display meter. Before each experiment, each sample was allowed to come to thermal equilibrium for 30 minutes prior to data acquisition. No chemical shift change in the signal for the primary chemical shift reference solution was observed between 25° and 90°C, within the experimental error (± 0.02 ppm) of these measurements. This was determined by referencing the position of the signal to the end of the spectrum across this temperature range while running with lock.

#### A.2.b. NMR of Solids

Solid state NMR spectra were obtained in the static (non-spinning) and magic angle spinning modes using a Doty Scientific probe equipped with a 7 mm dia. stator assembly mounted at the magic angle (54° 44'), at 22°C.

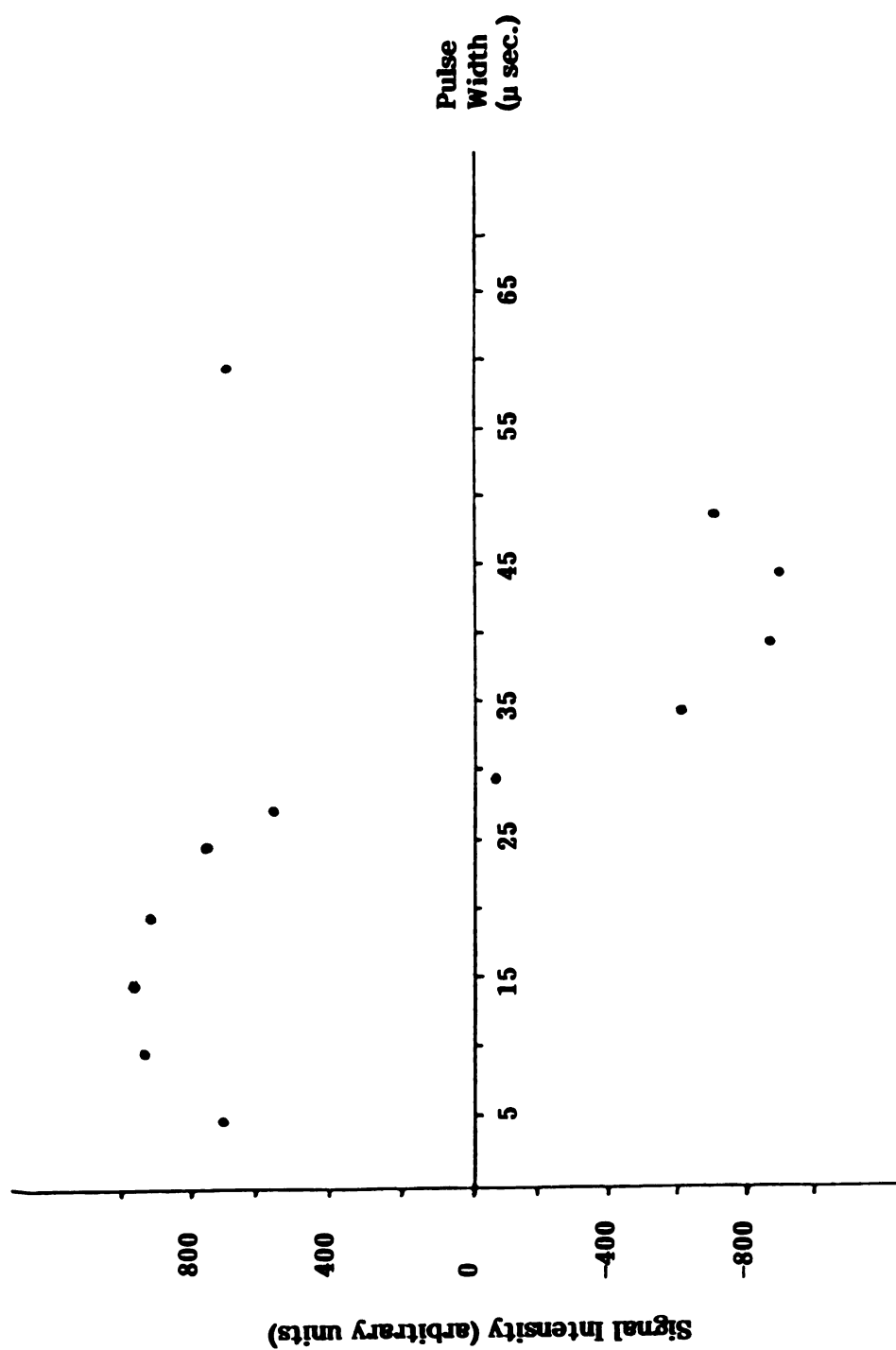


Figure 5. Intensities of the  ${}^7\text{Li}$  NMR signal of 4 M  $\text{LiClO}_4/\text{D}_2\text{O}$  versus pulse width for the 10 mm high frequency probe.

Sample spinning was driven by compressed nitrogen from the variable temperature unit of the Bruker WH-180 NMR spectrometer. Spin rates (0.8 to 2.5 kHz) were measured using an Eldorado Instruments model 1656 digital frequency counter. Solid samples were contained in Delrin or Vespel plastic rotors (7 mm dia. by 18 mm) with end caps. Samples were loaded in the dry box, capped, and transported to the instrument in a desiccator.

Data were collected with a sweep width of  $\pm 15,000$  Hz on 4K memory block size, and zero-filled to 16K for transformation. The optimum pulse width for the  $90^\circ$  flip angle was determined to be 6  $\mu\text{sec}$ . for this probe. A left shift (LS) of two data points was executed to eliminate baseline wobble in all spectra. Measurements were made without deuterium lock.

The static spectrum of 0.015 M LiCl in water was measured for referencing purposes. In view of the need to operate the instrument without lock, the removal of the probe from the magnet to switch samples, and the uncertainty in phasing of the spectra for the solid sample, the uncertainty in chemical shifts for these sample was estimated to be  $\pm 0.1$  ppm.

### **A.3. NMR of Other Nuclei**

A list of NMR characteristics for other nuclei studied in this work is given in Table 8.

Zinc-67 NMR measurements were obtained using a 20 mm bore Bruker probe with a tuning range of 8 to 24 MHz. Data were collected using a sweep width of  $\pm 10,000$  Hz on 2K block size, with zero-filling to 8K for transformation. The  $90^\circ$  flip angle was approximated with a 100  $\mu\text{sec}$ . P2 value.

For all other nuclei, the 10 mm probe described in section A.2.a(1) was used. Data were collected on an 8K block size and zero-filled to 32K for transformation. Sweep widths were  $\pm 10,000$  to  $\pm 20,000$  Hz, and P2 = 15  $\mu\text{sec}$ .



Table 8

NMR Characteristics of Selected Nuclei Studied in  $\text{AlCl}_3\text{-BPCI}$  Melts

Nucleus	Spin	Quadrupole Moment ( $\times 10^{-28} \text{m}^2$ )*	Resonance Frequency (MHz) @ $B_0 = 42.28 \text{ kG}$	Receptivity (vs. $^{13}\text{C}$ )*	Magnetogyric Ratio ( $\times 10^7 \text{ rad/T sec}$ )*
$^{27}\text{Al}$	5/2	0.149	46.89	1170	6.9704
$^{63}\text{Cu}$	3/2	- 0.211	47.73	365	7.0965
$^{67}\text{Zn}$	3/2	0.15	11.26	0.665	1.6737
$^{113}\text{Cd}$	1/2	--	39.93	7.6	- 5.9328
$^{117}\text{Sn}$	1/2	--	64.14	19.54	- 9.5319
$^{119}\text{Sn}$	1/2	--	67.11	25.2	- 9.9756
$^{199}\text{Hg}$	1/2	--	31.77	5.42	4.7912
$^{207}\text{Pb}$	1/2	--	37.62	11.8	5.5797

\* ref. 94

For nuclei with very large ( $> 10^2$  ppm) chemical shift ranges, the frequency synthesizer was reset so that successive spectral windows could be accessed to search for NMR signals across these shift ranges.

The concentric NMR tube configuration described in section A.2.a(1) was used for all nuclei except  $^{117}\text{Sn}$  and  $^{119}\text{Sn}$ . For these latter nuclei, stannic chloride was sealed under vacuum in a 5 mm NMR tube for use as a chemical shift standard. Signals observed in basic melt solutions were referenced to the standard sample by exchange of 5 mm NMR tubes. Standard and sample tubes were contained inside 10 mm NMR tubes containing  $\text{D}_2\text{O}$  for instrument lock. The uncertainty of the chemical shifts of the samples was estimated to be ca. 0.1 ppm when using this tube exchange method.

Since all other chemical shift reference solutions were aqueous, only the susceptibility correction from basic melt to water was applied. For  $^{117}\text{Sn}$  and  $^{119}\text{Sn}$  NMR spectra, the magnetic susceptibility correction factor from basic melt to  $\text{SnCl}_4$  is -0.93 ppm. A list of the chemical shift reference solutions, and their shifts relative to the primary standards reported in the literature is given in Table 9.

#### **A.4. Potentiometry**

##### **A.4.a. Cell Design**

As discussed in Chapter I, section B.1.c.(3), the cells used in the potentiometric determination of chlorocomplex formation constants and metal ion coordination numbers are constructed with an aluminum electrode dipping in acidic melt as the reference half cell, and the metal working electrode ( $\text{M}/\text{M}^{n+}$  couple) which responds reversibly to changes in the metal ion activity in the working compartment. This method is based on the ability of the metal working electrode to remain in contact with the melt components without undergoing oxidation. Gale and Osteryoung observed this type of secondary

**Table 9**  
**Chemical Shift Reference Solutions Used in NMR Measurements of Some**  
**Nuclei Studied in the  $\text{AlCl}_3$ -BPCl Melts**

Nucleus	Reference Solution	$\delta$ (ppm)
$^{67}\text{Zn}$	1.0 <u>M</u> $\text{Zn}(\text{NO}_3)_2/\text{D}_2\text{O}$	0.0
$^{113}\text{Cd}$	0.5 <u>M</u> $\text{CdCl}_2/\text{D}_2\text{O}$	+ 93.2(a)
$^{117}\text{Sn}$	$\text{SnCl}_4$ (neat)	-150(b)
$^{119}\text{Sn}$	$\text{SnCl}_4$ (neat)	-150(b)
$^{199}\text{Hg}$	0.2 <u>M</u> $\text{HgCl}_2/\text{D}_2\text{O}$	-1533(c)
$^{207}\text{Pb}$	1.0 <u>M</u> $\text{Pb}(\text{NO}_3)_2/\text{D}_2\text{O}$	-2961(d)

(a) Versus 0.1 M  $\text{Cd}(\text{ClO}_4)_2/\text{H}_2\text{O}$ ; Ref. 159.

(b) Versus  $(\text{CH}_3)_4\text{Sn}$ ; Ref. 123.

(c) Versus  $(\text{CH}_3)_2\text{Hg}$ ; Ref. 94.

(d) Versus 3.7 M  $(\text{CH}_3)_4\text{Pb}$ /toluene; Ref. 158.

reaction at an aluminum electrode in basic  $\text{AlCl}_3\text{-BPCl}$  melt (160). In this medium, the  $\text{BP}^+$  ion was reduced to 4,4'-tetrahydrobipyridine, which subsequently dissociated to the stable electroactive 1,1'-dibutyl-4,4'-bipyridinium radical cation. This latter species imparted a blue color to the melt solution.

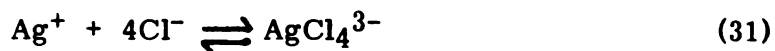
In devising a potentiometric technique to study lithium chlorocomplexation in basic melt, it was recognized that a similar reaction could very likely occur with the  $\text{BP}^+$  ion if the  $\text{Li/Li}^+$  couple was used as an electrode of the first kind in the cell design. Further support for this supposition is that the reduction potential for the  $\text{Li/Li}^+$  couple is ca. 1.8 V more negative than the  $\text{Al/Al}^{3+}$  couple in the electromotive series determined in several molten halide systems (161).

Therefore, an alternative approach that used a metal electrode of the second kind (responsive to changes in chloride ion activity) was devised. The cell design incorporates silver reference and working electrodes, with the reference electrode dipping in a 45.000 mol%  $\text{AlCl}_3$  melt solution. In this solution, the chloride ion mole fraction (or activity, assuming the Temkin model) is 0.1000; ie. the solution  $\text{pCl}$  is 1.000. Thus, changes in the  $\text{pCl}$  of the working compartment brought about by dissolution of  $\text{LiCl}$  or other lithium salts could be measured. It was also expected that, in the cases of crown or cryptand complexation of lithium ion in this medium, a change in solution  $\text{pCl}$  would accompany these macrocyclic complexation reactions.

Laher and Hussey (76) studied silver chlorocomplex formation in the  $\text{AlCl}_3\text{-BPCl}$  and  $\text{AlCl}_3\text{-ImCl}$  molten salt systems at  $40^\circ\text{C}$  and  $60^\circ\text{C}$ . Their results indicated that at  $40^\circ\text{C}$ , more than 90% of the total silver in the 45.5 mol%  $\text{AlCl}_3\text{-BPCl}$  melt exists as the  $\text{AgCl}_4^{3-}$  chlorocomplex (see Table 4, Chapter I for  $\beta_4$  for this species). It is reasonable to expect that in very dilute basic melt solutions of silver ion, the concentrations of the other complexes

( $\text{AgCl}_2^-$  and  $\text{AgCl}_3^{2-}$ ) are negligible. For example, a basic melt solution with  $X_{\text{AgCl}} = 10^{-3}$  has a chloride-to-silver ion ratio of ca. 100 ( $X_{\text{Cl}^- \text{ melt}} = 0.1$ ). Thus, the silver working electrode is made reversible to the  $\text{pCl}$  of the solution without introducing significant errors in the calculation of the number of chloride ions associated with each lithium ion in the basic melt.

For the equilibrium



the mole fraction-based formation constant is given by

$$\beta_4 = X_{\text{AgCl}_4^{3-}} / (X_{\text{Ag}^+})(X_{\text{Cl}^-})^4 \quad (32)$$

Using the approximation stated above about neglecting the  $\text{AgCl}_2^-$  and  $\text{AgCl}_3^{2-}$  complexes, we get,

$$X_{\text{Ag}}^{\text{Total}} = X_{\text{Ag}^+} + X_{\text{AgCl}_4^{3-}} \quad (33)$$

which rearranges to

$$\frac{X_{\text{Ag}}^{\text{total}}}{X_{\text{Ag}^+}} = 1 + \frac{X_{\text{AgCl}_4^{3-}}}{X_{\text{Ag}^+}} \quad (34)$$

$$X_{\text{Ag}^+} = X_{\text{Ag}}^{\text{total}} / 1 + \frac{X_{\text{AgCl}_4^{3-}}}{X_{\text{Ag}^+}} \quad (35)$$

$$X_{\text{Ag}^+} = X_{\text{Ag}}^{\text{total}} / 1 + \beta_4 X_{\text{Cl}^-}^4 \quad (36)$$

The potential of the silver working electrode is given by

$$E_W = E^{\circ'}_{Ag/Ag^+} + \frac{RT}{F} \ln X_{Ag^+} \quad (37)$$

where  $E^{\circ'}_{Ag/Ag^+}$  is the apparent standard potential of the  $Ag/Ag^+$  couple in a melt with negligible chloride ion activity (ie., acidic melt). Substituting equation (36) for  $X_{Ag^+}$  yields

$$E_W = E^{\circ'}_{Ag/Ag^+} + \frac{RT}{F} \ln \frac{X_{Ag}^{total}}{1 + \beta_4 X_{Cl^-}^4} \quad (38)$$

$$E_W = E^{\circ'}_{Ag/Ag^+} + \frac{RT}{F} \ln \frac{X_{Ag}^{total}}{\beta_4 X_{Cl^-}^4} \quad (39)$$

where the approximation that  $1 \ll \beta_4 X_{Cl^-}^4$  is used. If  $X_{Cl^-} = 10^{-1}$  and  $\beta_4 = 10^{23}$ , it is clear that this approximation is justified. After regrouping terms and recalling the definition for  $pCl$ .

$$E_W = E^{\circ'}_{Ag/Ag^+} + \frac{RT}{F} \ln \frac{X_{Ag}^{total}}{\beta_4} + \frac{2.303 \cdot 4 \cdot RT}{F} pCl_W \quad (40)$$

By similar reasoning, the potential of the silver reference electrode is

$$E_{REF} = E^{\circ'}_{Ag/Ag^+} + \frac{RT}{F} \ln \frac{X_{Ag}^{total}}{\beta_4} + \frac{2.303 \cdot 4 \cdot RT}{F} pCl_{REF} \quad (41)$$

Taking  $E_{\text{right}} = E_W$  and  $E_{\text{left}} = E_{\text{REF}}$ , the cell potential is

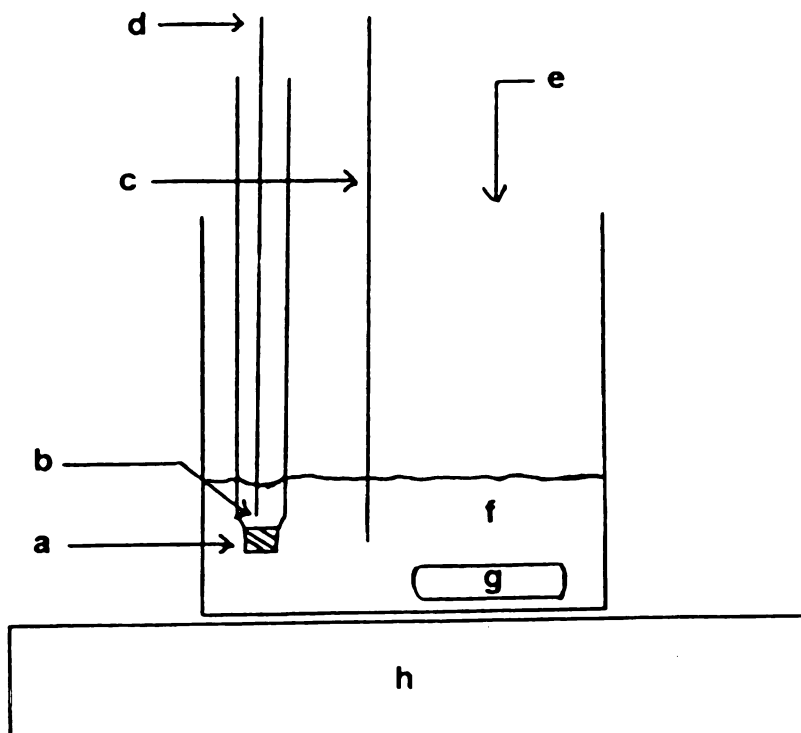
$$E_{\text{cell}} = E_{\text{right}} - E_{\text{left}} = \frac{2.303 \cdot 4 \cdot RT}{F} (pCl_W - pCl_{\text{REF}}) \quad (42)$$

As basic melt is titrated with acidic melt in the working compartment, the  $pCl_W$  increases as the chloride ion is consumed. Thus, the cell potential increases as the titration progresses. A schematic diagram and the standard notation description for this cell is shown in Figure 6.

The silver electrodes were prepared by rinsing 2 cm lengths of 1 mm dia. silver wire (Aldrich; 99.99% GOLD LABEL) with concentrated nitric acid, deionized water, and acetone, and then air-dried. These wire segments were then attached to copper wire leads by brazing with a torch to ensure good electrical contact.

The reference compartment was constructed from 0.5 in. Pyrex glass tubing with fine porosity (4-5.5 micron) Pyrex frits sealed into the tube constrictions. The frits were conditioned prior to use in the titrations by placing ca. 0.25 g of basic melt, spiked with silver acetate ( $X_{\text{Ag}}^{\text{total}} = 2.0 \times 10^{-5}$ ), inside the tube, and soaking the outer surface of the frit in the same solution for two days. In this way, the pores of the frits were completely wetted with the melt. Before immersion in the melt solution to be titrated, excess melt was wiped from the outer surface of the frit, and a silver reference electrode was inserted into the tube so that the wire was in contact with the melt above the frit.

The working compartment (a 25 x 40 mm Pyrex weighing bottle) was filled with 3.0 g of the solution to be titrated, and the working silver electrode was dipped into this solution. Cell potentials were measured with a Markson Science ElectroMark Analyzer multipurpose meter in the millivolt mode. The error



- a: 4-5.5 micron Pyrex glass frit.  
 b: basic melt reference melt solution ( $pCl = 1.000$ ).  
 c: silver working electrode.  
 d: silver reference electrode.  
 e: titrant.  
 f: basic melt solution to be titrated.  
 g: Teflon-coated stirring bar.  
 h: magnetic stirrer.



**Figure 6.** Concentration electrochemical cell used in potentiometric titrations of basic  $AlCl_3$ - $BPCl$  melt solutions.



in cell potentials was estimated to be  $\pm 1$  mV. All titrations were carried out at  $35 \pm 2^\circ\text{C}$  in the dry box. Factors which could contribute to the development of liquid junction potentials at the glass frits are discussed in the following sections.

#### **A.4.b. Titration methods**

##### **A.4.b(1) titration of pure basic melt and basic melt solutions of lithium salts**

The concentration cell was set up as described in the previous section, and the meter was adjusted to read zero millivolts. In practice, this adjustment was small ( $< 15$  mV). This is consistent with previous studies which suggest that the liquid junction potentials for cells of this type are small, and may be neglected (77,164). Acidic melt titrant was prepared according to the procedures given in section A.1.a(3). After filtering the titrant through a medium porosity Pyrex glass frit (5-15 micron), silver acetate was added ( $X_{\text{Ag}}^{\text{total}} = 2.0 \times 10^{-5}$ ), and the solution was stirred until it was homogeneous ( $\sim 10$  min.). Since the basic melt solutions to be titrated contained an equivalent mole fraction of silver acetate, the buildup of a junction potential due to a concentration gradient for silver acetate across the frit as the titration proceeded, was avoided.

The titrant was added with a Brinkmann Eppendorf digital pipettor (10  $\mu\text{l}$  to 100  $\mu\text{l}$   $\times$  0.1  $\mu\text{l}$ ). Disposable glass pipette tips were calibrated just prior to the start of a titration. This was done by measuring the weight of five successive aliquots of titrant on an analytical balance (to  $\pm 0.0001$  g). The mean aliquot weight and the standard deviations in these quantities (N-1 weighting) were then calculated. Aliquots ranging from 12 to 48 mg were used; smaller amounts were used near the equivalence point of the titrations. In general, the uncertainties in the amounts used were less than  $\pm 5\%$ .

Continuous mechanical stirring of the working compartment solutions was accomplished with a Teflon-coated magnetic stirring bar. A waiting time between aliquot additions of 5 to 15 minutes was used to ensure no further change in cell potentials. Cell potentials were found to stabilize within about 30 sec. after each aliquot addition.

For titrations of basic melt solutions containing lithium salts, the lithium salts were added (to 1.0 mol%) to the silver-spiked basic melt solutions, and stirred for 24 hr until homogeneous. The solutions were then titrated as described above.

#### **A.4.b.(2) titration of LiCl-basic melt solutions with crown and cryptand ligands**

The procedure used in these experiments was identical to that described in the previous section up to the point of titration. Instead of the acidic melt, 15-crown-5 and cryptand C2<sub>B</sub>22 were used as titrants. Pyrex glass pipet tips were calibrated for both liquid titrants. Ligand aliquots were 12 mg  $\pm$  5%, with titrations carried out to ligand-to-lithium ion mole ratios of 5:1.

### **A.5. Infrared Spectrophotometry**

#### **A.5.a. Instrumentation**

Infrared spectra of basic melt solutions were obtained by J. Rovang using a Bomem DA3 FTIR Spectrophotometer equipped with a glowbar source (range: 100 to 10,000  $\text{cm}^{-1}$ ) for mid-IR, and a mercury-xenon arc lamp (range: 10 to 1000  $\text{cm}^{-1}$ ) for far-IR measurements. MCT (mercury-cadmium-tellurium; range: 400 to 10,000  $\text{cm}^{-1}$ ) and pyroelectric (range: 10 to 1000  $\text{cm}^{-1}$ ) detectors were used for the mid- and far-IR regions, respectively. A KBr beam splitter was used for the mid-IR, and a 3 micron Mylar beam splitter used in far-IR studies. Instrument operation was controlled by a Digital PDP-11 minicomputer

equipped with a 15.9 Mbyte Winchester hard magnetic disk drive, a Bomem high speed vector processor, and RSX11M version 4.1c software package.

Data were collected on 32K memory block size, and treated with a Hamming apodization function prior to Fourier transformation to minimize fringe patterns in the spectra. Each spectrum resulted from the averaging of 1000 interferograms, with an estimated resolution of  $2\text{ cm}^{-1}$ . The cell compartment was purged with nitrogen during acquisition to minimize the possibility of contamination of the contents of the cell with oxygen or water vapor from the atmosphere.

#### **A.5.b. Cell configuration**

Mid-IR spectra ( $550$  to  $3500\text{ cm}^{-1}$ ) of melt solutions were obtained using an Aries model 20500 vacuum-tight liquid cell with 5 mm thick sodium chloride windows and 0.025 mm Teflon spacers. The pre-assembled cell was wrapped with Teflon tape to prevent leaking of the melt, and also to afford extra protection against  $\text{O}_2/\text{H}_2\text{O}$  contamination of the contents. Far-IR spectra ( $150$  to  $600\text{ cm}^{-1}$ ) were obtained using the above cell, with 2 mm thick polyethylene windows and 0.1 mm Teflon spacers.

After each run, the cell was flushed with  $\text{CCl}_4$  (Fisher: "Spectranalyzed" grade), acetone (J.T. Baker; PHOTREX reagent grade), and again with  $\text{CCl}_4$ . The remaining traces of these solvents were removed at  $10^{-2}$  torr (pumped for 30 min.). From the dry box to the FTIR instrument, the filled cell was transported in a dessicator.

### **B. Data Treatment**

#### **B.1. Lithium-7 NMR**

##### **B.1.a. KINFIT Nonlinear Least Squares Curve-fitting Program**

The analysis of  $^7\text{Li}$  NMR chemical shift data was performed on a CDC

6500 computer system using the KINFIT Program (162). Data were fitted to equations derived from proposed solution equilibria models to calculate association constants, crown complex formation constants, and limiting chemical shifts of various solution species. These models are discussed in Chapter III.

#### **B.1.b. Nicolet 1180 NTCCAP Subroutine**

This subroutine in the Nicolet 1180 software package permits the deconvolution of an NMR spectrum of up to 26 overlapping lines, providing the positions, intensities, widths, and relative areas of the individual lines. The position, height, and width parameters are varied by the operator to obtain optimum visual fit of the calculated spectrum to the experimental spectrum. The subroutine then calculates the peak areas and the root-mean square (RMS) deviation between the calculated and experimental spectra based on 1024 units full scale. The documentation for this subroutine does not provide a detailed explanation of just how the individual uncertainties for the height, width, and intensity parameters are incorporated into the calculated RMS error. However, experience has shown that the height and intensity parameters are both easier to adjust visually than the width parameter. This is particularly important for some of the broader ( $> 20$  Hz)  $^7\text{Li}$  NMR lines observed in these studies.

The multi-line  $^7\text{Li}$  NMR spectra observed in the cryptand complexation studies (Chapter IV) were deconvoluted using the NTCCAP subroutine. The calculated relative areas of the signals for free and complexed lithium ion in the melt solutions were used to determine the cryptate complex formation constants, using the expression

$$K_F = \frac{f_c \cdot C_{\text{Li}}}{[C_c - (f_c)(C_{\text{Li}})][(f_f)(C_{\text{Li}})]} \quad (43)$$

where  $f_f$  and  $f_c$  are the fractions of free and complexed lithium ion, respectively.  $C_c$  and  $C_{Li}$  are the analytical concentrations of the cryptand and the lithium ion, respectively.

### **B.1.c. Relaxation Data Reduction**

Two subroutines are available in the Nicolet 1180 software package for treatment of relaxation data; T11R and T13R permit fitting of the data to two, and three parameter equations, respectively. In both cases an (x,y) data set is constructed from the resonance line intensities associated with each  $\tau$  value ( $\tau$ , I).

The automation sequence for transformation of the sequential FID data files acquired in the experiment (section A.2.a.(2)) is

$$LI = GA \ EM \ FT \ PS \ AI \ SB. \quad (44)$$

In this list, GA retrieves each FID in turn, EM applies the pre-set linebroadening factor (LB, in Hz), FT Fourier-transforms the data file, PS applies the pre-set zero and first order phase corrections to each spectrum, AI scales the spectra to enable direct comparison of signal intensities, and SB saves the spectra on the hard disk.

In the final automation sequence,

$$LI = GR \ DR \quad (45)$$

GR extracts the ( $\tau$ , I) data set from the transformed spectra, and DR calls and applies the pre-selected data reduction subroutine (T11R or T13IR).

In T11R, the data set is fitted to the equation

$$M(\tau) = M_{\infty} \left\{ 1 - (2 - e^{-PD/T_1}) e^{-\tau/T_1} \right\} \quad (46)$$

where  $M(\tau)$  is the signal intensity at time  $\tau$ , and  $M_{\infty}$  is the intensity at  $\tau \geq 5 T_1$ . When  $PD \gg T_1$ , this expression reduces to,

$$M(\tau) = M_{\infty} \left\{ 1 - 2 e^{-\tau/T_1} \right\} \quad (47)$$

which is the equation for the standard IRFT experiment. Values for the adjustable parameters  $M_{\infty}$  and  $T_1$  (with their respective standard deviations) are calculated by this subroutine.

In T13R, the equation

$$M(\tau) = M_{\infty} \left\{ 1 - \left[ (1+W) - e^{-PD/T_1} e^{-\tau/T_1} \right] \right\} \quad (48)$$

is used, with  $M_{\infty}$ ,  $T_1$ , and  $W$  (see eq. (30)) as adjustable parameters. For a hypothetically perfect rf pulse,  $W = 1$ .

According to Levy and Peat (156), the full equation which describes the recovery of the magnetization for the FIRFT experiment is

$$M(\tau) = M_{\infty} \left\{ \frac{1 - \{(1+W) - e^{-PD/T_1} \cdot e^{-\tau/T_1}\}}{1 - W^2 e^{-PD/T_1} \cdot e^{-\tau/T_1}} \right\} \quad (49)$$

Therefore, in the T13IR subroutine, the second term in the denominator of eq. (49) is ignored. Weiss and Ferretti (163) have argued that this simplification is justified only when both  $PD$  and  $\tau$  are small compared to  $T_1$ . As a check

on the values of  $M_\infty$  and  $T_1$  (from T11R), and  $M_\infty$ ,  $T_1$ , and  $W$  (from T13IR), the data were also fitted to eq. (49) using KINFIT. The  $(\tau, I)$  data sets were obtained by reading off the intensity of each line in a set, and matching it with the associated  $\tau$  value. Since experience showed that the results calculated with KINFIT were more reliable (in some cases the GR command would ignore a spectrum if the line intensity was too small; thus,  $T_1$  values determined by the subroutines were at times based on fewer data points), all results for  $T_1$  relaxation times reported in Chapter III were obtained by using KINFIT.

## B.2. Potentiometry

In basic  $\text{AlCl}_3$ -BPCl melts ( $X_{\text{AlCl}_3} < 0.5$ ), the mole fraction of free chloride ions in solution is given by

$$X_{\text{Cl}^-} = \frac{n^\circ \text{Cl}^-}{n^\circ_{\text{total}}} = \frac{n^\circ \text{Cl}^-}{n^\circ \text{AlCl}_3 + n^\circ \text{BPCl}} \quad (50)$$

where the superscript ( $^\circ$ ) refers to the initial number of moles. In addition,

$$n^\circ \text{Cl}^- = n^\circ \text{BPCl} - n^\circ \text{AlCl}_3 \quad (51)$$

where the reaction between  $\text{AlCl}_3$  and chloride ion from the BPCl is assumed to be quantitative. By the same reasoning, the number of moles of  $\text{Al}_2\text{Cl}_7^-$  ions in each aliquot ( $m$ ) of acidic melt titrant is given by

$$n^\circ \text{AlCl}_7^- = n^\circ \text{AlCl}_3 - n^\circ \text{BPCl} \quad (52)$$

Thus, the mole fraction of free chloride ion remaining in the working

compartment as the titration progresses is

$$X_{Cl^-} = \frac{n^{\circ}Cl^- - m n_{Al_2Cl_7^-}}{n^{\circ}_{total} + m [n_{AlCl_3} + n_{BPCl}]} \quad (53)$$

where  $m = 0, 1, 2, \dots$

As discussed in section A.1.a.(3), acidic melts are observed to be more susceptible to  $O_2/H_2O$  contamination than basic melt mixtures. Although the reactions which produce the darkening of color of acidic melts have not yet been fully characterized (86), it is clear that the contamination reduces the melt acidity to a value somewhat less than that expected based on the original melt composition. Therefore, the actual composition of acidic melt titrant was determined as follows.

Prior to the start of a titration of basic melt with acidic melt (section A.4.b.(1)), the values of  $n_{Al_2Cl_7^-}$ ,  $n^{\circ}Cl^-$ , and  $n^{\circ}_{total}$  are used to calculate the number of aliquots required to reach the equivalence point. This value is compared to the actual number of aliquots used in the titration. In practice,  $m_{actual}$  is greater than  $m_{calc}$ . due to the lower actual titrant acidity. Assuming that contamination reduces only the amount of  $AlCl_3$  (as  $Al_2Cl_7^-$ ) in the titrant, a new value of  $n_{Al_2Cl_7^-}$ , and the actual titrant composition is calculated. New values of  $X_{Cl^-}$  are also determined, and the corrected titration curve (with respect to  $pCl$ ) is obtained.

Assuming that a lithium chlorocomplex of the general formula  $LiCl_x^{(1-x)}$  is formed on dissolution of a lithium salt in basic melt, its reaction with acidic melt titrant is given by





Thus, one mole of LiCl precipitates for each mole of the lithium chlorocomplex titrated. The formula for the lithium chlorocomplex is based on the assumption that one mole of this complex forms for each mole of LiCl added to the melt. At the onset of precipitation of LiCl, a small amount of free chloride ion from the melt remains to be titrated. Once the reaction in eq. (54) is nearly complete, the LiCl is titrated, and the equivalence point is reached. Therefore, the number of moles of titrant required to go from the precipitation point to the equivalence point is given by

$$n^{P \rightarrow e} = n^{*}Cl^{-} + (x-1)n_{complex} + n^{\circ}LiCl \quad (55)$$

where (\*) refers to the precipitation onset point. If  $n_{complex} = n^{\circ}LiCl$ , eq. (55) reduces to

$$n^{P \rightarrow e} = n^{*}Cl^{-} + x n^{\circ}LiCl \quad (56)$$

To determine the value for  $n^{*}Cl^{-}$ , the potential at the precipitation point is equated with  $E_{cell}$  for the titration of pure basic melt. The value of  $pCl_w$ , and hence,  $X_{Cl^{-}}$  is then obtained. Referring once again to the LiCl-basic melt titration, the total number of moles in solution at the point of precipitation ( $n^{*}_{total}$ ) is known. Therefore,  $n^{*}Cl^{-}$  is given by

$$n^{*}Cl^{-} = n^{*}_{total} X_{Cl^{-}} \quad (57)$$

Rearranging eq. (56),

$$x = n^{P \rightarrow e} - n^{*}Cl^{-} / n^{\circ}LiCl \quad (58)$$

It must be stressed that  $x$  is the number of chloride ions associated with each lithium ion added as LiCl. Thus, it is not possible to distinguish between monomeric lithium chlorocomplexes, and dimeric or higher aggregate complexes (which would all have the same  $\text{Cl}^-/\text{Li}^+$  ratio), using this potentiometric technique.

For titrations of LiCl-basic melt solutions with crown and cryptand titrants, the number of chloride ions released into solution as the macrocyclic complexation reactions occur is determined by calculating  $\Delta p\text{Cl}_w$  from the observed change in cell potential. Since these ligands are not electroactive in basic melt, it is assumed that no liquid junction potential is produced by their addition to the melt solution.

## **CHAPTER III**

### **SOLVATION AND CROWN ETHER COMPLEXATION OF THE LITHIUM ION IN THE $\text{AlCl}_3$ -BPCl SYSTEM**

## **A. Introduction**

Taulelle and Popov (59) have reported that LiCl is insoluble in  $\text{AlCl}_3$ -BPCl melts with  $0.48 \leq X_{\text{AlCl}_3} \leq 0.50$ , but soluble in the composition regions  $0.45 \leq X_{\text{AlCl}_3} \leq 0.47$  and  $0.50 < X_{\text{AlCl}_3} < 0.67$ . Striking differences in chemical shifts and linewidths of the  $^7\text{Li}$  NMR signals were observed for LiCl solutions in basic versus acidic melts. These results were interpreted by the authors as indicating that the environment of the lithium ion changes dramatically from basic to acidic melts. The manner in which LiCl is solvated in basic melts is particularly intriguing. In basic melts, the chloride ion concentration can be as high as 10 mol%. Based on the common ion effect, one would not expect to observe high LiCl solubility in this medium. Taulelle and Popov proposed the  $\text{LiCl}_2^-$  chlorocomplex in LiCl-basic melt solutions to account for the observed solubility of LiCl.

In this work, multinuclear NMR ( $^7\text{Li}$  and  $^{27}\text{Al}$ ), potentiometry, and infrared spectrophotometry have been used to characterize the proposed  $\text{LiCl}_2^-$  complex in basic melt, and also to study solvation of the lithium ion in acidic melt. In addition, complexation of the lithium ion with crown ethers in basic melt has been studied by using  $^7\text{Li}$  NMR and potentiometry.

## **B. Solvation of Lithium Salts in Basic and Acidic $\text{AlCl}_3$ -BPCl Melts**

### **B.1. Lithium-7 NMR**

#### **B.1.a. Chemical Shift Studies**

##### **B.1.a.(1) Lithium salts in basic melt**

The effects of lithium salt concentration, of type of counterion, and of temperature on the  $^7\text{Li}$  NMR chemical shifts and linewidths for these salts in basic melt were studied. The  $^7\text{Li}$  NMR signal for 1.0 mol% LiCl in basic melt at 40°C is shown in Figure 7. The chemical shift of this signal (after

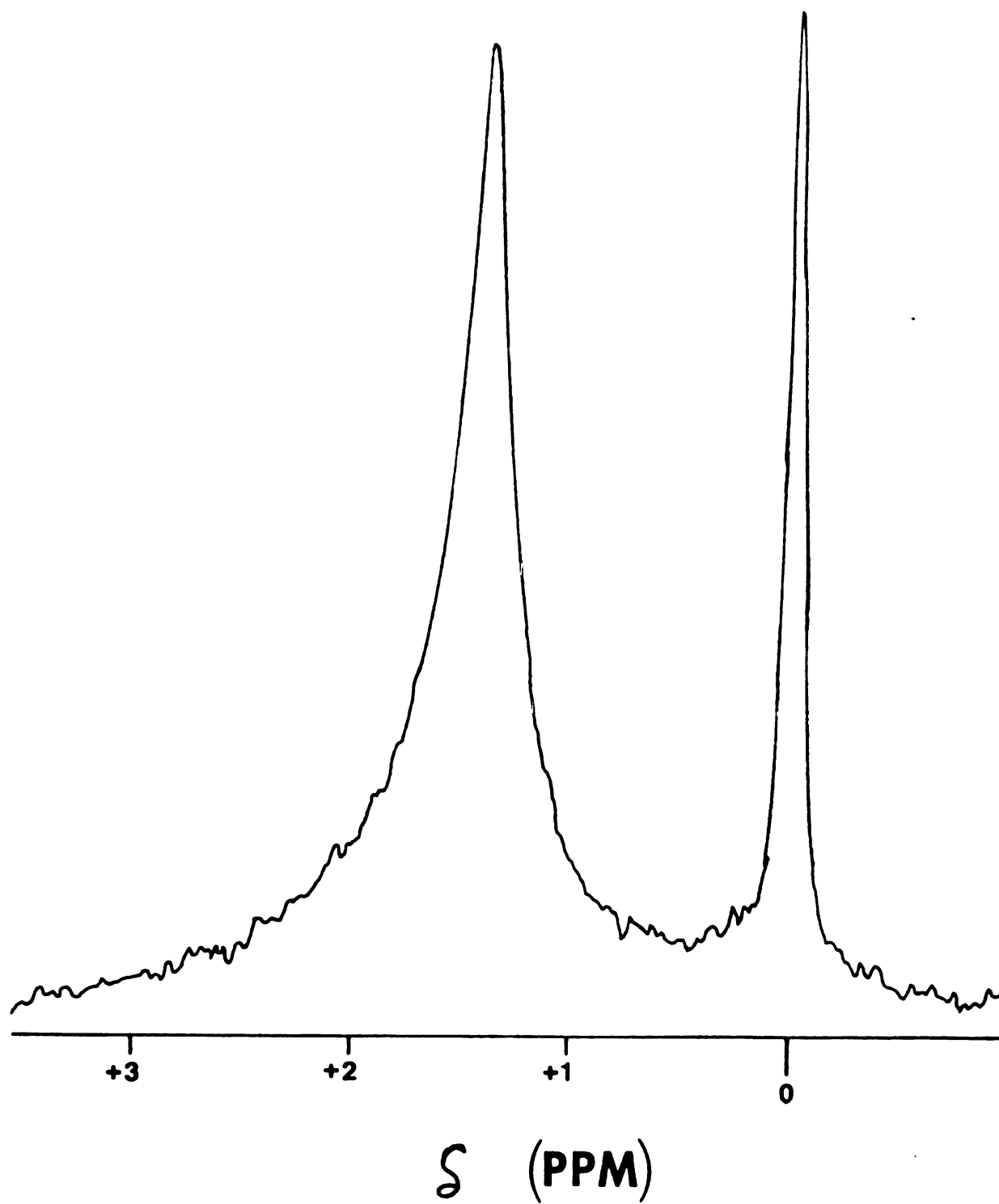


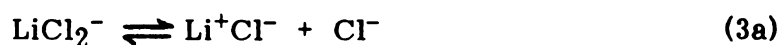
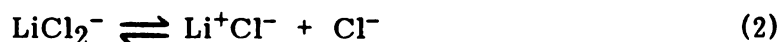
**Figure 7. Lithium-7 NMR Spectrum: 1.0 Mol% LiCl in Basic  $\text{AlCl}_3$ -BPCl Melt at 40°C.**

using the correction factor of +0.176 ppm to account for the difference in magnetic susceptibilities of basic melt and water) is  $+1.56 \pm 0.01$  ppm. At 25 Hz, the linewidth of this signal is ca.  $10^2$  times broader than the signals routinely observed for 4 M LiClO<sub>4</sub> in D<sub>2</sub>O ( $\Delta\nu_{1/2} = 0.3$  Hz).

The approximate solubility limit of LiCl in basic melt at 40°C is 2 mol%. As the temperature is lowered to 25°C, a 2 mol% solution of LiCl in basic melt becomes heterogeneous; fine needle-like transparent crystals are dispersed in the solution. Attempts to characterize this material were unsuccessful.

The <sup>7</sup>Li resonance line observed at 40°C for basic melt solutions of LiCl shifts downfield with decreasing LiCl concentration (Figure 8, Table 10). The LiCl concentrations given in Table 10 are expressed in molar units so that the calculated values of the equilibrium constants may be compared directly with literature values.

Several two-site or three-site fast chemical exchange models were proposed to fit these data (equations 1-3).



It was found that the experimental data could not be fitted to any of the above models. However, the model

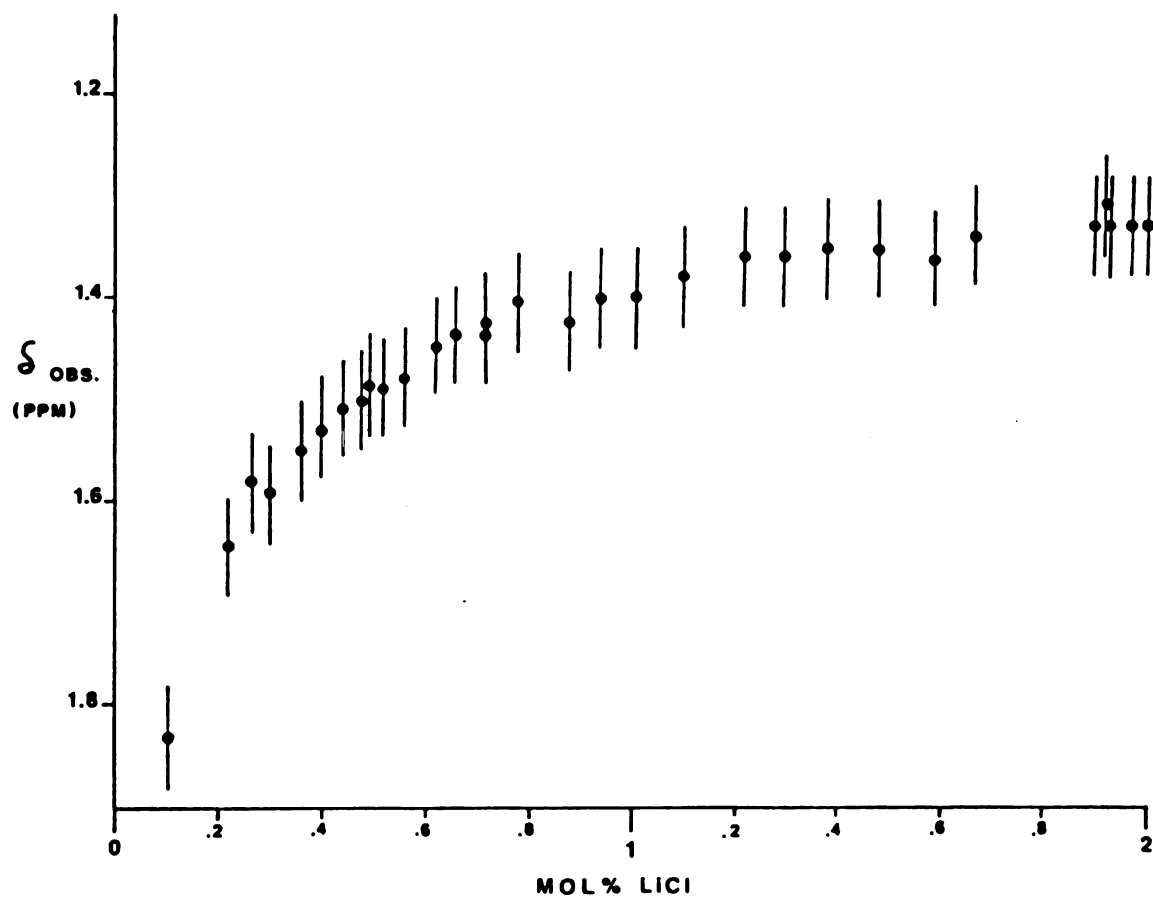


**Figure 8.** Concentration Dependence of the  $^7\text{Li}$  Chemical Shift of LiCl in Basic Melt at  $40^\circ\text{C}$ .

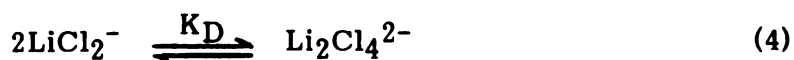
Table 10

## Lithium-7 Chemical Shift Data for LiCl-Basic Melt Solutions at 40°C

LiCl Conc. ( <u>M</u> x 10 <sup>-3</sup> )	$\delta$ (ppm)	LiCl Conc. ( <u>M</u> x 10 <sup>-3</sup> )	$\delta$ (ppm)
8.23	+1.83	61.2	+1.40
17.4	+1.65	65.5	+1.44
20.5	+1.58	69.2	+1.43
23.0	+1.59	73.7	+1.40
28.2	+1.55	79.0	+1.40
30.9	+1.56	86.2	+1.38
31.0	+1.53	95.4	+1.36
34.2	+1.51	102.	+1.36
37.3	+1.50	108.	+1.35
38.0	+1.49	117.	+1.35
40.2	+1.49	125.	+1.36
43.8	+1.48	132.	+1.34
48.1	+1.45	150.	+1.33
51.7	+1.44	152.	+1.31
55.8	+1.44	153.	+1.33
56.2	+1.43	156.	+1.33
		158.	+1.33

(a) Versus external 0.015 M LiCl in D<sub>2</sub>O uncorrected for magnetic susceptibility; the uncertainty in  $\delta$  is  $\pm 0.02$  ppm.





(suggested by J. Rovang) was found to adequately fit the  $^7\text{Li}$  chemical shift behavior of LiCl in basic melt (Figure 9). The limiting chemical shifts, calculated by using the KINFIT program (see Appendix 1 for SUBROUTINE EQN), for the monomer and dimer are  $+3.78 (\pm 0.99)$  ppm and  $+1.15 (\pm 0.01)$  ppm, respectively. When corrected for magnetic susceptibility, these values are  $+3.96$  and  $+1.33$  ppm, respectively. From the  $\log K_D$  value of  $2.82 (\pm 0.39)$ , it is estimated that ca. 90% of the total lithium ion in a 1.0 mol% LiCl-basic melt solution occurs as the dimer species. In addition, the free energy of dimerization ( $\Delta G_D = -RT \ln K_D$ ) is  $-4.1 (\pm 0.5)$  kcal/mole.

The formation of  $\text{Li}^+\text{X}^-$  ion pairs and higher order aggregates in nonaqueous solutions has been observed by several investigators. In a series of investigations by Chabanel and co-workers, vibrational spectroscopy was used to show the existence of dimers and tetramers of LiSCN in ether (164) and in tertiary amine (165) solutions. Most recently (166), dimerization of LiSCN was observed in THF and 1,3-dioxolane ( $K_D = 0.24$  and  $0.45 \text{ M}^{-1}$ , respectively). The structure of the dimer is known to be planar ( $D_{2h}$ ), while the tetramer has a tetrahedral geometry (Figure 10). Similar structures have been shown to occur for covalently-bonded alkyllithium aggregates in ether solutions (167).

In a  $^7\text{Li}$  NMR study of lithioisobutyrophenone/LiCl mixtures in dioxolane, dioxane and dimethoxyethane solutions at  $40^\circ\text{C}$  (field strength = 21.14 kG), Jackman and Szeverenyi (168) observed fast chemical exchange between free lithium ion and the tetramer species formulated as  $\text{Li}_4\text{Cl}(\text{C}_{10}\text{H}_{11}\text{O})_3$ , where  $\text{C}_{10}\text{H}_{11}\text{O}^-$  is the enolate ion. Slow chemical exchange at room temperature (field strength = 21.14 kG) has been reported by Cambillau and Ourevitch (169) in a  $^7\text{Li}$  NMR study of cryptated lithium enolates in dichloromethane and DMSO



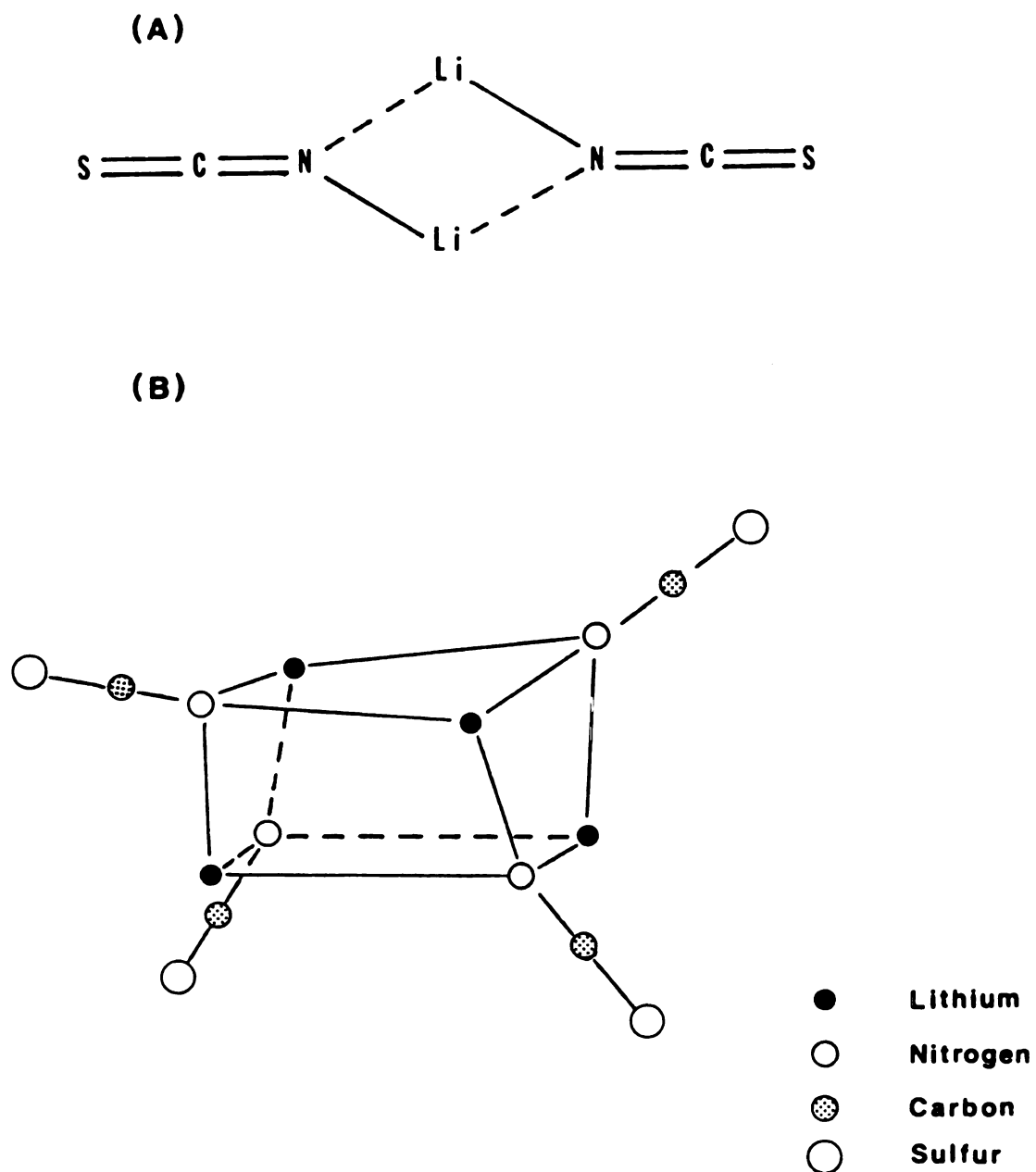


**Figure 10. Structures of the LiSCN Dimers and Tetramers in Nonaqueous Solvents; (A) Dimer, (B) Tetramer. Taken from References 164 and 165.**

solutions. Separate  $^7\text{Li}$  NMR signals were observed at +2.1 ppm (in dichloromethane) and +1.7 ppm (in DMSO) for the lithium enolate triple ion, and  $\delta_c = -0.4$  ppm for the  $\text{Li}^+\text{C}_{211}$  cryptate ion. The structure proposed by these authors for the triple ion is shown in Figure 11. The tetrahedral symmetry about the lithium ion is produced by bidentate coordination of each enolate ion.

Thus, it can be seen that in either the ionic or covalently-bonded state, lithium has a marked tendency to form aggregates in nonaqueous solvents of low polarity. Some controversy exists as to what is the coordination number for lithium ion in dilute nonaqueous solutions (170). However, two recent theoretical calculations (171,172) for aqueous lithium ion, and the MD study by Okada *et al.* (10) of LiCl-KCl eutectic melt support the supposition that the lithium ion strongly favors four-coordination in solutions.

It is then reasonable to assume that four-coordination of the lithium ion (probably tetrahedral) is occurring in LiCl-basic melt solutions. The formation of a lithium dimer chlorocomplex is not surprising, particularly if it is recalled that strong ionic associations (electrostriction) are a basic characteristic of ionic liquids.

A possible structure for the  $\text{Li}_2\text{Cl}_4^{2-}$  chlorocomplex is shown in Figure 12.

In this figure, the solid lines are drawn only to differentiate the two monomer units which make up the dimer, and should not be construed to imply formal covalent bonding between lithium and chlorine. The degree of covalent character in these bonds is not known. The four-coordination of the lithium ion at the left is probably completed by bidentate coordination of the  $\text{AlCl}_4^-$  ion. Similar coordination of the  $\text{LiCl}_2^-$  monomer seems logical.

Several other LiX salts ( $\text{X} = \text{SCN}^-$ ,  $\text{Br}^-$ ,  $\text{AsF}_6^-$ ,  $\text{ClO}_4^-$ , and  $\text{NO}_3^-$ ) were

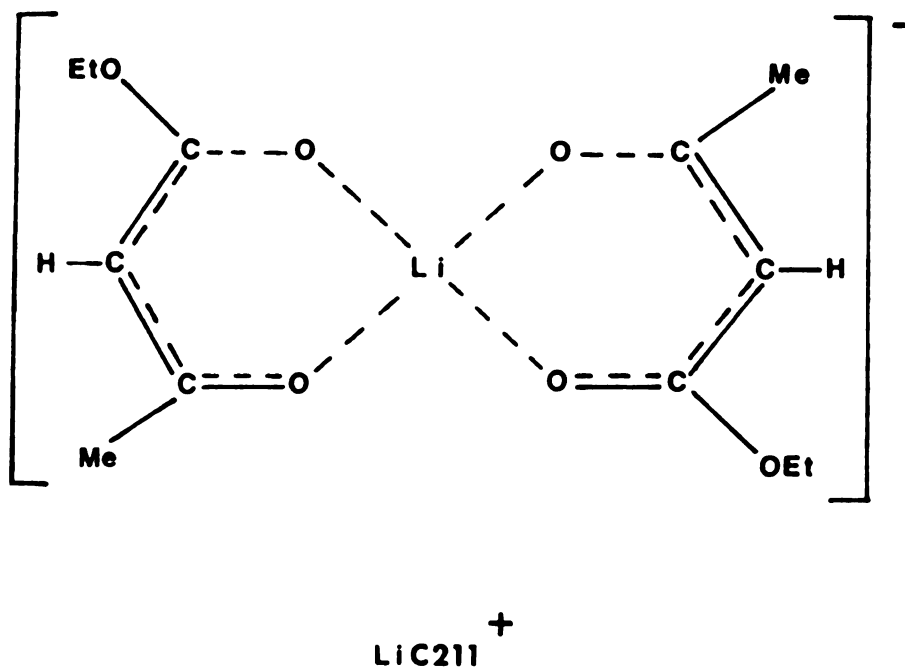


**Figure 11. Proposed Structure of the Lithium Enolate Triple Ion -  $\text{Li}^+\text{C}_{211}$  Complex.**

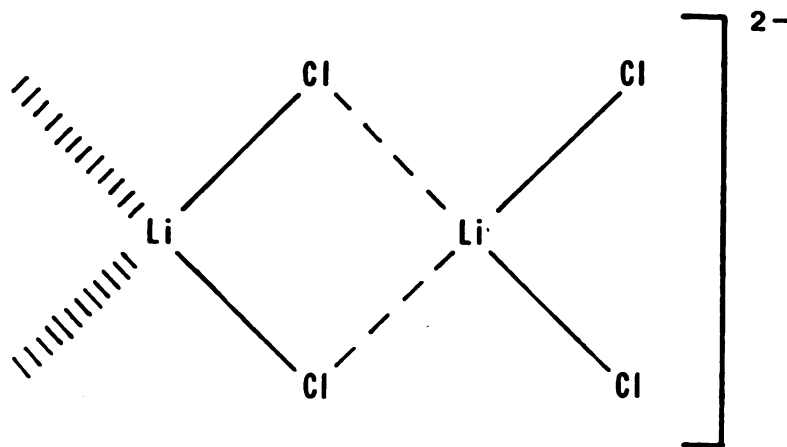


**Figure 12. Proposed Structure of the Lithium Dimer Chlorocomplex in LiCl-Basic Melt Solutions.**

found to soluble to 1 mol% in basic melt at 40°C. Lithium fluoride was only sparingly soluble, and was not studied in detail. None of these other lithium salts were found to be as soluble as LiCl at this temperature; the ubiquitous transparent crystals were observed in LiX-basic melt solutions at  $1.5 \leq X_{\text{LiX}} < 2.0$ . The higher solubility of LiCl versus the other LiX salts in basic melt indicates that the  $X^-$  ions do not participate in the solvation of the lithium ion. Moreover, an extra chloride ion from the melt is required per mole of the LiX salts to form  $\text{LiCl}_2^-$  and its dimer. This conclusion is supported by the fact that the  $^7\text{Li}$  chemical shifts at 40°C for 1 mol% basic melt solutions of LiBr, LiSCN,  $\text{LiClO}_4$ ,  $\text{LiAsF}_6$ , and  $\text{LiNO}_3$  are equal ( $\pm 0.02$  ppm) to that of 1 mol% LiCl in basic melt. The lack of an appreciable shielding influence by the  $X^-$  ions indicates that they do not reside in the first neighbor coordination sphere of the lithium ion. This shielding effect has been shown to be large (ca. 1 ppm) in a  $^7\text{Li}$  NMR study of lithium ion solvation in low donor solvents by Cahen *et al.* (115).

The effect of increasing temperature on the chemical shift of the  $^7\text{Li}$  NMR signal of 1 mol% LiCl in basic melt is shown in Figure 13. Although this effect is small ( $\Delta\delta/\Delta T \approx +0.003$  ppm/°C), the observed downfield shift change with increasing temperature is consistent with the behavior expected for an increasing population of the monomer (dimer dissociation) at higher temperatures.

#### **B.1.a. Lithium salts in acidic melt**

The  $^7\text{Li}$  NMR spectrum for 1.0 mol% LiCl in acidic melt at 40°C is shown in Figure 14. The observed chemical shift (-1.14 ppm vs. aqueous lithium ion at infinite dilution) is not corrected for the magnetic susceptibility of acidic melt since this quantity has not been measured. As was pointed out by Taulelle and Popov (59), the smaller linewidth ( $2 \pm 1$  Hz) for LiCl in acidic melt suggests

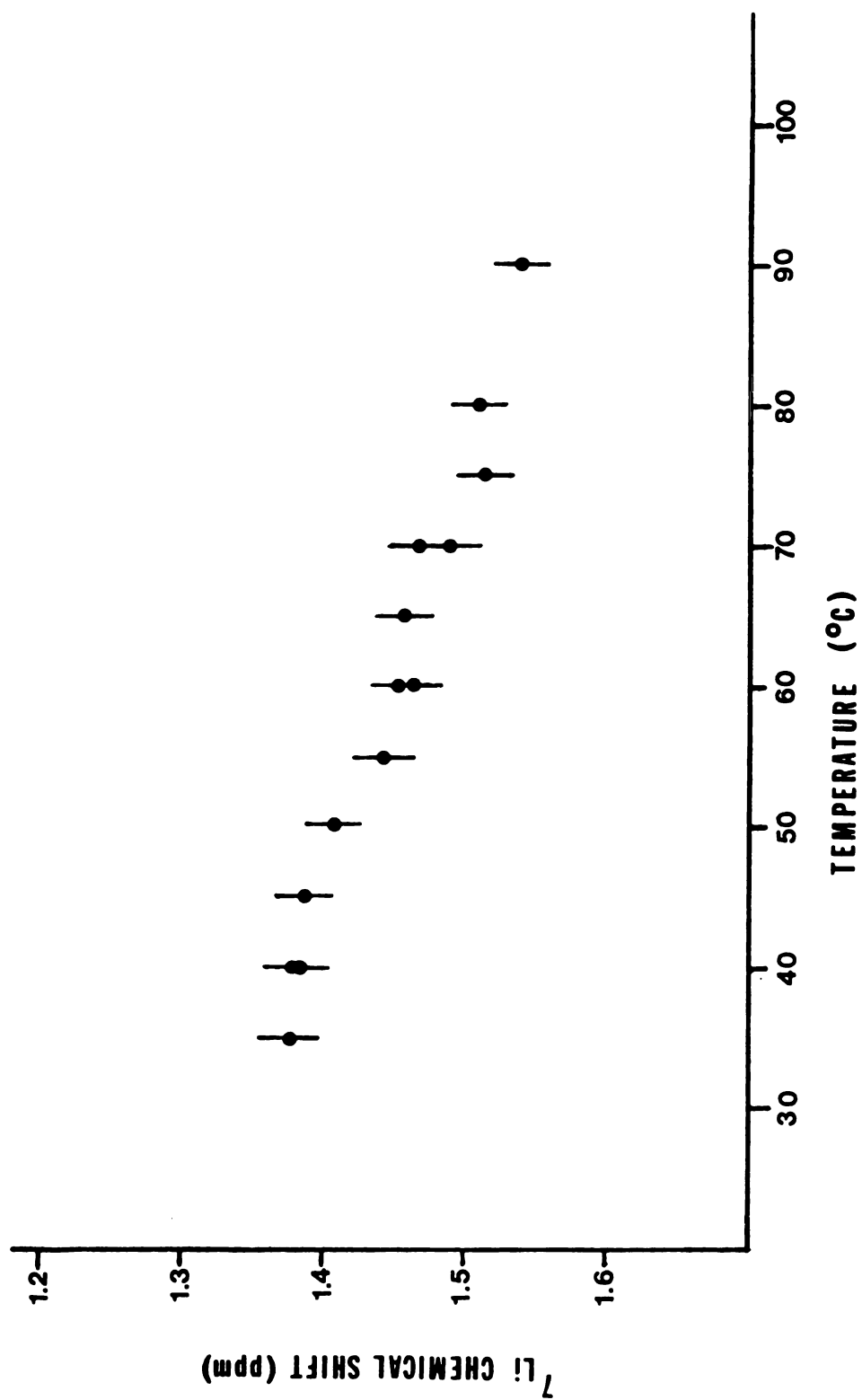
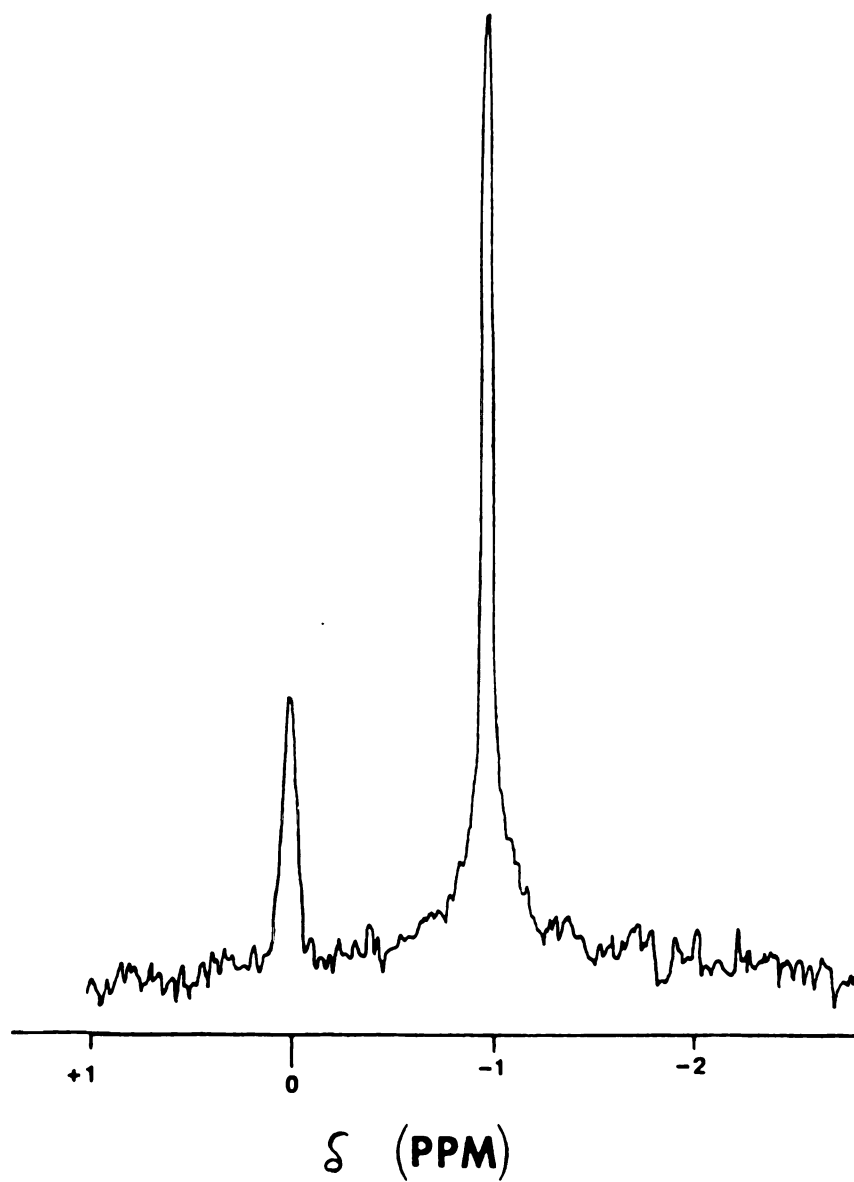


Figure 13. Lithium-7 Chemical Shifts versus Temperature for 1.0 Mol%  $\text{LiCl}$  in Basic Melt





**Figure 14.** Lithium-7 NMR Spectrum: 1.0 Mol%LiCl in Acidic  $\text{AlCl}_3$ -BPCl Melt at 40°C

that the lithium ion resides in a more symmetric environment than in basic melt. It should be borne in mind however, that the viscosity of basic melt is more than twice that of acidic melt (Table 3, Chapter I). Thus, if the quadrupolar mechanism is the main relaxation pathway for the  $^7\text{Li}$  nucleus in acidic and basic melts, the melt viscosities must be taken into account when comparing linewidths of these signals. Lithium-7 relaxation in these media is discussed in the following section.

The  $^7\text{Li}$  chemical shift of  $\text{LiCl}$  in acidic melt is insensitive to  $\text{LiCl}$  concentration (Table 11). Chloride ion from  $\text{LiCl}$  reacts with  $\text{Al}_2\text{Cl}_7^-$  ion in the acidic melt, making the mixture more basic. Thus, the higher solubility of  $\text{LiCl}$  in acidic melt (vs.  $\text{LiCl}$  in basic melt) is readily understood. The constancy of  $^7\text{Li}$  chemical shifts is attributed to essentially equal shielding influences of the  $\text{Al}_2\text{Cl}_7^-$  and  $\text{AlCl}_4^-$  ions.

A detailed study of the solubility limits of other  $\text{LiX}$  salts in acidic melt was not pursued. However, the  $^7\text{Li}$  chemical shifts of 1 mol%  $\text{LiF}$ ,  $\text{LiAsF}_6$ ,  $\text{LiClO}_4$ ,  $\text{LiBr}$  and  $\text{LiNO}_3$  were observed to be equal (to  $\pm 0.02$  ppm) to that of 1 mol%  $\text{LiCl}$  in acidic melt. As was observed for the basic melt solutions of these salts, the  $\text{X}^-$  counterions are incorporated into the acidic melt as spectators who exert no appreciable shielding influence on the lithium ion.

#### **B.1.b. Relaxation Measurements**

As a test of the FIRFT method for determining spin-lattice ( $T_1$ ) relaxation times, the  $^7\text{Li}$   $T_1$  values for 4 M  $\text{LiCl}$  in  $\text{H}_2\text{O}$  and  $\text{D}_2\text{O}$ , and 4 M  $\text{LiClO}_4$  in  $\text{D}_2\text{O}$  were obtained at  $25^\circ\text{C}$  and  $40^\circ\text{C}$ . A sequential plot of the  $^7\text{Li}$  NMR spectra for 4 M  $\text{LiClO}_4$  in  $\text{D}_2\text{O}$  at  $40^\circ\text{C}$  as a function of the post- $180^\circ$  ( $\tau$ ) delay time is shown in Figure 15. The results of these experiments are given in Table 12. For 4 M  $\text{LiCl}$  in  $\text{H}_2\text{O}$  and  $\text{D}_2\text{O}$  at  $25^\circ\text{C}$ , reasonable agreement was obtained with the  $T_1$  values reported by Hertz et al. (103) of 13.6 and 23.3 sec.,

Table 11

**Lithium-7 Chemical Shift Data for LiCl-Acidic  
Melt Solutions at 40°C**

<b>Mol% LiCl</b>	<b><math>\delta</math> (ppm) (a)</b>
0.092	- 1.15
0.411	- 1.16
0.677	- 1.15
0.877	- 1.15
0.991	- 1.15
2.08	- 1.14
4.69	- 1.14
9.42	- 1.15

(a) Versus external 0.015 M LiCl in D<sub>2</sub>O  
uncorrected for diamagnetic susceptibility;  
the uncertainty in  $\delta$  is  $\pm 0.02$  ppm.

DELAY TIMES :

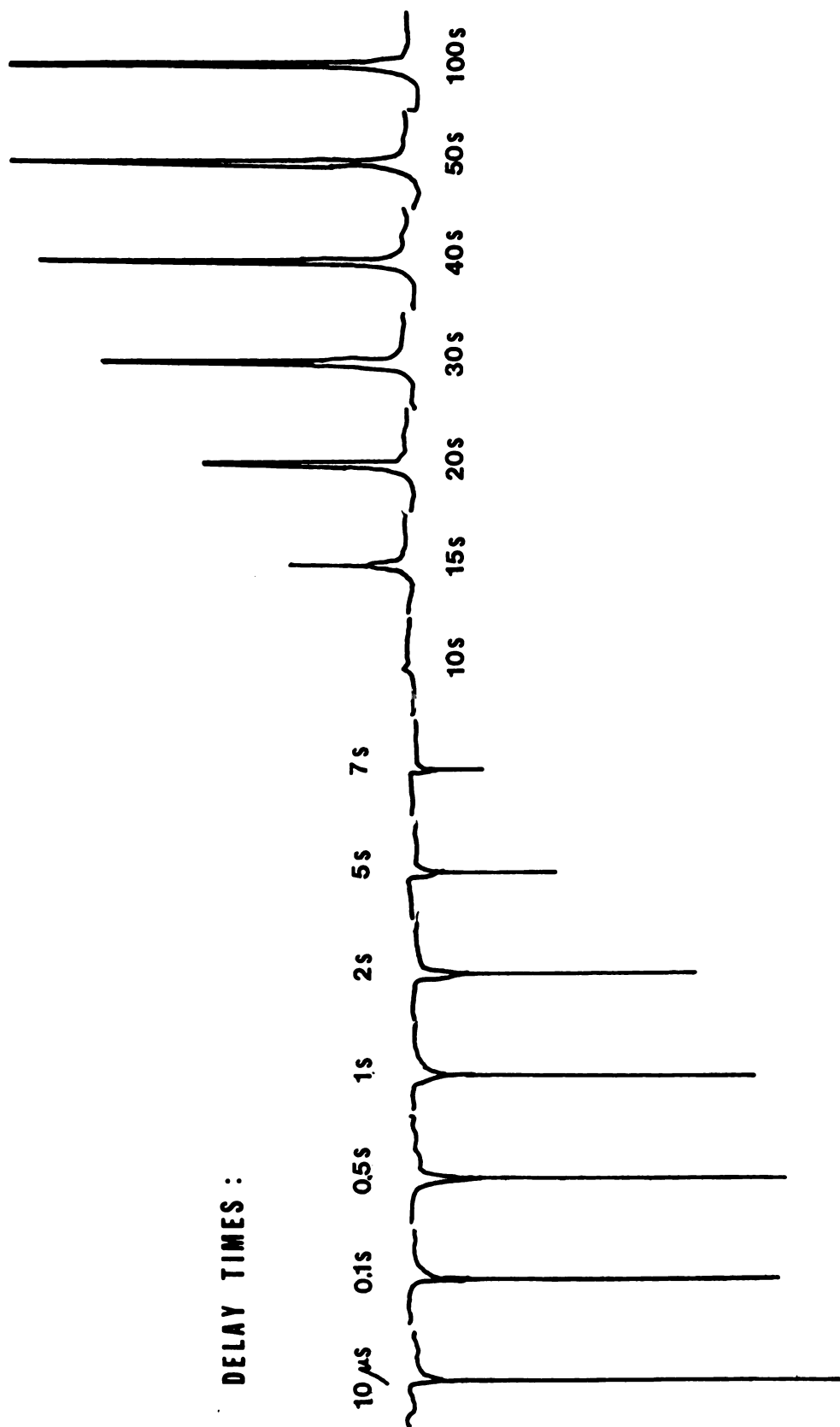


Figure 15. Lithium-7 NMR Spectra: Signal Intensities Versus Delay Time for 4 M  $\text{LiClO}_4$  in  $\text{D}_2\text{O}$  at  $40^\circ\text{C}$ .

**Table 12**  
**Lithium-7  $T_1$  Relaxation Times for Aqueous LiCl**  
**and LiClO<sub>4</sub> Solutions at 25°C and 40°C**

Sample	Temp. (°C)	$T_1$ (sec)
<hr/>		
4 <u>M</u> LiCl/H <sub>2</sub> O		
Run #1:	25	14.38 ± 2.68
Run #2:	25	12.27 ± 1.23
Run #1:	40	17.58 ± 2.30
Run #2:	40	17.33 ± 1.90
4 <u>M</u> LiCl/D <sub>2</sub> O		
Run #1:	25	22.00 ± 1.65
Run #2:	25	---
Run #1:	40	34.39 ± 4.18
Run #2:	40	---
4 <u>M</u> LiClO <sub>4</sub> /D <sub>2</sub> O		
Run #1:	25	13.67 ± 0.77
Run #2:	25	---
Run #1:	40	19.38 ± 1.79
Run #2:	40	16.98 ± 1.96

respectively. The average value for the inhomogeneity factor (W) determined from the fits of the  $T_1$  relaxation data is 0.9519, and is in good agreement with the value determined experimentally ( $W = 0.9541$ ).

With the reliability of the FIRFT method confirmed, the  $^7\text{Li}$  spin-lattice relaxation rates for LiCl and several other LiX salts in basic melt, and LiCl in acidic melt were measured at 25°C and 40°C (Table 13). No significant anion dependence in the calculated  $T_1$  values is observed at either temperature. These results are taken as further evidence for the coordination of the lithium ion by chloride ions to the exclusion of the counterions from the parent LiX salts.

A substantial (ca. 20%) decrease in the  $T_1$  relaxation rate occurs as the LiCl concentration is increased from 1 mol% to 2 mol%. If the spin-lattice relaxation process for the  $^7\text{Li}$  nucleus is dominated by the quadrupolar mechanism (Chapter I, equation 18), this result is interpreted as follows.

In equation 18 (Chapter I), the motional narrowing limit ( $\omega\tau_c \ll 1$ ) is assumed. If this condition is not met, the full expression is given by

$$R_1^Q = \frac{1}{T_1^Q} = C \chi^2 \left\{ \frac{\tau_c}{1 + (\omega\tau_c)^2} + \frac{4\tau_c}{1 + 4(\omega\tau_c)^2} \right\} \quad (6)$$

where  $C = (3\pi^2)(2I+3)/10 I^2(2I-1)$ ,  $\chi = e^2qQ/h$ ,  $\omega$  is the resonance frequency in radians per second, and  $\sigma$  is assumed to be zero for axial symmetry. If the rotational correlation time is known, the quadrupole coupling constants can be estimated. In the Gierer-Wirtz model (98), the rotational correlation time may be determined by using equation 7,

$$\tau_c = \frac{4\pi r^3 \eta f}{3kT} \quad (7)$$

**Table 13**  
**Lithium-7  $T_1$  Relaxation Times for Some Lithium Salts**  
**in the  $\text{AlCl}_3$ -BPCl System at 25°C and 40°C**

Sample	$T_1$ (sec.)	
	at 25°C	at 40°C
1.0 Mol% LiCl	$0.046 \pm 0.002$	$0.043 \pm 0.002$
2.0 Mol% LiCl	$0.063 \pm 0.004$	$0.061 \pm 0.003^{(a)}$
1.0 Mol% LiBr	$0.050 \pm 0.003$	$0.049 \pm 0.005^{(a)}$
1.0 Mol% $\text{LiClO}_4$	$0.051 \pm 0.003$	$0.048 \pm 0.002$
1.0 Mol% $\text{LiAsF}_6$	$0.050 \pm 0.003$	$0.052 \pm 0.003$
1.0 Mol% $\text{LiNO}_3$	$0.041 \pm 0.002$	$0.039 \pm 0.008^{(a)}$
1.0 Mol% LiCl (in acidic melt)	$1.10 \pm 0.27$	$1.52 \pm 0.08$

(a) Single experiment; all other values are the averages of two experiments.

where  $\eta$  is the dynamic viscosity and  $f$  is the microviscosity factor (Chapter I, equation 24). To calculate  $f$  for the monomer and dimer species, for  $a$  and  $a_s$  (radii of the solute ion and the solvent ion, respectively estimated from the proposed structural model for the lithium ion in bas (Figure 5).

Taking  $a = r_{Li} + r_{Cl^-} = 2.56 \text{ \AA}$  (136) for the monomer, and  $a_s = r_{Li} + r_{Cl^-} = 2.13 \text{ \AA}$  (Chapter IV, section C.3),  $f_{\text{monomer}} = 0.19$ . For the dimer,  $a$  is as the radius of the sphere swept out in solution by this species  $= 5.3 \text{ \AA}$ ,  $a_s = 2.13 \text{ \AA}$ ,  $f_{\text{dimer}} = 0.36$ . Assuming that the dynamic viscosity of a 0.037 mol% LiCl-basic melt solution is equal to that of pure basic melt (0.037 Kg/m s; Chapter I, Table 3) at 40°C, the rotational correlation times for the monomer ( $\tau_c^{\text{monomer}} = 3.5 \times 10^{-10} \text{ s}$ ) and the dimer ( $\tau_c^{\text{dimer}} = 1.1 \times 10^{-9} \text{ s}$ ) are obtained. For comparison, the  $\tau_c$  value for D<sub>2</sub>O at 30°C is  $1.1 \times 10^{-12} \text{ s}$  with  $\eta = 0.011 \text{ Kg/m s}$  (112). Considering the approximations made, the agreement of the  $\tau_c$  values for the monomer and dimer is acceptable. Since better than 90% of the lithium species in basic melt (1 mol% or 2 mol% LiCl concentrations) is found as the dimer,  $\tau_c^{\text{dimer}}$  is used in the following calculation.

Rearranging equation 6,

$$\chi = \left( \frac{R_1 Q}{C \tau_r} \right)^{1/2}$$

where  $\tau_r$  is given as the bracketed portion of equation 6. Assuming  $\tau_r$  value obtained for the 2 mol% LiCl-basic melt solution at 40°C (Chapter IV, Table 4) is characteristic of the dimer only ( $X_{\text{monomer}} \approx 0.07$ ), a value of  $\pm 30 \text{ kHz}$  is obtained. A similar calculation for 1.0 mol% LiCl in acid at 40°C yields  $f = 0.03$  ( $a = r_{Li^+} = 0.86 \text{ \AA}$ ;  $a_s = r_{Al_2Cl_7^-} = 4.2 \text{ \AA}$ ),



$\times 10^{-13}$  s ( $\eta = 0.0143$  Kg/m s from Table 3, Chapter I), and  $X = 0.2$  kHz. Some representative quadrupolar coupling constants for the  $^7\text{Li}$  nucleus in the gas, solution, and solid states are listed in Table 14 for comparison (101,176,174).

The  $\chi$  value which is obtained for the lithium ion in basic melt is in good agreement with the values for concentrated aqueous lithium ion solutions. However, the  $^7\text{Li}$  coupling constant for the lithium ion in acidic melt is smaller than those for the aqueous solutions by a full order of magnitude.

The tetrahedral coordination of the lithium ion in the dimer model must be viewed within the context of the dynamics of the liquid state. Collisions between ions can give rise to a nonzero EFG at the  $^7\text{Li}$  nucleus without permanently disrupting the nominal tetrahedral symmetry about the lithium ion. This collisional model for quadrupolar nuclei was developed by Deverell (177) to account for the nonzero NMR linewidths for these nuclei in highly symmetric solution environments. However, it is likely that some distortion from tetrahedral symmetry is occurring in the dimer considering the size of the coupling constant. For the lithium ion in acidic melt, it appears that the  $\text{Al}_2\text{Cl}_7^-$  ions provide a more symmetric environment (closer to a regular tetrahedron); thus, a smaller coupling constant is obtained.

The  $^7\text{Li}$   $T_1$  relaxation times for 1.0 mol% LiCl in basic melt were determined at six temperatures from 40°C to 85°C. these results are given in Table 15. A plot of  $\ln (1/T_1)$  versus  $1000/T(\text{K})$  for these data is shown in Figure 16. A roughly linear decrease in  $\ln (1/T_1)$  with increasing temperature is observed between 40° and 75°C. A very slight increase of the relaxation rate (considering the size of the error bars) seems to occur between 80°C and 85°C. In view of the evidence presented thus far in support of the dimer model in LiCl-basic melt solutions, it is possible that this peculiar reversal of temperature dependence may arise from a change in aggregation (i.e., dimer

**Table 14**  
**Lithium-7 Nuclear Quadrupole Coupling Constants**  
**in Various Substances**

System	$\chi$ (kHz)	Ref.
<b>Gas Phase:</b>		
Li <sub>2</sub>	60	
LiF	408	
LiCl	192	176
LiBr	184	
LiI	172	
<b>Solutions:</b>		
6 <u>M</u> LiI/H <sub>2</sub> O	35	
6 <u>M</u> LiCl/H <sub>2</sub> O	44	101
6.2 <u>M</u> LiCl/glycerol	28	
<b>Solid State:</b>		
"A" zeolite <sup>(a)</sup>	62	
Li <sub>2</sub> CO <sub>3</sub>	60	174
Li <sub>2</sub> SO <sub>4</sub> ·(H <sub>2</sub> O)	45	

(a) Li<sub>11.67</sub>Na<sub>0.13</sub>(AlO<sub>2</sub>)<sub>12</sub>(SiO<sub>2</sub>)<sub>12</sub>·27H<sub>2</sub>O

**Table 15**

**Lithium-7  $T_1$  Relaxation Times for 1.0 Mol% LiCl  
in Basic Melt as a Function of Temperature  
(40°C to 85°C)**

<b>Temp. (°C)</b>	<b><math>T_1</math> (sec)</b>
40	0.046 ± 0.002
50	0.051 ± 0.003
60	0.053 ± 0.005
71	0.060 ± 0.005
80	0.062 ± 0.007
85	0.057 ± 0.008

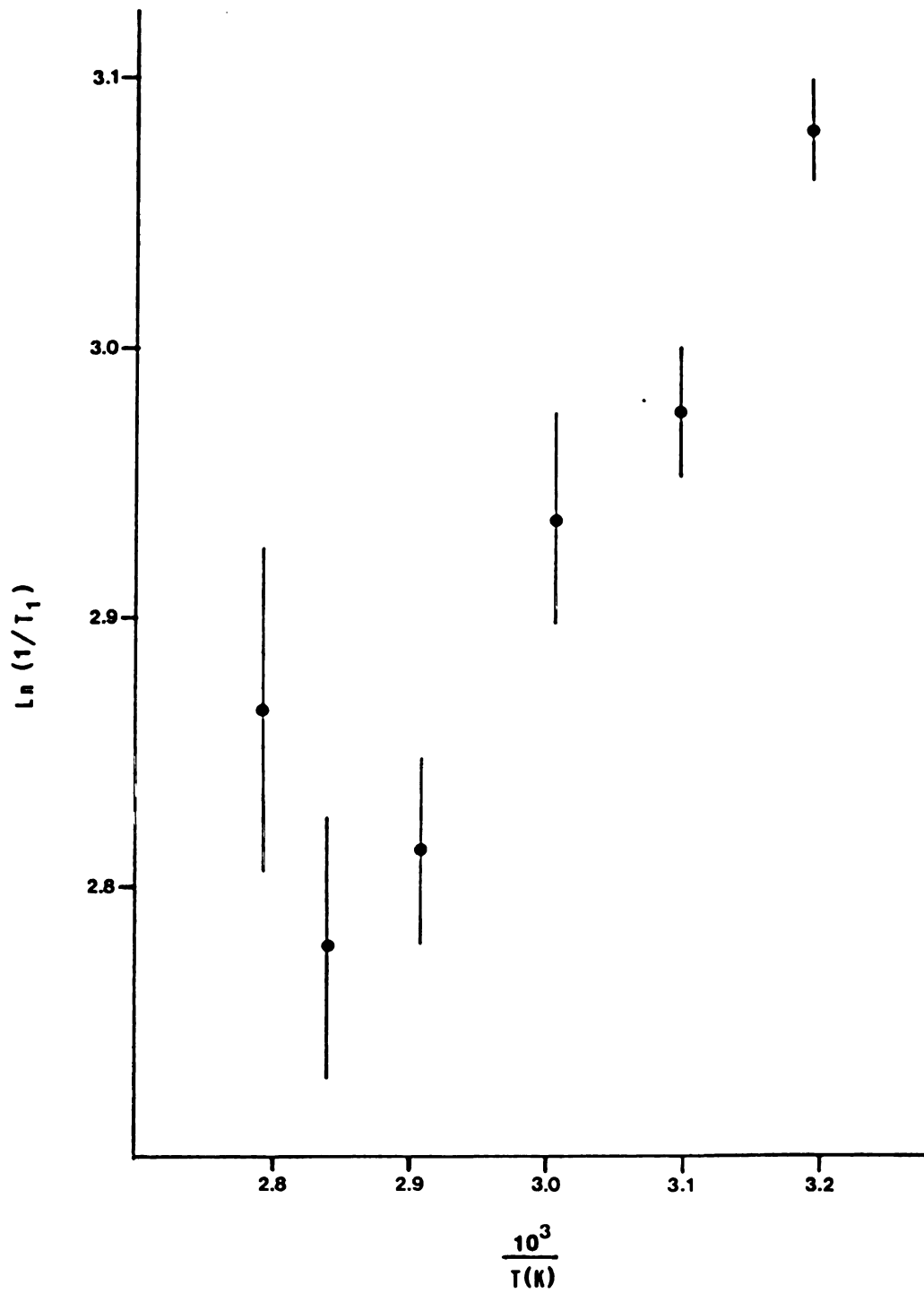


**Figure 16.**  $\ln(1/T_1)$  Versus  $1/T(K)$  for  $^7\text{Li}$  in 1.0 Mol% LiCl-Basic Melt Solution.

monomer). Although the onset of the spin rotation relaxation mechanism is another possible explanation for this behavior, it is considered to be unlikely (107,110). More relaxation data at higher temperatures could aid in clarifying this point.

The linewidth of the  $^7\text{Li}$  NMR signal for 1.0 mol% LiCl in basic melt is found to be sensitive to temperature. Values for  $\Delta\nu_{1/2}$  and  $T_2^*$  ( $= 1/\pi\Delta\nu_{1/2}$ ) are listed in Table 16 as a function of temperature (27°C to 150°C). These data are shown in the form of a plot of  $\ln(1/T_2^*)$  versus  $1000/T(\text{K})$  in Figure 17. Qualitatively, the curve described by these points is similar to the one in Figure 16 for the  $T_1$  relaxation data. However, the minima in these curves occur at two different temperatures; ca. 80°C in Figure 16, and ca. 125°C in Figure 17. If a change in aggregation at 80°C is the correct interpretation of the anomalous spin-lattice relaxation behavior, at 125°C it would be logical to assume that most of the total amount of the lithium ion is in the monomer form ( $\text{LiCl}_2^-$ ). Since no further dissociation is likely, the onset of the spin rotation mechanism above 125°C could account for the increasing spin-spin relaxation rate of the  $^7\text{Li}$  nucleus. Spin rotation relaxation arises from the interaction between nuclear magnetic moments and rotational magnetic moments of the molecules containing these nuclei. With the exception of  $^{73}\text{Ge}$ ,  $^7\text{Li}$  has the largest nuclear moment of all of the quadrupolar nuclei ( $2.13 \times 10^{-26} \text{ J/T}$ ). In addition, the rotational magnetic moment for the monomer might be expected to be rather large.

## B.2. Aluminum-27 NMR

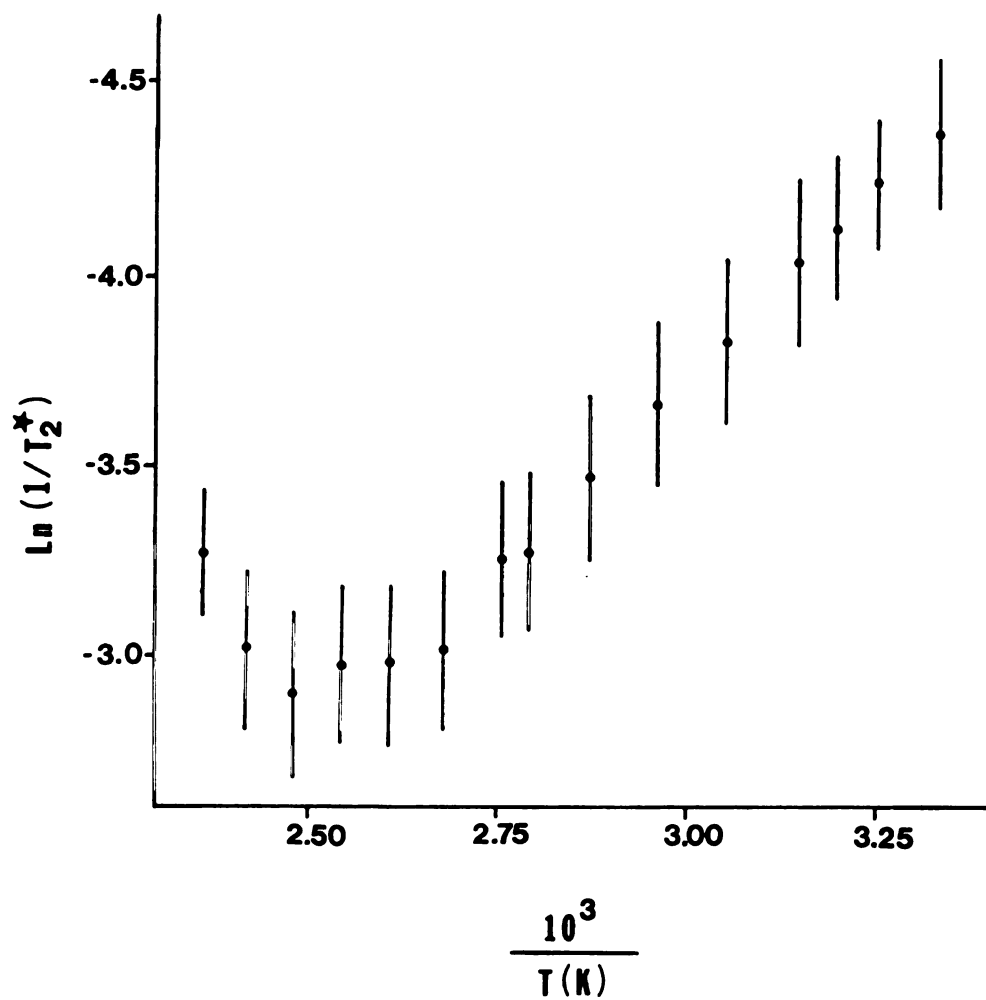
The  $\text{Al}^{27}$  NMR spectrum for pure basic melt at 40°C is shown in Figure 18. The downfield signal ( $\delta = +102.4 \pm 0.5 \text{ ppm}$  vs. external 0.5 M  $\text{Al}(\text{NO}_3)_3$  in 1 M aqueous  $\text{HNO}_3$ ,  $\Delta\nu_{1/2} = 31 \pm 2 \text{ Hz}$ ) is assigned to the  $\text{AlCl}_4^-$  ion. The chemical shift of this signal is in agreement with the value of +102.6 ppm

Table 16

**Linewidths ( $\Delta\nu_{1/2}$ ) and Apparent Spin-Spin Relaxation Times ( $T_2$ )  
for the  $^7\text{Li}$  NMR Signal of 1.0 Mol% LiCl in Basic Melt as a  
Function of Temperature (27°C to 150°C)**

Temp. (°C)	$\Delta\nu_{1/2}$ (Hz)(a)	$T_2$ (sec)
27	25.8	$0.012 \pm 0.006$
35	22.5	$0.014 \pm 0.006$
40	20.0	$0.016 \pm 0.007$
45	18.3	$0.017 \pm 0.009$
55	14.8	$0.022 \pm 0.011$
65	12.5	$0.026 \pm 0.013$
75	10.3	$0.031 \pm 0.016$
85	8.4	$0.038 \pm 0.019$
90	8.3	$0.039 \pm 0.019$
100	6.5	$0.049 \pm 0.024$
110	6.3	$0.051 \pm 0.025$
120	6.3	$0.051 \pm 0.025$
130	5.8	$0.055 \pm 0.028$
140	6.5	$0.049 \pm 0.024$
150	8.4	$0.038 \pm 0.019$

(a) The uncertainty in  $\Delta\nu_{1/2}$  is estimated to be  $\pm 0.5$  Hz.



**Figure 17.**  $\ln(1/T_2^*)$  Versus  $1/T(K)$  for  $^7\text{Li}$  in 1.0 Mol% LiCl-Basic Melt Solution.

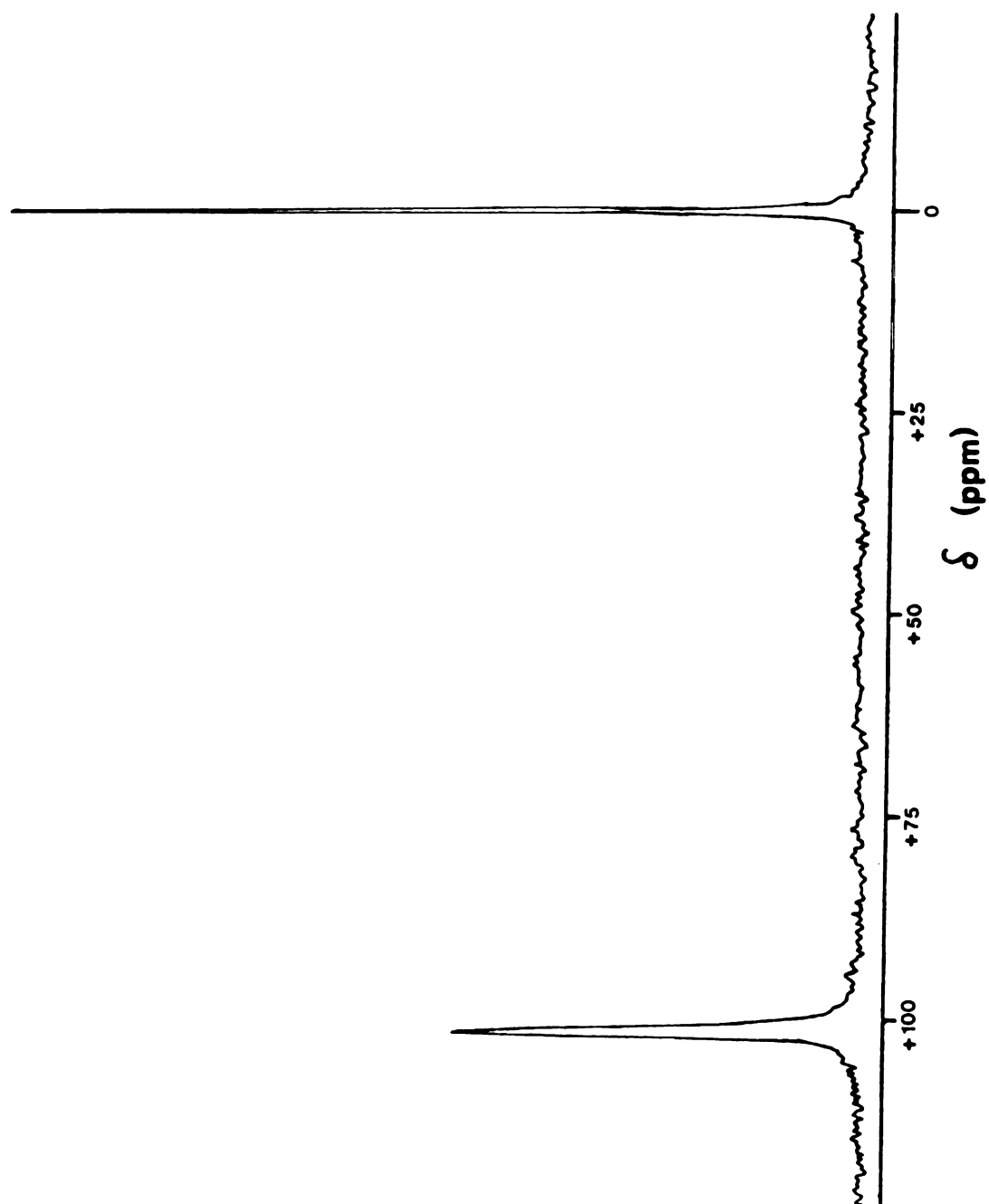


Figure 18. Aluminum-27 NMR Spectrum: 45 Mol%  $\text{AlCl}_3$ -BPCI Melt at  $40^\circ\text{C}$ .



by Kidd and Truax (178). Gray and Maciel (179) obtained  $\Delta\nu_{1/2} = 40$  Hz for basic  $\text{AlCl}_3\text{-BPCl}$  melt at  $36^\circ\text{C}$ . In this latter work, these authors observed a sharp increase in  $\Delta\nu_{1/2}$  for melt compositions with  $X_{\text{AlCl}_3} > 0.5$ . Their plot of  $\Delta\nu_{1/2}$  vs. melt composition is reproduced in Figure 19. Chemical exchange between the  $\text{AlCl}_4^-$  and  $\text{Al}_2\text{Cl}_7^-$  ions, and lower symmetry for the  $\text{Al}_2\text{Cl}_7^-$  ion (quadrupole effect) were cited as the sources of this broadening of the  $^{27}\text{Al}$  line with increasing melt acidity (182).

The  $^{27}\text{Al}$  NMR spectra for 1 mol%  $\text{LiCl}$ ,  $\text{LiBr}$ ,  $\text{LiNO}_3$ ,  $\text{LiAsF}_6$ , and  $\text{LiClO}_4$ -basic melt solutions were obtained at  $40^\circ\text{C}$ . No effect on the chemical shift, and very little effect on the linewidth ( $\pm 5$  Hz) of the signal for the  $\text{AlCl}_4^-$  ion was observed. Thus, it is concluded that the  $^{27}\text{Al}$  nucleus is not particularly useful as a secondary probe (to  $^7\text{Li}$ ) for the study of dilute  $\text{LiX}$ -basic melt solutions. However, the extreme sensitivity of linewidths to changes in melt composition (above  $X_{\text{AlCl}_3} = 0.5$ ) suggests that  $^{27}\text{Al}$  NMR may be used, as an alternative to electrochemical methods, to further investigate the acid-base equilibria in  $\text{AlCl}_3$ -based molten salt systems.

### B.3. Potentiometry

The potentiometric titration curves for the titration of pure basic melt with acidic melt titrant are shown in Figure 20. The reproducibility of the observed cell potential on the basic side of the equivalence point (i.e., from zero to ca. 1 g of the acidic melt titrant) is clearly demonstrated. Fluctuations in the cell potential beyond the equivalence point were often observed in these experiments; however, this behavior was considered to be unimportant since the behavior of the cell potential on the basic side was of foremost interest in these studies. The corrected composition of the titrant (section B.2, Chapter II) is 65.51 mol%  $\text{AlCl}_3$ . The corrected mole fraction of the free chloride ion ( $X_{\text{Cl}^-}$ ),  $p\text{Cl}$ , and observed cell potentials for titration #1 used in subsequent

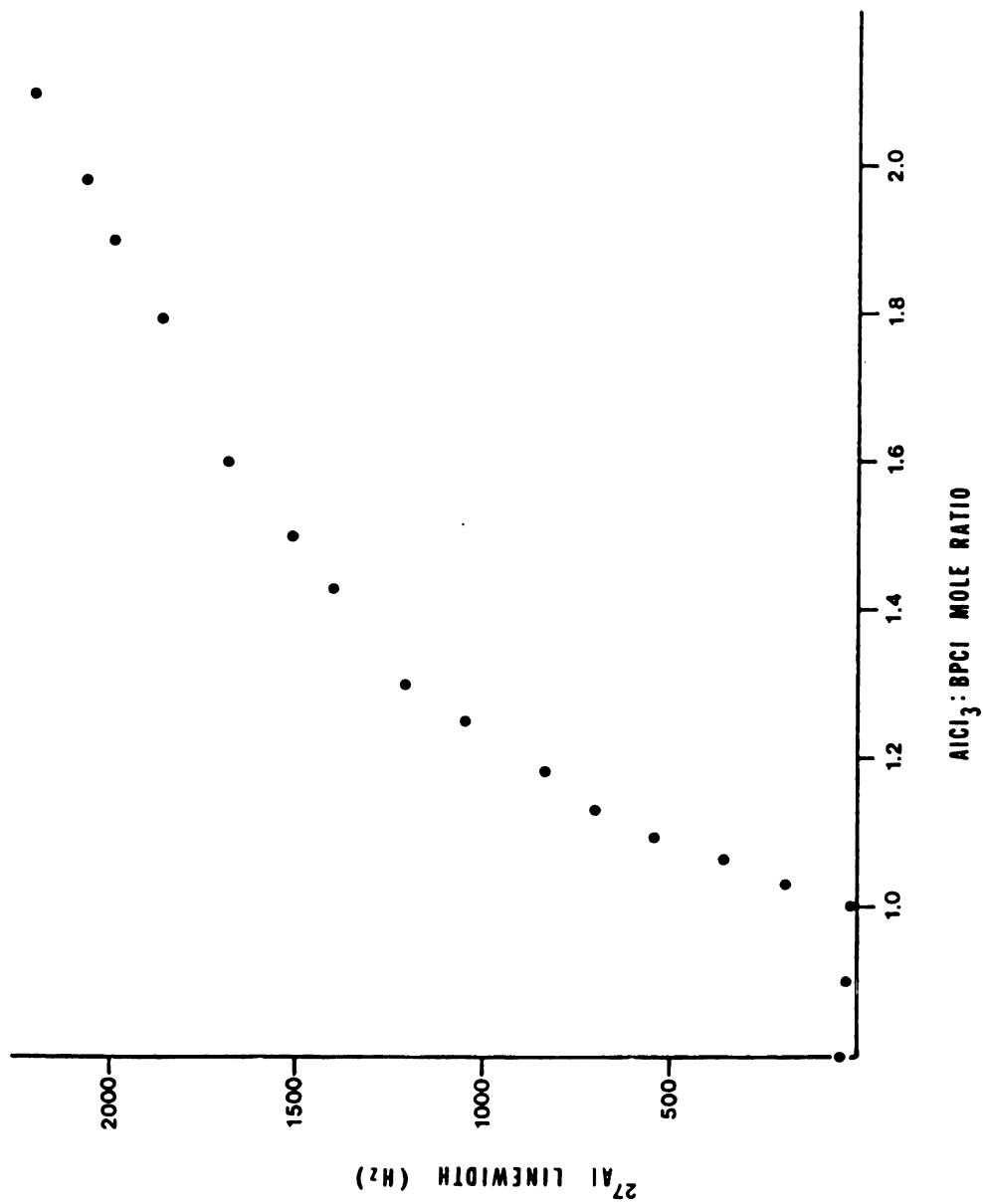
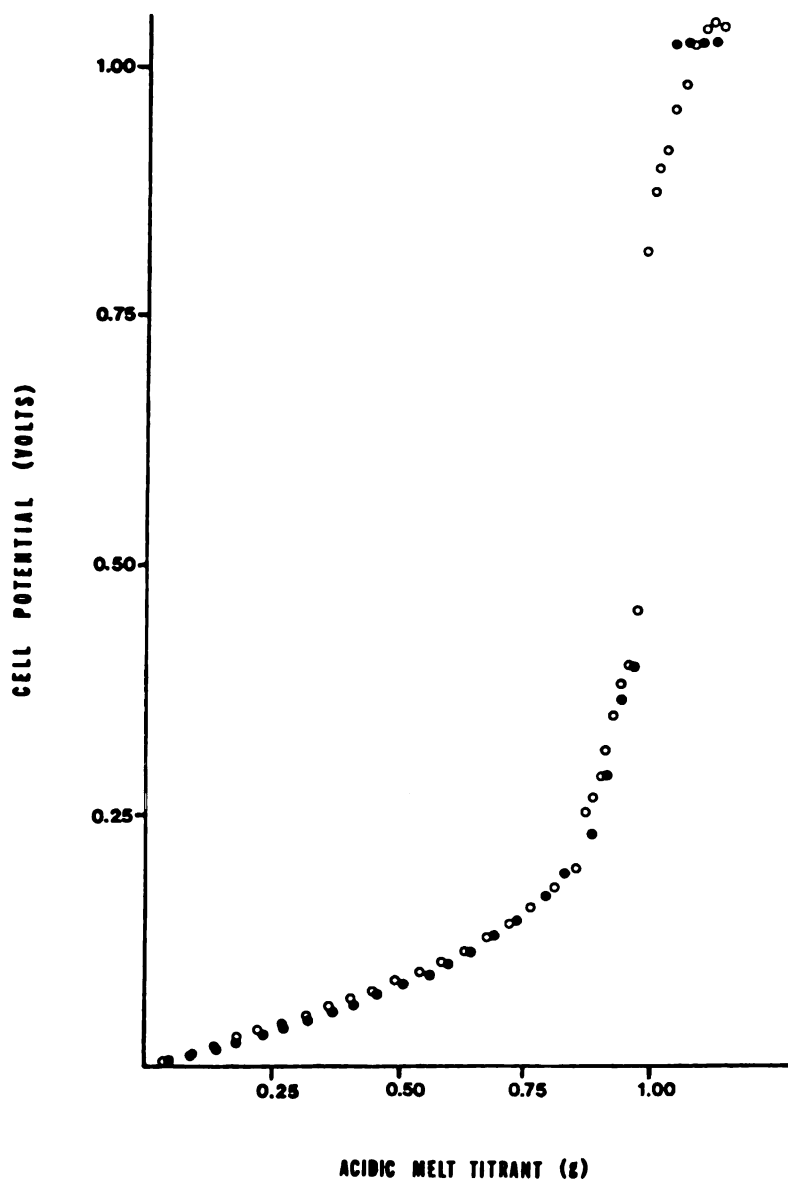


Figure 19. Aluminum-27 NMR: Linewidth as a Function of Composition in  $\text{AlCl}_3$ -Basic Melts at  $36^\circ\text{C}$ . Taken From Reference 182.



**Figure 20. Potentiometry:  $E_{\text{cell}}$  Versus Acidic Melt Titrant (g) for the Titration of 45 Mol%  $\text{AlCl}_3$ -Basic Melt. The Results for Duplicate Titrations are Shown; Titration #1 (O), Titration #2 (●). The Uncertainties in the Cell Potential and in the Mass of the Titrant are Smaller than the Size of the Data Points.**

calculations are given in Table 17.

A plot of  $E_{\text{cell}}$  versus  $p\text{Cl}$  (corrected) is shown in Figure 21. A least squares fit of the first ten data points to equation 42 (Chapter II) yields a slope of 0.2445 Volts at 35°C (theoretical slope = 0.2434 Volts). The "tailing off" of the actual curve is a consequence of the displacement of the equilibria involving the various silver chlorocomplexes (i.e., equation 42 no longer holds) as the chloride ions released by these species are titrated (76).

The titration curves for 0.977 mol% LiCl and 0.960 mol% LiClO<sub>4</sub>-basic melt solutions titrated with acidic melt are shown in Figure 22. The points marked (PPT.) in each curve are the points where the first signs of cloudiness in the melt solutions (presumably, dispersions of LiCl precipitate) were observed. These precipitates persisted in the solutions until the end points of the titrations. The label (CLEAR) designates the points at which the precipitates could no longer be discerned.

Both curves start at positive (ca. 30 to 40 mV), rather than zero potentials (cf. Figure 20). If each LiCl molecule requires one chloride ion from the melt to be solublized (i.e.,  $\text{LiCl}_2^-$  is formed), equation 42 (Chapter II) predicts a positive cell potential of ca. 10 mV for a 1.0 mol% LiCl-basic melt solution. For the same concentration of LiClO<sub>4</sub> in basic melt, the potential should be ca. 24 mV. However, it should be recalled (Chapter II, section A.4.b(1).) that the zero adjustment at the start of a given titration amounted to about 15 mV. Thus, a quantitative interpretation of the nonzero starting potentials in these titrations is not justified.

The two curves are shifted slightly with respect to each other since the cell potential is plotted versus the acidic melt titrant, and not  $p\text{Cl}$ . The cell potentials at which the precipitates form in these solutions are 175 mV (LiCl) and 140 mV (LiClO<sub>4</sub>). Working from Figure 21, these potentials correspond

**Table 17****Potentiometric Titration Data: Corrected Values of  $X_{Cl^-}$** **Are Calculated by Using Equation 53;  $pCl = -\log X_{Cl^-}$ .**

<b>Aliq. #</b>	<b>Titrant (g)(a)</b>	<b><math>X_{Cl^-}</math></b>	<b>pCl</b>	<b><math>E_{cell}</math> (mV)(b)</b>
0	0.0	0.1000	1.000	0
1	0.0457	0.0938	1.028	8
2	0.0915	0.0878	1.057	16
3	0.1372	0.0819	1.087	24
4	0.1830	0.0762	1.118	31
5	0.2287	0.0707	1.151	39
6	0.2744	0.0653	1.185	47
7	0.3202	0.0601	1.221	56
8	0.3659	0.0550	1.260	64
9	0.4117	0.0501	1.300	74
10	0.4574	0.0453	1.344	83
11	0.5031	0.0406	1.392	94
12	0.5489	0.0360	1.443	105
13	0.5946	0.0316	1.500	117
14	0.6404	0.0273	1.565	129
15	0.6861	0.0230	1.638	145
16	0.7318	0.0189	1.723	162
17	0.7776	0.0149	1.827	185
18	0.8233	0.0110	1.959	211
19	0.8691	0.0072	2.145	252

Table 17 continued

Aliq. #	Titrant (g)(a)	X <sub>Cl<sup>-</sup></sub>	pCl	E <sub>cell</sub> (mV)(b)
20	0.8939	0.0050	2.298	285
21	0.9188	0.0029	2.532	337
22	0.9437	0.0009	3.063	418
23	0.9686	--	--	1040
24	0.9935	--	--	1045
25	1.0183	--	--	1046
26	1.0432	--	--	1046
27	1.0681	--	--	1046

(a)  $\pm 0.0001$  g(b)  $\pm 1$  mV

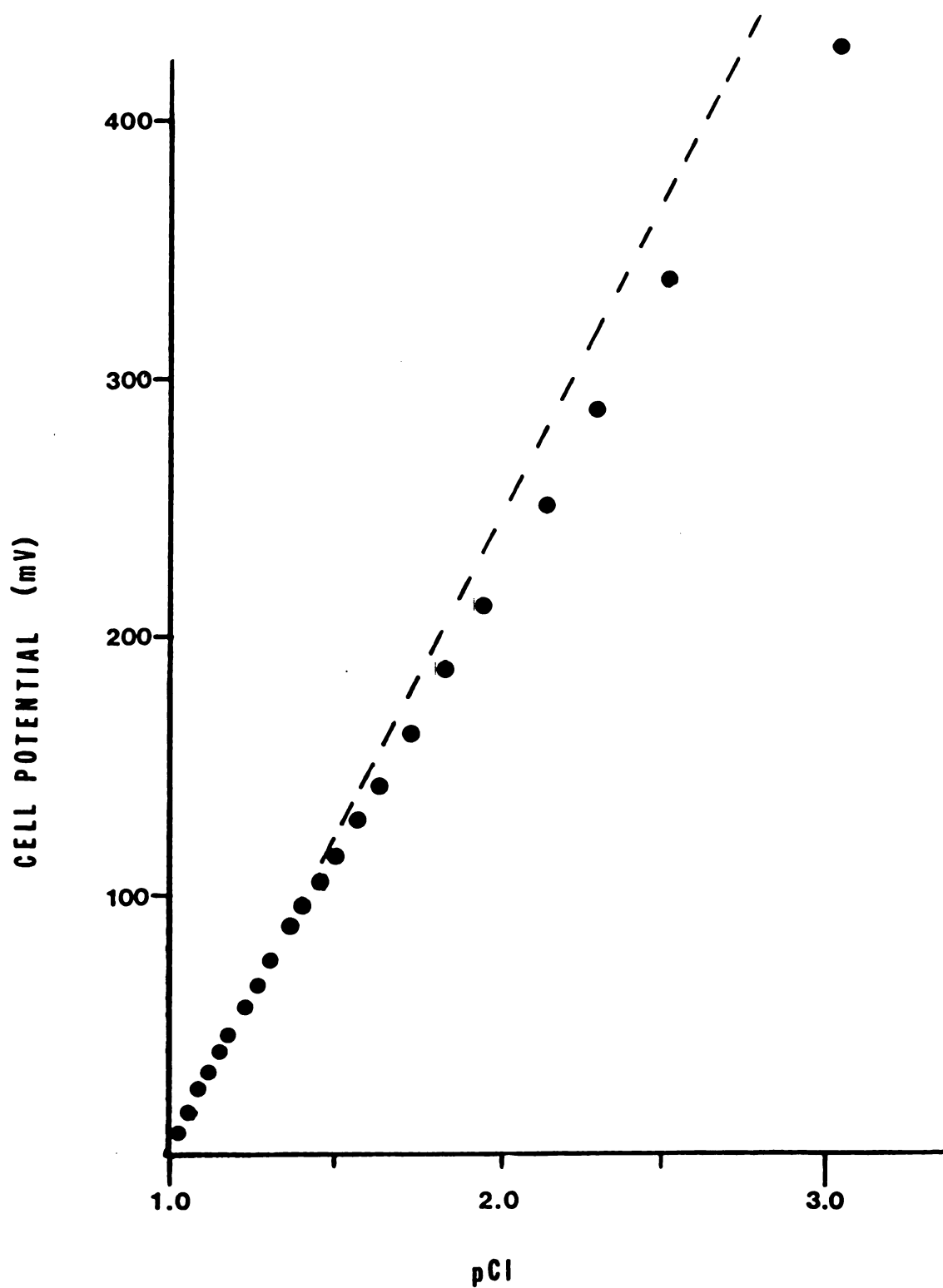


**Figure 21.** Potentiometry:  $E_{\text{cell}}$  Versus  $p\text{Cl}$  (Corrected) for the Titration (#1) of Basic Melt with Acidic Melt Titrant.

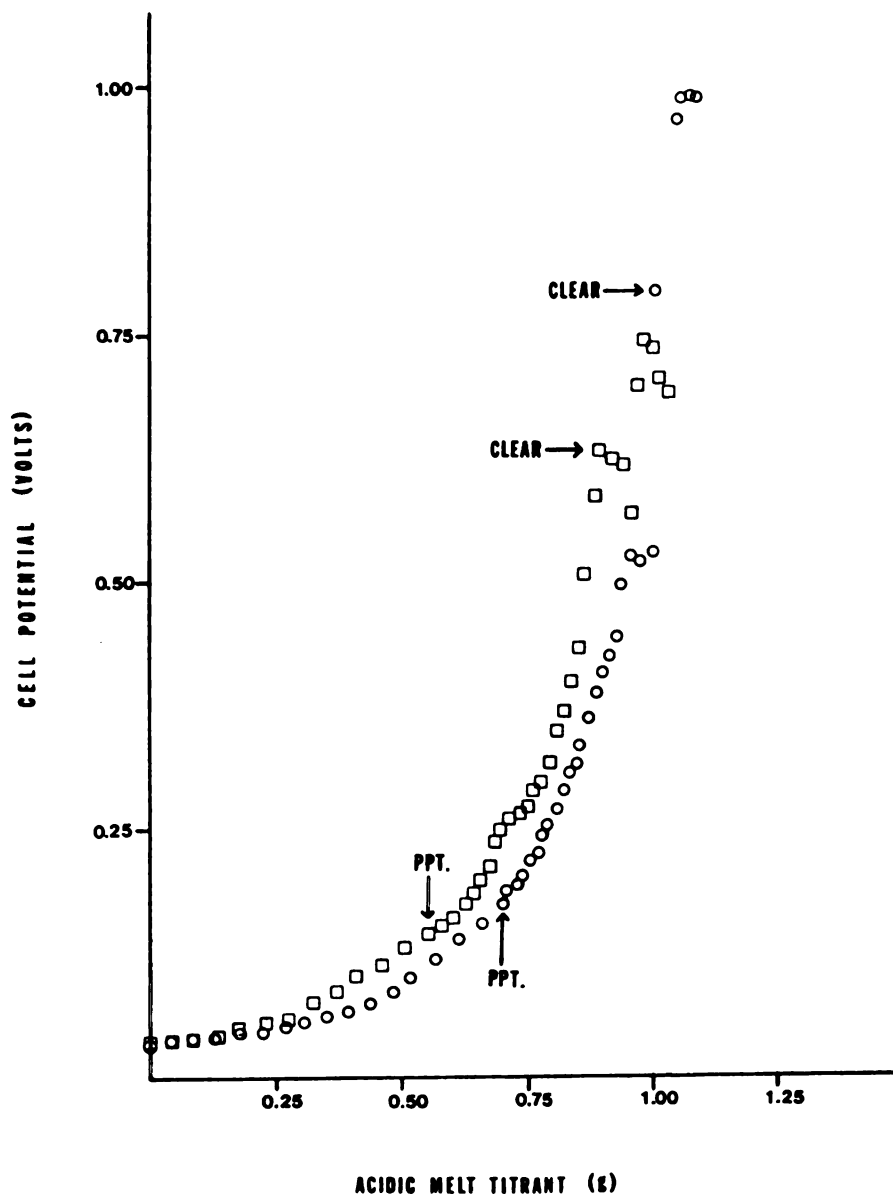


**Figure 22.** Potentiometry:  $E_{\text{cell}}$  Versus Acidic Melt Titrant (g) for the Titrations of 0.977 Mol% LiCl-Basic Melt (O) and 0.960 Mol% LiClO<sub>4</sub>-Basic Melt (□) Solutions. The Uncertainties in the Cell Potential and in the Mass of the Titrant are Smaller than in the Size of the Data Points.



to pCl values of 1.780 (LiCl) and 1.615 (LiClO<sub>4</sub>). These results are consistent with the model which is proposed for the solvation of lithium salts in basic melt; LiCl requires only one chloride ion from the melt to form LiCl<sub>2</sub><sup>-</sup> (and Li<sub>2</sub>Cl<sub>4</sub><sup>2-</sup>), while LiClO<sub>4</sub> requires two chloride ions. This is also further evidence (see section B.1, this chapter) for the spectator status of the perchlorate ion.

The values for  $n^{p \rightarrow e}$ ,  $n^*_{Cl^-}$ ,  $n^o_{LiX}$ , and  $n^*_{total}$  used to calculate the value of  $x$  for the assumed LiCl<sub>x</sub><sup>(1-x)</sup> complexes (see equations 50-58, section B.2 Chapter II) for the LiCl and LiClO<sub>4</sub>-basic melt titrations are given in Table 18. Equation 55 is modified for the calculation of  $x$  for the titration of the LiClO<sub>4</sub>-basic melt solution. In this case, no chloride ion is provided to the solution by LiClO<sub>4</sub>. Then equation 55 becomes

$$n^{p \rightarrow e} = n^*_{Cl^-} + (x-1)n_{complex} \quad (9)$$

If  $n_{complex} = n^o_{LiClO_4}$ ,

$$x = \frac{n^{p \rightarrow e} - n^*_{Cl^-}}{n^o_{LiClO_4}} + 1 \quad (10)$$

The values of  $x$  which are obtained are in agreement with the value of two expected for the LiCl<sub>2</sub><sup>-</sup> or Li<sub>2</sub>Cl<sub>4</sub><sup>2-</sup> chlorocomplexes.

#### B.4. Far-IR Measurements

As discussed in Chapter V (section D.), the far-IR spectrum of basic melt is dominated by the  $\nu_3(F_2)$  (490 and 527 cm<sup>-1</sup>) and  $\nu_4(F_2)$  vibrational modes of the AlCl<sub>4</sub><sup>-</sup> ion. The formally IR-forbidden  $\nu_1(A_1)$  mode for this ion is barely discernable at 345 cm<sup>-1</sup> (Figure 23). It is assumed that this mode can be observed in the IR due to strong ionic associations occurring in basic melt (59).

Table 18

Values for  $n^{p \rightarrow e}$ ,  $N_{Cl^-}$ ,  $n^o_{LiX}$ , and  $n_{total}$  Used in the  
 Calculation of  $x$  for the Assumed  $LiCl_x$  Chlorocomplexes  
 Formed in  $LiCl$  and  $LiClO_4$ - Basic Melt Solutions

Value (moles)	Lithium Salt (Mol%)	
	0.977 $LiCl$	0.960 $LiClO_4$
$n^{p \rightarrow e}$	$6.33 \times 10^{-4}$	$6.59 \times 10^{-4}$
$n^*_{Cl^-}$	$2.21 \times 10^{-4}$	$4.84 \times 10^{-4}$
$n^o_{LiX}$	$1.91 \times 10^{-4}$	$1.70 \times 10^{-4}$
$n^*_{total}$	$2.43 \times 10^{-2}$	$1.91 \times 10^{-2}$
$x$	2.2	2.0

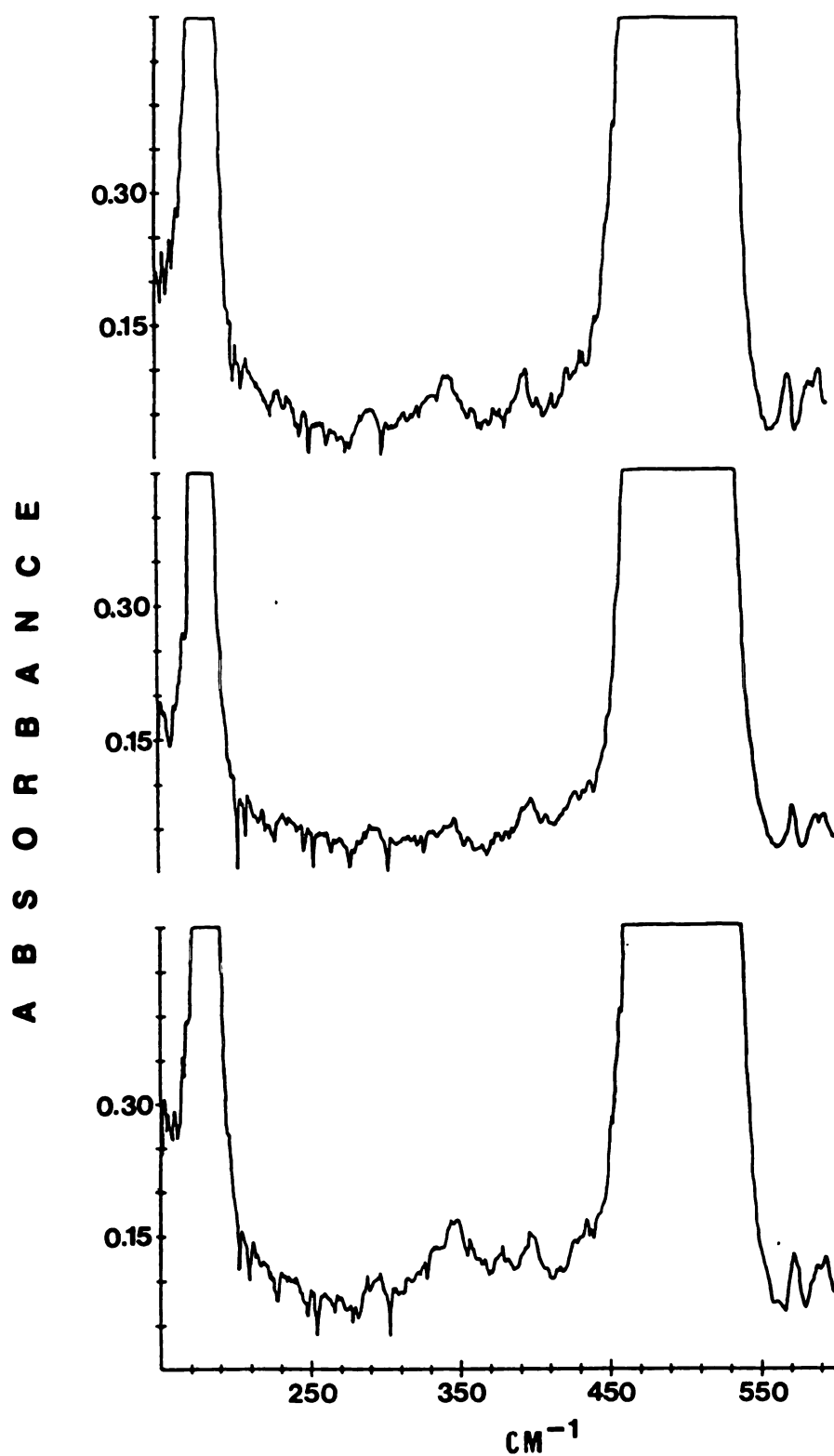


**Figure 23.** Far-IR Spectra (150 to 600 cm<sup>-1</sup>): A. Basic Melt, B. 1 Mol% LiCl-Basic Melt Solution. C. 1 Mol% LiCl-1.5 Mol% C211-Basic Melt Solution.

The far-IR spectra for basic melt, 1.0 mol% LiCl-basic melt solution, and 1.0 mol% LiCl -1.5 mol% C211-basic melt solution are shown in Figure 23. In view of the low S/N ratio of the  $345\text{ cm}^{-1}$  band in all three spectra, the effects of the addition of LiCl or LiCl and C211 to basic melt are considered to be negligible. In either case, no new spectral features are observed.

In the far-IR spectrum for 1.0 mol%  $^6\text{LiCl}$  in basic melt (Figure 24), two or more bands are observed between  $275$  and  $425\text{ cm}^{-1}$  that are not seen for LiCl with a natural abundance of lithium-6. The positions of these bands at  $293\text{ cm}^{-1}$ , ca.  $360\text{ cm}^{-1}$  (very broad), and ca.  $400\text{ cm}^{-1}$  do not correspond to the values reported by Klemperer and Norris (180) for the  $\text{Li}_2\text{Cl}_2$  gas phase dimer ( $335$  and  $460\text{ cm}^{-1}$ ), nor those reported by Snelson and Pitzer (175) in inert gas matrices.

Bands at  $186$  and  $313\text{ cm}^{-1}$  ( $^6\text{Li}_2\text{Cl}_2$ ), and  $174$  and  $293\text{ cm}^{-1}$  ( $^7\text{Li}_2\text{Cl}_2$ ) have been observed in the matrix isolation far-IR study of Freiberg *et al.* (176).

Isotopic enrichment with  $^6\text{Li}$  causes high frequency shifts of ca.  $20\text{ cm}^{-1}$  in far-IR spectra of lithium salts and cryptated lithium ion in nonaqueous solutions (143,181). If it is assumed that one or more bands for the  $\text{LiCl}_2^-$  or  $\text{Li}_2\text{Cl}_4^{2-}$  chlorocomplexes are masked by the  $\nu_4(\text{F}_2)$  band for the  $\text{AlCl}_4^-$  ion at  $184\text{ cm}^{-1}$  for natural abundance LiCl in basic melt, it is difficult to believe that  $^6\text{Li}$  enrichment can enable a frequency shift of more than  $100\text{ cm}^{-1}$  to give rise to the  $293\text{ cm}^{-1}$  (or higher frequency) band. A low frequency shift brought about by  $^6\text{Li}$  enrichment (thereby moving the band(s) from beneath the  $490\text{ cm}^{-1}$  band of the  $\text{AlCl}_4^-$  ion) is considered to be very unlikely; such an effect would be contrary to the supposed increase in the  $^6\text{Li}-\text{Cl}$  force constant versus that of  $^7\text{Li}-\text{Cl}$ . Thus a logical interpretation of the  $^6\text{LiCl}$ -basic melt far-IR spectrum is not possible at this time. Improved resolution in this region of the spectrum could aid in this interpretation.

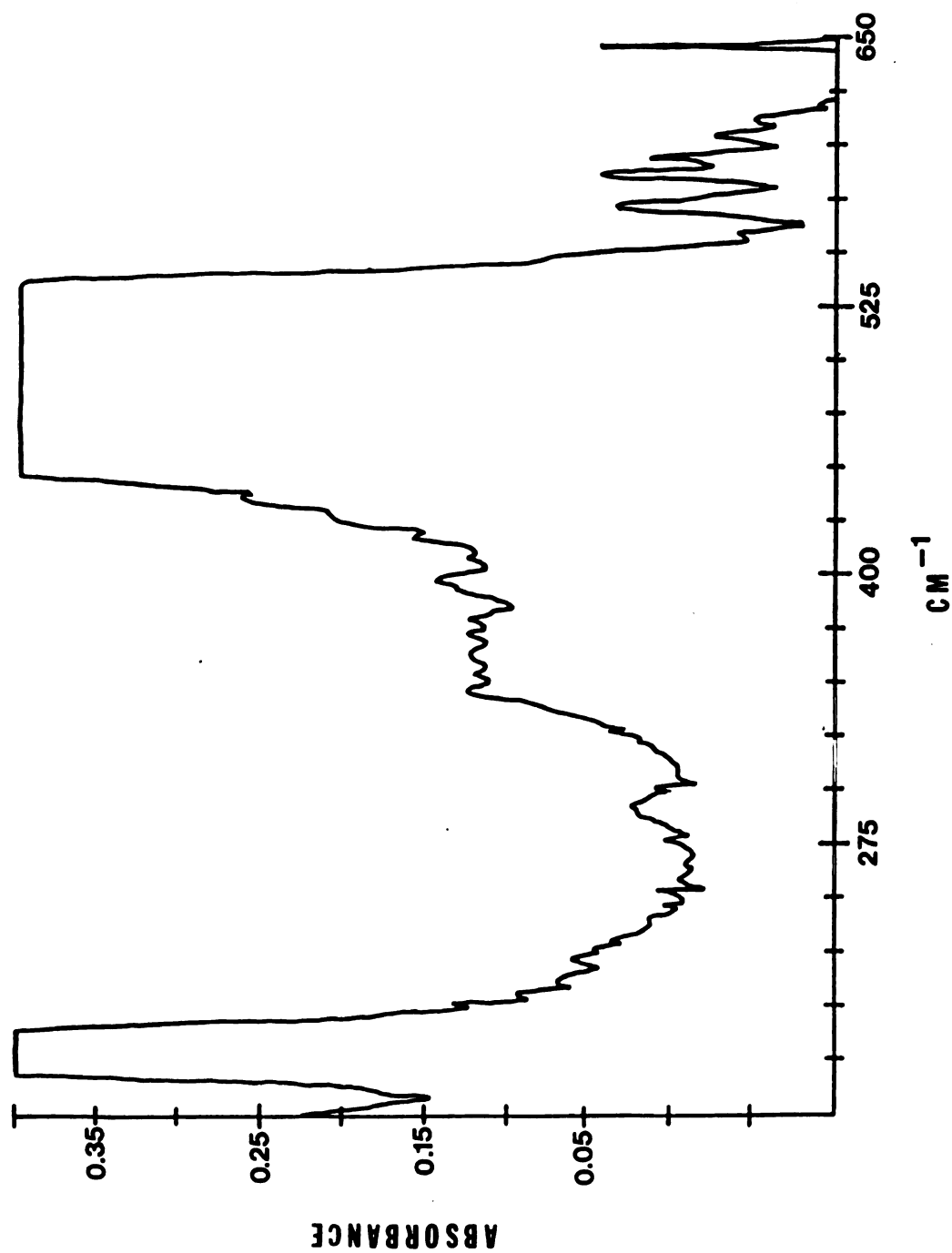


Figure 24. Far-IR Spectrum (150 to 650  $\text{cm}^{-1}$ ): 1.0 Mol%  $^6\text{LiCl}$  in Basic Melt.

## C. Complexation of the Lithium Ion in Basic Melt by Crown Ethers

### C.1. Lithium-7 NMR

#### C.1.a. Crown/lithium ion mole ratio studies

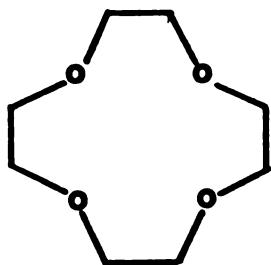
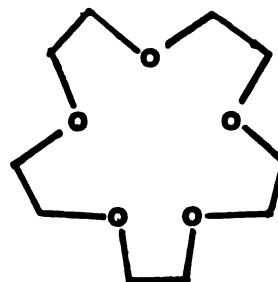
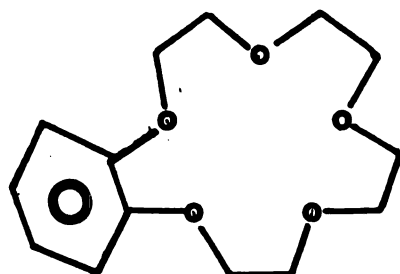
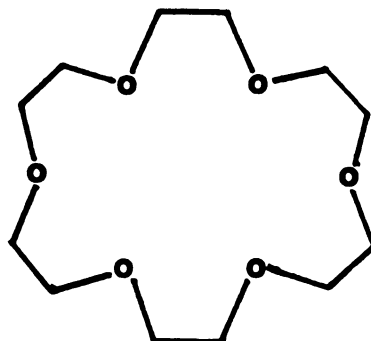
Lithium-7 chemical shifts were measured at 40°C as a function of crown ether/lithium ion mole ratio for ligands 12C4, 15C5, B15C5, and 18C6 in 1.0 mol% LiCl-basic melt solutions. The structures of these ligands are shown in Figure 25. A single  $^7\text{Li}$  resonance line was observed (fast chemical exchange at this temperature and magnetic field strength), with signals shifting upfield (-) as the crown ether/lithium ion mole ratios were increased. Lithium-7 chemical shift data obtained in these studies is given in Table 19. A plot of  $^7\text{Li}$  chemical shifts versus crown/ $\text{Li}^+$  ion mole ratios is shown in Figure 26.

Initial computer fits of these data were based on a model which assumed a two-site fast exchange between "free" and crown-complexed lithium ion in basic melt.



After the successful fitting of the dependence of  $^7\text{Li}$  chemical shifts on LiCl concentration in basic melt (section B.1.a), the crown complexation data were fitted to a three-site fast exchange model.



**12-CROWN-4****15-CROWN-5****BENZO-15-CROWN-5****18-CROWN-6**

**Figure 25. The Structures of 12C4, 15C5, B15C5, and 18C6.**

**Table 19****Lithium-7 Chemical Shifts as a Function of Crown/Lithium****Ion Mole Ratio in Basic Melt at 40°C****12C4:  $\text{Li}^+ = 0.0771 \text{ M}$** 

<b>Ligand (<u>M</u>)</b>	<b>Mole Ratio</b>	<b><math>\delta</math> (ppm) (a)</b>
0.0	--	+ 1.39
0.013	0.17	+ 1.23
0.038	0.49	+ 0.87
0.040	0.52	+ 0.88
0.042	0.54	+ 0.79
0.047	0.61	+ 0.93
0.053	0.69	+ 0.77
0.073	0.95	+ 0.37
0.078	1.0	+ 0.45
0.079	1.0	+ 0.32
0.089	1.2	+ 0.25
0.092	1.2	+ 0.10
0.132	1.71	+ 0.08
0.152	1.97	+ 0.06
0.286	3.71	- 0.05
0.339	4.40	- 0.08
0.399	5.18	- 0.09
1.027	13.3	- 0.22



Table 19 continued

15C5:  $\text{Li}^+ = 0.0774 \text{ M}$ 

Ligand ( <u>M</u> )	Mole Ratio	$\delta$ (ppm) (a)
0.0	--	+ 1.39
0.022	0.28	+ 0.93
0.041	0.53	+ 0.65
0.046	0.60	+ 0.53
0.046	0.59	+ 0.23
0.074	0.96	- 0.33
0.074	0.96	- 0.58
0.079	1.0	- 0.30
0.089	1.2	- 0.75
0.095	0.96	- 0.70
0.111	1.44	- 0.78
0.137	1.78	- 0.86
0.187	2.43	- 0.90
0.218	2.83	- 0.91
0.285	3.70	- 0.92
0.421	5.46	- 0.93
0.506	6.56	- 0.93

Table 19 continued

B15C5:  $\text{Li}^+ = 0.0776 \text{ M}$ 

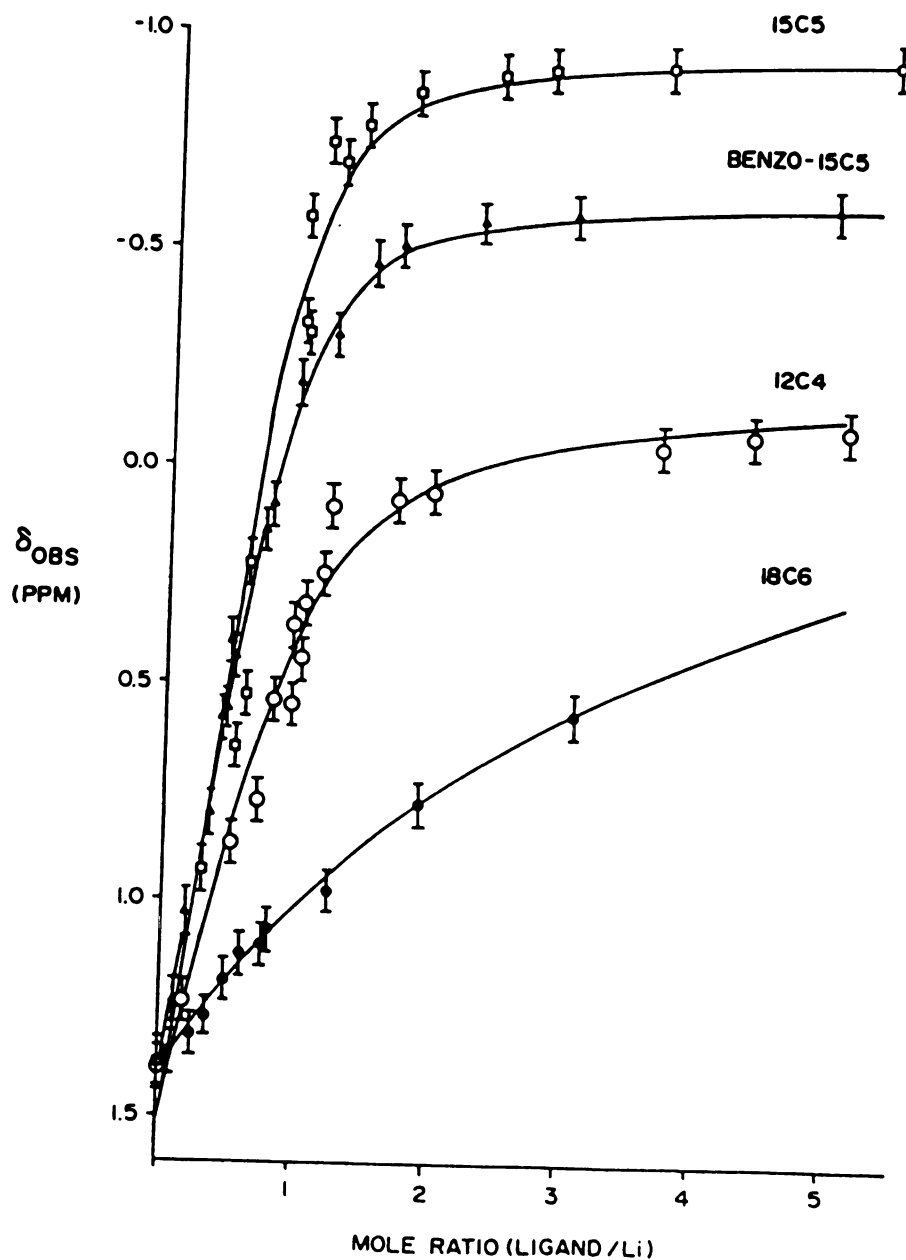
Ligand ( <u>M</u> )	Mole Ratio	$\delta$ (ppm) (a)
0.0	--	+ 1.40
0.008	0.1	+ 1.23
0.012	0.16	+ 1.03
0.026	0.33	+ 0.80
0.032	0.43	+ 0.58
0.036	0.46	+ 0.56
0.036	0.48	+ 0.41
0.041	0.52	+ 0.44
0.058	0.76	+ 0.16
0.059	0.77	+ 0.09
0.074	0.96	- 0.19
0.095	1.2	- 0.31
0.115	1.49	- 0.47
0.133	1.71	- 0.51
0.177	2.28	- 0.56
0.235	3.03	- 0.59
0.392	5.11	- 0.60

Table 19 continued

18C6:  $\text{Li}^+ = 0.0776 \text{ M}$ 

Ligand ( <u>M</u> )	Mole Ratio	$\delta$ (ppm)(a)
0.0	--	+ 1.39
0.007	0.09	+ 1.35
0.018	0.24	+ 1.33
0.026	0.34	+ 1.29
0.038	0.49	+ 1.22
0.045	0.57	+ 1.18
0.059	0.77	+ 1.12
0.098	1.3	+ 0.98
0.148	1.91	+ 0.82
0.239	3.08	+ 0.56

(a) Versus external 0.015 M LiCl in D<sub>2</sub>O uncorrected for magnetic susceptibility; the uncertainty in  $\delta$  is  $\pm 0.02$  ppm.



**Figure 26.** Lithium-7 Chemical Shifts as a Function of Ligand/Lithium Ion Mole Ratio for the Determination of the Concentration Formation Constants of  $\text{Li}^+$ -Crown Complexes in Basic Melt at  $40^\circ\text{C}$ . Solid Lines are the Computer-Generated Curves.

where, for the moment, it was assumed that the chloride ions maintain contact with the  $\text{Li}^+$  ion in the crown complex. In this model, the values for  $K_{\text{Diss.}}$ ,  $\delta_{\text{monomer}}$ , and  $\delta_{\text{dimer}}$  were entered as constants.

The formation constants and limiting chemical shifts for the crown complexes of the lithium ion in basic melt calculated from both models are given in Table 20. In comparing these results, it is clear that the monomer-dimer equilibrium does not appreciably effect the formation constants for the stronger 15C5 and B15C5-lithium ion complexes. However, the formation constants for the weaker 12C4 and 18C6 complexes are increased by 0.25 and 0.92 log  $K_F$  units, respectively. The log  $K_F$  value for the 18C6 complex is still the smallest of the four (crown complexes), reflecting the disparity between the size of the lithium ion and the diameter of the 18C6 molecule ( $r_{\text{Li}^+} = 0.86 \text{ \AA}$  vs.  $d_{18\text{C6}} = 2.6 \text{ to } 3.2 \text{ \AA}$ ).

The results obtained with the three-site exchange model are listed in Table 21 along with the previous results of Smetana and Popov (135) for the crown complexation of the lithium ion in various nonaqueous solvents. The selectivity of the 15C5 ring size for the lithium ion (vs. 12C4 and 18C6) is apparently reduced in the molten salt as compared to nonaqueous solvents. This leveling effect is probably due to the strength of the dimer formation ( $\log K_D = 2.82 \pm 0.39$ ) in the melt.

The  $^7\text{Li}$  chemical shift data give no indication as to the number (if any) of chloride ions which are associated with the lithium ion in the lithium-crown complexes. Considering the nominally two-dimensional geometry of the crown molecules, it is possible that one or two chloride ions remain coordinated to the lithium-crown complexes in basic melt. Several examples of counterion participation in the coordination of the lithium ion in crown complexes are discussed in section B.3.a, Chapter I. Similar coordination of the lithium ion

**Table 20**  
**Crown Complexation of the Lithium Ion in Basic Melt;**  
**Complex Formation Constants and Limiting**  
**Chemical Shifts for the Complexes**

Model #1: $\text{Li}^+ + \text{CROWN} \rightleftharpoons \text{Li}^+ \cdot \text{CROWN}$		
Crown	Log $K_F$	$\delta_c$ (ppm)
12C4	$1.87 \pm 0.12$	$- 0.18 \pm 0.05$
15C5	$2.39 \pm 0.17$	$- 0.96 \pm 0.06$
B15C5	$2.33 \pm 0.05$	$- 0.64 \pm 0.02$
18C6	$0.59 \pm 0.12$	$- 0.48 \pm 0.28$
Model #2: $\text{Li}_2\text{Cl}_4^{2-} \rightleftharpoons 2\text{LiCl}_2^- \quad (\text{A})$ $\text{LiCl}_2^- + \text{CROWN} \rightleftharpoons \text{Li} \cdot \text{CROWN} \cdot \text{Cl}_2^- \quad (\text{B})$		
Crown	Log $K_F^{(a)}$	$\delta_c$ (ppm)
12C4	$2.12 \pm 0.05$	$- 0.36 \pm 0.09$
15C5	$2.32 \pm 0.08$	$- 1.91 \pm 0.14$
B15C5	$2.36 \pm 0.03$	$- 1.23 \pm 0.05$
18C6	$1.51 \pm 0.06$	$+ 0.14 \pm 0.20$

(a) Calculated errors do not reflect propagation  
of errors from the monomer-dimer equilibrium

Table 21

Log  $K_F$  and  $\delta_C$  Values for Lithium Ion-Crown Complexes in Basic  $AlCl_3$ -BPCI  
Melts and in Various Nonaqueous Solvents

Ligand	Basic Melt(a)		Pyridine(b)		Acetonitrile(b)		Acetone(b)	
	Log $K_F$	$\delta_C$ (ppm)	Log $K_F$	$\delta_C$ (ppm)	Log $K_F$	$\delta_C$ (ppm)	Log $K_F$	$\delta_C$ (ppm)
12C4	2.12	- 0.36	0.70	- 0.74	4.25	- 1.04	1.62	- 0.30
	$\pm 0.05$	$\pm 0.09$	$\pm 0.05$	$\pm 0.26$	$\pm 0.46$	$\pm 0.05$	$\pm 0.03$	$\pm 0.05$
15C5	2.32	- 1.91	2.48	- 1.15	> 4	- 1.79	3.59	- 0.80
	$\pm 0.08$	$\pm 0.14$	$\pm 0.02$	$\pm 0.05$	--	$\pm 0.05$	$\pm 0.08$	$\pm 0.05$
B15C5	2.36	- 1.23	--	--	--	--	--	--
	$\pm 0.03$	$\pm 0.05$	--	--	--	--	--	--
18C6	1.51	+ 0.14	0.62	- 0.44	2.34	- 1.32	1.50	- 0.52
	$\pm 0.06$	$\pm 0.20$	$\pm 0.07$	$\pm 0.30$	$\pm 0.04$	$\pm 0.05$	$\pm 0.02$	$\pm 0.39$

(a) From Model #2, Table 20

(b) Reference 135

by chloride ions at axial positions (with respect to the planes of the crown molecules) in the basic melt solutions seems reasonable.

### C.2. Potentiometry

The effect of the addition of 15C5 to a 1.0 mol% LiCl-basic melt solution was measured at 35°C potentiometrically. Titration data are listed in Table 22, and a plot of these data is shown in Figure 27.

If the crown complexation reaction proceeds by the release of one or two chloride ions from the  $\text{LiCl}_2^-$  ion, it would be expected that the amount of free chloride ion in the melt would increase (i.e., the pCl of the working compartment of the cell would decrease), resulting in a lower cell potential as the 15C5/lithium ion mole ratio is increased. If the complexation reaction proceeds with retention of both of the chloride ions, no change in the pCl (and cell potential) would be expected to occur. The slight increase in the cell potential with increasing 15C5/ $\text{Li}^+$  mole ratio is puzzling, since it suggests that additional chloride ions are being removed in the process of crown complexation. Although transport of the crown complex across the boundary might product a positive change in the cell potential, the lack of a time-dependence for this change is unexplainable at this time. In the electrochemical study by Dymek et al. (93) of mass transport in the  $\text{AlCl}_3\text{-ImCl}$  ( $\text{Im}^+ = 1\text{-methyl-3-ethylimidazolium}$  ion) molten salt system, the majority charge carrier in these melts was determined to be the  $\text{Im}^+$  ion ( $t_+ = 0.80 \pm 0.09$ ).

Based on conductance measurements on NaI and RbI-acetonitrile solutions in the presence of various crown ethers, Della Monica et al. (182) have concluded that "In the systems with crowns characterized by a central hole big enough to place the positive ion in the center of the molecule, the charge carried



**Table 22**

**Potentiometric Titration Data: Observed Cell Potentials as a  
Function of 15C5 Titrant (mg) and the 15C5/Lithium Ion Mole Ratio at 35°C**

<b>Aliq. #</b>	<b>15C5 (mg)(a)</b>	<b>15C5/Li<sup>+</sup>(b) Mole Ratio</b>	<b>Cell Potential (mV)(c)</b>
0	0.0	---	29
1	10.4	0.24	32
2	20.8	0.49	33
3	31.2	0.73	33
4	41.6	0.97	33
5	52.0	1.2	34
6	62.4	1.5	35
7	72.8	1.7	36
8	83.2	1.9	36
9	93.6	2.2	37
10	104.0	2.4	38
11	114.4	2.7	38
12	124.8	2.9	39
13	135.2	3.2	39
14	145.6	3.4	39
15	156.0	3.7	40
16	166.4	3.9	40
17	176.8	4.1	40
18	187.2	4.4	40
19	197.6	4.6	40

Table 22 continued

Aliq. #	15C5 (mg)(a)	15C5/Li <sup>+</sup> (b) Mole Ratio	Cell Potential (mV)(c)
20	208.0	4.9	40
21	218.4	5.1	40
22	228.8	5.4	40

(a)  $\pm 0.1$  mg

(b)  $[\text{Li}^+] = 0.0790$  M

(c)  $\pm 1$  mV

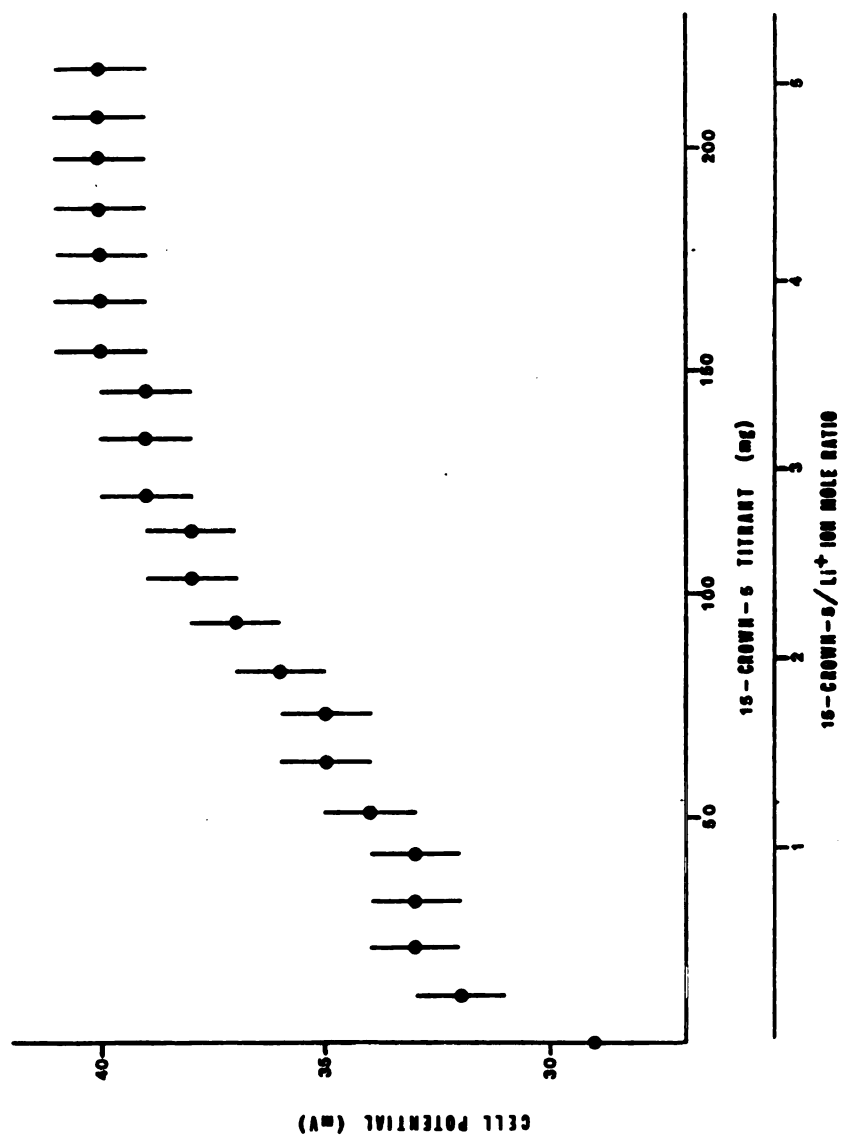


Figure 27. Potentiometry: E<sub>cell</sub> Versus 15C5 (mg) and 15C5/Lithium Ion Mole Ratio.

by the cations is sufficiently shielded so that both interactions between the cation and the solvent, and those with the negative ions of the solution are greatly decreased." It may be possible to apply this argument to explain the anomalous behavior of the cell potential in the titration of the LiCl-basic melt solution with 15C5, but conductance or transference number measurements would be required to shed more light on this phenomenon.

#### D. Conclusions

The  $^7\text{Li}$  NMR data obtained in this study indicate that two different chlorocomplexes of the lithium ion are formed in basic melt solutions of LiCl and other lithium salts. Although the only evidence for the monomer-dimer equilibrium is based on a computer fit of these data, no other reasonable model was successful in accounting for the observed chemical shift behavior. The magnitudes of the  $^7\text{Li}$  quadrupole coupling constants calculated from spin-lattice relaxation rates of the lithium ion in basic and acidic melts suggest that the electric field gradient at this nucleus in basic melt is similar to that of lithium halide dimers in the gas phase. In acidic melt, the EFG for the  $^7\text{Li}$  nucleus is more comparable to that of the lithium ion in aqueous or nonaqueous solutions.

The results obtained from the potentiometric titrations of LiCl and  $\text{LiClO}_4$ -basic melt solutions confirm that two chloride ions are associated with each lithium ion in basic melt solutions. The cell which was designed for these experiments seems well suited to the studies of chlorocomplex formation with other metal ions in basic melt.

The crown-lithium ion complex formation constants obtained in basic melt solutions decrease in the same order ( $15\text{C}5 > 12\text{C}4 > 18\text{C}6$ ) as that observed for lithium-crown complexation in nonaqueous solutions. However, it appears that the monomer-dimer equilibrium tends to minimize the selectivity of

complexation (correlation of the complex stability with matching of the ion/cavity size) as compared with macrocyclic complexation in nonaqueous solutions.

Further electrochemical studies of LiCl-basic melts with 15C5 are called for to ascertain the cause for the observed increase in cell potential with increasing 15C5/Li<sup>+</sup> mole ratio.

**CHAPTER IV**  
**CRYPTAND COMPLEXATION OF THE LITHIUM ION**  
**IN THE  $\text{AlCl}_3$ -BPCl SYSTEM**

## **A. Introduction**

Previous investigations have demonstrated the utility of  $^{23}\text{Na}$  (183),  $^{39}\text{K}$  (184), and  $^{133}\text{Cs}$  (185) NMR methods for the study of cryptand complexation of the respective alkali metal cations in aqueous and nonaqueous solutions. Similar  $^7\text{Li}$  NMR solution studies are discussed in Chapter I (142,143). It should be pointed out that in these previous studies, all  $^7\text{Li}$  NMR measurements were made at a field strength of 14.09 kG. Cahen et al. (142) observed slow exchange at 30°C (two  $^7\text{Li}$  NMR signals at cryptand/lithium ion mole ratios less than 1:1) for the  $\text{Li}^+$ -C211 system in various solvents, and for the  $\text{Li}^+$ -C221 system in pyridine.

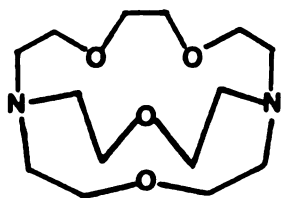
The purpose of this study was to investigate the complexation of the lithium ion in basic melt by cryptands C211, C221, C222, and C2B22. The structures of these cryptands are shown in Figure 28. In addition to  $^7\text{Li}$  NMR, potentiometry and x-ray crystallography have been used in these investigations.

## **B. Basic Melt Solutions Studies**

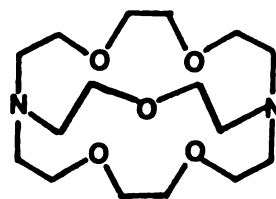
### **B.1. Lithium-7 NMR**

Lithium-7 NMR spectra were obtained at 40°C for cryptand/lithium ion mole ratios from zero up to 4.2:1 (C211), 3.3:1 (C221), and 1.2:1 (C2B22) in basic melt solutions. For C222, C222/lithium ion mole ratios from 0.76 to 2.8:1 were studied. Some typical spectra from these studies are shown in Figures 29-32. No samples were prepared for the  $\text{Li}^+$ -C2B22 system in basic melt above the 1.2:1 mole ratio due to precipitate formation. Attempts to resolublize the precipitate by adding excess cryptand (mole ratio 2:1) were unsuccessful. On warming to ca. 60°C, some of the solid dissolved, but reappeared when the melt was cooled to room temperature.

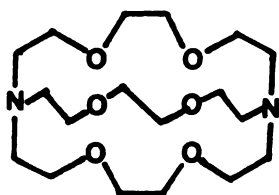
Over the three week conditioning period for the  $\text{Li}^+$ -C211 mole ratio



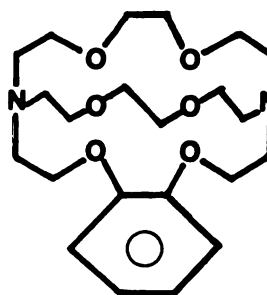
C 211



C221



C 222

C2<sub>B</sub>22

**Figure 28.** The Structures of C211, C221, C222, and C2<sub>B</sub>22.



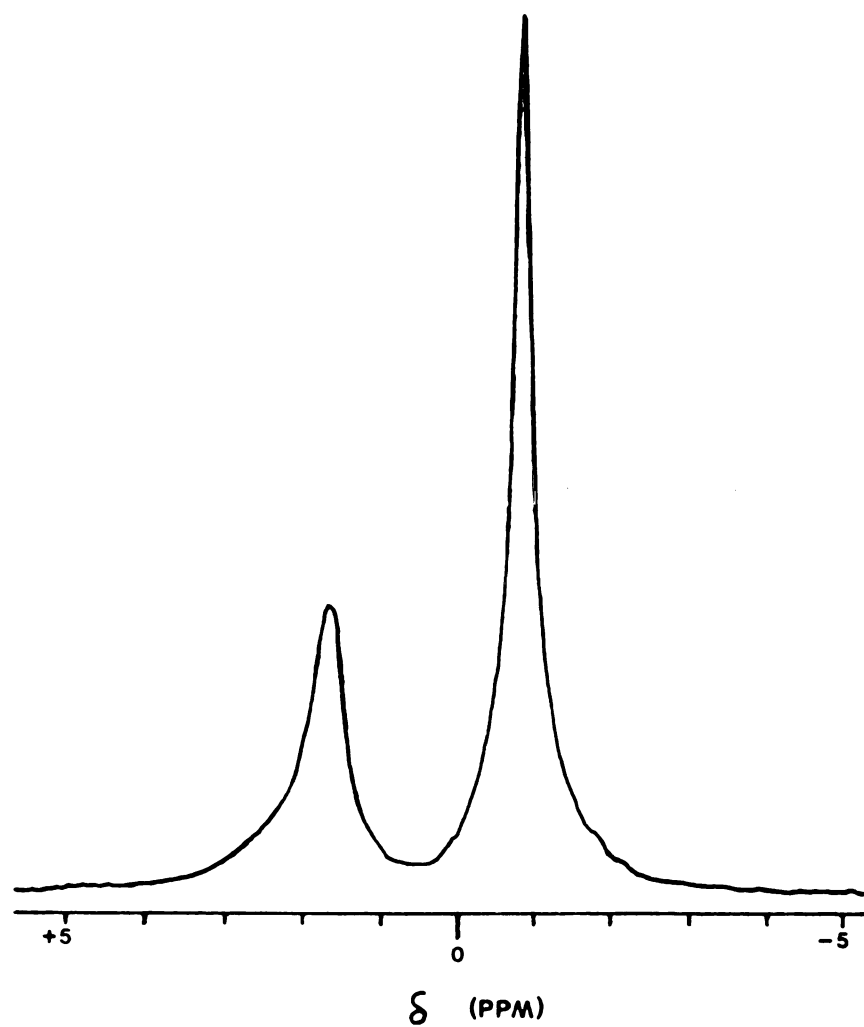


**Figure 29.** Lithium-7 NMR Spectrum: 0.985 Mol% LiCl-0.888 Mol% C211 in Basic Melt at 40°C. The Upfield Signal is Assigned to the Complexed Lithium Ion Site.

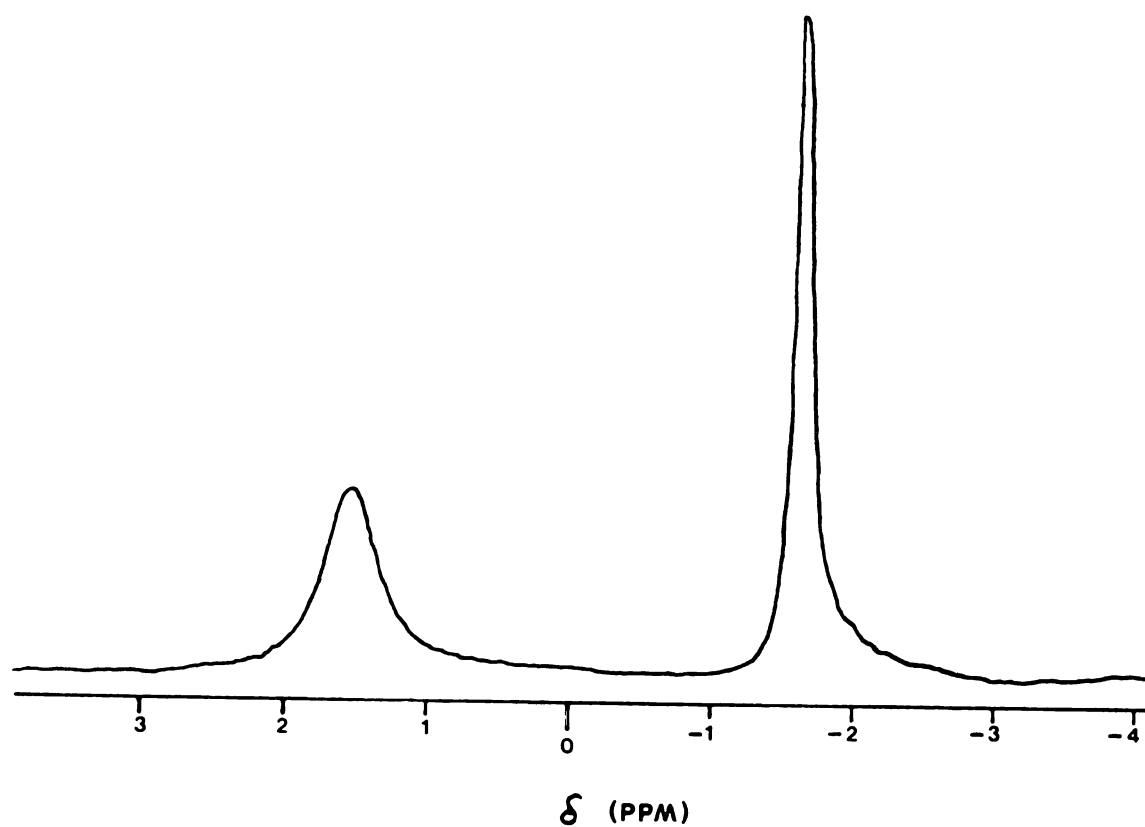


**Figure 30. Lithium-7 NMR Spectrum: 0.992 Mol% LiCl – 0.988 Mol% C221 in Basic Melt at 40°C. The Upfield Signal is Assigned to the Complexed Lithium Ion Site.**

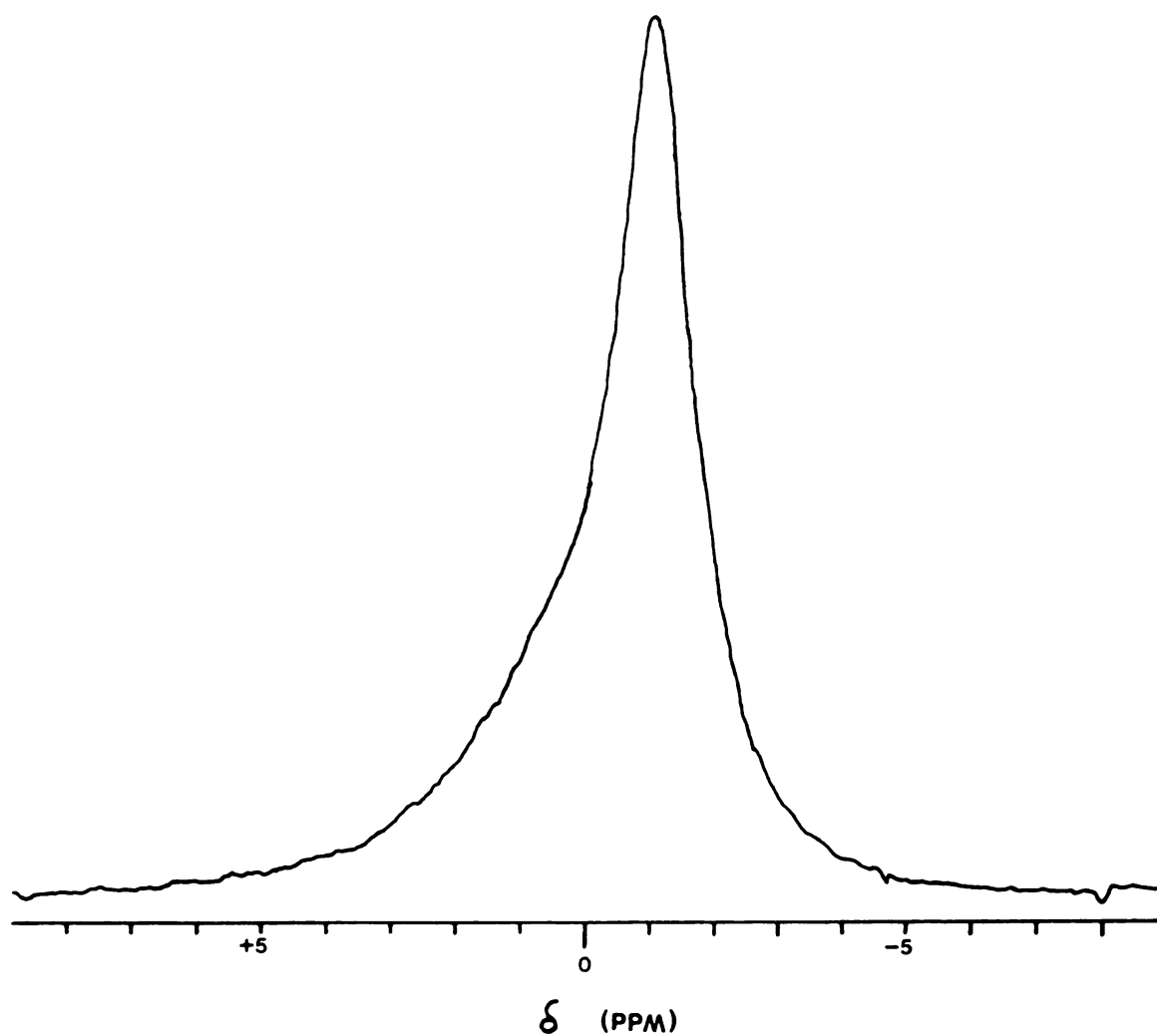


**Figure 31. Lithium-7 NMR Spectrum: 0.980 Mol% LiCl - 0.987 Mol% C222 in Basic Melt at 40°C. The Position of the Maximum of the Unresolved Bandshape is Taken to Correspond to the Chemical Shift of the Complexed Lithium Ion Site.**

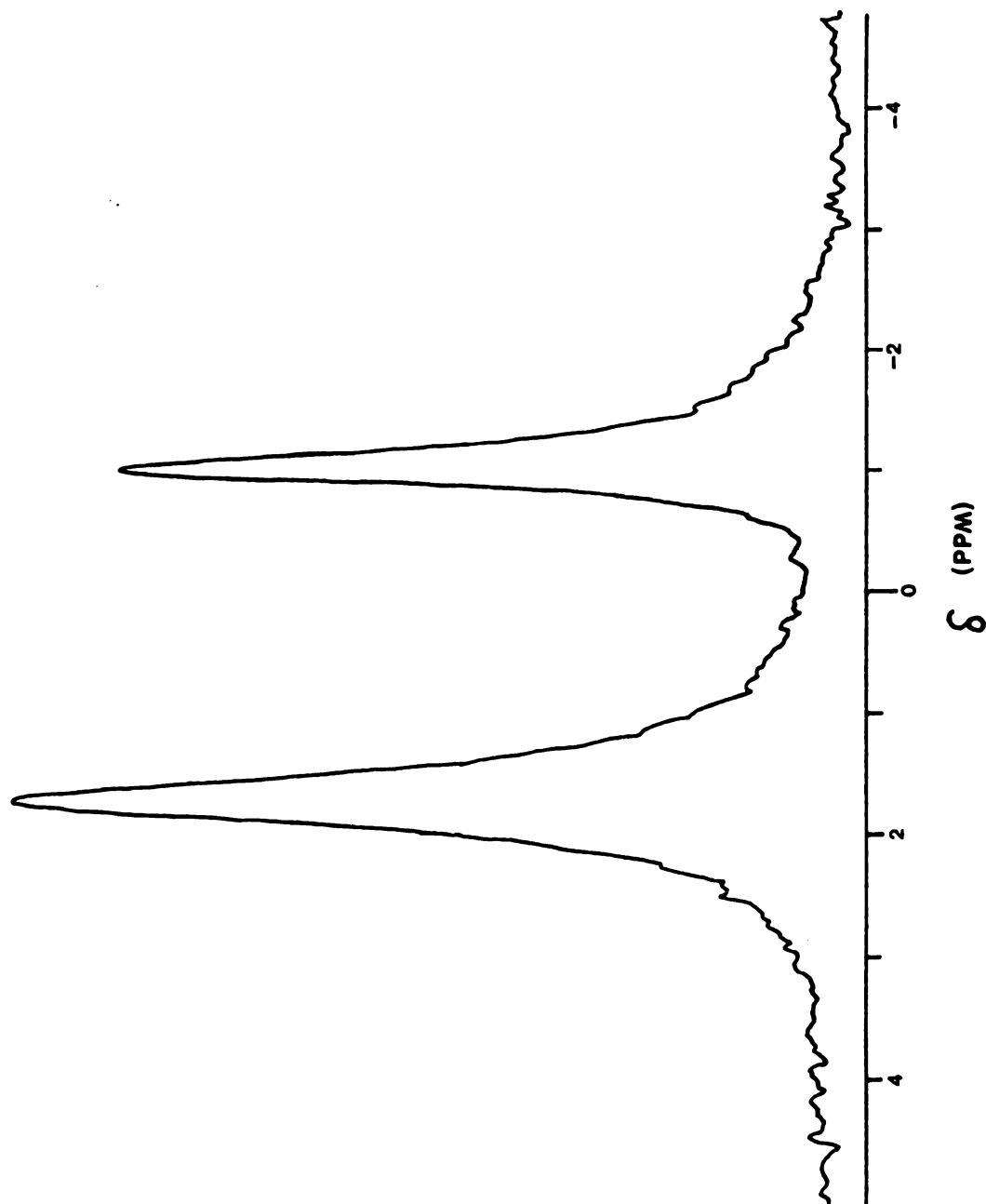


**Figure 32.** Lithium-7 NMR Spectrum: 1.00 Mol% LiCl - 0.949 Mol% C<sub>2</sub>B<sub>22</sub> in Basic Melt at 40°C. The Upfield Signal is Assigned to the Complexed Lithium Ion Site.

samples, small amounts of a crystalline material were observed to precipitate from the solutions with a mole ratio of less than 1:1. Above this mole ratio, all samples were homogeneous. This precipitate did not completely dissolve on warming the solutions to 40°C. All samples prepared for the C221-Li<sup>+</sup> and C222-Li<sup>+</sup> mole ratio studies remained homogeneous at 25°C or 40°C.

Slow chemical exchange was observed under the stated experimental conditions of 40°C and 42.28 kG field strength for all four lithium-cryptand systems in basic melt. For C211, C221 and C2B22, the chemical shift of the lithium ion complex signals were observed to be insensitive to the cryptand/lithium ion mole ratios. However, the chemical shift of the signal for "free" lithium ion (ie., the fast exchange signal due to the monomer and dimer lithium chlorocomplexes) was observed to shift downfield with increasing cryptand/lithium ion mole ratio (Figures 33-35; Table 23). This downfield shift is taken as strong evidence for the dissociation of the Li<sub>2</sub>Cl<sub>4</sub><sup>2-</sup> dimer, and subsequent complexation of the lithium ion coming from the dissociation of the LiCl<sub>2</sub><sup>-</sup> species. The constancy of the chemical shifts of the complex signals suggests that the lithium ion is shielded from the chloride ions in the melt by the organic "skin" of the cryptands; i.e., the lithium ion resides within the cryptand cavities (inclusive complexes). If this is the case, then upon complexation two chloride ions must be released from the LiCl<sub>2</sub><sup>-</sup> ion. Therefore, the chloride ion activity of the melt solution should increase (decreasing pCl) as the complexation reaction proceeds. A test of this hypothesis is provided in the potentiometry experiment discussed in the following section.

The <sup>7</sup>Li NMR spectra for the Li<sup>+</sup>-C222 system in basic melt were observed to be much different from those for the other three Li<sup>+</sup>-cryptand systems (Figure 36). In this case, the "free" and complexed lithium signals overlapped yielding broad (ca. 10<sup>2</sup>Hz) lineshapes. In addition, the signal assigned to the

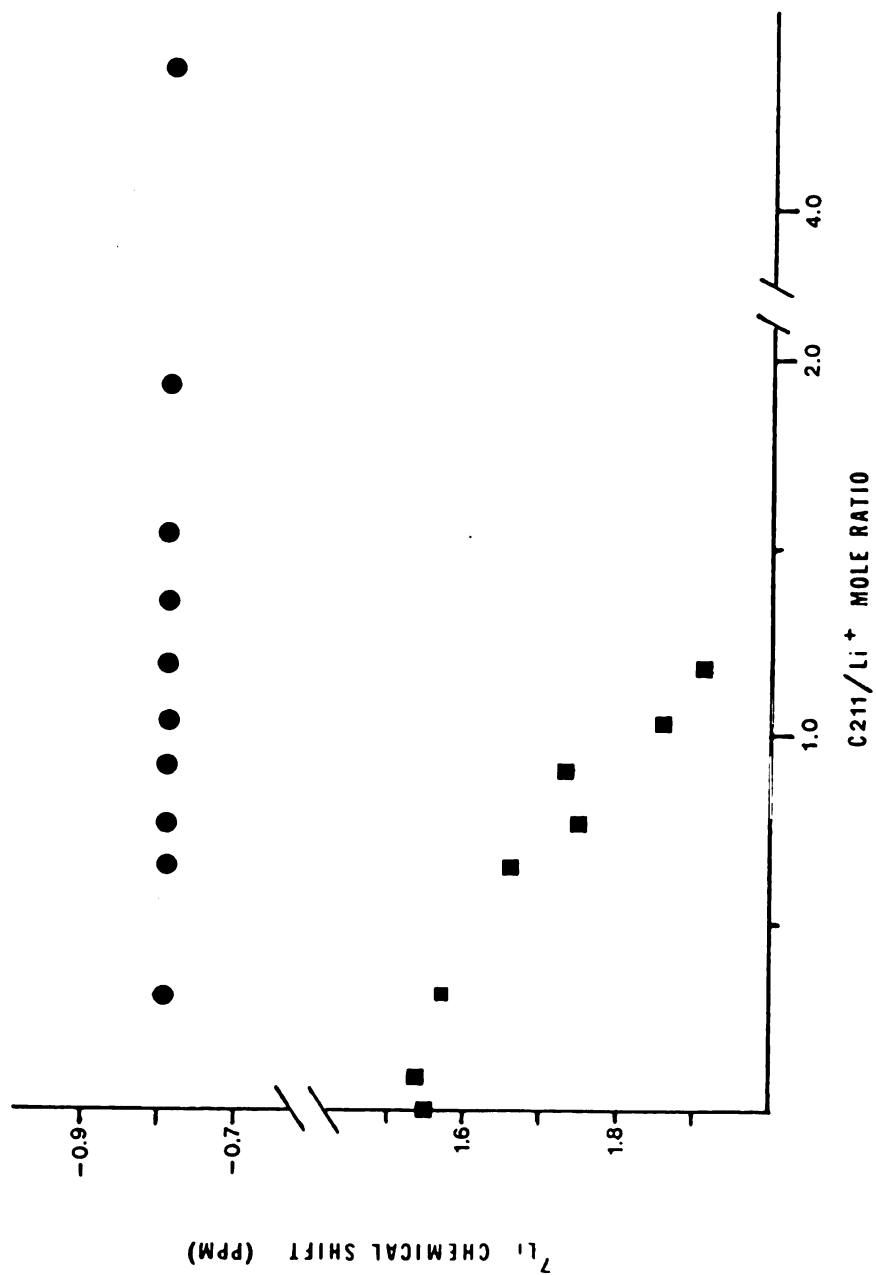


**Figure 33.** Lithium-7 Chemical Shifts for "Free" and Complexed Lithium Ion at 40°C as Functions of the C211/Lithium Ion Mole Ratio in Basic Melt. Uncertainties in the Chemical Shifts are Indicated by the Size of the Data Points.

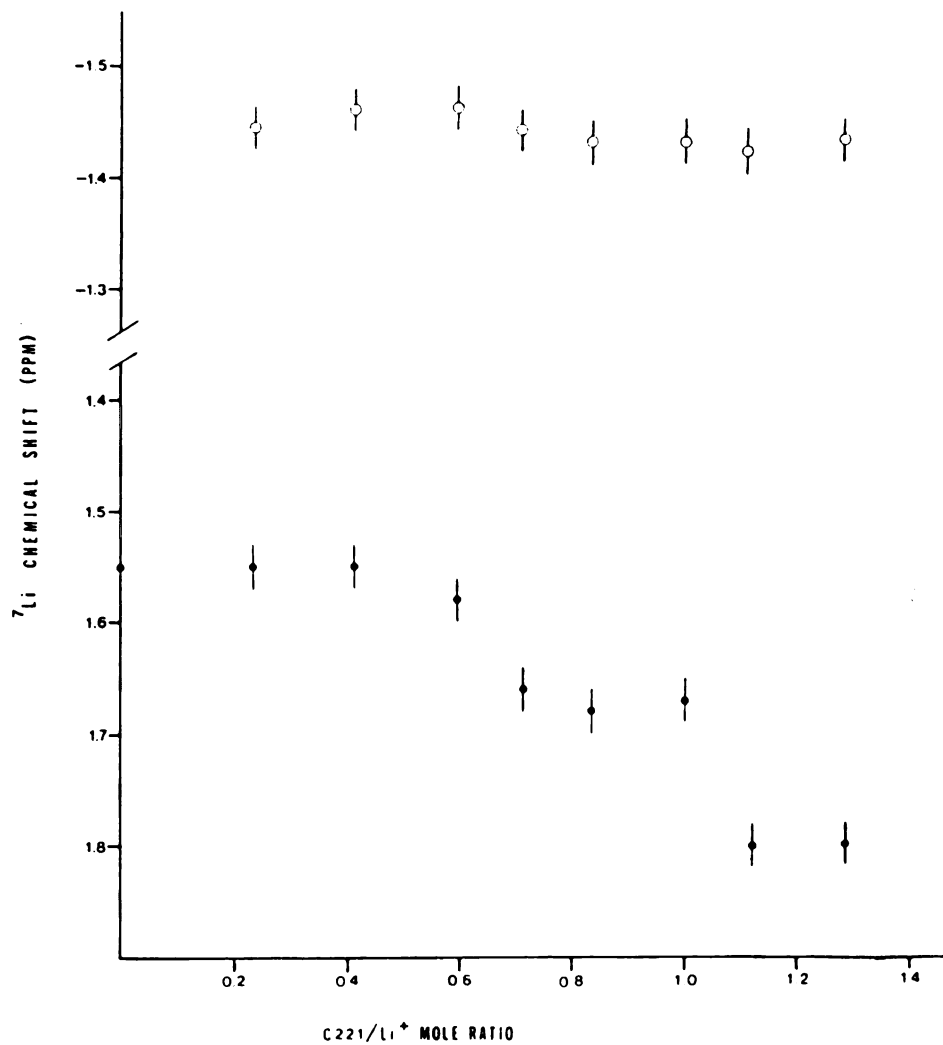


**Figure 34. Lithium-7 Chemical Shifts for "Free" and Complexed Lithium Ion at 40°C as Functions of the C221/Lithium Ion Mole Ratio in Basic Melt.**

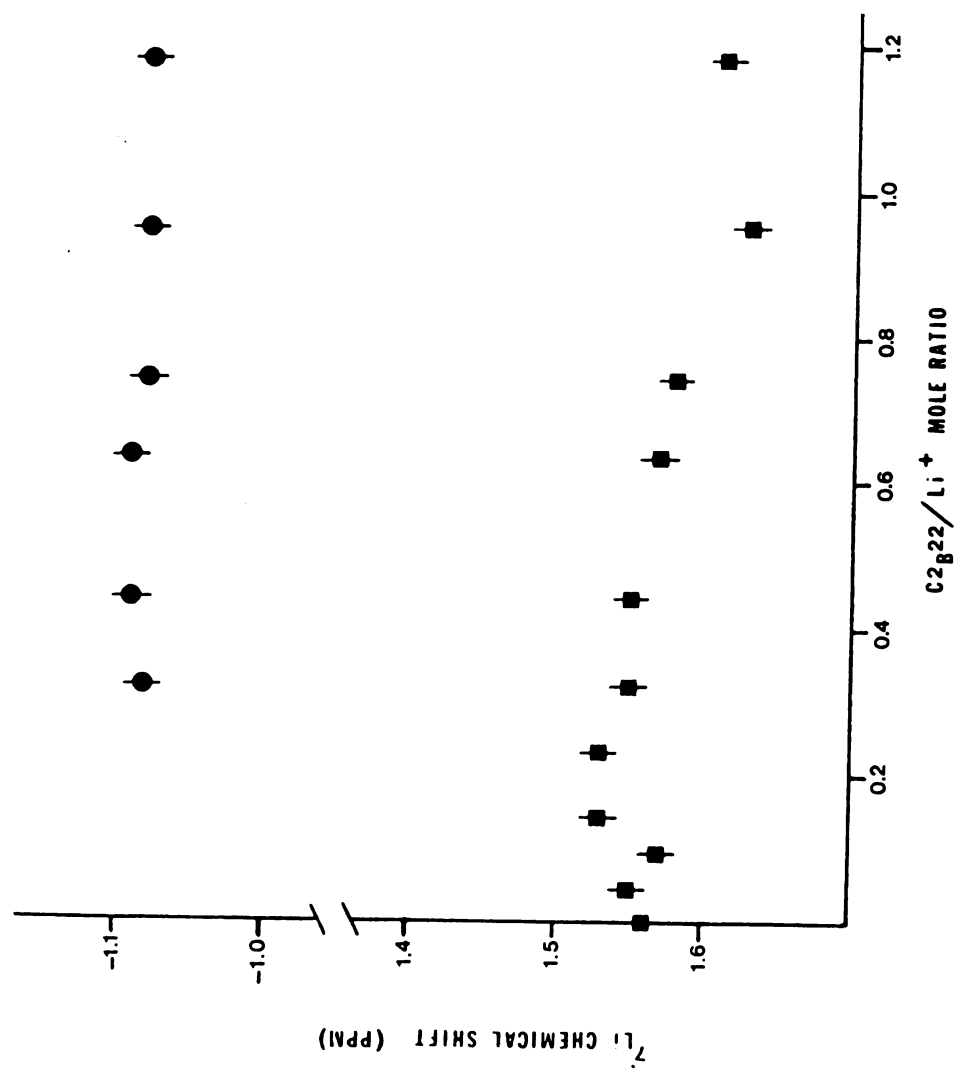


**Figure 35.** Lithium-7 Chemical Shifts for "Free" and Complexed Lithium Ion at 40° as Functions of The  $C_2B_{22}/Li^+$  Mole Ratio in Basic Melt.



Table 23

**Lithium-7 Chemical Shifts Observed for the Cryptand C211, C221, C222, and C2B22 - Lithium Ion Mole Ratio Studies in Basic Melt at 40°C**

**C211**

<b>Cryptand/Li<sup>+</sup> Mole Ratio</b>	<b><math>\delta_F</math> (ppm)(a)</b>	<b><math>\delta_C</math> (ppm)(a)</b>
0.0	+ 1.55	--
0.089	+ 1.54	--
0.31	+ 1.57	- 0.79
0.645	+ 1.66	- 0.79
0.759	+ 1.75	- 0.79
0.901	+ 1.73	- 0.79
1.03	+ 1.86	- 0.79
1.18	+ 1.91	- 0.79
1.35	(b)	- 0.79
1.53	(b)	- 0.79
1.93	(b)	- 0.79
2.42	(b)	- 0.79
2.96	(b)	- 0.79
3.63	(b)	- 0.79
4.37	(b)	- 0.79

**C221**

0.0	+ 1.55	--
0.23	+ 1.55	- 1.44
0.41	+ 1.55	- 1.46
0.594	+ 1.58	- 1.46

Table 23 continued

Cryptand/Li <sup>+</sup> Mole Ratio	$\delta_F$ (ppm)(a)	$\delta_C$ (ppm)(a)
0.716	+ 1.66	- 1.44
0.835	+ 1.68	- 1.43
1.00	+ 1.67	- 1.43
1.12	+ 1.80	- 1.42
1.28	+ 1.79	- 1.43
1.65	(b)	- 1.42
2.06	(b)	- 1.43
2.53	(b)	- 1.43
3.44	(b)	- 1.43
<b>C222</b>		
0.757	+ 0.94	- 1.01(c)
0.791	(b)	- 1.01(c)
0.842	(b)	- 1.01
0.876	(b)	- 1.08
1.01	(b)	- 1.19
1.14	(b)	- 1.34
1.45	(b)	- 1.41
1.76	(b)	- 1.49
2.80	(b)	- 1.50
<b>C2B22</b>		
0.0	+ 1.56	--
0.046	+ 1.55	--
0.092	+ 1.57	--

Table 23 continued

Cryptand/Li <sup>+</sup> Mole Ratio	$\delta_F$ (ppm)(a)	$\delta_C$ (ppm)(a)
0.14	+ 1.53	--
0.23	+ 1.53	--
0.318	+ 1.55	- 1.08
0.439	+ 1.55	- 1.09
0.635	+ 1.57	- 1.09
0.740	+ 1.58	- 1.08
0.948	+ 1.63	- 1.08
1.18	+ 1.61	- 1.08

(a) Versus external 0.015 M LiCl/D<sub>2</sub>O; chemical shifts are corrected for the magnetic susceptibility of basic melt vs. that of water.

(b) Signal no longer detectable.

(c) Calculated from the NTCCAP deconvolution of the spectrum.

C222/Li<sup>+</sup>  
MOLE RATIO :

2.80

1.76

1.01

0.847

0.791

0.757

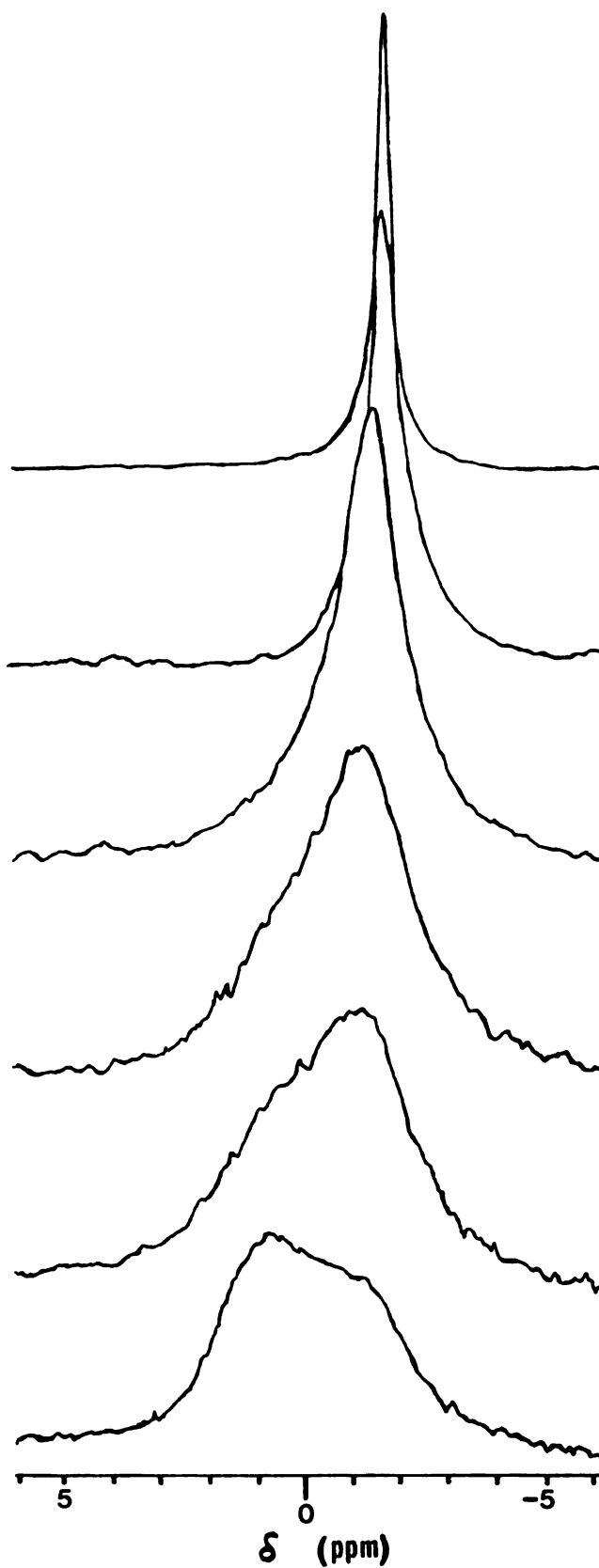


Figure 36.

Lithium-7 NMR Spectra: Observed Bandshapes at 40°C for C222/Lithium Ion Mole Ratios of 0.757 to 2.80; 1.

$\text{Li}^+$ -C222 cryptate complex exhibited a significant ( $\Delta\delta = -0.5$  ppm) upfield chemical shift as the mole ratio was increased (Figure 37). It should be noted that the linewidths of the complex signals for the other three  $\text{Li}^+$ -cryptand systems ranged from ca. 8 Hz (C221) to ca. 20 Hz (C2B22). The spectra for the  $\text{Li}^+$ -C222 system were deconvoluted by using the NTCCAP subroutine (section B.1.b., Chapter II) to estimate the linewidths of the complex signals as a function of the C222/lithium ion mole ratio. These results are given in Table 24.

The linewidths of the complex signals decrease with increasing mole ratio, tending to values similar to those of the other cryptate complexes (ca. 13 Hz). Thus, it seems that the temperature at which these spectra were measured (40°C) is near, but slightly below the coalescence temperature for the system. The exchange is slow on the NMR time scale, with two signals observed ("free" and complexed lithium ion) which are broadened by the exchange to the point where the signals overlap.

At the coalescence temperature, the rate of a first-order decomplexation process ( $k_{-1}$ ) is given by (186),

$$k_{-1} = \frac{\pi \Delta\nu}{\sqrt{2}} \quad (1)$$

where  $\Delta\nu = \nu_A - \nu_B$  and A and B refer to the free and complex sites in the absence of exchange. Let us assume that equation (1) applies to the  $\text{Li}^+$ -C222 system at 40°C, and that the chemical shift observed for the complex at a C222/ $\text{Li}^+$  mole ratio of 2.80:1 ( $\delta = \delta_B = -1.49$  ppm) is a fair approximation of the limiting chemical shift of the complex site. The chemical shift of "free" lithium ion (site A; no C222 present) is  $\delta_A = +1.55$  ppm. Thus,  $\Delta\delta = 3.04$  ppm which, with a resonance frequency of 69.951 MHz, gives a value of  $\Delta\nu = 213$

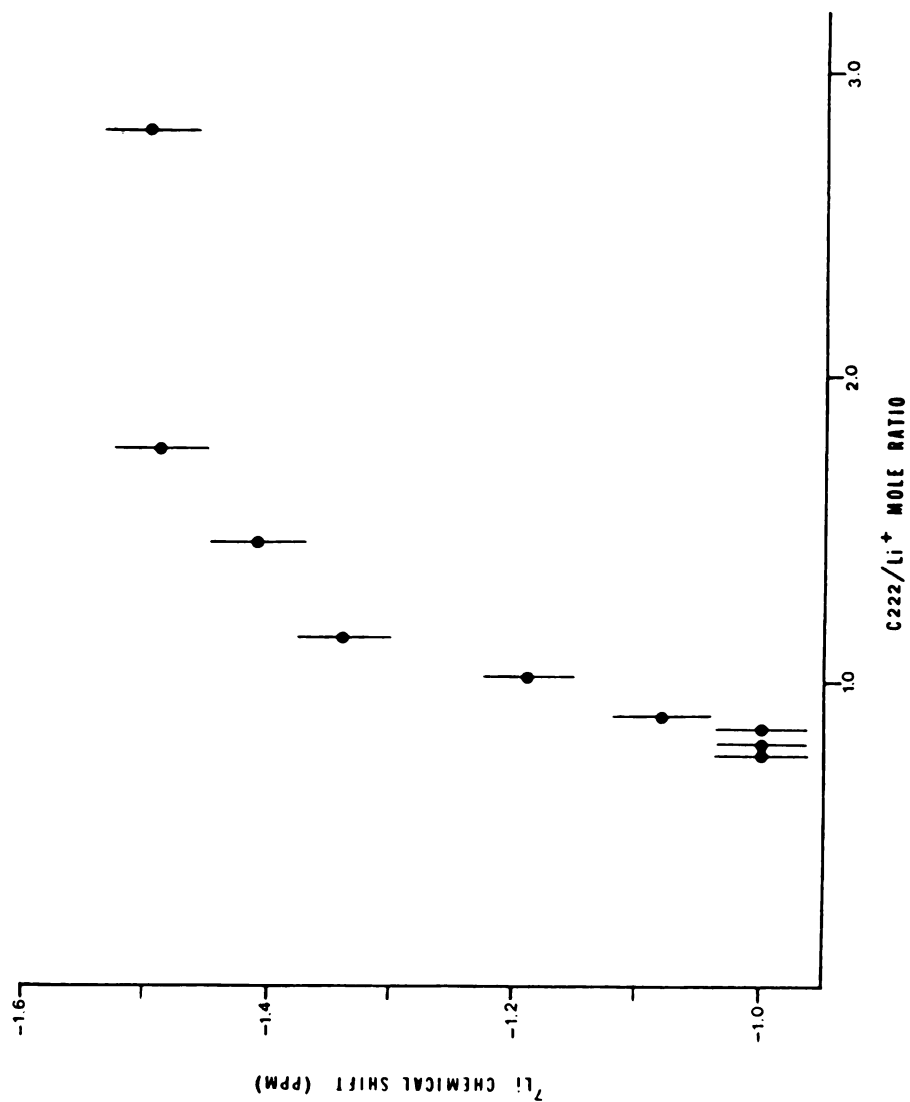


**Figure 37.** Lithium-7 Chemical Shifts for the  $\text{Li}^+ - \text{C}_{222}$  Complex in Basic Melt at  $40^\circ\text{C}$  as a Function of the  $\text{C}_{222}/\text{Lithium Ion}$  Mole Ratio.

**Table 24**

**Calculated Linewidths of the  $^7\text{Li}$  NMR Signals of the  
 $\text{Li}^+\text{C222}$  Complex in Basic Melt at 40°C**

<b>C222/<math>\text{Li}^+</math> Mole Ratio</b>	<b><math>\Delta\nu_{1/2}</math> complex (Hz)(a)</b>
0.757	177 $\pm$ 44
0.791	123 $\pm$ 8
0.842	121 $\pm$ 6
0.876	101 $\pm$ 6
1.01	85 $\pm$ 5
1.14	63 $\pm$ 5
1.45	58 $\pm$ 5
1.76	46 $\pm$ 3
2.80	13 $\pm$ 2

(a) Obtained by using the NTCCAP deconvolution subroutine.

Hz. Substituting this value into equation (1) yields  $k_{-1} = 5 \times 10^2 \text{ s}^{-1}$  (only one significant figure is given here in light of the assumptions upon which the calculation is based). Cox et al. (187) have estimated a  $k_{-1}$  value of  $> 3 \times 10^2 \text{ s}^{-1}$  for the  $\text{Li}^+$ -C222 system in methanol at 25°C.

The NTCCAP subroutine was also used to calculate integrated areas for the signals due to the "free" and complex sites in the  $\text{Li}^+$ -C221,  $\text{Li}^+$ -C222, and  $\text{Li}^+\text{C}_{2\text{B}}22$  systems at 40°C in basic melt. These areas were then used to calculate the respective cryptate complex formation constants. A similar procedure was not possible for the  $\text{Li}^+$ -C211 system due to the observed precipitate formation. At mole ratios 1:1 where samples remained homogeneous, the "free" lithium ion signal was too low in intensity to be detected.

According to Szczygiel (186), the absorption part of an NMR resonance line is given approximately by

$$S(\omega) = \frac{K(1/T^*_2)e^{(-DE/T^*_2)}}{(1/T^*_2)^2 + (\Delta\omega)^2} \quad (2)$$

where  $K$  is a constant,  $T^*_2$  is the apparent spin-spin relaxation time,  $DE$  is the post-90° pulse delay time, and  $\Delta\omega$  is the frequency in rad/s. Since

$$T^*_2 = 1/\pi LW' \quad (3)$$

where  $LW'$  is the apparent linewidth ( $=\Delta\nu_{\text{true}} + LB$ ) and

$$\Delta\omega = 2\Delta\nu\pi \quad (4)$$

equation (2) becomes



$$S(\omega) = \frac{K(\pi LW')e^{(-DE\pi LW')}}{(\pi LW')^2 + 4(\pi \Delta\nu)^2} \quad (5)$$

Multiplying the numerator and denominator by  $1/(\pi LW')^2$ ,

$$S(\omega) = \frac{K(\pi LW')^{-1} e^{(-DE\pi LW')}}{1 + 4(\Delta\nu/LW')^2} \quad (6)$$

In the documentation for the Nicolet 1180 computer software, the expression for  $S(\omega)$  is given as

$$S(\omega) = \frac{I}{1 + 4(\Delta\nu/LW')^2} \quad (7)$$

where  $I$  is the observed signal intensity. Comparing equations (6) and (7),

$$I = K(\pi LW')^{-1} e^{(-DE\pi LW')} \quad (8)$$

Rearranging,

$$K = I\pi LW' e^{(DE\pi LW')} \quad (9)$$

where  $K$  is now identified as the signal intensity corrected for artificial linebroadening (LB) and the delay time. Therefore, the corrected area of the resonance line is given by

$$A^t = \pi K \quad (10)$$

and,

$$A^t = I \pi^2 L W' e^{(DE \pi L W')} \quad (11)$$

This preceding derivation has been suggested by R. Boss (188). In practice, it was found that corrections of the areas by using equation (11) did not significantly change the  $K_F$  values, considering the uncertainties in these results.

The fraction of complexed lithium ion is given by

$$f_c = A_c^t / A_f^t A_c^t \quad (12)$$

To explicitly take into account the monomer-dimer equilibrium, equation 43 (section B.1.b., Chapter II) is modified to give

$$K_F = \frac{4 K_D f_c C_{Li}}{[(1 + 8 K_D C_{Li} f_f)^{1/2} - 1] [C_c - f_c C_{Li}]} \quad (13)$$

where  $f_f = 1 - f_c$  and  $K_D$  is the dimerization constant.

The  $^7\text{Li}$  NMR spectra chosen for deconvolution were selected so that large differences between  $A_f^t$  and  $A_c^t$  were avoided. This was found to reduce the subsequent errors in the calculated  $K_F$  values. The results of these calculations are given in Table 25. Averaged  $\log K_F$  values for the  $\text{Li}^+$ -C221,  $\text{Li}^+$ -C222, and  $\text{Li}^+$ -C2<sub>B</sub>22 systems in basic melt are listed in Table 26 along with some results from previous studies in aqueous and nonaqueous solutions for comparison.

In basic melt, the stability constants for the complexes increase in the order  $\text{Li}^+$ -C2<sub>B</sub>22 <  $\text{Li}^+$ -C222 <  $\text{Li}^+$ -C221. The larger value for C221 versus C222 is reasonable since the cavity size of C221 ( $2.2 \overset{0}{\text{\AA}}$ ) is a better match

**Table 25**

**The Fractions of "Free" and Complexed Lithium Ion Obtained by Deconvolution of  $^7\text{Li}$  NMR Spectra in the Cryptand/Lithium Ion Mole Ratio Studies in Basic Melt. Cryptate Complex Formation Constants Calculated by Using Equation 4.**

	<b>Mole Ratio</b>	<b><math>f_f</math></b>	<b><math>f_c</math></b>	<b><math>K_F</math> (<math>\text{M}^{-1}</math>)</b>
<b>C211</b>	0.594	0.6502	0.3498	245
		0.6605	0.3395	226
		0.6615	0.3385	225
	0.716	0.5197	0.4803	394
		0.4200	0.5800	494
		0.4210	0.5790	491
		0.4493	0.5507	406
	1.00	0.4158	0.5842	309
		0.4523	0.5477	255
		0.5098	0.4902	189
<b>C222</b>	0.757	0.7021	0.2979	107
		0.7003	0.2997	108
	0.791	0.6344	0.3656	149
		0.7160	0.2840	91
		0.6244	0.3756	158
	0.842	0.7046	0.2954	89
		0.6738	0.3263	106
		0.7119	0.2881	85
	0.876	0.6492	0.3508	114
		0.6749	0.3251	99

Table 25 continued

Mole Ratio	$f_f$	$f_c$	$K_F$ ( $\underline{M}^{-1}$ )
	0.6750	0.3250	99
1.01	0.4864	0.5136	208
	0.6075	0.3925	113
	0.5626	0.4374	142
1.14	0.6261	0.3739	85
	0.6051	0.3949	94
	0.5051	0.4949	150
	0.6167	0.3833	89
0.439	0.9129	0.0871	35
	0.9472	0.0528	19
	0.9446	0.0554	20
0.635	0.8642	0.1358	39
	0.9026	0.0974	26
	0.8804	0.1096	30
0.740	0.7515	0.2485	79
	0.7632	0.2368	73

**Table 26**  
**Lithium Cryptate Stability Constants<sup>(a)</sup> in Basic Melt,**  
**Water, and Various Nonaqueous Solvents**

Solvent	Cryptand			
	C211	C221	C222	C2B22
H <sub>2</sub> O	5.5	2.5 <sub>0</sub>	0.99 <sup>(b)</sup>	--
MeOH	8.0 <sub>4</sub>	5.3 <sub>8</sub>	2.6	2.19 <sup>(d)</sup>
EtOH	8.4 <sub>7</sub>	5.3 <sub>8</sub>	2.3	--
AN	10	10.3	7.0	--
PC	12.4 <sub>4</sub>	9.6 <sub>0</sub>	6.9 <sub>4</sub>	--
NMP <sup>(c)</sup>	6.4 <sub>3</sub>	3.4 <sub>8</sub>	2.9 <sub>7</sub>	--
DMF	6.8 <sub>5</sub>	3.5 <sub>8</sub>	--	--
DMSO	5.8 <sub>4</sub>	2.7 <sub>7</sub>	1.0	--
PYR	--	--	2.9 <sub>4</sub> <sup>(b)</sup>	--
Basic Melt	--	2.51	2.06	1.60
		(±0.15)	(±0.12)	(±0.25)

(a) Taken from reference 189.

(b) Taken from reference 142.

(c) NMP = N-methylpropionamide

(d) Taken from reference 191.

for the lithium ion ( $r_{\text{Li}^+} = 0.86 \text{ \AA}$ ) than that of C222 ( $2.8 \text{ \AA}$ ). The smaller value for C2<sub>B</sub>22 versus C222 is probably due to the reduced conformational flexibility of the former versus the latter cryptand. Cox *et al.* (190) have also observed, in various nonaqueous solutions, smaller stability constants for the C2<sub>B</sub>22·M<sup>+</sup> (M<sup>2+</sup> = alkaline earth cations) cryptates than for the C222·M<sup>2+</sup> cryptates. In methanol solutions, Cox *et al.* (191) also determined that the stability constant for the C222 complex of the lithium ion is ca. 0.4 log K<sub>f</sub> units larger than that of the C2<sub>B</sub>22-Li<sup>+</sup> cryptate.

From Table 26, it appears that the stability constants for the complexes in basic melt are generally smaller than those in aqueous or nonaqueous solutions. In addition, the change in the complex stability from the C222 to the C221 complexes is either equal to, or less than (by 2 to 3 log K<sub>f</sub> units) that found for the other solvents. As was found in the lithium-crown complexation studies (section C.1., Chapter III), it seems that the equilibrium between the monomer and dimer lithium chlorocomplexes tends to minimize the selectivity of the cryptand complexation of the lithium ion.

## B.2. Potentiometry

The observed changes in the cell potential as a function of C2<sub>B</sub>22 titrant and the C2<sub>B</sub>22/lithium ion mole ratio in the titration of a 1.0 mol% LiCl-basic melt solution with C2<sub>B</sub>22 are shown in Figure 38. Data from this experiment are listed in Table 27.

Recalling the discussion of the results for the similar titration using 15C5 as the titrant (section C.2., Chapter III), the titration curve in Figure 38 clearly indicates that chloride ions are released in the process of C2<sub>B</sub>22 complexation of the lithium ion in basic melt. It is reasonable to expect an analogous response of the cell potential to titrations with C211, C221, or C222. Cryptand C2<sub>B</sub>22 was chosen for this experiment since the precipitation of the C2<sub>B</sub>22·LiAlCl<sub>4</sub> complex provides a visual cue as to when the 1:1 cryptand/lithium ion mole

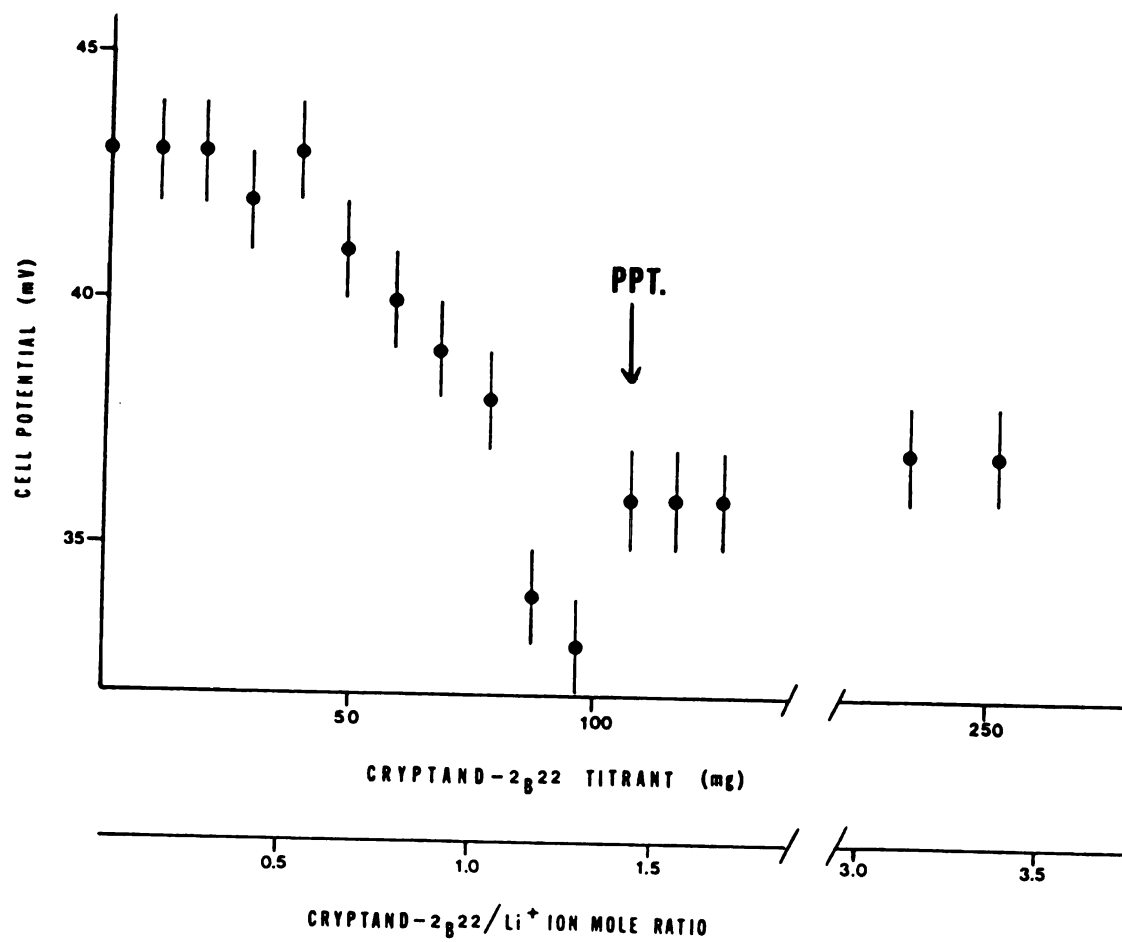


**Figure 38.** Potentiometry:  $E_{\text{cell}}$  Versus  $\text{C}_{2\text{B}22}$  Titrant (mg) and the  $\text{C}_{2\text{B}22}$ /Lithium Ion Mole Ratio.

**Table 27**

**Potentiometric Titration Data: Observed Cell Potentials as a Function  
of C<sub>2</sub>B<sub>22</sub> Titrant (mg) and the C<sub>2</sub>B<sub>22</sub>/Lithium Ion Mole Ratio**

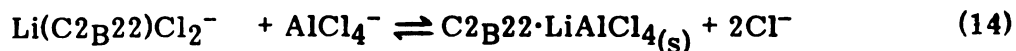
<b>Aliq. #</b>	<b>C<sub>2</sub>B<sub>22</sub> (mg)</b>	<b>C<sub>2</sub>B<sub>22</sub>/Li<sup>+</sup>(a) Mole Ratio</b>	<b>E<sub>cell</sub> (mV)(b)</b>
0	0.0	--	43
1	9.7	0.13	43
2	19.4	0.259	43
3	29.1	0.388	42
4	38.8	0.518	43
5	48.5	0.647	41
6	58.2	0.777	40
7	67.9	0.906	39
8	77.6	1.04	38
9	87.3	1.17	34
10	97.0	1.29	33
11	106.7	1.42	36
12	116.4	1.55	36
13	126.1	1.68	36
14	135.8	1.81	36
15	145.5	1.94	36
16	155.2	2.07	35
18	174.6	2.33	36
24	232.8	3.11	37
26	252.2	3.37	37

(a) [Li<sup>+</sup>] = 0.790 M; (b) ± 1 mV



ratio is reached (section B.1.). As shown in Figure 38, the onset of the precipitation was observed to occur at about a mole ratio of 1.4:1. The slight increase in the cell potential for the 1.4:1 and higher mole ratios is probably not significant in light of the heterogeneous nature of the solution at the higher mole ratios.

The heterogeneous equilibrium



is proposed to account for the behavior of the cell potential in the course of the titration, as well as the constancy of the chemical shifts of the  $\text{C}_{2\text{B}22}$  complex signals with increasing  $\text{C}_{2\text{B}22}$ /lithium ion mole ratio.

## C. Characterization of the Solid Lithium Cryptate Complexes

### C.1. Elemental Analyses

The results of the elemental analyses of the assumed  $\text{C}_{2\text{B}22}\cdot\text{LiAlCl}_4$  and  $\text{C}_{211}\cdot\text{LiAlCl}_4$  complexes performed by Galbraith Laboratories are shown in Table 28. Fair agreement between the actual and theoretical analyses for the  $\text{C}_{2\text{B}22}\cdot\text{LiAlCl}_4$  complex was obtained. Less satisfactory agreement was obtained for the  $\text{C}_{211}\cdot\text{LiAlCl}_4$  complex, particularly for nitrogen (5.28 vs. 6.04 wt%), oxygen (18.84 vs. 13.79 wt%), and lithium (0.87 vs. 1.50 wt%). However, the actual results are in better agreement with the theoretical composition based on the  $\text{C}_{211}\cdot\text{LiAlCl}_4$  stoichiometry than formulations such as  $\text{C}_{211}\cdot\text{LiCl}$  (carbon: 52.96 wt%) or  $\text{C}_{211}\cdot\text{LiCl}\cdot\text{BPCl}$  (carbon: 55.52 wt%).

Considerable difficulty was encountered in drying the crystalline solids isolated from basic melt solutions of  $\text{C}_{221}$  and  $\text{LiCl}$ , and  $\text{C}_{222}$  with  $\text{LiCl}$ ; traces of basic melt and benzene from the mother liquor clung tenaciously to the

Table 28

Summary of the Elemental Analyses of the C<sub>2</sub>B<sub>22</sub>·LiAlCl<sub>4</sub> and C<sub>2</sub>B<sub>22</sub>·LiAlCl<sub>4</sub> Cryptate Complexes

Element	C <sub>2</sub> B <sub>22</sub> ·LiAlCl <sub>4</sub>		C <sub>2</sub> B <sub>22</sub> ·LiAlCl <sub>4</sub>	
	Actual (wt%)	Theor. (wt%)	Actual (wt%)	Theor. (wt%)
C	40.58	41.79	36.36	36.23
H	6.33	5.74	6.04	6.08
N	4.57	4.43	5.28	6.04
O	18.47	20.24	18.84	13.79
Li	0.95	1.10	0.87	1.50
Al	3.69	4.27	4.95	5.81
Cl	21.83	22.43	28.15	30.55
	96.42%	100%	100.49	100%

crystals, even after one week of pumping at  $\leq 10^{-5}$  torr. Although this posed no problem for the election and mounting of single crystals for x-ray analysis, samples which were sufficiently dry for submission for elemental analysis could not be obtained.

### C.2. Lithium-7 Magic Angle Spinning NMR

The  $^7\text{Li}$  MASNMR spectra (spinning and static) for powder samples of  $\text{LiCl}$ ,  $\text{LiAlCl}_4$ ,  $\text{C}_{2\text{B}22}\cdot\text{LiAlCl}_4$ , and  $\text{C}_{211}\cdot\text{LiAlCl}_4$  at  $22^\circ\text{C}$  are shown in Figures 39-42. Chemical shift and linewidth data for these spectra are given in Table 29. Solid state spectra could not be obtained for the (assumed)  $\text{C}_{221}\cdot\text{LiAlCl}_4$  and  $\text{C}_{222}\cdot\text{LiAlCl}_4$  complexes due to the drying problems described in the preceeding section.

The classic Pake doublet ( $m = 1/2$   $m = -1/2$  transition) was observed for  $\text{LiCl}$  in the static mode (Figure 39, top). According to Fyfe (192), for a nucleus with a spin of  $3/2$  experiencing large quadrupolar interactions in a glass or polycrystalline powder, the observed spacing of the doublet equals  $(25/9)A_2$  with  $A_2$  defined by

$$A_2 = \frac{3}{64} \frac{1}{\nu_0} (\chi)^2 \quad (15)$$

where  $\chi$  is the nuclear quadrupole coupling constant ( $= e^2qQ/h$ ). From Table 29, the observed splitting (5.5 kHz) yields a value of  $A_2 = 2000$  Hz. Substituting this value into equation 15, a coupling constant of 1.7 MHz is obtained for  $\text{LiCl}$ . This result is within an order of magnitude of the value for  $^7\text{Li}$  in lithium silicate glasses (910 kHz) obtained by Tokuhiro et al. (174).

No splitting was observed in the static spectrum of  $\text{LiAlCl}_4$  (Figure 40, top), which indicates a smaller quadrupolar interaction for the  $^7\text{Li}$  nucleus in this compound. In this case (192),

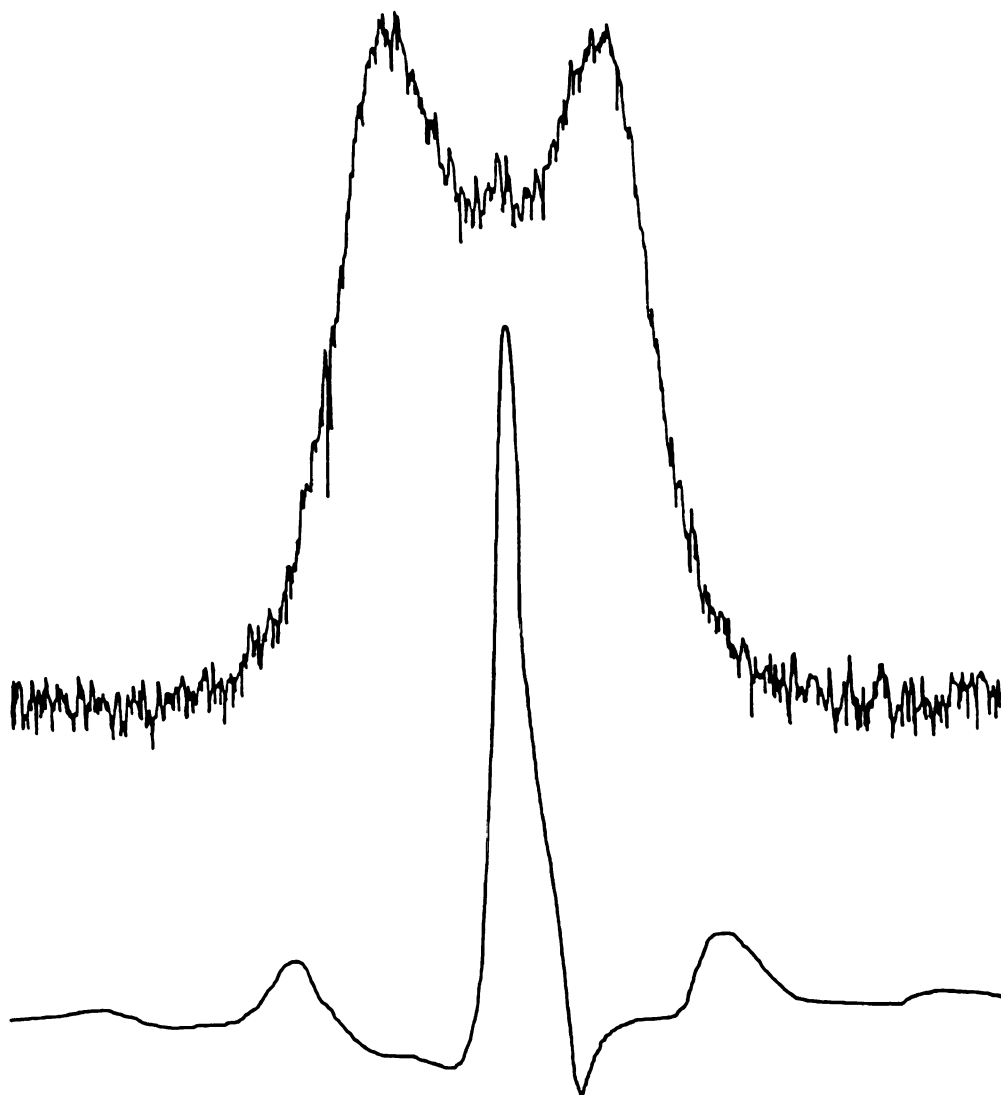


**Figure 39. Lithium-7 Solid State NMR Spectra: Static (top) and Magic Angle Spinning (@2.7 kHz) (bottom) Spectra for Polycrystalline LiCl at 22°C (100 Scans).**

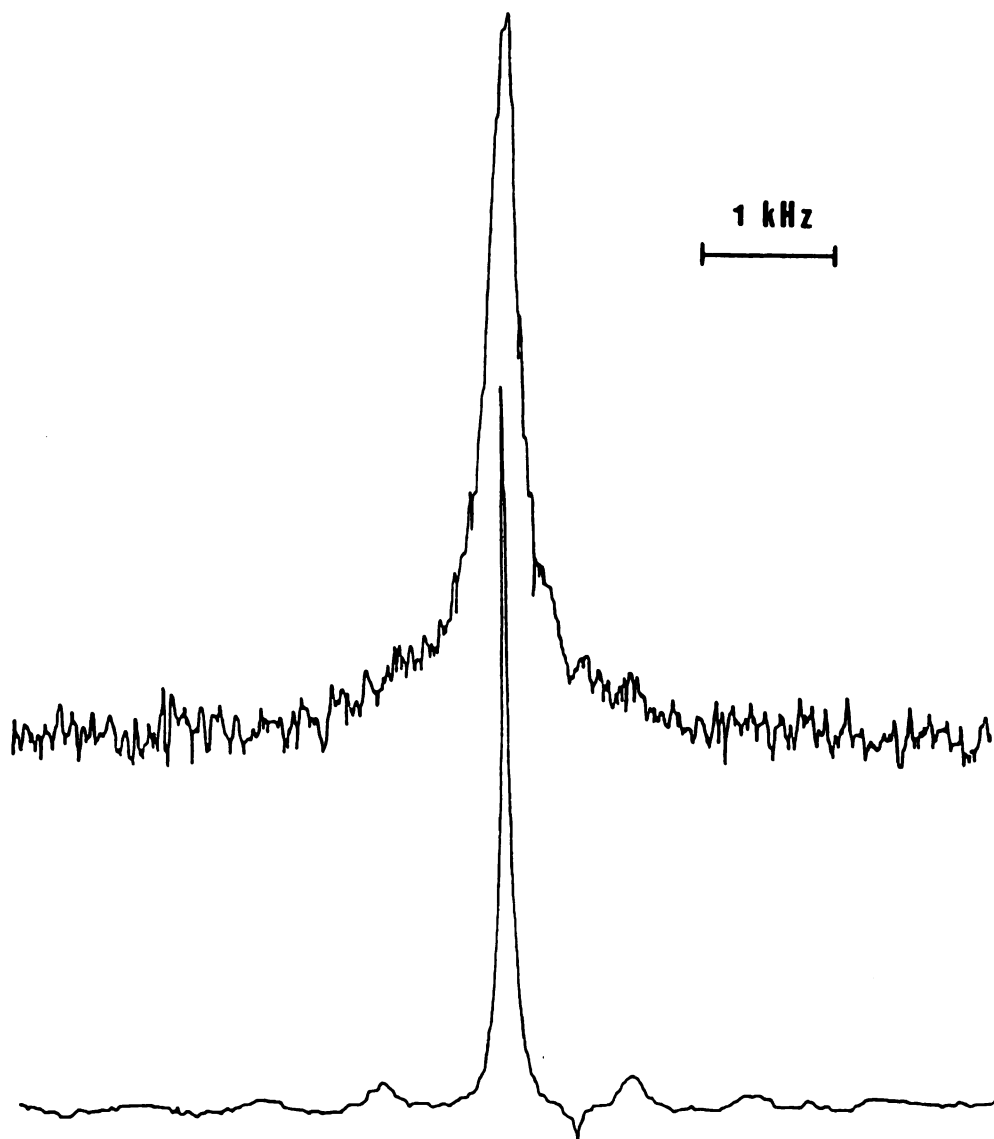


**Figure 40. Lithium-7 Solid State NMR Spectra: Static (top) and Magic Angle Spinning (@1.8 kHz) (bottom) Spectra for Polycrystalline  $\text{LiAlCl}_4$  at 22°C (100 Scans).**

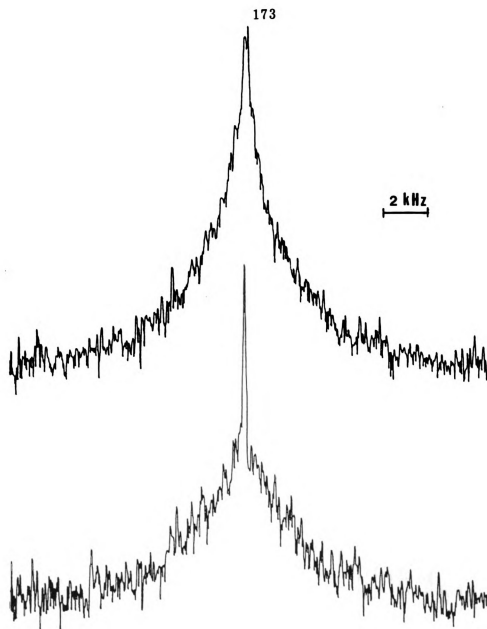


**Figure 41. Lithium-7 Solid State NMR Spectra: Static (top) and Magic Angle Spinning (@2.1 kHz) (bottom) Spectra for Polycrystalline C<sub>2</sub>B<sub>22</sub>·LiAlCl<sub>4</sub> at 22°C (20,000 Scans).**

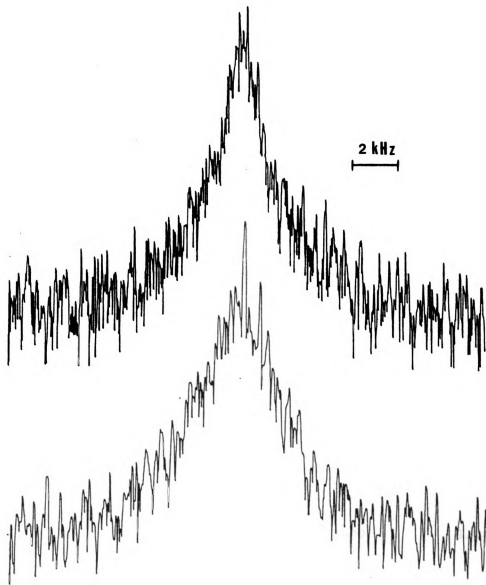


**Figure 42.** Lithium-7 Solid State NMR Spectra: Static (top) and Magic Angle Spinning (@0.8 kHz) (bottom) Spectra for Polycrystalline  $\text{C}_{211}\text{-LiAlCl}_4$  at  $22^\circ\text{C}$  (20,000 Scans).

Table 29

## Lithium-7 Solid State NMR Results for Various Lithium Compounds

Sample	$\delta$ (ppm)	Linewidth (Hz)		$\chi$ (kHz)
		spinning	static	
0.015 <u>M</u>				
LiCl/D <sub>2</sub> O	0.0	--	19	--
LiCl	-3.2	450 @ 2.7 kHz	splitting: 5.5 kHz	1700
LiAlCl <sub>4</sub>	-0.8	58 @ 1.8 kHz	420	1.7
C <sub>2</sub> B <sub>22</sub> ·	+1.0	200 @ 2.1 kHz	1600	6.4
C <sub>2</sub> 11·	+1.0	ca. 2000 @ 1 kHz	ca. 2000	8.



$$\Delta\nu_{1/2} = A_1 = \frac{\chi}{4} \quad (16)$$

With  $\Delta\nu_{1/2} = 420$  Hz, a  $\chi$  value of 1.7 kHz is obtained for this sample. This very small value is reasonable in view of the known crystal structure of  $\text{LiAlCl}_4$  (space group  $P2_1/c$ ), which is made up of  $\text{LiCl}_6$  octahedra layers linked together by  $\text{AlCl}_4$  tetrahedra (193).

The considerable narrowing effect of magic angle sample spinning is seen in the spectra for  $\text{C}_{22}\text{B}_{22}\cdot\text{LiAlCl}_4$  (Figure 41). In the spinning mode, the central transition is partially resolved from the broad background; this broadening, due to dipolar interactions, is not completely removed at the spinning rate of 2.1 kHz. By using equation 16 and  $\Delta\nu_{1/2} = 1600$  Hz for the static spectrum, a coupling constant of 6.4 kHz is obtained for the complex.

For the  $\text{C}_{211}\cdot\text{LiAlCl}_4$  sample, stable spinning rates of greater than 1 kHz could not be obtained. Thus, very little reduction in the dipolar broadening was observed (Figure 42). In the bottom spectrum, the central transition is barely discernable at this spinning rate. A coupling constant of ca. 8 kHz is obtained by using equation 16 and  $\Delta\nu_{1/2} \approx 2000$  Hz.

The coupling constants for the  $^7\text{Li}$  nucleus in the two cryptate complexes are exceptionally small (cf. Table 14, Chapter III), indicating highly symmetric environments for the lithium ion in these complexes. As is shown in the following section, this high symmetry is confirmed in the crystal structure of the  $\text{C}_{22}\text{B}_{22}\cdot\text{LiAlCl}_4$  complex.

Evaluation of the differences in chemical shifts among the four compounds (Table 29) is difficult due to the lack of literature values for these or other lithium compounds in the solid state. In an unpublished work, Ellaboudy (194) reports chemical shifts of -2.8 ppm ( $\text{LiCl}$ ), -1.1 ppm ( $\text{LiI}$ ), -0.8 ppm ( $\text{Li}^+\text{C}_{211}\text{I}^-$ ), and -3.5 ppm ( $\text{Li}^+\text{C}_{211}\text{Na}^-$ ). From Table 29, it appears that the cryptands

effectively remove the shielding influence of the chlorine atoms in the  $\text{AlCl}_4^-$  ion on the  $^7\text{Li}$  nucleus; the shifts for  $\text{LiCl}$  and  $\text{LiAlCl}_4$  are more negative (by about 2 or 3 ppm) than those of the complexes. This shielding effect is understandable since the lithium ion is expected to reside within the ligand cavities.

### C.3. The Crystal Structure of $\text{C}_{22}\text{B}_{10}\text{LiAlCl}_4$

A single crystal of the  $\text{C}_{22}\text{B}_{10}\text{LiAlCl}_4$  complex was recovered from a 5 mm NMR tube sample of basic melt containing 0.637 mol%  $\text{C}_{22}\text{B}_{10}$  and 1.00 mol%  $\text{LiCl}$ . The crystal (0.6 x 0.6 x 1.0 mm) was mounted in a sealed 0.7 mm Pyrex capillary tube for data collection.

The crystal structure of this complex was determined by D.L. Ward, and data collected by using a Nicolet P3F four circle computer-controlled diffractometer. All data reduction routines (Enraf-Monius SDP program package) were performed on a VAX 11/750 computer. The crystallographic parameters and data collection conditions for this structure determination are listed in Table 30. The atomic numbering scheme (heavy atoms only) for the  $\text{C}_{22}\text{B}_{10}$  molecule is shown in Figure 43. A summary of all heavy atom bond distances and all bond angles is given in Appendix 2. An abbreviated list of important bond angles and distances is given in Table 31.

The structure of a single  $\text{C}_{22}\text{B}_{10}\text{LiAlCl}_4$  molecule is shown in Figure 44. In this perspective, the tetrahedral geometry of the  $\text{AlCl}_4^-$  ion is clearly observed. The large distance between the lithium ion and the nearest chlorine atom of the  $\text{AlCl}_4^-$  ion (5.90 Å) indicates that the latter is not coordinated to the lithium ion.

Two different views of the unit cell containing four complex molecules are shown in Figures 45 and 46. It can be seen that the cryptate ions are oriented in such a way that the bulky benzene rings on adjacent cryptates

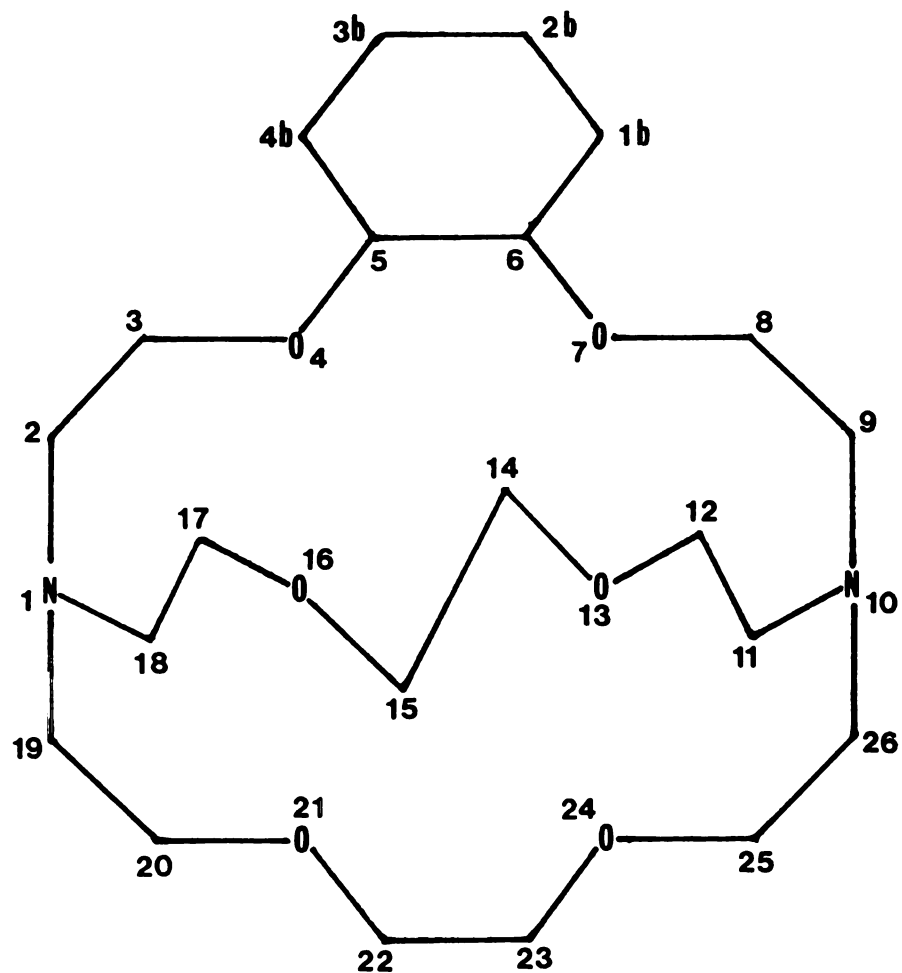


**Figure 43.** Atomic Numbering Scheme for Heavy Atoms in the C<sub>2</sub>B<sub>22</sub> Molecule.

**Table 30**

**Crystallographic Parameters and Data Collection Conditions  
for the Determination of the Structure of the  
C<sub>2</sub>B<sub>22</sub>-LiAlCl<sub>4</sub> Cryptate Complex**

Space Group:	P 2 <sub>1</sub> /n
Cell Parameters:	a = 11.099 ± 0.002 Å
	b = 11.796 ± 0.002 Å
	c = 22.345 ± 0.005 Å
	V = 2908.8 ± 10 Å <sup>3</sup>
	= 96.15 ± 0.02°
	Z = 4(a)
	D <sub>C</sub> = 1.371 mg/m <sup>3</sup>
Data Collection:	scan range = 4.5 to 55°
	scan speed - 1°/min
	scan width = 1.6 ± Δ2θ
number of reflections	used - 4571 (I > 3σ(I))
absorption correction	- 4.74 cm <sup>-1</sup>
class of reflections	- hkl, hk $\bar{l}$
	final R - 0.057
	final R <sub>w</sub> - 0.068

(a) Number of molecules in the unit cell.

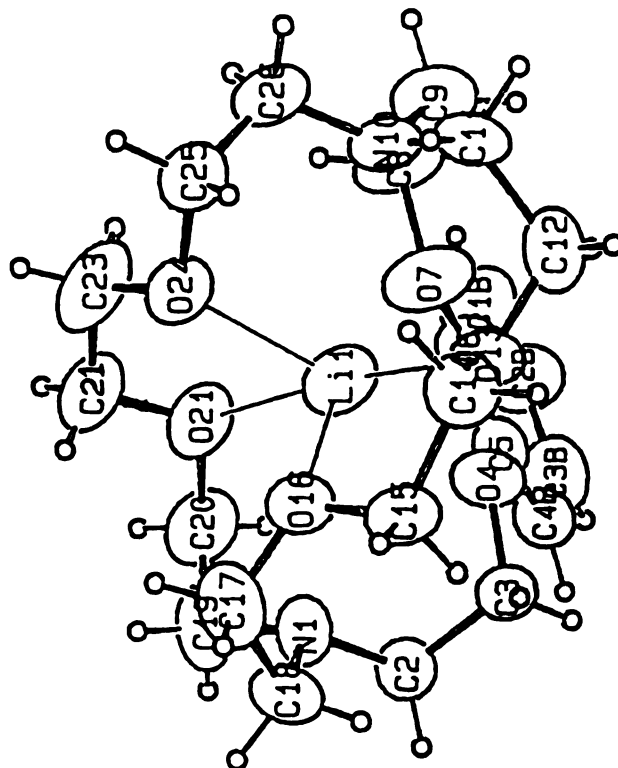
**Table 31**

**Some Important Bond Distances ( $\text{\AA}$ ) and Bond Angles (Degrees) for  
the C<sub>2</sub>B<sub>22</sub> LiAlCl<sub>4</sub> Complex**

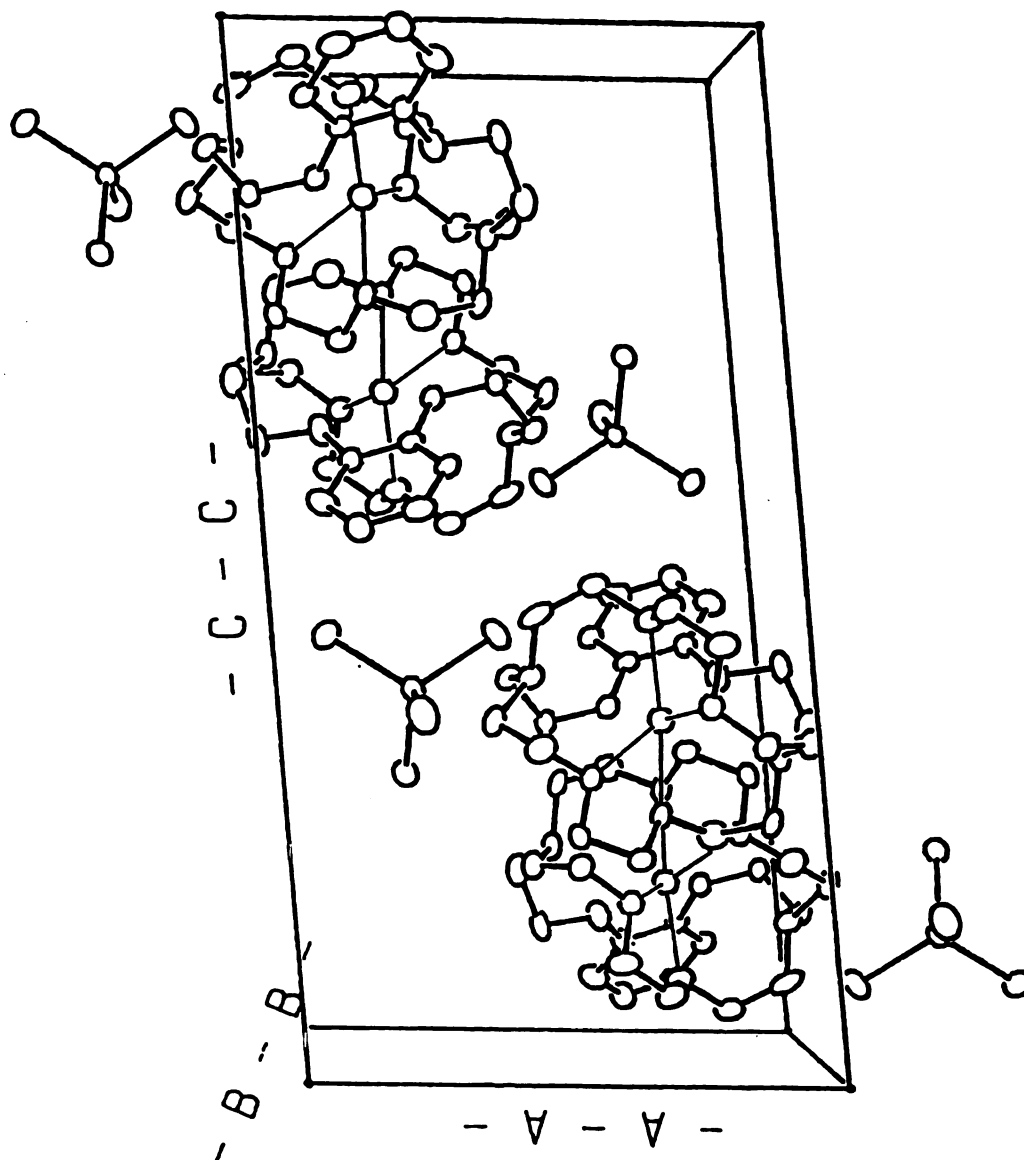
<b>Atom 1</b>	<b>Atom 2</b>	<b>Bond Distance (<math>\text{\AA}</math>)</b>	
A11	C11	2.13	
Li1	C11	5.90	
Li1	013	2.20	
Li1	016	2.37	
Li1	021	2.29	
Li1	024	2.20	
Li1	N1	2.97	
Li1	N10	2.75	

<b>Atom 1</b>	<b>Atom 2</b>	<b>Atom 3</b>	<b>Bond Angle (Degrees)</b>
C11	A11	C12	109.7
C11	A11	C13	109.8
C11	A11	C14	108.9
C12	A11	C13	109.4
C12	A11	C14	110.4
C13	A11	C14	108.6
C13	Li1	016	71.6
013	Li1	021	174.0
013	Li1	024	111.8
016	Li1	021	105.6
016	Li1	024	82.6
021	Li1	024	72.5



**Figure 44. The Crystal Structure of  $\text{C}_{2\text{B}_{22}}\text{LiAlCl}_4$ : The  $\text{C}_{2\text{B}_{22}}\text{LiAlCl}_4$  Molecule Viewed Along the  $\underline{b}$  Axis.**



**Figure 45.** The Crystal Structure of  $C_{2B_{22}} \cdot LiAlCl_4$ :  
A View of the Unit Cell Along the  $\underline{b}$  Axis.

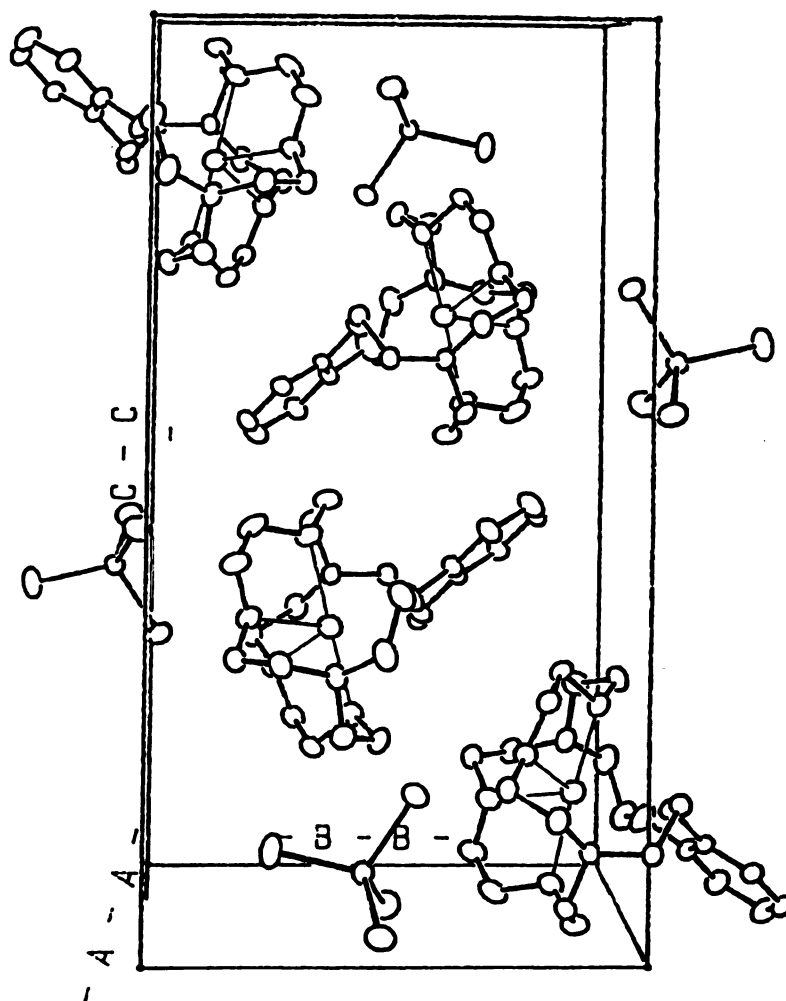


**Figure 46.** The Crystal Structure of  $C_{2B_{22}} \cdot LiAlCl_4$ :  
A View of the Unit Cell Along the a Axis.



are nearly parallel, thus minimizing steric interactions.

In Figure 47 the oxygen and nitrogen atoms of the cryptand are labeled; lines from each oxygen to the lithium ion are drawn to emphasize the geometry of the lithium ion coordination. A least squares calculation of the deviation of the lithium ion from a series of six planes was performed, each plane defined by the positions of a set of oxygens, or oxygen and nitrogen atoms in the cryptand. The results of these calculations are given in Table 32. It appears that the lithium ion is octahedrally coordinated by the six oxygen atoms (max. deviation =  $-0.175 \text{ \AA}$  from plane #5). The large Li-N distances (Li-N =  $2.97 \text{ \AA}$  and Li-N10 =  $2.75 \text{ \AA}$ ) suggest that the nitrogen atoms do not participate in the lithium ion coordination. This is in contrast to the reported structure of the C211·LiI complex (153), which has a mean Li-N bond distance of  $2.28 \text{ \AA}$ .

In the C<sub>2</sub>B<sub>22</sub>·LiAlCl<sub>4</sub> complex, it appears that a line drawn to connect Ni, Li, and N10 is coincident with one of the three-fold axes which intersects a face of the LiO<sub>6</sub> octahedron. The Li-O bond distances range from 2.20 to  $2.37 \text{ \AA}$  in the complex. These values are only slightly longer than the mean Li-O distance of  $2.13 \text{ \AA}$  in the C211·LiI structure (153). Thus, despite the large difference in the size of the lithium ion ( $r_{\text{Li}^+} = 0.86 \text{ \AA}$ ) versus the C<sub>2</sub>B<sub>22</sub> cavity size ( $d_{\text{C}_2\text{B}_{22}} = 2.8 \text{ \AA}$ ), and the supposed "stiffening" influence of the benzene ring, C<sub>2</sub>B<sub>22</sub> apparently possesses sufficient conformation flexibility to enable the coordination of the lithium ion within the cryptand cavity.

#### D. Conclusions

The <sup>7</sup>Li NMR data obtained in this study show that the chemical exchange between the "free" and cryptated lithium ions in basic melt solutions is slow at 40°C and a field strength of 42.28 kG. The NMR signals for the two sites

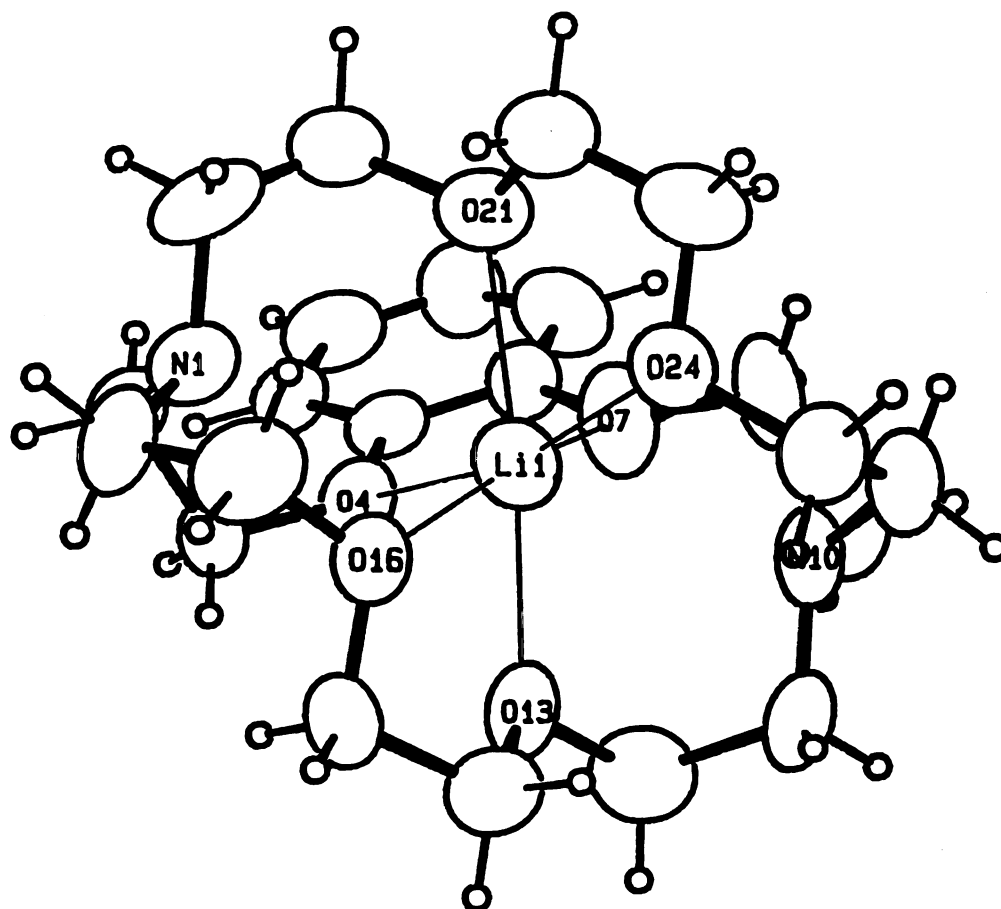


**Figure 47.** The Crystal Structure of C<sub>2</sub>B<sub>22</sub>·LiAlCl<sub>4</sub>: A Closeup View of the Cryptated Lithium Ion. The Oxygen and Nitrogen Atoms are Labeled According to the Scheme in Figure 16.

Table 32

**Least Squares Calculations: The Deviations (Å) of the Lithium Ion from  
Coincidence with Planes Defined by Sets of Oxygen and Nitrogen  
Atoms in the C<sub>2</sub>B<sub>22</sub>-LiAlCl<sub>4</sub> Cryptate Complex**

Plane	Set of Four Atoms	Deviation (Å)
1	04, 013, 021, 024	- 0.002 ± 0.010
2	07, 013, 016, 021	+ 0.169 ± 0.010
3	04, 07, 016, 024	+ 0.057 ± 0.010
4	013, 021, N1, N10	+ 0.062 ± 0.011
5	07, 016, N1, N10	- 0.175 ± 0.011
6	04, 024, N1, N10	+ 0.158 ± 0.010

are well resolved ( $\Delta\delta$  ca. 2 ppm;  $\Delta\nu_{1/2} \leq 20$  Hz) for the systems which contain C211, C222, or C2<sub>B</sub>22. For the lithium-C222 system, 40°C appears to be close to the coalescence temperature; the signals for the "free" and complexed lithium ion sites are broadened to the point of overlapping. The estimated decomplexation rate for this system ( $5 \times 10^3 \text{ s}^{-1}$ ) is higher by factors of  $10^3$  and  $10^6$  than that observed for the lithium-C221 and lithium-C211 systems in pyridine (174), respectively. The apparently more facile decomplexation of the lithium ion from the C222 cryptate (compared to the C2<sub>B</sub>22 cryptate) is attributed to the greater conformational flexibility of C222 versus that of C2<sub>B</sub>22.

Potentiometry has been used to show that complexation of the lithium ion with C2<sub>B</sub>22 occurs with the release of chloride ions in the basic melt. This is in contrast to the complexation of the lithium ion with 15C5 (section C.2, Chapter III), where retention of the chloride ions in the crown complex was indicated.

Single crystals of lithium cryptate complexes have been isolated from basic melt solutions of LiCl with C211, C221, C222, and C2<sub>B</sub>22. The crystal structure of the C2<sub>B</sub>22·LiAlCl<sub>4</sub> complex has been determined. The results of this analysis indicate that the lithium ion is contained within the cryptand cavity in a nearly regular octahedral coordination by the oxygen atoms of the cryptand. The Li-N distances appear to be too long to conclude that the nitrogen atoms participate in the lithium ion coordination.

**CHAPTER V**  
**HEAVY METAL CHLOROCOMPLEX FORMATION IN THE**  
 **$\text{AlCl}_3$ -BPCl SYSTEM**

## **A. Introduction**

In the previous studies of chlorocomplexation in the  $\text{AlCl}_3\text{-BPCl}$  and  $\text{AlCl}_3\text{-ImCl}$  molten salt systems (see Chapter I), electrochemical and UV-Vis spectrophotometric techniques were the principal methods of investigation. In only one of these studies (92) has vibrational spectroscopy been used to corroborate the structure of a chlorocomplex ( $\text{NpCl}_6^{3-}$ ) inferred from UV-Vis spectrophotometric and electrochemical data. The lack of IR or Raman data for these systems is surprising considering the extent to which these methods have been applied in previous molten salt studies (195).

No multinuclear NMR studies of chlorocomplexes in the  $\text{AlCl}_3\text{-BPCl}$  system have been reported before, or since the work of Taulelle and Popov (58). For the reasons cited in section B.1.c.(3), Chapter I, detection of NMR signals for most of the metal ions studied in this system is likely to be difficult. However, other metal ions exist which have NMR-active nuclei with more favorable NMR characteristics. Moreover, as is discussed herein, these metal ions have a marked tendency to form chlorocomplexes in ionic liquids which contain an excess of chloride ions.

Therefore, the purpose of this study was to investigate chlorocomplexation of selected heavy metal ions in the  $\text{AlCl}_3\text{-BPCl}$  molten salts by using vibrational spectroscopy (far-IR) and multinuclear NMR techniques. The metal ions selected for these studies were  $\text{Cd}^{2+}$ ,  $\text{Hg}^{2+}$ ,  $\text{Sn}^{2+}$ ,  $\text{Sn}^{4+}$ ,  $\text{Zn}^{2+}$ ,  $\text{Cu}^+$ , and  $\text{Pb}^{2+}$ .

## **B. Solvation of Heavy Metal Salts in Basic and Acidic $\text{AlCl}_3\text{-BPCl}$ Melts**

### **B.1. Basic Melt Solutions**

The heavy metal chlorides which were found to be soluble in basic melt are listed in Table 33. In this qualitative work, no attempt was made to determine thermodynamic solubility limits of these salts in this medium. Melt

**Table 33****Heavy Metal Chlorides in Basic  $\text{AlCl}_3$ -BPCl Melt:****Minimum Solubilities at 25°C**

<b>Salt</b>	<b>Solubility (Mol%)</b>
$\text{CdCl}_2$	3.0
$\text{SnCl}_2$	3.3
$\text{HgCl}_2$	9.5
$\text{CuCl}$	6.7
$\text{ZnCl}_2$	1.6
$\text{SnCl}_4$	(a)

(a) See text

solutions were prepared with metal chloride concentrations sufficient to enable far-IR and multinuclear NMR studies of these solutes.

Both  $\text{PbCl}_2$  and  $\text{Pb}(\text{NO}_3)_2$  were found to be insoluble in basic melt, even after six months of conditioning (see Chapter II, section A.1.c.(1)). In the case of  $\text{Pb}(\text{NO}_3)_2$ , the heterogeneous melt solution was observed to turn a bright yellow color over this conditioning period. This color change is similar to that observed for  $\text{LiNO}_3$  (which was soluble) in basic melt (see Chapter III, section B.1.). It is suspected that exchange of nitrate ion from the lead salt for chloride ion from the melt occurred in this solution, producing the yellow melt color and leaving behind the insoluble  $\text{PbCl}_2$  in the sample. The source of this yellow color is unknown; aqueous or nonaqueous solutions of nitrate ion are not, in general, colored.

All salts in Table 33, were found to dissolve in basic melt within 24 hours with stirring. Only  $\text{CuCl}$  produced a color change (to dark orange) when dissolved in the melt. This result is in contrast to the observations of Laher and Hussey (81) who found no color change in the melt on dissolving  $\text{CuCl}$  in  $\text{AlCl}_3\text{-BPCl}$  or  $\text{AlCl}_3\text{-ImCl}$  melts. Evidence for the  $\text{CuCl}_2^-$  chlorocomplex has been reported for other ambient temperature melts (25,32,33), as well as in nonaqueous solutions (204-206). From Table 33 it is seen that, in general, at  $25^\circ\text{C}$  the solubilities of these heavy metal salts are greater than than that of  $\text{LiCl}$  (ca. 2 mol%), or other lithium salts ( $\leq$  2 mol%).

The concentration obtained for  $\text{CdCl}_2$  in basic melt is thought to be very near the solubility limit for this salt, since stirring was often required to redissolve transparent needle-like crystalline material which sometimes formed when the solutions were allowed to stand overnight. The identity of these crystals is unknown; attempts to isolate them from basic melt solutions were unsuccessful. From previous literature reports (119,196) the  $\text{CdCl}_3^-$  or  $\text{CdCl}_4^{2-}$

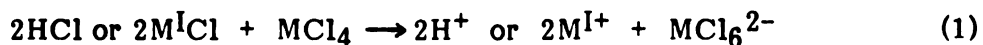


chlorocomplex ions were expected as the most likely cadmium species to exist in basic melt solutions of  $\text{CdCl}_2$ .

Based on previous studies by Vanderzee and Rhodes (197), and Clarke and Solomons (198), the  $\text{SnCl}_3^-$  complex was assumed to exist in  $\text{SnCl}_2$ -basic melt solutions. Chlorocomplexes of the  $\text{Hg}^{2+}$  ion have been observed in solutions and in the solid state (199-203). In light of the high solubility of  $\text{HgCl}_2$  in basic melt, it seemed likely that the formation of more than one complex for mercury in the melt was feasible.

Reynolds et al. (207) have recently inferred the existence of the  $\text{ZnCl}_4^{2-}$  chlorocomplex in dilute  $\text{ZnCl}_2$ -basic  $\text{AlCl}_3$ - $\text{ImCl}$  melts at  $30^\circ\text{C}$  from observed variations in  $^1\text{H}$  NMR chemical shifts of the  $\text{Im}^+$  ion as functions of  $\text{ZnCl}_2$  concentration. The  $\text{ZnCl}_4^{2-}$  species has been observed in several other previous solution and solid state studies (118,208-211).

An unusual reaction was observed upon addition of  $\text{SnCl}_4$  to a stirred basic melt solution at room temperature. After adding 0.5213 g of  $\text{SnCl}_4$  to 5.6320 g of basic melt, a granular white precipitate was observed to form within 2 minutes. The resulting slurry was vacuum-filtered to remove the bulk melt, leaving a fairly dry white powder. This reaction appears to be analogous to that described by Cotton and Wilkinson (9) for the preparation of hexachloro ions of germanium and tin,



where  $\text{M}^+$  is an alkali metal cation. Thus, for the  $\text{SnCl}_4$ -basic melt mixture,



where  $(BP)_2SnCl_6$  is assumed to be the solid adduct which was isolated from melt solution. This solid did not exhibit a sharp melting point. At  $\sim 30^\circ C$ , part of the solid (sealed in a capillary tube) melted, while the remaining solid melted at ca.  $100^\circ C$ . Since the reported melting point of  $(BP)AlCl_4$  is  $32^\circ C$  (212), it is likely that the solid is a double salt.

The results of elemental analyses of the solid by Galbraith Laboratories are given in Table 34.

Considering that the percentage of hydrogen is larger than expected, and that the analyses do not sum to 100%, it is considered likely that the sample was contaminated with moisture. Since the sample was never exposed to the atmosphere prior to sealing under high vacuum ( $\leq 10^{-5}$  torr), it is believed that the water contamination took place when the analyses were performed. Assuming that the missing 11.5% is due to oxygen from the water contaminant, the formula which is in best agreement with the reported analytical results is  $4.5 (BP)AlCl_4 \cdot (BP)_2SnCl_6 \cdot 16H_2O$ .

## B.2. Acidic Melt Solutions

Of the salts listed in Table 33, only  $CdCl_2$  was found to be soluble (at 3.95 mol%) in acidic melt at  $25^\circ C$ . Dispersions of the other salts ( $PbCl_2$ ,  $SnCl_2$ ,  $HgCl_2$ ,  $CuCl$ , and  $ZnCl_2$ ) remained heterogeneous after six months of conditioning. It is believed that the solubility of  $CdCl_2$  in this medium results from the reaction of chloride ions from  $CdCl_2$  with  $Al_2Cl_7^-$  ions from the melt according to the reaction,

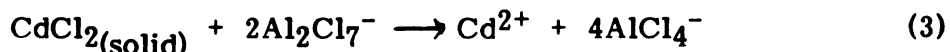


Table 34

**Elemental Analyses of the Solid Adduct of  $\text{SnCl}_4$  Isolated from  
Basic  $\text{AlCl}_3$ -BPCl Melt Solution**

<b>Element</b>	<b>Actual Composition<sup>(a)</sup></b>	<b>Theoretical Composition Based on <math>4.5(\text{BP})\text{AlCl}_4 \cdot</math> <math>(\text{BP})_2\text{SnCl}_6 \cdot 16\text{H}_2\text{O}</math></b>
C	29.38	31.18
H	6.02	5.01
N	3.93	4.04
Al	5.03	5.39
Sn	4.81	5.27
Cl	39.36	37.76
O	--	11.36
Total	88.52	100.01

(a) All values are given as wt%

## C. Solution NMR Studies

### C.1. Cadmium-113 NMR

A single  $^{113}\text{Cd}$  NMR resonance line was observed in all basic melt solutions of  $\text{CdCl}_2$  at  $40^\circ\text{C}$ . The chemical shift of this signal is +466 ppm vs. 0.1 M  $\text{Cd}(\text{ClO}_4)_2$  in water ( $\delta_{\text{obs}} = +373$  ppm vs. 0.5 M  $\text{CdCl}_2$  in  $\text{D}_2\text{O}$ ), and was observed to be independent of  $\text{CdCl}_2$  concentration in basic melt solutions. A typical  $^{113}\text{Cd}$  NMR spectrum for these solutions is shown in Figure 48. Mennitt et al. (213) have obtained the  $^{113}\text{Cd}$  CP/MAS NMR spectra for 27 solid complexes of the  $\text{Cd}^{2+}$  ion, to establish benchmarks for the shielding of this nucleus as a function of the number and type of donor atoms in various coordination geometries. These workers obtained chemical shifts for bis(tetraethylammonium) tetrachlorocadmiate ( $\delta = +483$  ppm) and thiaminium tetrachlorocadmiate ( $\delta = +460$  ppm). The similarity of these shifts to that observed for  $\text{CdCl}_2$  in basic melts strongly suggests that the  $\text{CdCl}_4^{2-}$  complex is the principal cadmium species in these solutions. The noted constancy of chemical shifts for the signals in  $\text{CdCl}_2$ -basic melt solutions is attributable to the fact that none of these solutions had a ratio of melt chloride ion to  $\text{CdCl}_2$  of less than 2.5:1. Thus, a  $^{113}\text{Cd}$  NMR signal for the  $\text{CdCl}_3^-$  complex ( $\delta = +296$  ppm; (119)) was not observed.

Several attempts were made to displace the chloride ions from the  $\text{CdCl}_4^{2-}$  complex by the addition of crown ethers or cryptands to  $\text{CdCl}_2$ -basic melt solutions; ie., to affect macrocyclic complexation of the  $\text{Cd}^{2+}$  ion such as was done with the lithium ion in basic melt (see Chapters III and IV). No new  $^{113}\text{Cd}$  NMR signals were observed on additions of these ligands. However, an appreciable (ca. 10 to 30%) reduction in the S/N ratio for the  $^{113}\text{Cd}$  signal for the chlorocomplex was observed for these samples. These results are interpreted as indicating that some interaction of the ligands with the  $\text{Cd}^{2+}$

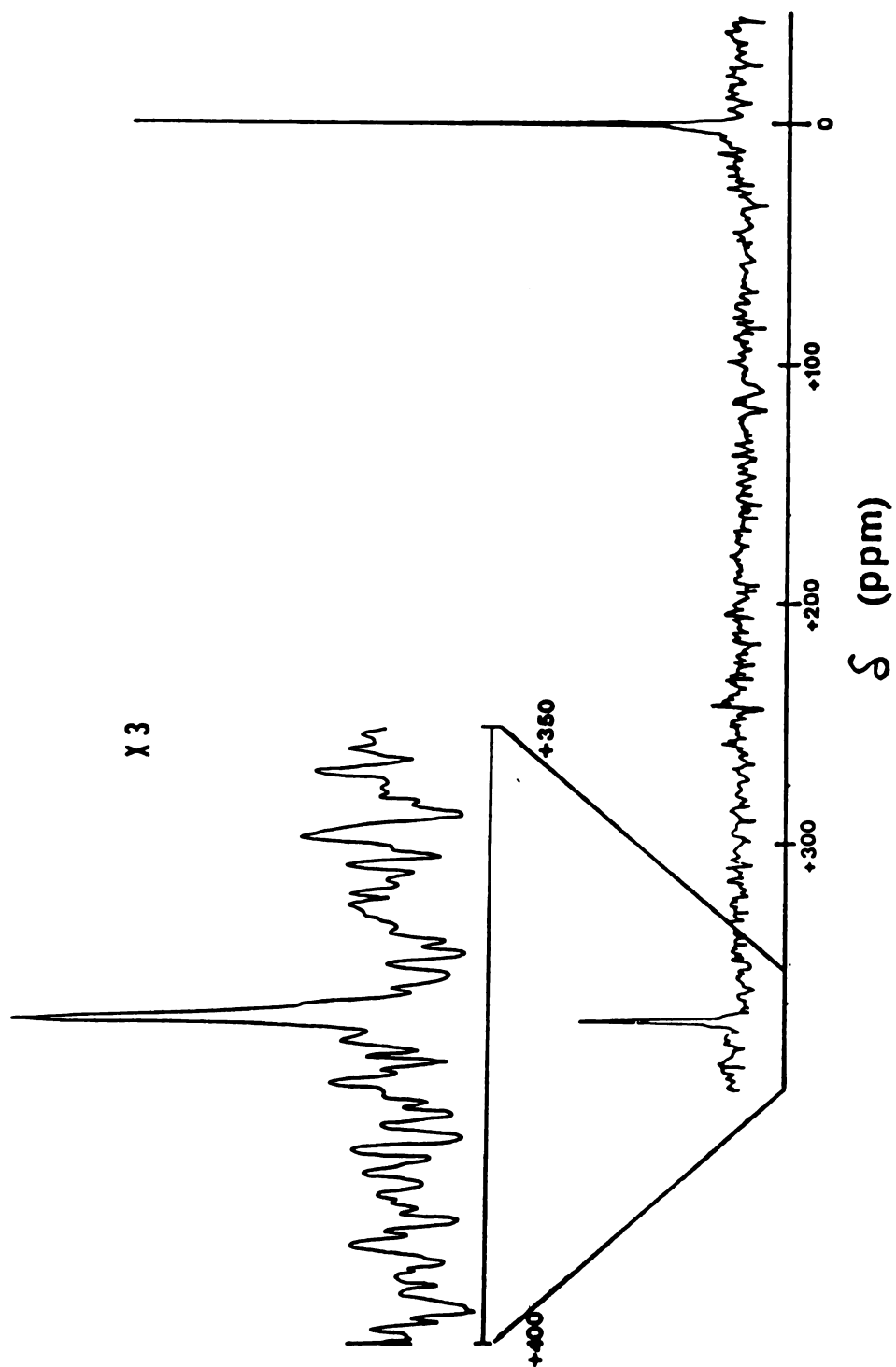


Figure 48. Cadmium-113 NMR Spectrum: 2.88 Mol%  $\text{CdCl}_2$  in Basic  $\text{AlCl}_3$ -BPCl Melt at  $40^\circ\text{C}$ . Chemical Shifts are Scaled to 0.5 M  $\text{CdCl}_2/\text{D}_2\text{O}$  Taken as 0.0 ppm.

ion is occurring in these solutions. Observation of  $^{113}\text{Cd}$  NMR signals for the cadmium macrocyclic complexes is apparently not possible due to fast multi-site chemical exchange between  $\text{CdCl}_4^{2-}$ , all intermediate chlorocadmium species, and the macrocyclic complexes.

In acidic melt, a  $^{113}\text{Cd}$  NMR signal was observed at  $\delta = +117$  ppm (+24 ppm vs. 0.5 M  $\text{CdCl}_2/\text{D}_2\text{O}$ ; Figure 49). It is interesting to note that this shift position falls within the range which is loosely defined as the octahedral coordination region (ca. +100 ppm to -40 ppm vs. 0.1 M  $\text{Cd}(\text{ClO}_4)_2/\text{H}_2\text{O}$ ) for  $^{113}\text{Cd}$  chemical shifts (214). This empirical correlation of  $^{113}\text{Cd}$  chemical shifts with coordination geometry is supported by the theoretical calculations of Nakatsuji and co-workers (215). They found that the diamagnetic and paramagnetic terms of the nuclear shielding constant for the  $\text{Cd}(\text{H}_2\text{O})_6^{2+}$  ion ( $\text{O}_h$  symmetry) cancel, such that the chemical shift of this species is zero. With its 2+ charge and the presence of  $\text{Al}_2\text{Cl}_7^-$  ions in acidic melt, octahedral coordination of the cadmium ion by two or more  $\text{Al}_2\text{Cl}_7^-$  ions in this medium seems plausible.

### C.2. Tin-119 and Tin-117 NMR

A single  $^{119}\text{Sn}$  NMR resonance line was observed for basic melt solutions of  $\text{SnCl}_2$  at 25°C, with chemical shifts insensitive to  $\text{SnCl}_2$  concentration. For 3.29 mol%  $\text{SnCl}_2$  in basic melt, the chemical shift of the signal was +9.1 ppm downfield from neat  $\text{SnCl}_4$  (-140.9 ppm vs.  $(\text{CH}_3)_4\text{Sn}$  primary standard), with a linewidth of 24 ( $\pm 1$ ) Hz (Figure 50). The width of this line increased to 92 Hz at 40°C. The signal for 0.955 mol%  $\text{SnCl}_2$ -basic melt solution was broader (75 Hz) than that observed for the 3.29 mol%  $\text{SnCl}_2$  solutions. This indicates that fast chemical exchange among several tin species in solution is occurring. The ratios of melt chloride ion/ $\text{SnCl}_2$  in these two samples is 3:1 for 3.29 mol%  $\text{SnCl}_2$ , and 10.5:1 for the 0.955 mol%  $\text{SnCl}_2$  solutions. The

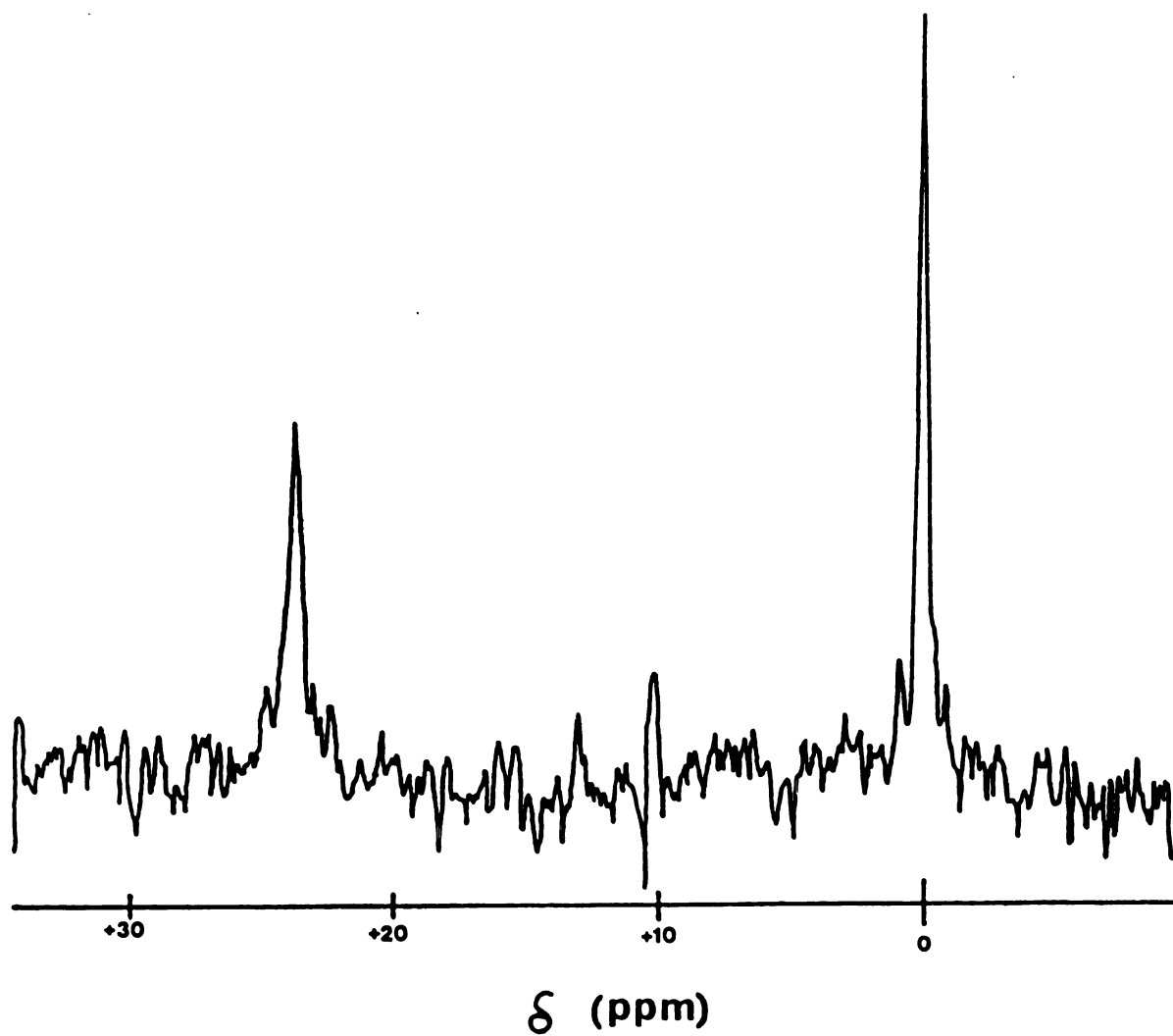


**Figure 49.** Cadmium-113 NMR Spectrum: 3.95 Mol% CdCl<sub>2</sub> in Acidic AlCl<sub>3</sub>-BPCl melt at 40°C. Chemical Shifts are Scaled as in Figure 48.

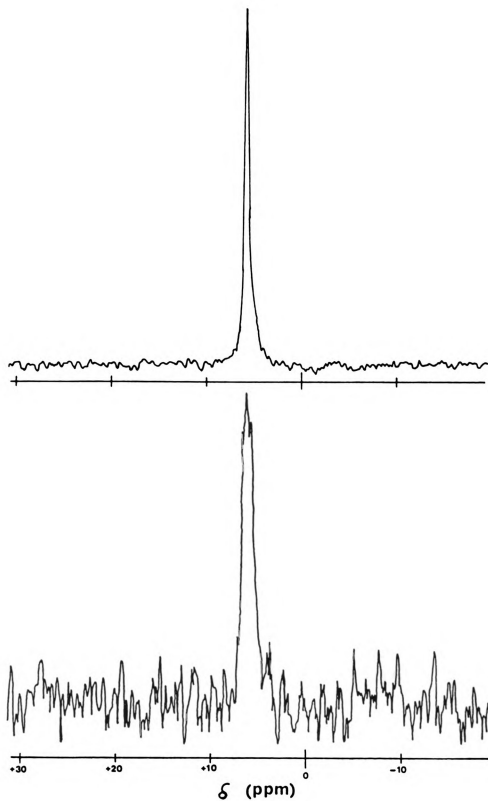


**Figure 50.** Tin-119 NMR Spectra: 3.29 Mol%  $\text{SnCl}_2$  (A) and 0.955 Mol%  $\text{SnCl}_2$  (B) in Basic  $\text{AlCl}_3$ -BPCl Melt.



observed broadening at the higher  $\text{Cl}^-_{(\text{melt})}/\text{SnCl}_2$  ratio indicates possible formation of the  $\text{SnCl}_4^{2-}$  chlorocomplex, or the polymerized  $(\text{SnCl}_2)_n$  species.

The  $^{117}\text{Sn}$  NMR spectrum for the 3.29 mol%  $\text{SnCl}_2$ -basic melt sample is shown in Figure 51. Because of the slight receptivity advantage of the  $^{119}\text{Sn}$  nucleus ( $R_{^{119}\text{Sn}}/R_{^{117}\text{Sn}} = 1.3$ ), no further studies of the  $^{117}\text{Sn}$  nucleus were pursued. However, it is interesting to note that the linewidth for the  $^{119}\text{Sn}$  signal for this sample is ca. 1.1 times that of the  $^{117}\text{Sn}$  NMR signal (24 vs. 22 Hz ( $\pm 1$  Hz) at  $25^\circ\text{C}$ ). Assuming that the spin-lattice relaxation process is dominated by the intramolecular dipole-dipole mechanism (216), and further, that the motional narrowing limit ( $T_1 = T_2$ ) obtains,

$$\nu_{1/2}^{\text{obs.}} = \frac{1}{\pi T_2^{\text{obs}}} = \frac{1}{\pi T_1} = \frac{\mu_0^2 \gamma_I^2 \gamma_S^2 h^2 S(S+1) \tau_c}{12\pi^2 r_{I-S}^6} \quad (4)$$

Therefore, the ratio of the linewidths of the  $^{119}\text{Sn}$  and  $^{117}\text{Sn}$  NMR signals is proportional to the ratio of the square of the respective magnetogyric ratios as,

$$1/T_{2[119]}^{\text{obs.}} = 1/T_{2[117]}^{\text{obs.}} = \Delta\nu_{1/2}^{^{119}\text{Sn}} / \Delta\nu_{1/2}^{^{117}\text{Sn}} = \gamma_{^{119}\text{Sn}}^2 / \gamma_{^{117}\text{Sn}}^2 \quad (5)$$

Using the magnetogyric ratios from Table 8 (Chapter II), a value of 1.1 is obtained from equation (5). Thus, it appears that the intramolecular dipolar mechanism does dominate the relaxation rates for both of these nuclei in this molten salt system.

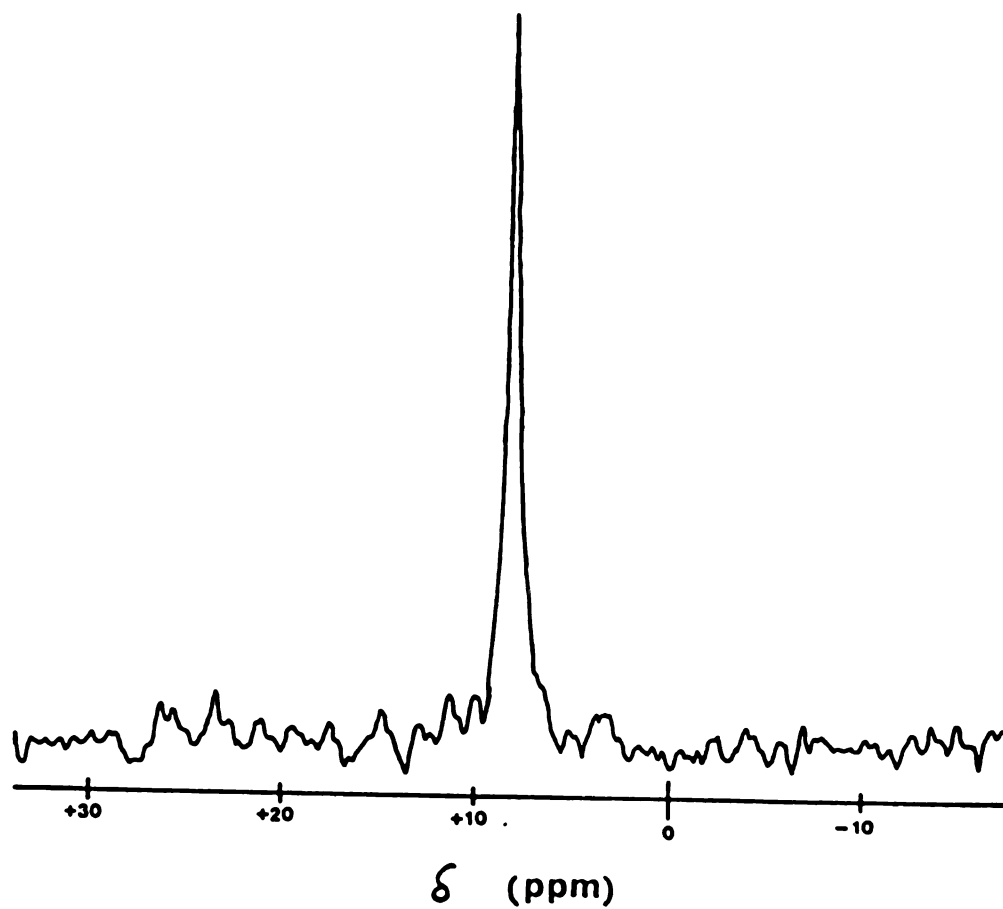


**Figure 51. Tin-117 NMR Spectrum: 3.29 Mol%  $\text{SnCl}_2$  in Basic  $\text{AlCl}_3$ -BPCl Melt.**

### C.3 Zinc-67 NMR

Detection of this nucleus in  $\text{ZnCl}_2$ -basic melt solutions was very difficult due to its low receptivity ( $R_{\text{vs. } ^{13}\text{C}} = 0.665$ ), and the sample configuration required in these experiments. Severe rf pulse attenuation was incurred in traversing the 10 mm dead space between the Helmholtz coil of the 20 mm probe and the 10 mm/5 mm (sample) coaxial NMR tube arrangement. The high concentration (1 M  $\text{Zn}(\text{NO}_3)_2$  in  $\text{D}_2\text{O}$ ) of the external reference solution further attenuated the pulse as well as the signals returning from the sample. By reducing the word size in the computer memory block from 12 to 6 bits (to prevent overflow of the A-D converter), and scanning for 48 hours ( $\sim 10^5$  scans), a very weak  $^{67}\text{Zn}$  NMR signal was obtained for 1.56 mol%  $\text{ZnCl}_2$  in basic melt (Figure 52).

The chemical shift of this signal is ca. +305 ppm downfield from the external reference solution. This result is in fair agreement with the value of +257 ppm for  $\text{ZnCl}_4^{2-}$  in aqueous solution obtained by Maciel and co-workers (118). No further experiments were performed on this nucleus in basic melt because of the extremely long acquisition times, and the poor quality of spectra obtained.

### C.4. Mercury-199 NMR

Mercury-199 NMR signals were obtained in nine  $\text{HgCl}_2$ -basic melt solutions at 25°C. Chemical shifts of these signals are listed in Table 35, and the chemical shift behavior as a function of  $\text{HgCl}_2$  concentration is depicted in Figure 53. A chemical shift range of ca. 250 ppm is spanned from 9.53 mol%  $\text{HgCl}_2$  to 0.77 mol%  $\text{HgCl}_2$  in the basic melt solutions. This concentration dependence of the chemical shift seems to indicate the presence of at least two complex sites for mercury in fast chemical exchange (one population-averaged NMR signal). An equilibrium which could account for this chemical shift behavior is,

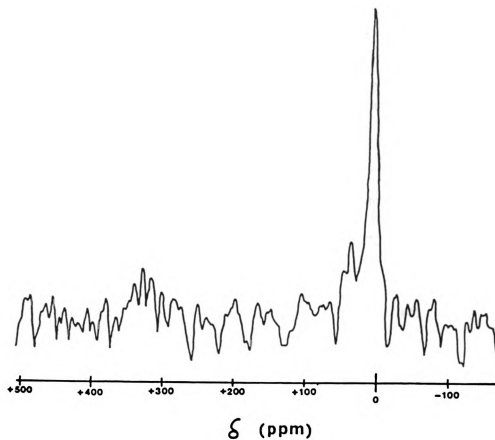


**Figure 52. Zinc-67 NMR Spectrum: 1.56 Mol%  $\text{ZnCl}_2$  in Basic  $\text{AlCl}_3\text{-BPCl}$  Melt.**

**Table 35**  
**Mercury-199 NMR Chemical Shift Data for**  
**HgCl<sub>2</sub>-Basic AlCl<sub>3</sub>-BPCl Melt Solutions**

<b>Mol% HgCl<sub>2</sub></b>	<b>Chemical Shift (ppm)(a)</b>
0.772	+ 611
3.99	+ 472
4.65	+ 460
5.79	+ 414
7.00	+ 383
7.57	+ 369
9.01	+ 358
9.30	+ 353
9.53	+ 348

(a) Chemical shift uncertainty is estimated at  $\pm 3$  ppm.

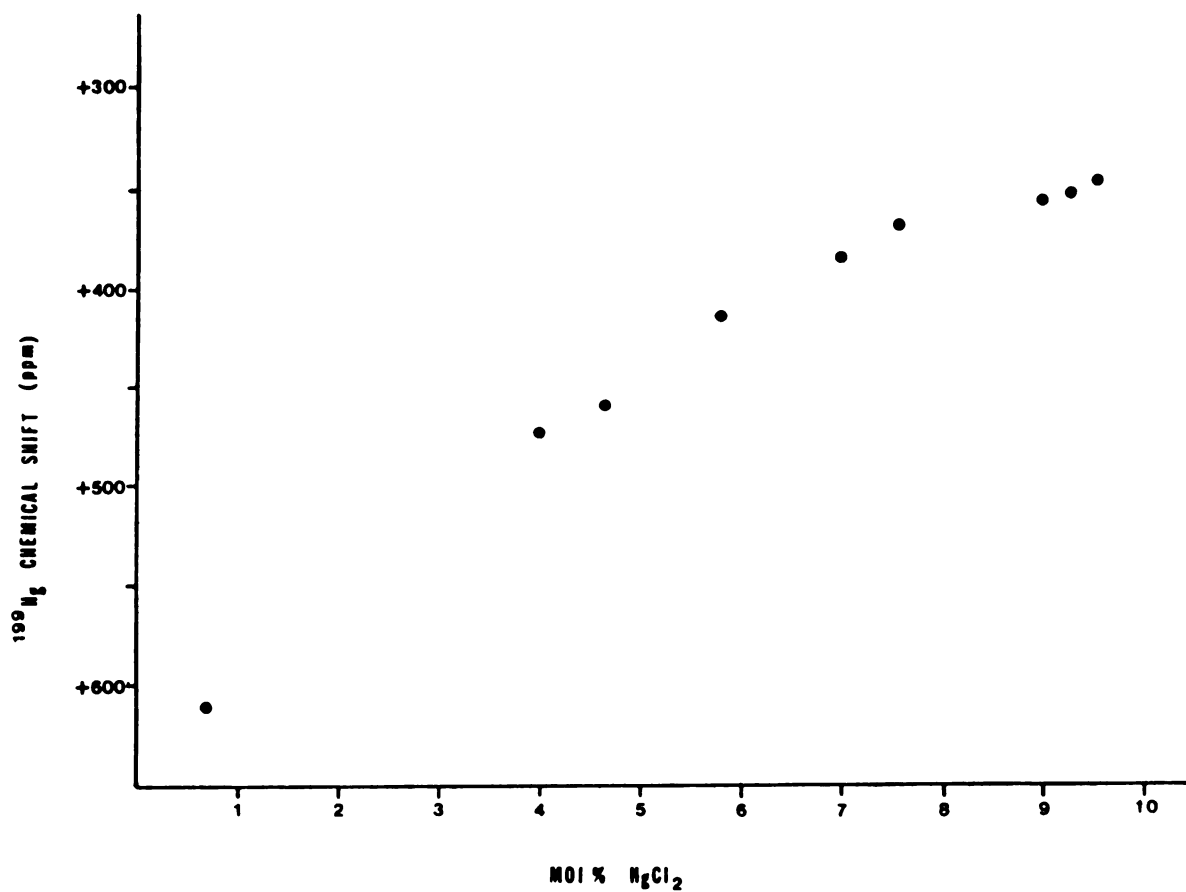


**Figure 53. Mercury-199 NMR: Chemical Shifts Versus Mol%  $\text{HgCl}_2$  in Basic  $\text{AlCl}_3$ -BPCl Melts.**



In view of the known  $\text{Cl}^-_{(\text{melt})}/\text{HgCl}_2$  ratio for these solutions, it is likely that the downfield NMR signals correspond to the predominant population of the  $\text{HgCl}_4^{2-}$  complex, and the upfield signals to the  $\text{HgCl}_3^-$  complex.

### C.5. Copper-63 and Lead-207 NMR

All attempts to detect  $^{63}\text{Cu}$  NMR signals in  $\text{CuCl}$ -basic melt solutions, and aqueous and nonaqueous solutions of  $\text{CuCl}$  were unsuccessful. Disproportionation of  $\text{Cu}^+$  to  $\text{Cu}^0$  and  $\text{Cu}^{2+}$  is suspected as the cause for no NMR signals for 1 M  $\text{K}_3\text{Cu}(\text{CN})_4$  (1 M  $\text{CuCN}$  with 3 M  $\text{KCN}$ ) solutions in  $\text{D}_2\text{O}$ , acetonitrile, and pyridine, since these solutions turned black within 2 to 3 hours of preparation. The reason for a lack of  $^{63}\text{Cu}$  NMR signals in  $\text{CuCl}$ -basic melt solutions is not clear. The yellow color of these solutions suggests that oxidation of  $\text{Cu}^+$  may have occurred with reduction of the pyridinium ion in a reaction similar to that described in Chapter II, section A.4.a. In any event, the 2+ oxidation state renders the  $^{63}\text{Cu}$  nucleus unobservable.

No  $^{207}\text{Pb}$  NMR signals were observed for  $\text{PbCl}_2$  or  $\text{Pb}(\text{NO}_3)_2$  in basic or acidic melt mixtures, after a systematic search from +5000 to -5000 ppm vs. 0.2 M  $\text{Pb}(\text{NO}_3)_2$  in  $\text{D}_2\text{O}$ . Since no difficulty was encountered in obtaining a  $^{207}\text{Pb}$  NMR signal for the external reference solution, it seems clear that lead salts are virtually insoluble in basic or acidic  $\text{AlCl}_3$ - $\text{BPCl}$  melts.

### D. Far-IR Measurements of Heavy Metal Salt-Basic $\text{AlCl}_3$ - $\text{BPCl}$ Melt Mixtures

In the far-IR region ( $150\text{--}600\text{ cm}^{-1}$ ), the spectrum of pure basic melt is dominated by the  $\nu_3(\text{F}_2)$  and  $\nu_4(\text{F}_2)$  normal vibrational modes of the  $\text{AlCl}_4^-$

ion (Figure 54). A summary of the results with band assignments (from Gale and Osteryoung, (53)), is shown in Table 36. The assignment of the  $\nu_4(F_2)$  and ( $184\text{ cm}^{-1}$ ) is made based on the Raman study of basic melt by Gale et al. (49). The  $\nu_1(A_1)$  band at  $345\text{ cm}^{-1}$  (Figure 54, part B) is barely discernable from the background absorption, even with the larger spacer size. Aside from this weak band, the region between  $200\text{ cm}^{-1}$  and  $450\text{ cm}^{-1}$  is essentially featureless, enabling observation of heavy metal-chlorine vibrational bands.

The far-IR spectra of basic melt solutions of  $\text{CdCl}_2$ ,  $\text{ZnCl}_2$ ,  $\text{CuCl}$ ,  $\text{HgCl}_2$ , and  $\text{SnCl}_2$  are shown in Figure 55. Band frequencies and assignments from the literature are given in Table 37.

In the Raman studies of Davies and Long (217) and Delwaulle (200), values of  $260\text{ cm}^{-1}$  and  $250\text{ cm}^{-1}$  were reported for the  $\nu_1(A_1)$  mode of the  $\text{CdCl}_4^{2-}$  chlorocomplex in aqueous solutions. However, in a far-IR study by Adams et al. (218), the band observed at  $260\text{ cm}^{-1}$  for  $\text{CdCl}_2$  in thionyl chloride was assigned to the  $\nu_3(F_2)$  mode. While it is possible that ionic associations in basic melt solutions could produce a perturbation strong enough to enable observation of a  $\nu_1(A_1)$  band for  $\text{CdCl}_4^{2-}$  in the far-IR (as was observed for the  $\text{AlCl}_4^-$  ions), it is unlikely that this band would be as intense as the IR-active  $\nu_3(F_2)$  mode. For this reason, the assignment made in Table 37, for the  $\text{CdCl}_4^{2-}$  species is favored. The band due to a lattice-like vibration of the  $(\text{CdCl}_2)_n$  polymeric species is expected to be at  $240\text{ cm}^{-1}$  (217). No such band was seen in the  $\text{CdCl}_2$ -basic melt solution. The  $\nu_3(E')$  mode for  $\text{CdCl}_3^-$  is expected to appear at ca.  $290\text{ cm}^{-1}$  (217). However, no such band was observed in the basic melt solution of  $\text{CdCl}_2$ . Due to the very poor quality of spectra obtained below  $150\text{ cm}^{-1}$ , the anticipated  $\nu_4(F_2)$  band for  $\text{CdCl}_4^{2-}$  could not be observed.

The frequency of the band observed in the  $\text{ZnCl}_2$ -basic melt solution is in good agreement with those identified for the  $\text{ZnCl}_4^{2-}$  complex ion in previous



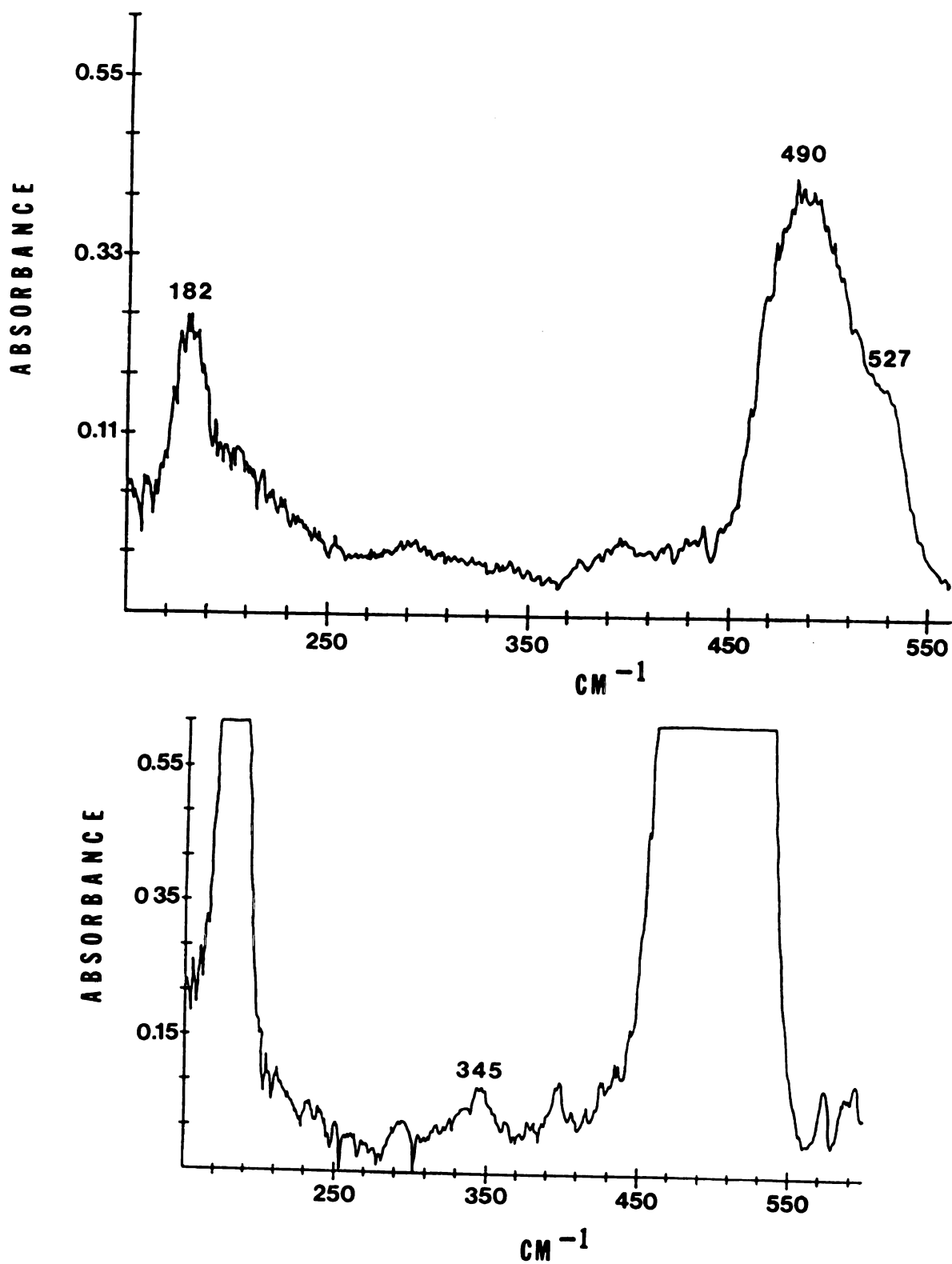
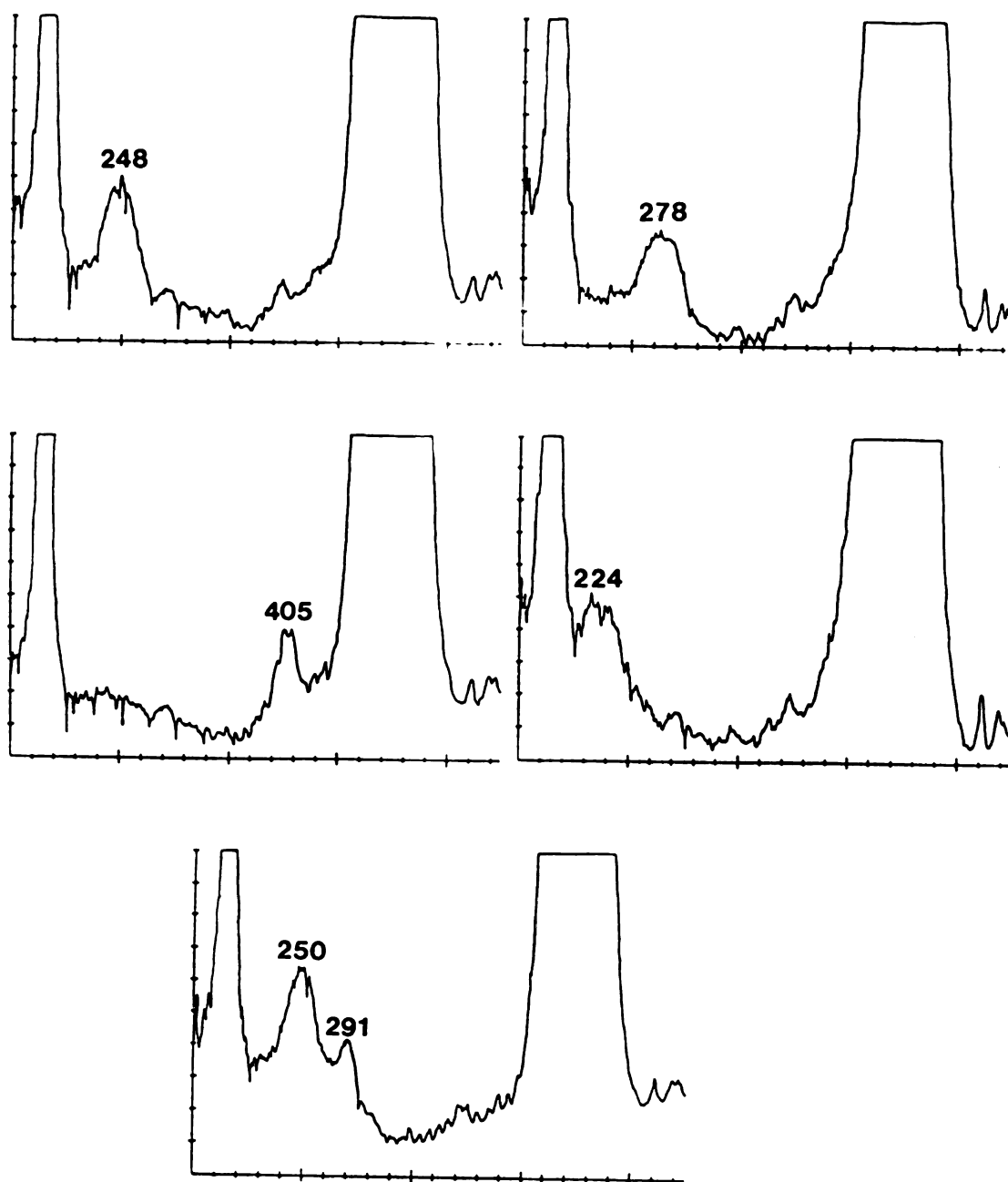


Figure 54. Far-IR Spectrum (150 to 600 cm<sup>-1</sup>): Basic AlCl<sub>3</sub>-BPCl Melt; (A) - 0.05 mm Spacer (B) - 0.1 mm Spacer.

Table 36

**Far-IR Bands and Assignments for the Normal Mode Vibrations  
of the  $\text{AlCl}_4^-$  Ion in Basic  $\text{AlCl}_3$ -BPCl Melt**

<b>This Work</b>	<b>Gale and Osteryoung<sup>(a)</sup></b>	<b>Assignment</b>
345	353	$\nu_1(\text{A}_1)$
--	476	
490	490	$\nu_3(\text{F}_2)$
527	525	
184	--	$\nu_4(\text{F}_2)$
(a) Reference 48.		



**Figure 55. Far-IR Spectra (150 to 600  $\text{cm}^{-1}$ ): Basic  $\text{AlCl}_3$ -BPCl Melt Solutions of Heavy Metal Chlorides; (A) - 2.98 Mol%  $\text{CdCl}_2$ , (B) - 1.56 Mol%  $\text{ZnCl}_2$ , (C) - 6.66 Mol%  $\text{CuCl}$ , (D) - 2.37 Mol%  $\text{HgCl}_2$ , (E) - 3.29 Mol%  $\text{SnCl}_2$ .**

Table 37

**Far-IR Studies of Heavy Metal Chloride - Basic  $\text{AlCl}_3$ -BPCl Melt Solutions:  
Band Frequencies and Assignments**

<b>Melt(a) Solution</b>	<b>Moles <math>\text{Cl}^-</math> (melt)/ Moles Solute</b>	<b><math>\bar{\nu}_{\text{obs.}}</math> (<math>\text{cm}^{-1}</math>)</b>	<b>Mode</b>	<b>Species</b>	<b>Symmetry</b>
2.98% $\text{CdCl}_2$	1.7	248	$\nu_3$ ( $\text{F}_2$ )	$\text{CdCl}_4^{2-}$	$\text{T}_d$
3.29% $\text{SnCl}_2$	1.5	250	$\nu_3$ (E)	$\text{SnCl}_3^-$	$\text{C}_{3v}$
		291	$\nu_1$ ( $\text{A}_1$ )		
2.37% $\text{HgCl}_2$	2.1	224	$\nu_3$ ( $\text{F}_2$ )	$\text{HgCl}_4^{2-}$	$\text{T}_d$
6.66% $\text{CuCl}$	0.76	405	$\nu_3$ ( $\Sigma^+$ )	$\text{CuCl}_2^-$ or	$\text{D}_{\infty h}$
				$\text{Cu}_2\text{Cl}_3^-$	?
1.56% $\text{ZnCl}_2$	3.3	278	$\nu_3$ ( $\text{F}_2$ )	$\text{ZnCl}_4^{2-}$	$\text{T}_d$

(a) mol%

studies (207-209). The  $\nu_4(F_2)$  mode for this species is expected to occur at ca.  $130\text{ cm}^{-1}$  (209), and could not be measured for the reasons just given. Irish and co-workers (219) have assigned the Raman band at  $230\text{ cm}^{-1}$  in  $\text{ZnCl}_2$  aqueous solutions to the bridge Zn-Cl stretching vibration of the  $(\text{ZnCl}_2)_n$  polymeric species. Since no band was observed near this frequency for the  $\text{ZnCl}_2$ -basic melt solution, the existence of this polymeric ion in this solution is considered to be unlikely.

The assignment of the  $405\text{ cm}^{-1}$  band in the CuCl-basic melt solution to the  $\nu_3(\Sigma^+)$  mode of the linear  $\text{CuCl}_2^-$  ion is consistent with IR and Raman studies of CuCl in nonaqueous solutions (25,204). However, Axtell *et al.* (33) have noted that the only difference in the far-IR spectra for triethylphosphonium chloride (TEPCl)-CuCl mixtures at the 1:1 ( $\text{CuCl}_2^-$ ) and 1:2 ( $\text{Cu}_2\text{Cl}_3^-$ ) mole ratios, is that the  $405\text{ cm}^{-1}$  band broadens slightly at the latter mole ratio versus the former one. The  $\nu_{2a/2b}$  modes (ca.  $109\text{ cm}^{-1}$  (25)) are outside the accessible spectral window of this work.

Two different chlorocomplexes of  $\text{Hg}^{2+}$  ion,  $\text{HgCl}_3^-$  and  $\text{HgCl}_4^{2-}$ , are possible for  $\text{HgCl}_2$  in basic melt. For the  $D_{3h}$  structure of  $\text{HgCl}_3^-$ , three IR-active modes ( $\nu_2(A'')$ ,  $\nu_3(E')$ ,  $\nu_4(E')$ ) and three Raman-active modes ( $\nu_1(A')$ ,  $\nu_3(E')$ ,  $\nu_4(E')$ ) are predicted (222). For the  $C_{3v}$  geometry, all four fundamental vibrations are allowed in the IR and Raman spectra.

In a Raman study of molten  $\text{HgCl}_2$ -(KCl or  $\text{NH}_4\text{Cl}$ ) mixtures by Janz and James (201), the  $\nu_4(E')$  band was observed at  $223\text{ cm}^{-1}$  for 45 mol%  $\text{HgCl}_2$ -55 mol% KCl melt at  $580^\circ\text{C}$ . These authors favored the planar arrangement for the  $\text{HgCl}_3^-$  ion based on the fact that this structure would enable maximum separation of the three chlorine atoms in the complex. In addition, the  $\nu_3(E')$  mode was observed for this melt at  $270\text{ cm}^{-1}$ . This band (which is also IR-active) is not observed in the  $\text{HgCl}_2$ -basic melt solution. The  $\nu_3(E')$  mode has been

observed at  $263\text{ cm}^{-1}$  in the IR spectrum of  $\text{Me}_3\text{SHgCl}_3$  by Biscarini et al. (202). The reliability of the assignment for this vibration is excellent since the crystal structure of the compound was reported in this work, confirming the planar  $\text{HgCl}_3^-$  ion.

Adams et al. (218) have assigned the band at  $228\text{ cm}^{-1}$  in the far-IR spectrum of tetraethylammonium tetrachloromercurate to the  $\nu_3(\text{F}_2)$  mode of the  $\text{HgCl}_4^{2-}$  ion. Deacon and co-workers (199) observed this mode at  $225\text{ cm}^{-1}$ . Thus, it appears that the band observed at  $224\text{ cm}^{-1}$  in the far-IR spectrum of 2.37 mol%  $\text{HgCl}_2$  in basic melt is due to the  $\nu_3(\text{F}_2)$  mode of the  $\text{HgCl}_4^{2-}$  complex.

Only Raman spectroscopic data are available for comparison with the results obtained for  $\text{SnCl}_2$  in basic melt. Clarke and Solomons (198) assigned Raman bands at  $268\text{ cm}^{-1}$  and  $220\text{ cm}^{-1}$  to the  $\nu_1(\text{A}_1)$  and  $\nu_3(\text{E})$  modes, respectively, of the  $\text{SnCl}_3^-$  ion, in 1:1  $\text{SnCl}_2$ -KCl mixtures at 300 and  $600^\circ\text{C}$ . In ether extracts of aqueous acidified  $\text{SnCl}_2$  solutions, Woodward and Taylor (221) obtained  $297\text{ cm}^{-1}$  ( $\nu_1(\text{A}_1)$ ) and  $256\text{ cm}^{-1}$  ( $\nu_3(\text{E})$ ) for the  $\text{SnCl}_3^-$  species. In both of these studies, the bands for the  $\nu_2(\text{A}_1)$  and  $\nu_4(\text{E})$  modes were observed below  $150\text{ cm}^{-1}$ . In view of the diversity in band frequencies reported in these studies, the frequencies observed for the  $\text{SnCl}_2$ -basic melt solution (and their respective assignments) appear to be reasonable for the  $\text{SnCl}_3^-$  complex.

The mid- and far-IR spectra of the solid adduct of  $\text{SnCl}_4$  isolated from basic melt solution (section B.1) were obtained in a KBr pellet. In the mid-IR region ( $550$  to  $3500\text{ cm}^{-1}$ ), the spectrum retains virtually all bands attributable to the stretching and bending modes of the  $\text{BP}^+$  cation. These bands are shifted by as much as  $\pm 40\text{ cm}^{-1}$  in the  $\text{SnCl}_4$  adduct versus those observed for pure  $\text{BP}^+\text{Cl}$ . The largest deviations are observed for one of the out-of-plane ring

bending modes ( $765\text{ cm}^{-1}$  for the tin adduct vs.  $804\text{ cm}^{-1}$  for  $\text{BPCl}$ ), and the methylene group bending mode ( $676\text{ cm}^{-1}$  for the tin adduct vs.  $699\text{ cm}^{-1}$  for  $\text{BPCl}$ ). Although the background absorption is stronger for the tin adduct, no new features are observed in this region compared to  $\text{BPCl}$ .

In the far-IR region ( $200$  to  $515\text{ cm}^{-1}$ ), the S/N ratio for the spectrum of the  $\text{SnCl}_4$  adduct was poorer than that obtained for the heavy metal chloride-basic melt solutions. However, the  $\nu_3(\text{F}_2)$  band at  $496\text{ cm}^{-1}$  for the  $\text{AlCl}_4^-$  ion ( $490\text{ cm}^{-1}$  in basic melt), and two new bands centered at  $238\text{ cm}^{-1}$  and  $303\text{ cm}^{-1}$  were observed (Figure 56). Of the six normal modes of vibration for an octahedral  $\text{XY}_6$  molecule, only the  $\nu_3(\text{F}_{1u})$  and  $\nu_4(\text{F}_{1u})$  modes are predicted to be active in the infrared (222). The vibrational bands which have been reported in previous studies of the  $\text{SnCl}_6^{2-}$  ion in the solid state are listed in Table 38 as well as those observed for the  $\text{SnCl}_4$  adduct.

The assignment of the  $238\text{ cm}^{-1}$  band to the normally IR-forbidden  $\nu_2(\text{E}_g)$  mode is based on the supposition that in the solid state, the effect of the crystal lattice can perturb the normal mode vibrations so that the normal IR/Raman selection rules are violated. This effect has been observed previously (224) for an analogous tin compound  $(\text{NH}_4)_2\text{SnF}_6$ . In view of the width of the band at  $303\text{ cm}^{-1}$ , and the generally poor resolution of the spectrum, it is possible that the  $\nu_1(\text{A}_{1g})$  band (also supposedly IR-forbidden) also occurs near this frequency.

## E. Conclusions

Based on the evidence obtained from these NMR and far-IR studies of basic melt solutions of heavy metal chlorides, the following conclusions are made.

The NMR chemical shifts and far-IR band frequencies for  $\text{CdCl}_2$  and

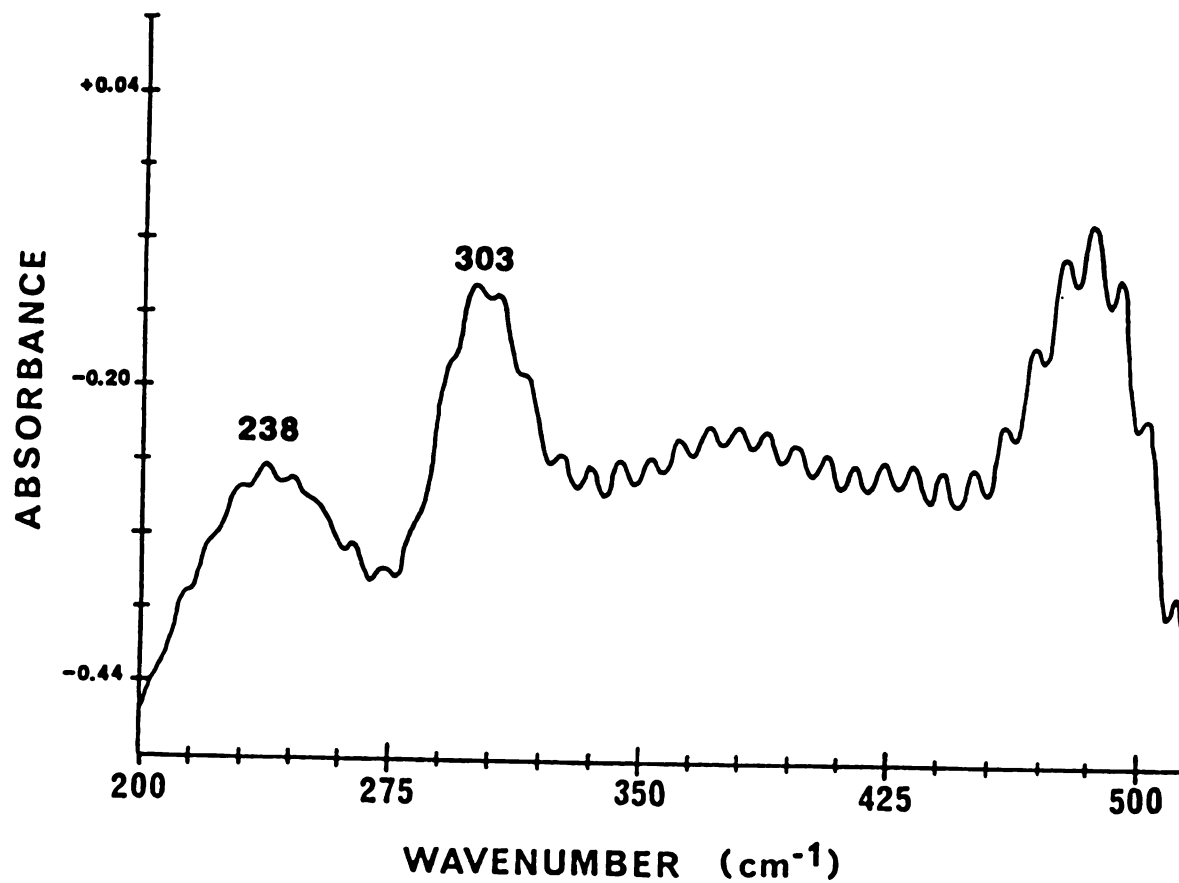


**Figure 56. Far-IR Spectrum (200 to 515  $\text{cm}^{-1}$ ): The  $\text{SnCl}_4$  Adduct Isolated from Basic  $\text{AlCl}_3$ -BPCl Melt Solution.**



Table 38

Raman and Far-IR Studies(a) of the  $\text{SnCl}_6^{2-}$  Chlorocomplex in the Solid State

Compound	Assignments				
	$\nu_1(A_{1g})(b)$	$\nu_2(E_g)(b)$	$\nu_3(F_{1u})(c)$	$\nu_4(F_{1u})(c)$	$\nu_5(F_{2g})(b)$
$\text{Rb}_2\text{SnCl}_6$	316	241	312	173	171
$(\text{Me}_4\text{N})_2\text{SnCl}_6$	307	--	298	172	--
$(\text{Et}_4\text{N})_2\text{SnCl}_6$	309	232	306 291	163	159
$(\text{Bu}_4\text{N})_2\text{SnCl}_6$	306	--	320 290	159	--
$\text{SnCl}_4$ Adduct from Basic Melt	--	238	303	--	--

(a) Reference 223  
 (b) Raman-allowed  
 (c) IR-allowed  
 (d) Forbidden

$\text{ZnCl}_2$ -basic melt solutions clearly support the supposition that the  $\text{CdCl}_4^{2-}$  and  $\text{ZnCl}_4^{2-}$  complex ions are the predominant species formed from the parent  $\text{MCl}_2$  salts. The existence of  $(\text{CdCl}_2)_n$  or  $(\text{ZnCl}_2)_n$  polymeric species is considered to be very unlikely.

The situation for  $\text{CuCl}$ -basic melt solutions is not as straightforward. It is likely that whatever its precise mechanism, the suspected charge transfer reaction is probably responsible for the inability to detect  $^{63}\text{Cu}$  NMR signals. The far-IR data indicate that either the  $\text{CuCl}_2^-$  or  $\text{Cu}_2\text{Cl}_3^-$  complex ions are possible in these solutions, although the former species is favored considering the ratio of free chloride ion to  $\text{CuCl}$  in the melt (see Table 37).

A more detailed  $^{199}\text{Hg}$  NMR study is required to test the validity of the fast chemical exchange model for the  $\text{HgCl}_3^-$  and  $\text{HgCl}_4^{2-}$  ions in basic melt solutions. The assignment of the  $224\text{ cm}^{-1}$  band observed in the  $\text{HgCl}_2$ -basic melt solution to the  $\text{HgCl}_4^{2-}$  complex is consistent with results reported in previous studies.

The constancy of  $^{119}\text{Sn}$  NMR chemical shifts with  $\text{SnCl}_2$  concentration in basic melt solutions, and the reasonable agreement of far-IR band frequencies with results from previous studies indicate that the  $\text{SnCl}_3^-$  chlorocomplex is the predominant tin species in these solutions.

The mid- and far-IR spectra of the  $\text{SnCl}_4$  adduct isolated from basic melt indicate that the  $\text{BP}^+$ ,  $\text{AlCl}_4^-$ , and  $\text{SnCl}_6^{2-}$  ions are the structural components of this material. Although the results of the elemental analyses were not completely satisfactory, the percentages of chlorine, tin, and aluminum in the sample are consistent with that expected for the  $\text{AlCl}_4^-$  and  $\text{SnCl}_6^{2-}$  ions.

## **CHAPTER VI**

### **SUGGESTIONS FOR FURTHER STUDIES**

### **A. Lithium Chlorocomplexes in Basic Melt**

Although it has been shown that the monomer-dimer ( $\text{LiCl}_2^-$  vs.  $\text{Li}_2\text{Cl}_4^{2-}$ ) equilibrium model satisfactorily accounts for the observed concentration dependence of the  $^7\text{Li}$  chemical shifts in basic melt, more information regarding the structure of these species and the nature of the lithium-chlorine bonds is required.

It is possible that the techniques of EXAFS (x-ray absorption fine structure spectroscopy) and XANES (x-ray absorption near edge structure spectroscopy) could be used to obtain this information. The structure of the  $\text{MnBr}_3^{2-}$  in molten  $(\text{Bu}_4\text{N})_2\text{MnBr}_3$  has been studied by using these methods (225). It has been shown that the  $\text{BP}^+$  ion can be observed in the gas phase by using the FAB (Fast Atom Bombardment) mass spectrometry method for the analysis of the  $\text{AlCl}_3\text{-BPCl}$  molten salt system (226). It is feasible that negative ions such as  $\text{AlCl}_4^-$ ,  $\text{Al}_2\text{Cl}_7^-$ , and, more importantly, the lithium chlorocomplexes in basic melt, could be observed by using this technique in the negative ion detection mode.

As a theoretical compliment to these experimental studies, a molecular dynamics calculation which models a dilute basic melt solution of  $\text{LiCl}$  would be useful to critically evaluate the coordination number of the lithium ion, and the distribution of the chloride ions (coordination geometry) about the lithium ion, which are implied in the monomer-dimer model.

### **B. Macrocyclic Complexation of the Lithium Ion and Other Alkali Metal Ions**

A detailed study of the kinetics of complexation of the lithium ion with C222 in basic melt by the NMR technique is clearly feasible, and may also be possible for the  $\text{Li}^+\text{-C2B22}$  system if the coalescence temperature for this

system is accessible. These studies would permit a quantitative measure of the effect of the benzene ring on the conformational flexibility of the C222 skeletal structure, through a comparison of the decomplexation rates for the  $\text{Li}^+$ -C222 and  $\text{Li}^+$ -C2<sub>B</sub>22 cryptates.

Considering the relative ease with which single crystals of the lithium cryptates were obtained from basic melt, it is feasible that the crown ether complexes of the lithium ion may be obtainable, as single crystals, by using the same method. In addition, crown ether or cryptate complexes of the sodium or cesium ions may be obtainable by first solubilizing the NaCl or CsCl salts in basic melt with the desired ligand, and then adding benzene to "salt out" the macrocyclic complexes.

### C. Heavy Metal Ion Chlorocomplex Formation

The qualitative results of this preliminary study demonstrate how vibrational spectroscopy and multinuclear NMR may be combined to identify discrete chlorocomplexes in the  $\text{AlCl}_3$ -BPCl system. Additional far-IR studies (including the region below  $150\text{ cm}^{-1}$ ) and Raman spectroscopy would enable a more complete analysis of the vibrational modes of these complexes. The observed high ( $> 9\text{ mol}\%$ ) solubility of  $\text{HgCl}_2$  in basic melt, and the sensitivity of  $^{199}\text{Hg}$  chemical shifts to  $\text{HgCl}_2$  concentration in this medium may be used to obtain the formation constant for the  $\text{HgCl}_4^{2-}$  ion. Far-IR studies at high and low  $\text{HgCl}_2$  concentrations could confirm the identity of the mercury chlorocomplexes assumed for the fast exchange modeling of the  $^{199}\text{Hg}$  NMR chemical shift data.

The potentiometric technique used in the study of lithium chlorocomplexes in basic melt is certainly applicable to the heavy metal complexes, to confirm the chloride ion/metal ion stoichiometry in these species. In addition, the

standard potentiometric method (by using Cs, Hg, Sn, etc. working electrodes of the first kind) could be used to determine the formation constants for the  $MCl_x^{(n-x)}$  complexes in basic melt.

## **APPENDICES**

## Appendix 1

### A. The Two-Site Fast Exchange Model for the Determination of Equilibrium Constants

The  $^7\text{Li}$  chemical shift data obtained from the studies of crown ether complexation of the lithium ion in basic melt were fitted, as a first approximation, to a simple two-site fast exchange model,



where formal charges are omitted. Then

$$K_F = C_{\text{ML}} / C_{\text{M}} \cdot C_{\text{L}} \quad (2)$$

and

$$\delta_{\text{obs}} = X_{\text{M}} \delta_{\text{M}} + X_{\text{ML}} \delta_{\text{ML}} \quad (3)$$

From the derivation by Bodner et al. (227), it can be shown that

$$\delta_{\text{obs}} = \left\{ (K_F C_{\text{M}}^{\text{t}} - K_{\text{f}} C_{\text{L}}^{\text{t}} - 1) + [(K_F C_{\text{L}}^{\text{t}} - K_{\text{f}} C_{\text{M}}^{\text{t}} + 1)^2 + 4 K_{\text{f}} C_{\text{M}}^{\text{t}}]^{1/2} \right\} \cdot \left\{ \frac{\delta_{\text{M}} - \delta_{\text{ML}}}{2 K_F} \right\} + \delta_{\text{ML}} \quad (3)$$

where  $C_{\text{M}}^{\text{t}}$  and  $C_{\text{L}}^{\text{t}}$  are the analytical concentrations of the metal ion and the crown ether, respectively.



In this expression,  $K_F$ ,  $\delta_M$ , and  $\delta_{ML}$  are the adjustable parameters whose final values are calculated by the KINFIT program, and  $C_L^+$  is the independent variable.

For the equilibrium between the monomer (M) and dimer (D) chlorocomplexes of the lithium ion,



$$K_D = D/M^2 \quad (6)$$

The analytical concentration of the lithium ion ( $C_M^t$ ) is given by

$$C_M^t = M + 2D \quad (7)$$

Solving (6) for D, and substituting into (7),

$$C_M^t = M + 4K_D M^2 \quad (8)$$

$$4K_D M^2 + M - C_M^t = 0 \quad (9)$$

Solving (9) and taking the positive root,

$$M = \frac{-1 + (1 + 8K_D C_M^t)^{1/2}}{4K_D} \quad (10)$$

Dividing (7) by  $C_M^t$

$$\frac{M}{C_M^t} + \frac{2D}{C_M^t} = 1 = X_M + X_D \quad (11)$$

thus,  $X_M = M/C_M^t$ .

For fast exchange between the monomer and dimer chlorocomplexes of the lithium ion,

$$\delta_{\text{obs}} = X_M \delta_M + X_D \delta_D \quad (12)$$

where  $\delta_M$  and  $\delta_D$  are the limiting chemical shifts of the monomer and dimer, respectively.

From (11),  $X_D = 1 - X_M$  and (21) becomes

$$\delta_{\text{obs}} = X_M (\delta_M - \delta_D) + \delta_D \quad (13)$$

$$\delta_{\text{obs}} = \frac{M(\delta_M - \delta_D)}{C_M^t} + \delta_D \quad (14)$$

Substituting (10) for M into (14),

$$\delta_{\text{obs}} = \frac{[(1 + 8K_D C_M^t)^{1/2} - 1] (\delta_M - \delta_D)}{4K_D C_M^t} + \delta_D \quad (15)$$

In this expression,  $\delta_M$ ,  $\delta_D$  and  $K_D$  are the adjustable parameters, and  $C_M^t$  is the independent variable. The  $(C_M^t, \delta_{\text{obs}})$  data set is entered for fitting by equation (15). The SUBROUTINE EQN listings in the KINFIT program for the calculations using equations (4) and (15) are given below.

SUBROUTINE EQN for the calculation of Li -crown complex formation constants; two-site fast exchange between free and complexed lithium ion.

```

SUBROUTINE EQN
COMMON KOUNT,ITAPE,JTAPE,IWT,LAP,XINCR,NOPT,NOVAR,NOUNK,X,U,ITMAX,
1WTX,TEST,I,AV,RESID,IAR,EPS,ITYP,XX,RXTYP,DX1,FOP,FO,FU,P,ZL,TO,E
2IGVAL,XST,T,DT,L,M,JJ,Y,DY,VECT,NCST,CONST,NDAT,JDAT,MOPT,LOPT,
3YYY,CONSTS
COMMON/FREDT/IMETH
COMMON/POINT/KOPT,JOPT,XXX
DIMENSION X(4,300),U(20),WTX(4,300),XX(4),FOP(300),FO(300),FU(300)
1,P(20,21),VECT(20,21),ZL(300),TO(20),EIGVAL(20),XST(300),Y(10),
2DY(10),CONSTS(50,16),NCST(50),ISMIN(50),RXTYP(50),DX1(50),IRX(50)
3,MOPT(50),LOPT(50),YYY(50),CONST(16),XXX(15)
GO TO (2,3,4,5,1,7,8,9,10,11,12)  ITYP
1 CONTINUE
ITAPE=60
JTAPE=61
RETURN
7 CONTINUE
NOUNK=3
NOVAR=2
RETURN
8 CONTINUE
RETURN
2 CONTINUE
U(2)=1.0E+02
1000 CONTINUE
A=U(2)*CONST(1)
B=U(2)*XX(1)
C=(U(3)-U(1))/(2.*A)
D=(B-A+1)**2
CALC=((A-B-1)+SQRT(D+4.*A))*C+U(1)
IF(IMETH.NE.-1) GO TO 35
RETURN
35 CONTINUE
RESID=CALC-XX(2)
RETURN
3 CONTINUE
RETURN
4 CONTINUE
RETURN
5 CONTINUE
IF(IMETH.NE.-1) GO TO 20
RETURN
20 CONTINUE
RETURN
9 CONTINUE

```

```
      RETURN  
10  CONTINUE  
      RETURN  
11  CONTINUE  
      RETURN  
12  CONTINUE  
      RETURN  
      END
```

SUBROUTINE EQN for the calculation of the lithium chlorocomplex dimerization constant; two-site fast exchange between the monomer and the dimer.

```

SUBROUTINE EQN
COMMON KOUNT,ITAPE,JTAPE,IWT,LAP,XINCR,NOPT,NOVAR,NOUNK,X,U,ITMAX,
1WTX,TEST,I,AV,RESID,IAR,EPS,ITYP,XX,RXTYP,DX1,FOP,FO,FU,P,ZL,TO,E
2IGVAL,XST,T,DT,L,M,JJJ,Y,DY,VECT,NCST,CONST,NDAT,JDAT,MOPT,LOPT,
3YYY,CONSTS
COMMON/FREDT/IMETH
COMMON/POINT/KOPT,JOPT,XXX
DIMENSION X(4,300),U(20),WTX(4,300),XX(4),FOP(300),FO(300),FU(300)
1,P(20,21),VECT(20,21),ZL(300),TO(20),EIGVAL(20),XST(300),Y(10),
2DY(10),CONSTS(50,16),NCST(50),ISMIN(50),RXTYP(50),DX1(50),IRX(50)
3,MOPT(50),LOPT(50),YYY(50),CONST(16),XXX(15)
GO TO (2,3,4,5,1,7,8,9,10,11,12)  ITYP
1 CONTINUE
ITAPE=60
JTAPE=61
RETURN
7 CONTINUE
NOUNK=3
NOVAR=2
RETURN
8 CONTINUE
RETURN
2 CONTINUE
U(1)=ABS(U(1))
ARG=1.0+8.0*U(1)*XX(1)
IF(U(1).EQ.0.00) GO TO 55
ALPH=(-1.0+SQRT(ARG))/4.0*U(1)*XX(1)
CALC=ALPH*(U(2)-U(3))+U(3)
GO TO 37
55 CALC=U(2)
37 CONTINUE
IF(IMETH.NE.-1) GO TO 35
RETURN
35 CONTINUE
RESID=CALC-XX(2)
RETURN
3 CONTINUE
RETURN
4 CONTINUE
RETURN
5 CONTINUE
IF(IMETH.NE.-1) GO TO 20
RETURN
20 CONTINUE
RETURN
9 CONTINUE

```

```
      RETURN  
10  CONTINUE  
      RETURN  
11  CONTINUE  
      RETURN  
12  CONTINUE  
      RETURN  
      END
```

## B. The Three-Site Fast Exchange Model for the Determination of Equilibrium Constants

The three-site fast exchange model is given as



where M is the  $\text{LiCl}_2^-$  monomer, D is the  $\text{Li}_2\text{Cl}_4^{2-}$  dimer, and  $K_D$  is the dimerization constant. In this case,

$$\delta_{\text{obs}} = X_M \delta_M + X_D \delta_D + X_{ML} \delta_{ML} \quad (18)$$

The values for  $K_D$ ,  $\delta_M$ , and  $\delta_L$  are entered as constants from the monomer-dimer equilibrium model (section A.). The adjustable parameters are  $K_F$  and  $\delta_{ML}$ , and  $C_M^t$  is the independent variable.

The procedure for this calculation is an iterative one, and is summarized as follows. For each concentration ( $C_M^t$ ) equation (10) is used to calculate a value for the monomer in solution (M). Complexation of the monomer by the crown ether is then assumed, and a new value for M ( $M'$ ) is calculated by first defining

$$B = K_F C_M^t + K_F M + 1 \quad (19)$$

$$B1 = 4K_F^2 C_M^t M \quad (20)$$

then,

$$M' = \frac{B - (B^2 - B_1)^{1/2}}{2K_F} \quad (21)$$

which is analogous to the quadratic root that appears in (13). The  $M'$  value is then entered into equation (6), and the difference between  $M'$  and  $M$  calculated. This process is continued until the change in  $M$  is less than  $10^{-6}$   $M$ , where convergence is assumed.

The SUBROUTINE EQN listing for this calculation is given below.



SUBROUTINE EQN for the calculation of Li -crown complex formation constants; three-site fast exchange between monomer and dimer lithium chlorocomplexes, and the crown-complexed lithium ion.

```

SUBROUTINE EQN
COMMON KOUNT,ITAPE,JTAPE,IWT,LAP,XINCR,NOPT,NOVAR,NOUNK,X,U,ITMAX,
1WTX,TEST,I,AV,RESID,IAR,EPS,ITYP,XX,RXTYP,DX1I,FOP,FO,FU,P,ZL,TO,E
2IGVAL,XST,T,DT,L,M,JJJ,Y,DY,VECT,NCST,CONST,NDAT,JDAT,MOPT,LOPT,
3YYY,CONSTS
COMMON/FREDT/IMETH
COMMON/POINT/KOPT,JOPT,XXX
DIMENSION X(4,300),U(20),WTX(4,300),XX(4),FOP(300),FO(300),FU(300)
1,P(20,21),VECT(20,21),ZL(300),TO(20),EIGVAL(20),XST(300),Y(10),
2DY(10),CONSTS(50,16),NCST(50),ISMIN(50),RXTYP(50),DX1I(50),IRX(50)
3,MOPT(50),LOPT(50),YYY(50),CONST(16),XXX(15)
GO TO (2,3,4,5,1,7,8,9,10,11,12)  ITYP
1 CONTINUE
ITAPE=60
JTAPE=61
RETURN
7 CONTINUE
NOUNK=2
NOVAR=2
RETURN
8 CONTINUE
RETURN
2 CONTINUE
U(1)=ABS(U(1))
CN=-1+SQRT(1+8.*CONST(1)*CONST(2))
CM=CN/(4.*CONST(2))
CD=(CONST(1)-CM)/2.
IF(XX(1).EQ.0.00) GO TO 1500
2000 CONTINUE
B=U(1)*XX(1)+U(1)*CM+1.0
B1=4.0*(U(1)**2.)*XX(1)*CM
B2=(B-SQRT((B**2.)-B1))/2.*U(1))
FREEL=XX(1)-B2
FREED=CM-B2
IF(FREED.LT.0.00)FREED=0.0
C=2.*CONST(2)*FREED+1
C1=(C**2.)-4.*(CONST(2))*((CONST(2))*(FREED**2.)-CD)
FCHANG=(C-SQRT(C1))/2.*CONST(2)
CD=CD+FCHANG
FREED=FREED-FCHANG
FCHANG=ABS(FCHANG)
IF(FCHANG.LT.0.000001) GO TO 1000
CM=FREED+(XX(1)-FREEL)
GO TO 2000

```

```
1000 CONTINUE
      XM=FREED/CONST(1)
      XD=(2.*CD)/CONST(1)
      XC1=(U(1)*FREEL*FREED)/CONST(1)
      CALC=CONST(3)*XM+CONST(4)*XD+U(2)*XC1
      GO TO 36
1500 XM=CM/CONST(1)
      XD=(2.*CD)/CONST(1)
      CALC=XM*CONST(3)+XD*CONST(4)
36  CONTINUE
      IF(IMETH.NE.-1) GO TO 35
      RETURN
35  CONTINUE
      RESID=CALC-XX(2)
      RETURN
3  CONTINUE
      RETURN
4  CONTINUE
      RETURN
5  CONTINUE
      IF(IMETH.NE.-1) GO TO 20
      RETURN
20  CONTINUE
      RETURN
9  CONTINUE
      RETURN
10 CONTINUE
      RETURN
11 CONTINUE
      RETURN
12 CONTINUE
      RETURN
      END
```

**APPENDIX 2****A. Crystallographic data for the C<sub>2</sub>B<sub>22</sub>·LiAlCl<sub>4</sub> Complex****1. Bond distances and angles**

In the first two tables which follow, the bond distances (in Angstroms) and bond angles (in degrees) which were calculated in the least squares refinement of the crystal structure of the C<sub>2</sub>B<sub>22</sub>·LiAlCl<sub>4</sub> complex, are listed. The values in parentheses are the estimated standard deviations in the bond distances and bond angles.

**2. Least squares planes**

The following calculations were performed to evaluate the site symmetry of the lithium ion in the cryptand cavity with respect to the oxygen and nitrogen donor atoms. The reader is referred to Figure 47 and Table 31. In this procedure, a set of four donor atoms (combinations of oxygens or oxygens and nitrogens) are selected which roughly describe a plane in the cryptand cavity. The computer program then calculates the "best" plane of these atoms by using a least squares routine and an equation of the form

$$Ax + By + Cz + D = 0 \quad (1)$$

where A,B,C, and D are variable parameters, and x,y, and z are the orthogonalized atom coordinates.

The program then calculates the distance between the calculated plane and the lithium ion. This procedure is repeated for the other five possible sets of donor atoms. The details of these calculations, and the resulting dihedral angles between the calculated planes are given in the following table.

Table of Bond Distances (in Angstroms) for  
the C222B Complex of Lithium Tetrachloroaluminate

Atom1	Atom2	Distance
-----	-----	-----
C11	A11	2.131(2)
C12	A11	2.120(2)
C13	A11	2.125(2)
C14	A11	2.121(2)
O4	L11	2.457(11)
O7	L11	2.492(11)
O13	L11	2.200(11)
O16	L11	2.371(11)
O21	L11	2.291(11)
O24	L11	2.195(11)
N1	L11	2.980(11)
N10	L11	2.729(11)
O4	C3	1.400(5)
O4	C5	1.383(6)
O7	C6	1.380(7)
O7	C8	1.403(6)
O13	C12	1.403(7)
O13	C14	1.412(6)
O16	C15	1.409(6)
O16	C17	1.375(7)
O21	C20	1.478(8)
O21	C22	1.411(8)
O24	C23	1.392(7)
O24	C25	1.460(7)
N1	C2	1.461(7)
N1	C18	1.489(7)
N1	C19	1.455(7)
N10	C9	1.446(8)
N10	C11	1.465(7)
N10	C26	1.448(7)
C2	C3	1.524(7)
C1B	C2B	1.405(9)
C1B	C6	1.385(8)
C2B	C3B	1.335(9)
C3B	C4B	1.394(8)
C4B	C5	1.393(7)
C5	C6	1.359(7)
C8	C9	1.489(9)
C11	C12	1.524(8)
C14	C15	1.516(8)
C17	C18	1.546(8)
C19	C20	1.453(8)
C22	C23	1.426(10)
C25	C26	1.450(8)

Table of Bond Distances (Continued) for  
the C222B Complex of Lithium Tetrachloroaluminate

Atom1	Atom2	Distance
-----	-----	-----
C2	H2a	0.950(5)
C2	H2b	0.950(5)
C3	H3a	0.950(5)
C3	H3b	0.950(5)
C1B	H1B	0.950(7)
C2B	H2B	0.950(6)
C3B	H3B	0.950(6)
C4B	H4B	0.950(5)
C8	H8a	0.950(6)
C8	H8b	0.950(6)
C9	H9a	0.950(6)
C9	H9b	0.950(7)
C11	H11a	0.950(5)
C11	H11b	0.950(6)
C12	H12a	0.950(6)
C12	H12b	0.950(6)
C14	H14a	0.950(5)
C14	H14b	0.950(6)
C15	H15a	0.950(5)
C15	H15b	0.950(5)
C17	H17a	0.950(6)
C17	H17b	0.950(6)
C18	H18a	0.950(6)
C18	H18b	0.950(6)
C19	H19a	0.950(6)
C19	H19b	0.950(6)
C20	H20a	0.950(6)
C20	H20b	0.950(7)
C22	H22a	0.950(6)
C22	H22b	0.950(6)
C23	H23a	0.950(7)
C23	H23b	0.950(7)
C25	H25a	0.950(5)
C25	H25b	0.950(6)
C26	H26a	0.950(6)
C26	H26b	0.950(6)

-----  
Numbers in parentheses are estimated standard deviations  
in the least significant digits.

Table of Bond Angles (in Degrees) for  
the C222B Complex of Lithium Tetrachloroaluminate

Atom1 -----	Atom2 -----	Atom3 -----	Angle -----
C11	A11	C12	109.7(1)
C11	A11	C13	109.8(1)
C11	A11	C14	108.9(1)
C12	A11	C13	109.4(1)
C12	A11	C14	110.4(1)
C13	A11	C14	108.6(1)
C3	O4	Li1	113.1(4)
C5	O4	Li1	119.4(4)
C6	O7	Li1	118.1(4)
C8	O7	Li1	116.3(4)
C12	O13	Li1	117.1(4)
C14	O13	Li1	115.1(4)
C15	O16	Li1	111.0(4)
C17	O16	Li1	120.1(4)
C20	O21	Li1	121.1(4)
C22	O21	Li1	111.2(4)
C23	O24	Li1	115.1(5)
C25	O24	Li1	116.4(4)
C2	N1	Li1	106.9(4)
C18	N1	Li1	106.6(4)
C19	N1	Li1	103.0(4)
C9	N10	Li1	110.7(4)
C11	N10	Li1	102.6(3)
C26	N10	Li1	103.0(4)
O4	Li1	O7	61.3(3)
O4	Li1	O13	82.1(4)
O4	Li1	O16	106.0(4)
O4	Li1	O21	93.8(4)
O4	Li1	O24	165.6(5)
O4	Li1	N1	63.1(3)
O4	Li1	N10	113.1(4)
O7	Li1	O13	97.9(4)
O7	Li1	O16	165.2(5)
O7	Li1	O21	83.8(4)
O7	Li1	O24	111.5(4)
O7	Li1	N1	112.6(4)
O7	Li1	N10	63.8(3)
O13	Li1	O16	71.6(3)
O13	Li1	O21	174.0(5)
O13	Li1	O24	111.8(5)
O13	Li1	N1	109.2(4)
O13	Li1	N10	70.6(3)
O16	Li1	O21	105.6(4)
O16	Li1	O24	82.6(4)
O16	Li1	N1	63.4(3)

Table of Bond Angles (Continued) for  
the C222B Complex of Lithium Tetrachloroaluminate

Atom1 -----	Atom2 -----	Atom3 -----	Angle -----
016	Li1	N10	119.7(4)
021	Li1	O24	72.5(4)
021	Li1	N1	65.0(3)
021	Li1	N10	115.2(4)
024	Li1	N1	112.9(4)
024	Li1	N10	70.4(3)
N1	Li1	N10	176.1(5)
C3	O4	C5	119.5(4)
C6	O7	C8	121.9(4)
C12	O13	C14	111.6(4)
C15	O16	C17	116.8(4)
C20	O21	C22	112.8(5)
C23	O24	C25	113.7(4)
C2	N1	C18	111.7(4)
C2	N1	C19	113.5(4)
C18	N1	C19	114.3(4)
C9	N10	C11	111.6(5)
C9	N10	C26	114.7(4)
C11	N10	C26	113.1(5)
N1	C2	C3	109.2(4)
O4	C3	C2	112.2(4)
C2B	C1B	C6	118.0(6)
C1B	C2B	C3B	121.5(6)
C2B	C3B	C4B	120.6(6)
C3B	C4B	C5	118.3(5)
O4	C5	C4B	124.0(4)
O4	C5	C6	115.1(4)
C4B	C5	C6	120.9(5)
O7	C6	C1B	124.6(5)
O7	C6	C5	114.7(4)
C1B	C6	C5	120.6(5)
O7	C8	C9	106.3(5)
N10	C9	C8	113.9(5)
N10	C11	C12	110.3(5)
O13	C12	C11	111.1(5)
O13	C14	C15	106.1(4)
O16	C15	C14	107.4(4)
O16	C17	C18	113.4(5)
N1	C18	C17	107.5(4)
N1	C19	C20	112.1(5)
O21	C20	C19	112.6(5)
O21	C22	C23	110.1(6)
O24	C23	C22	110.5(5)
O24	C25	C26	112.0(5)
N10	C26	C25	114.3(4)

Table of Bond Angles (Continued) for  
the C222B Complex of Lithium Tetrachloroaluminate

Atom1 -----	Atom2 -----	Atom3 -----	Angle -----
N1	C2	H2a	110.3(4)
N1	C2	H2b	108.6(4)
C3	C2	H2a	111.1(4)
C3	C2	H2b	108.2(4)
H2a	C2	H2b	109.5(5)
O4	C3	H3a	109.3(4)
O4	C3	H3b	109.2(4)
C2	C3	H3a	108.5(4)
C2	C3	H3b	108.0(4)
H3a	C3	H3b	109.5(5)
C2B	C1B	H1B	121.3(6)
C6	C1B	H1B	120.7(6)
C1B	C2B	H2B	118.5(6)
C3B	C2B	H2B	119.9(6)
C2B	C3B	H3B	119.7(6)
C4B	C3B	H3B	119.7(6)
C3B	C4B	H4B	120.8(5)
C5	C4B	H4B	120.9(5)
O7	C8	H8a	110.2(6)
O7	C8	H8b	110.9(5)
C9	C8	H8a	110.4(6)
C9	C8	H8b	109.5(6)
H8a	C8	H8b	109.5(6)
N10	C9	H9a	108.2(6)
N10	C9	H9b	107.9(5)
C8	C9	H9a	109.2(6)
C8	C9	H9b	108.0(6)
H9a	C9	H9b	109.5(6)
N10	C11	H11a	109.3(4)
N10	C11	H11b	109.0(5)
C12	C11	H11a	110.2(6)
C12	C11	H11b	108.6(4)
H11a	C11	H11b	109.5(6)
O13	C12	H12a	109.7(5)
O13	C12	H12b	109.0(6)
C11	C12	H12a	108.8(6)
C11	C12	H12b	108.7(5)
H12a	C12	H12b	109.5(6)
O13	C14	H14a	109.8(5)
O13	C14	H14b	111.2(5)
C15	C14	H14a	109.4(5)
C15	C14	H14b	110.8(5)
H14a	C14	H14b	109.5(6)
O16	C15	H15a	109.6(5)
O16	C15	H15b	109.7(5)
C14	C15	H15a	110.1(5)
C14	C15	H15b	110.6(5)



Table of Bond Angles (Continued) for  
the C222B Complex of Lithium Tetrachloroaluminate

Atom1 -----	Atom2 -----	Atom3 -----	Angle -----
H15a	C15	H15b	109.5(5)
O16	C17	H17a	107.5(6)
O16	C17	H17b	110.1(5)
C18	C17	H17a	107.2(5)
C18	C17	H17b	109.0(6)
H17a	C17	H17b	109.5(6)
N1	C18	H18a	110.1(5)
N1	C18	H18b	109.2(5)
C17	C18	H18a	110.8(5)
C17	C18	H18b	109.8(6)
H18a	C18	H18b	109.5(5)
N1	C19	H19a	108.6(5)
N1	C19	H19b	109.3(5)
C20	C19	H19a	108.0(5)
C20	C19	H19b	109.4(6)
H19a	C19	H19b	109.5(6)
O21	C20	H20a	108.4(5)
O21	C20	H20b	107.7(5)
C19	C20	H20a	109.6(6)
C19	C20	H20b	109.0(6)
H20a	C20	H20b	109.5(6)
O21	C22	H22a	110.2(6)
O21	C22	H22b	108.7(6)
C23	C22	H22a	111.6(6)
C23	C22	H22b	106.6(6)
H22a	C22	H22b	109.5(7)
O24	C23	H23a	110.5(6)
O24	C23	H23b	108.3(6)
C22	C23	H23a	111.2(6)
C22	C23	H23b	106.8(6)
H23a	C23	H23b	109.5(7)
O24	C25	H25a	108.9(5)
O24	C25	H25b	107.4(5)
C26	C25	H25a	110.3(5)
C26	C25	H25b	108.7(5)
H25a	C25	H25b	109.5(6)
N10	C26	H26a	107.5(5)
N10	C26	H26b	109.3(5)
C25	C26	H26a	107.3(5)
C25	C26	H26b	108.9(5)
H26a	C26	H26b	109.5(5)

Numbers in parentheses are estimated standard deviations  
in the least significant digits.

Table of Least-Squares Planes  
in the C222B Complex of Lithium Tetrachloroaluminate

The equation of the plane is of the form:

$$Ax + By + Cz - D = 0$$

where A, B, C & D are constants and  
x, y & z are orthogonalized coordinates.

Plane No. 1      A = -0.8889, B = -0.4152, C = -0.1935, D = -9.8441  
Chi Squared = 1995.

Atom	x	y	z	Distance	Esd
----	-	-	-	-----	---
-----Atoms in Plane-----					
O4	6.3798	6.6327	7.7298	-0.077	0.003
O13	7.4904	4.9806	5.4008	0.073	0.003
O21	7.0483	3.8733	9.7239	0.089	0.004
O24	8.3126	2.4439	7.8781	-0.084	0.004
-----Other Atoms-----					
Li1	7.3839	4.3999	7.5196	-0.002	0.010
O7	8.7676	6.2508	8.4516	-2.180	0.004
O16	5.8216	3.0914	6.3071	2.165	0.003
N1	4.5487	4.5234	8.4270	2.292	0.004
N10	9.9938	4.4683	6.7264	-2.197	0.004

Plane No. 2      A = 0.7595, B = -0.6442, C = -0.0907, D = 1.9221  
Chi Squared = 1126.

Atom	x	y	z	Distance	Esd
----	-	-	-	-----	---
-----Atoms in Plane-----					
O7	8.7676	6.2508	8.4516	-0.057	0.004
O13	7.4904	4.9806	5.4008	0.068	0.003
O16	5.8216	3.0914	6.3071	-0.065	0.004
O21	7.0483	3.8733	9.7239	0.053	0.004
-----Other Atoms-----					
Li1	7.3839	4.3999	7.5196	0.169	0.010
O4	6.3798	6.6327	7.7298	-2.051	0.003
O24	8.3126	2.4439	7.8781	2.102	0.004
N1	4.5487	4.5234	8.4270	-2.146	0.004
N10	9.9938	4.4683	6.7264	2.179	0.004

Table of Least-Squares Planes (Continued)  
in the C2228 Complex of Lithium Tetrachloroaluminate

Plane No. 3      A = 0.4598, B = 0.1727, C = -0.8711, D = -2.4519  
Chi Squared = 10353.

Atom	x	y	z	Distance	Esd
----	-	-	-	-----	---
-----Atoms in Plane-----					
O4	6.3798	6.6327	7.7298	-0.203	0.003
O7	8.7676	6.2508	8.4516	0.201	0.004
O16	5.8216	3.0914	6.3071	0.169	0.004
O24	8.3126	2.4439	7.8781	-0.166	0.004
-----Other Atoms-----					
Li1	7.3839	4.3999	7.5196	0.057	0.010
O13	7.4904	4.9806	5.4008	2.051	0.004
O21	7.0483	3.8733	9.7239	-2.109	0.004
N1	4.5487	4.5234	8.4270	-2.016	0.004
N10	9.9938	4.4683	6.7264	1.959	0.004

Plane No. 4      A = -0.0896, B = -0.9626, C = -0.2557, D = -6.8820  
Chi Squared = 299.

Atom	x	y	z	Distance	Esd
----	-	-	-	-----	---
-----Atoms in Plane-----					
O13	7.4904	4.9806	5.4008	0.035	0.004
O21	7.0483	3.8733	9.7239	0.035	0.004
N1	4.5487	4.5234	8.4270	-0.035	0.004
N10	9.9938	4.4683	6.7264	-0.035	0.004
-----Other Atoms-----					
Li1	7.3839	4.3999	7.5196	0.062	0.011
O4	6.3798	6.6327	7.7298	-2.051	0.004
O7	8.7676	6.2508	8.4516	-2.082	0.004
O16	5.8216	3.0914	6.3071	1.771	0.004
O24	8.3126	2.4439	7.8781	1.770	0.004

Plane No. 5      A = -0.2142, B = 0.6773, C = -0.7039, D = -3.7193  
Chi Squared = 3784.

Atom	x	y	z	Distance	Esd
----	-	-	-	-----	---
-----Atoms in Plane-----					
O7	8.7676	6.2508	8.4516	0.126	0.004
O16	5.8216	3.0914	6.3071	0.127	0.004
N1	4.5487	4.5234	8.4270	-0.123	0.004
N10	9.9938	4.4683	6.7264	-0.130	0.004
-----Other Atoms-----					
Li1	7.3839	4.3999	7.5196	-0.175	0.011
O4	6.3798	6.6327	7.7298	1.404	0.004
O13	7.4904	4.9806	5.4008	1.687	0.004
O21	7.0483	3.8733	9.7239	-2.012	0.004
O24	8.3126	2.4439	7.8781	-1.951	0.004

Table of Least-Squares Planes (Continued)  
in the C222B Complex of Lithium Tetrachloroaluminate  
-----

Plane No. 6      A = -0.2953, B = -0.1695, C = -0.9402, D = -10.1548  
Chi Squared = 3898.

Atom	x	y	z	Distance	Esd
----	-	-	-	-----	---
-----Atoms in Plane-----					
O4	6.3798	6.6327	7.7298	-0.121	0.003
O24	8.3126	2.4439	7.8781	-0.122	0.004
N1	4.5487	4.5234	8.4270	0.121	0.004
N10	9.9938	4.4683	6.7264	0.122	0.005
-----Other Atoms-----					
Li1	7.3839	4.3999	7.5196	0.158	0.010
O7	8.7676	6.2508	8.4516	-1.440	0.004
O13	7.4904	4.9806	5.4008	2.021	0.004
O16	5.8216	3.0914	6.3071	1.981	0.004
O21	7.0483	3.8733	9.7239	-1.726	0.004

Dihedral Angles Between Planes:  
-----

Plane No.	Plane No.	Dihedral Angle
-----	-----	-----
1	2	113.0
1	3	108.2
1	4	58.1
1	5	87.4
1	6	59.0
2	3	71.5
2	4	54.9
2	5	122.4
2	6	91.7
3	4	89.1
3	5	50.8
3	6	49.2
4	5	116.9
4	6	64.5
5	6	52.4

## REFERENCES

## References

1. Bloom, H. and Bockris, J.O'M. in "Fused Salts", B.R. Sundheim - ed., McGraw-Hill Book Co., New York (1964).
2. Bockris, J.O'M. "Modern Electrochemistry", Plenum Press, New York (1970).
3. Furth, R. Proc. Cambridge Phil. Soc. (1941), 37, 252, 276, 281.
4. Frenkel, Y.I. Acta Physicochim. URSS (1935), 3, 633, 913.
5. Adams, D. and Hills, G. in "Ionic Liquids", D. Inman and D.G. Lovering - eds., Plenum Press, New York (1981).
6. Woodcock, L.V. and Singer, K. Trans. Faraday Soc. (1970), 67, 12.
7. Larsen, B.; Forland, T.; and Singer, K. Mol. Phys. (1973), 26, 1521.
8. Caccamo, C. and Dixon, M. J. Phys. C.: Solid St. Phys. (1980), 13, 1887.
9. Cotton, F.A. and Wilkinson, G. "Advanced Inorganic Chemistry" -4th Ed., John Wiley & Sons, New York (1980).
10. Okada, I.; Okano, H.; Ohtaki, H.; and Takagi, R. Chem. Phys. Lett. (1983), 100, 436.
11. Saboungi, M.-L.; Rahman, A.; and Blander, M. J. Chem. Phys. (1984), 80, 2141.
12. Woodcock, L.V. in "Advances in Molten Salt Chemistry", Vol. 3, J. Braunstein, G. Mamantov, and G.P. Smith - eds., Plenum Press, New York (1975).
13. Blomgren, G.E. and Van Artsdalen, E.R. in "Annual Review of Physical Chemistry", Vol. 11, Annual Reviews, Inc., Palo Alto, CA (1960).
14. C.R.C. Handbook of Chemistry and Physics - 47th ed., The Chemical Rubber Co., Cleveland, OH (1964).
15. Reinsborough, V.C. Rev. Pure and Appl. Chem. (1968), 18, 281.
16. Bloom, H. and Reinsborough, V.C. Aust. J. Chem. (1967), 20, 2583.

17. Newman, D.S.; Rohr, W.; Kirklin, D.; and Frame, H.D. J. Electrochem. Soc. (1972), 119, 797.
18. Newman, D.S.; Morgan, D.P.; and Tillack, R.T. J. Chem. and Engin. Data (1976), 21, 279.
19. Newman, D.S. and Bikkani, P.B. in "Proceedings of the Fourth International Symposium on Molten Salts", M. Blander, D.S. Newman, M.-L. Saboungi, G. Mamantov, and K. Johnson - eds., pp. 206-216, The Electrochemical Society Softbound Proceedings Series, Pennington, NJ (1984).
20. Robinson, J. and Osteryoung, R.A. J. Amer. Chem. Soc. (1979), 101, 323.
21. Newman, D.S. and Stevens, R.M. J. Electrochem. Soc. (1984), 131, 1275.
22. Newman, D.S.; Rhinebarger, R.R.; Siconolfi, D.; and Banjoko, O.A. J. Electrochem. Soc. (1981), 128, 2331.
23. Wilkes, J.S.; Levisky, J.A.; Wilson, R.A.; and Hussey, C.L. Inorg. Chem. (1982), 21, 1263.
24. Chan, B.K.; Chang, N.-H.; and Grimmett, M.R. Aust. J. Chem. (1977), 30, 2005.
25. Bowmaker, G.A.; Brockliss, L.D.; and Whiting, R. Aust. J. Chem. (1973), 26, 29.
26. Dr. Davis S. Newman - private communication.
27. Hurley, F.H. and Weir, T.P. J. Electrochem. Soc. (1951), 98, 203.
28. Chum, H.L.; Koran, D.; and Osteryoung, R.A. J. Organomet. Chem. (1977), 349.
29. Koch, V.R.; Miller, L.L.; and Osteryoung, R.A. J. Amer. Chem. Soc. (1976), 98, 5277.
30. Chum, H.L. and Osteryoung, R.A. in "Ionic Liquids", D. Inman and D.G. Lovering - eds., Plenum Press, New York (1981).
31. Wilkes, J.S. and Levisky, J.A.; Frank J. Seiler Research Laboratory Technical Report #0001 (1981).
32. Yoke, J.T.; Wiss, J.F.; and Tollin, G. Inorg. Chem. (1963), 2, 1210.
33. Axtell, D.D.; Good, B.W.; Porterfield, W.W.; and Yoke, J.T. J. Amer. Chem. Soc. (1973), 95, 4555.
34. Clifton, J.R. and Yoke, J.T. Inorg. Chem. (1967), 6, 1258.
35. Janz, G.J.; Krebs, U.; Siegenthaler, H.F.; and Tomkins, R.P.T. J. Phys. Chem. Ref. Data (1972), 1, 581.

36. Ibid; (1974), 3, 1.
37. Ibid; (1975), 4, 871.
38. Ibid; (1977), 6, 409.
39. Ibid; (1979), 8, 125.
40. Ibid; (1980), 9, 791, 831.
41. Ibid; (1982), 11, 505.
42. Ibid; (1983), 12, 591.
43. Boston, C.R. in "Advances in Molten Salt Chemistry", Vol. 1, J. Braunstein, G. Mamantov, and G.P. Smith - eds., Plenum Press, New York (1973).
44. Lind, J.E. in "Advances in Molten Salt Chemistry", Vol. 2, J. Braunstein, G. Mamantov, and G.P. Smith - eds., Plenum Press, New York (1973).
45. Kleppa, O.J. in "Annual Review of Physical Chemistry", Vol. 16, H. Eyring, C.J. Christensen, and H.S. Johnston - eds., Annual Reviews, Inc., Palo Alto, CA (1965).
46. Yosim, S.J. and Reiss, H. in "Annual Review of Physical Chemistry", Vol. 19, H. Eyring, C.J. Christensen, and H.S. Johnston - eds., Annual Reviews, Inc., Palo Alto, CA (1971).
47. Angell, C.A. in "Annual Review of Physical Chemistry", Vol. 22, H. Eyring, C.J. Christensen, and H.S. Johnston - eds., Annual Reviews, Inc., Palo Alto, CA (1971).
48. Gale, R.J. and Osteryoung, R.A. Inorg. Chem. (1979), 18, 1603.
49. Gale, R.J.; Gilbert, B.; and Osteryoung, R.A. Inorg. Chem. (1978), 17, 2728.
50. Schoebrechts, J.P. and Gilbert, B.P. J. Electrochem. Soc. (1981), 128, 2679.
51. Robinson, J. and Osteryoung, R.A. J. Electrochem. Soc. (1980), 127, 122.
52. Blander, M. in "Molten Salt Chemistry", M. Blander - ed., Interscience Publishers, New York (1964).
53. Gale, R.J. and Osteryoung, R.A. Inorg. Chem. (1980), 19, 2240.
54. Tait, S. and Osteryoung, R.A. Inorg. Chem. (1984), 23, 4352.
55. Carpio, R.A.; King, L.A.; Lindstrom, R.E.; Nardi, J.C.; and Hussey, C.L. J. Electrochem. Soc. (1979), 126, 1644.



56. Nanjundiah, C.; Shimizu, K.; and Osteryoung, R.A. J. Electrochem. Soc. (1982), 129, 2474.
57. Fannin, A.A.; Floreani, D.A.; King, L.A.; Landers, J.S.; Piersma, B.J.; Stech, D.J.; Vaughn, R.L.; Wilkes, J.S.; and Williams, J.L.; Frank J. Seiler Research Laboratory Technical Report #0006 (1980).
58. Robinson, J.; Bugle, R.C.; Chum, C.L.; Koran, D.; and Osteryoung, R.A. J. Amer. Chem. Soc. (1979), 101, 3776.
59. Taulelle, F. and Popov, A.I. Polyhedron (1983), 2, 889.
60. Matsumoto, T. and Ichikawa, K. J. Amer. Chem. Soc. (1984), 106, 4316.
61. Wilkes, J.S.; Levisky, J.A.; Pflug, J.L.; Hussey, C.L.; and Scheffler, T.B. Anal. Chem. (1982), 54, 2378.
62. Fannin, A.A.; King, L.A.; Levisky, J.A.; and Wilkes, J.S. J. Phys. Chem. (1984), 88, 2609.
63. Bloom, H. and Heymann, E. Proc. Roy. Soc. (London) (1947), A188, 392.
64. Wilmshurst, J.K. J. Chem. Phys. (1963), 39, 1779.
65. Angell, C.A. and Gruen, D.M. J. Phys. Chem (1966), 70, 1601.
66. Øye, H.A. and Gruen, D.M. Inorg. Chem. (1965), 4, 1173.
67. Angell, C.A. and Moynihan, C.T. in "Molten Salts", G. Mamantov - ed., Marcel Dekker, New York (1969).
68. Rowland, T.J. and Bromberg, J.P. J. Chem. Phys. (1958), 29, 626.
69. Hafner, S. and Nachtrieb, N.H. J. Chem. Phys. (1964), 40, 2891.
70. Mamantov, G.; Norvell, V.E.; Katt, L.; Tanemoto, K.; Marassi, R.; Ogata, Y.; Matsunago, M.; Wiaux, J.P.; and Mamantov, C.B. in "Proceedings of the Third International Symposium on Molten Salts", G. Mamantov, M. Blander, and G.P. Smith - eds., pp. 158-166, The Electrochemical Society Softbound Proceedings Series, Pennington, NJ (1981).
71. Gale, R.J.; Gilbert, B.; and Osteryoung, R.A. Inorg. Chem. (1979), 18, 2723.
72. Hussey, C.L.; King, L.A.; and Wilkes, J.S. J. Electroanal. Chem. (1979), 102, 321.
73. Linga, H.; Stojek, Z.; and Osteryoung, R.A. J. Amer. Chem. Soc (1981), 103, 3754.
74. Hussey, C.L. and Laher, T.M. Inorg. Chem. (1981), 20, 4201.

75. Laher, T.M. and Hussey, C.L. Inorg. Chem. (1982), 21, 4079.
76. Laher, T.M. and Hussey, C.L. Inorg. Chem. (1983), 22, 1279.
77. Nanjundiah, C. and Osteryoung, R.A. J. Electrochem. Soc. (1983), 130, 1312.
78. Sheffler, T.B.; Hussey, C.L.; Seddon, K.R.; Kear, C.M.; and Armitage, P.D. Inorg. Chem. (1983), 22, 2099.
79. Schoebrechts, J.P.; Gilbert, B.P.; and Duychaerts, G. J. Electroanal. Chem (1983), 145, 127.
80. Schoebrechts, J.P.; Gilbert, B.P.; and Duychaerts, G. ibid. (1983), 145, 139.
81. Laher, T.M. and Hussey, C.L. Inorg. Chem. (1983), 22, 3247.
82. Scheffler, T.B. and Hussey, C.L. Inorg. Chem. (1984), 23, 1926.
83. Lipsztajn, M. and Osteryoung, R.A. Inorg. Chem. (1984), 23, 1735.
84. Sahami, S. and Osteryoung, R.A. Inorg. Chem. (1984), 23, 2511.
85. Pickup, P.G. and Osteryoung, R.A. J. Amer. Chem. Soc. (1984), 106, 2294.
86. Karpinski, Z.J. and Osteryoung, R.A. J. Electroanal. Chem. (1984), 164, 281.
87. Karpinski, Z.J.; Nanjundiah, C.; and Osteryoung, R.A. Inorg. Chem. (1984), 23, 3358.
88. Habboush, D.A. and Osteryoung, R.A. Inorg. Chem. (1984), 23, 1726.
89. Pickup, P.G. and Osteryoung, R.A. J. Electrochem. Soc. (1983), 130, 1965.
90. DeWaele, R.; Heerman, L.; and D'Olieslager, W. J. Electroanal. Chem. (1982), 142, 137.
91. Pickup, P.G. and Osteryoung, R.A. J. Electroanal. Chem. (1985), 186, 99.
92. Schoebrechts, J.P. and Gilbert, B. Inorg. Chem. (1985), 24, 2105.
93. Dymek, C.J.; Williams, J.L.; Graeger, D.J.; and Auborn, J.J. J. Electrochem. Soc. (1984), 131, 2887.
94. Brevard, C. and Granger, P. "Handbook of High Resolution Multinuclear NMR", John Wiley & Sons, NY (1981).
95. Abragam, A. "Principles of Nuclear Magnetism", Clarendon Press, NY (1983).

96. Martin, M.L.; Delpuech, J.J.; and Martin, G.J. "Practical NMR Spectroscopy", Heydon, London (1980).
97. Farrar, T.C. and Becker, E.Q. "Pulse and Fourier Transform NMR", Academic Press, New York (1971).
98. "Annual Reports of NMR Spectroscopy", Vol. 1-15, E.F. Mooney and G.A. Webb - eds., Academic Press, New York (1968-1983).
99. "Advances in Magnetic Resonance", Vol. 1-10, J.S. Waugh - ed., Academic Press, New York (1965- ).
100. Harris, R.K. and Mann, B.E. -eds., "NMR and the Periodic Table", Academic Press, New York (1978).
101. Lambert, J.B. and Riddell, F.G. - eds., "The Multinuclear Approach to NMR Spectroscopy", D. Reidel Publishing Co., Boston (1983).
102. "NMR of Newly Accessible Nuclei", Vol. 1&2, P. Laszlo - ed., Academic Press (1983).
103. Hertz, H.G.; Tutsch, R.; and Versmold, H. Ber. Bunsenges. Phys. Chem. (1971), 75, 1177.
104. Hertz, H.G.; Weingartner, H.; and Rode, B.M. Ber. Bunsenges. Phys. Chem. (1975), 79, 1190.
105. Weingartner, H. and Hertz, H.G. Ber. Bunsenges. Phys. Chem. (1977), 81, 1204.
106. Hartwell, G.E. and Allerhand, A. J. Amer. Chem. Soc. (1971), 93, 4415.
107. Harold-Smith, D. J. Chem. Phys. (1974), 60, 1405.
108. Matsumoto, T. and Ichikawa, K. Nippon Kagaku Kaishi (1982), 6, 1100.
109. Nakamura, Y. and Shimokawa, S. Ber. Bunsenges. Phys. Chem. (1985), 89, 371.
110. Wehrli, F.A. Org. Magn. Reson. (1978), 11, 106.
111. McKeever, L.D.; Waack, R.; Doran, M.A.; and Baker, E.B. J. Amer. Chem. Soc. (1969), 91, 1057.
112. Boere, R.T. and Kidd, R.G. in "Annual Reports on NMR Spectroscopy", G.A. Webb - ed., Academic Press, New York (1982).
113. Maciel, G.E.; Hancock, J.K.; Lafferty, L.F.; Mueller, P.A.; and Musker, W.K. Inorg. Chem. (1966), 5, 554.
114. Akitt, J.W. and Downs, A.J. in "The Alkali Metals Symposium", The Chemical Society, London (1967).

115. Cahen, Y.M.; Handy, P.R.; Roach, E.T.; and Popov, A.I. J. Phys. Chem. (1975), 79, 80.
116. Kidd, R.G. in "Annual Reports on NMR Spectroscopy", Vol. 10a, G.A. Webb - ed., Academic Press, New York (1980).
117. Khazaeli, S., Ph.D. Thesis, Michigan State University, East Lansing, MI (1982).
118. Maciel, G.E.; Simeral, L.; and Ackerman, J.J.H. J. Phys. Chem. (1977), 81, 263.
119. Ackerman, J.J.H.; Orr, T.V.; Bartuska, V.J.; and Maciel, G.E. J. Amer. Chem. Soc. (1979), 101, 341.
120. Sens, M.A.; Wilson, N.K.; Ellis, P.D.; and Odom, J.D. J. Magn. Reson. (1975), 19, 323.
121. Godfrey, P.D.; Hefferman, M.L.; and Kerr, D.F. Aust. J. Chem. (1964), 17, 701.
122. Smith, P.J. and Tupciauskas, A.P. in "Annual Reports on NMR Spectroscopy", Vol. 8, G.A. Webb - ed., Academic Press, New York (1978).
123. Burke, J.J. and Lauterbur, P.C. J. Amer. Chem. Soc. (1961), 83, 326.
124. Yamakawa, T.; Shinoda, S.; Saito, Y.; Mariyama, H.; and Pregosin, P.S. Magn. Reson. Chem. (1985), 23, 202.
125. Pederson, C.J. J. Amer. Chem. Soc. (1967), 89, 7017.
126. Dietrich, B.; Lehn, J.-M.; and Sauvage, J.-P. Tetrahedron Lett. (1969), 2885.
127. Lehn, J.-M. in "Structure and Bonding", Vol. 16, J.D. Dinity, P. Hemmerlich, J.A. Ibers, C.K. Jørgensen, J.B. Neilands, D. Remen, and R.J.P. Williams - eds., Springer-Verlag, NY (1973).
128. Izatt, R.M.; Eatough, D.J.; and Christensen, J.J. ibid., ref. 127.
129. "Synthetic Multidentate Macrocyclic Compounds", R.M. Izatt and J.J. Christensen - eds., Academic Press, New York (1978).
130. Hiraoka, M. "Crown Compounds: Their Characteristics and Applications", Elsevier Scientific Publishing Co., New York (1982).
131. Popov, A.I. Pure Appl. Chem. (1979), 51, 101.
132. Cahen, Y.M., Ph.D. Thesis, Michigan State University, East Lansing, MI (1975).
133. Smetana, A.J., Ph.D. Thesis, Michigan State University, East Lansing, MI (1979).

134. Rounahgi, G. and Popov, A.I. J. Inorg. Nucl. Chem. (1981), 43, 911.
135. Smetana, A.J. and Popov, A.I. J. Soln. Chem. (1980), 9, 183.
136. Ladd, M.F.C. Theor. Chim. Acta (1968), 12 333.
137. Mandolini, L. and Masci, B. J. Amer. Chem. Soc. (1984), 106, 168.
138. Kitazawa, S.; Kimura, K.; Yano, H.; and Shono, T. J. Amer. Chem. Soc. (1984), 106, 6978.
139. Chen, C.S.; Wang, S.J.; and Wu, S.C. Inorg. Chem. (1984), 23, 3901.
140. Shamsipur, M. and Popov, A.I. Inorg. Chim. Acta (198), 43, 243.
141. Mosier-Boss, P. and Popov, A.I., in press.
142. Cahen, Y.M.; Dye, J.L.; and Popov, A.I. J. Phys. Chem. (1975), 79, 1289.
143. Hourdakis, A. and Popov, A.I. J. Soln. Chem. (1977), 6, 299.
144. Chantooni, M.K. and Kolthoff, I.M. J. Soln. Chem. (1985), 14, 1.
145. Bhagwat, V.W.; Manohar, H.; and Poonia, N.S. Inorg. Nucl. Chem. Lett. (1980), 16, 373.
146. Groth, P. Acta Chem. Scand. (1981), A35, 460.
147. Groth, P. Acta Chem. Scand. (1982), A36, 109.
148. Shoham, G.; Lipscomb, W.M.; and Olsher, U. J. Amer. Chem. Soc. (1983), 105, 1247.
149. Holt, E.M.; Malpass, G.D.; Ghirardelli, R.G.; Palmer, R.A.; and Rubin, B. Acta Cryst. (1984), C40, 394.
150. Shoham, G.; Christianson, D.W.; Bartsch, R.A.; Heo, G.D.; Olsher, U.; and Lipscomb, W.N. J. Amer. Chem. Soc. (1984), 106, 1285.
151. Power, P.P. and Xiaojie, X. J. Chem. Soc., Chem. Comm. (1984), 358.
152. Doughty, S.M.; Sloddart, J.F.; Colquhoun, H.M.; Slawin, A.M.Z.; and Williams, D.J. Polyhedron (1985), 4, 567.
153. Morass, P.D. and Weiss, R.; Acta Cryst. (1973), B29, 400.
154. Mosier-Boss, P.; Ph.D. Thesis, Michigan State University, East Lansing, MI (1985).
155. Canet, D.; Levy, G.C.; and Peat, I.R. J. Magn. Reson. (1975), 18, 199.

156. Levy, G.C. and Peat, I.R. J. Magn. Reson. (1975), 18, 500.
157. Hanssum, H.; Mauer, W.; and Ruterjans, H. J. Magn. Reson. (1978), 31, 231.
158. Maciel, G.E. and Dallas, J.L. J. Am. Chem. Soc. (1973), 95, 3039.
159. Cardin, A.D.; Ellis, P.D.; Odom, J.D.; and Howard, J.W. J. Am. Chem. Soc. (1975), 97, 1672.
160. Gale, R.J. and Osteryoung, R.A. J. Electrochem. Soc. (1981), 127, 2167.
161. Alabyshev, A.F.; Lantratov, M.F.; and Morachevskii, A.G. "Reference Electrodes for Fused Salts", The Sigma Press, Publishers, Washington, DC (1965).
162. Dye, J.L. and Nicely, J.A. J. Chem. Educ. (1971), 68, 443.
163. Weiss, G.H. and Ferretti, J.A. J. Magn. Reson. (1985), 61, 499.
164. Paoli, D.; Lucon, M.; and Chabanel, M. Spectrochim. Acta (1979), A35, 593.
165. Chabanel, M.; Lucon, M.; and Paoli, D. J. Phys. Chem. (1981) 85, 1058.
166. Chabanel, M. and Wang, Z. J. Phys. Chem. (1984), 88, 1441.
167. Scherr, P.A.; Hogan, R.J.; and Oliver, J.P. J. Amer. Chem. Soc. (1974), 96, 6055.
168. Jackman, L.M. and Szeverenyi, N.M. J. Amer. Chem. Soc. (1977), 99, 4954.
169. Cambillau, C. and Ourevitch, M. J. Chem. Soc.: Chem. Comm. (1981), 996.
170. Kale, K.M. and Zana, R. J. Soln. Chem. (1977), 6, 733.
171. Kollman, P.A. and Kuntz, I.D. J. Amer. Chem. Soc. (1974), 96, 4766.
172. Zhogolev, D.A.; Kruglyak, Y.A.; Eunyatyan, B.K.; Matyash, I.U. Theor. Exp. Chem. (1972), 8, 614.
173. Logan, R.A.; Cote, R.E.; and Kusch, P. Phys. Rev. (1952), 86, 280.
174. Tokuhiro, T.; Iton, L.E.; and Peterson, E.M. J. Chem. Phys. (1983), 78, 7473.
175. Snelson, A. and Pitzer, K.S. J. Phys. Chem. (1963), 67, 882.
176. Freiberg, M.; Ron, A.; and Schnepf, O. J. Phys. Chem. (1968), 72, 3526.

177. a. Deverell, C. Prog. NMR Spectrosc. (1969), 4, 235.  
b. Deverell, C. Mol. Phys. (1969), 16, 491.
178. Kidd, R.G. and Truax, R.G. J. Amer. Chem. Soc. (1968), 90, 6867.
179. Gray, J.L. and Maciel, G.E. J. Amer. Chem. Soc. (1981), 103, 7147.
180. Klemperer, W. and Norris, W.G. J. Chem. Phys. (1961), 34, 1071.
181. Cahen, Y.M. and Popov, A.I. J. Soln. Chem. (1975), 4, 599.
182. Della Monica, M.; Ceglie, A.; and Agostiano, A. Electrochim. Acta (1983), 28, 529.
183. Lin, J.D. and Popov, A.I. J. Amer. Chem. Soc. (1981), 103, 3773.
184. Shih, J.-S. and Popov, A.I. Inorg. Chem. (1980), 19, 1689.
185. Kauffman, E.; Dye, J.L.; Lehn, J.-M.; and Popov, A.I. J. Amer. Chem. Soc. (1980), 102, 2274.
186. Szczygiel, P., M.S. Thesis, Michigan State University, East Lansing, MI (1984).
187. Cox, B.G.; Schneider, H.; and Stroka, J. J. Amer. Chem. Soc. (1978), 100, 4746.
188. Boss, R.D. - private communication.
189. Cox, B.G.; Garcia-Rosas, J.; and Schneider, H. J. Amer. Chem. Soc. (1981), 103, 1384.
190. Cox, B.G.; van Troung, N.; and Schneider, H. J. Amer. Chem. Soc. (1984), 106, 1273.
191. Cox, B.G.; Knop, D.; and Schneider, H. J. Phys. Chem. (1980), 84, 320.
192. Fyfe, C.A. "Solid State NMR for Chemists", C.F.C. Press, Guelph, Ontario, Canada (1983).
193. Mairesse, G.; Barbier, P.; and Wignacourt, J.-P. Acta Cryst. (1979), B35, 1573.
194. Ellaboudy, A.S. - private communication.
195. Wait, S.C. and Janz, G.J. Quart. Rev. (1963), 17, 225.
196. Tanaka, M.; Balasubramanyam, K.; and Bockris, J.O'M. Electrochim. Acta (1963), 8, 621.
197. Vanderzee, C.E. and Rhodes, D.E. J. Am. Chem. Soc. (1952), 74, 3552.

198. Clarke, J.H.R. and Solomons, C. J. Chem. Phys. (1967), 47, 1823.
199. Deacon, G.B. Rev. Pure Appl. Chem. (1963), 13, 189.
200. Delwaulle, M.-L. Bull. Soc. Chim. France (1955), 1294.
201. Janz, G.J. and James, D.W. J. Chem. Phys. (1963), 38, 905.
202. Biscarini, P.; Fusina, L.; Nivellini, G.; and Pelizzi, G. J. Chem. Soc., Dalton Trans. (1977), 664.
203. Deacon, G.B.; Green, J.H.S.; and Kynaston, W. Aust. J. Chem. (1966), 19, 1603.
204. Waters, D.N. and Basak, B. J. Chem. Soc. (A) (1971), 2733.
205. Manahan, S.E. and Iwamoto, R.T. Inorg. Chem. (1965), 4, 1409.
206. Eswein, R.P.; Howald, E.S.; Howald, R.A.; and Keeton, D.P. J. Inorg. Nucl. Chem. (1967), 29, 437.
207. Reynolds, G.F.; Scheffler, T.B.; and Wilkes, J.S.; Frank J. Seiler Research Laboratory Technical Report #0002, (1981).
208. Morris, D.F.C.; Short, E.L.; and Waters, D.N. J. Inorg. Nucl. Chem. (1963), 25, 975.
209. Quicksall, C.O. and Spiro, T.G. Inorg. Chem. (1966), 5, 2232.
210. Long, T.V.; Herlinger, A.W.; Epstein, E.F.; and Bernal, I. Inorg. Chem. (1970), 9, 459.
211. Easteal, A.J. and Angell, C.A. J. Phys. Chem. (1970), 74, 3987.
212. Desjardins, C.D.; Salter, R.S.; and Cadger, T.G. in "Proceedings of the Fourth International Symposium on Molten Salts", M. Blander, D.S. Newman, M.-L. Saboungi, G. Mamantov, and K. Johnson - Eds., pp. 146-162. The Electrochemical Society Softbound Proceedings Series, Pennington, NJ (1984).
213. Mennitt, P.G.; Shatlock, M.P.; Bartuska, V.J.; and Maciel, G.E. J. Phys. Chem. (1981), 85, 2087.
214. Ellis, P.D. Science (1983), 221, 1141.
215. Nakatsuji, H.; Kanda, K.; Endo, K.; and Yonezawa, T. J. Am. Chem. Soc. (1984), 106, 4653.
216. Ando, I. and Webb, G.A. "Theory of NMR Parameters", Academic Press, New York, (1983).
217. Davies, J.E.D. and Long, D.A. J. Chem. Soc. (A) (1968), 2054.
218. Adams, D.M.; Chatt, J.; Davidson, J.M.; and Gerratt, J. J. Chem. Soc. (1963), 2189.



219. Irish, D.E.; MacCarrol, B.; and Young, T.F. J. Chem. Phys. (1963), 39, 3436.
220. Creighton, J.A. and Lippincott, E.R. J. Chem. Soc. (1963), 5134.
221. Woodward, L.A. and Taylor, M.J. J. Chem. Soc. (A) (1962), 407.
222. Nakamoto, K., "Infrared Spectra of Inorganic and Coordination Compounds", J. Wiley & Sons, Inc., New York, (1963).
223. Adams, D.M. and Morris, D.M. J. Chem. Soc. (A) (1967), 1669.
224. Ross, S.D. "Inorganic Infrared and Raman Spectra", McGraw-Hill Book Co., New York (1972).
225. Crozier, E.D.; Aberding, N.; and Sundheim, B.R. J. Chem. Phys. (1983), 79, 939.
226. Ackermann, B.L.; Tsarbopoulos, A; and Allison, J. Anal. Chem. (1985), 57, 1768.
227. Bodner, R.L.; Greenberg, M.S.; and Popov, A.I. Spectrosc. Lett. (1972), 5, 489.